

TURBULENT STRUCTURE IN OPEN-CHANNEL FLOWS

(Translation of Doctoral Dissertation in Japanese)

by Iehisa NEZU

July 1977

Department of Civil Engineering
Kyoto University
Kyoto 606, Japan

CONTENTS

	Page
ABSTRACT	1
PART 1 TURBULENT STRUCTURE OVER SOLID BED	
CHAPTER 1 INTRODUCTION	4
CHAPTER 2 THEORETICAL CONSIDERATION ON TURBULENT STRUCTURE	
2.1 Introduction	
2.2 Basic equations of turbulent flow over smooth bed	
2.2.1 Budget of mean-flow energy	6
2.2.2 Budget of turbulent energy	8
2.3 Spectral density function of turbulent energy	
2.3.1 Relation between one- and three-dimensional spectra	10
2.3.2 Distribution of one-dimensional spectrum	10
2.3.3 Modelling of transport of turbulent energy	12
2.4 Subdivision of flow field and its turbulence characteristics	
2.4.1 Subdivision of open-channel flow field	14
2.4.2 Wall region ($y^+ \leq 100$)	14
2.4.3 Free-surface region ($0.6 \leq \xi \leq 1.0$)	15
2.4.4 Equilibrium region ($100R_* \leq \xi \leq 0.6$)	16
2.4.5 Overall distribution of mean velocity	17
2.5 Turbulence characteristics over rough bed	18
2.6 Mechanism of turbulence-production and structure of fluctuating Reynolds stress	
2.6.1 Qualitative explanation of bursting phenomenon	18
2.6.2 Probability density function of fluctuating velocity	19
2.6.3 Conditional probability distribution of fluctuating Reynolds stress	20
2.6.4 Behaviour of velocity fluctuations with a trigger level H	22
CHAPTER 3 METHOD OF TURBULENCE MEASUREMENT AND ITS ANALYSIS	
3.1 Introduction	25
3.2 Properties of dual-sensor hot-film anemometers	
3.2.1 Principle of hot-film anemometer	25
3.2.2 Directional sensitivity of hot-film sensor	26
3.2.3 Calibration of dual-sensor hot-film anemometer	27

3.3	Effect of various factors on the properties of hot-film anemometer	
3.3.1	Effect of the noise	27
3.3.2	Effect of the water temperature changes	28
3.3.3	Effect of the nonhomogeneity of velocity along the sensor	29
3.3.4	Other effects	29
3.4	Hydrogen-bubble technique	
3.4.1	Principle of hydrogen-bubble tracer and its analysis	30
3.4.2	Effects of various factors upon the hydrogen-bubble method	30

CHAPTER 4 EXPERIMENTAL CONSIDERATION ON TURBULENT STRUCTURE AND ENERGY BUDGET

4.1	Introduction	31
4.2	Experimental equipment and data analysis	31
4.3	Universal characteristics of turbulence intensities	32
4.3.1	Mean velocity distribution and friction velocity	33
4.3.2	Effect of the Reynolds number on turbulence intensities	34
4.3.3	Effect of the Froude number on turbulence intensities	35
4.3.4	Effect of the wall roughness on turbulence intensities	36
4.4	Relative turbulence intensity and Reynolds stress	
4.4.1	Relative turbulence intensity u'/U	38
4.4.2	Reynolds stress distribution	38
4.4.3	Correlation coefficients of Reynolds stress	39
4.5	Effect of the surface wave on turbulent structure	
4.5.1	Analysis of surface-wave fluctuations	40
4.5.2	Analysis of wall-pressure fluctuations	42
4.6	Spectral distribution of velocity fluctuation and characteristic eddy-scale	
4.6.1	Wave-number spectrum of each velocity component	44
4.6.2	Spectral distribution normalized by L_x	45
4.6.3	Local isotropy and dissipation spectrum	47
4.6.4	Characteristic eddy-scale and their relations	48
4.7	Turbulent energy budget in open-channel flow	
4.7.1	Turbulent energy dissipation	50
4.7.2	Production and diffusion of turbulent energy	52
4.7.3	Turbulent energy budget	54

CHAPTER 5 EXPERIMENTAL CONSIDERATION ON MECHANISM OF TURBULENCE PRODUCTION

5.1	Introduction	57
5.2	Probability distributions of the velocity fluctuations and the instantaneous Reynolds stress	
5.2.1	Probability density function of velocity and its higher moments	57
5.2.2	Probability density function of instantaneous Reynolds stress	59
5.2.3	Conditional probability distribution of instantaneous Reynolds stress	61
5.3	Internal structure of Reynolds stress and mechanism of turbulence-production	
5.3.1	Internal structure of Reynolds stress	64
5.3.2	Relative intensity of the different events	65
5.3.3	Mechanism of turbulence-production in the wall region and its prediction	68
5.3.4	Effect of wall roughness upon bursting events	69
5.3.5	Behaviour of velocity fluctuations when turbulence occurs	71
5.4	Periodic characteristics of the bursting phenomenon	
5.4.1	Brief recapitulation of the bursting period obtained previously	73
5.4.2	Discrimination criterion and definition of bursting period	75
5.4.3	Bursting period and its probability characteristics	77
5.5	Internal structure of bursting phenomenon	
5.5.1	Dependence of the bursting phenomenon upon the inner and outer parameters	79
5.5.2	Further suggestions on bursting phenomenon	81
5.6	Visual observation of bursting phenomenon	
5.6.1	Instantaneous velocity profiles in vertical plane	82
5.6.2	Instantaneous velocity profiles in horizontal plane	83

CHAPTER 6 PHYSICAL MODEL OF WALL TURBULENCE

6.1	Introduction	86
6.2	Π -eddy model	
6.2.1	Constitution of a Π -eddy model and its formulation	87
6.2.2	Turbulence intensities and Reynolds stresses evaluated by a Π -eddy	90
6.2.3	Spectral density functions of energy	91
6.2.4	Comparison of turbulence intensities with the experimental data	94
6.3	Renewal model	
6.3.1	Formulation of a renewal model	96
6.3.2	Further consideration of renewal model by taking account of the probability distribution of bursting period	99
6.3.3	Turbulent characteristics evaluated by the present renewal model	100
6.3.4	Explanation of the bursting process by the renewal model	103
6.4	Combined model	105

PART 2	TURBULENT STRUCTURE OVER PERMEABLE BED	
CHAPTER 7	INTRODUCTION	109
CHAPTER 8	INTERACTION BETWEEN MAIN AND SEEPAGE FLOWS	
8.1	Introduction	110
8.2	Theoretical consideration	
8.2.1	Basic equations of seepage flow	111
8.2.2	Analysis of turbulent fluctuations of seepage flow	113
8.2.3	Additional shear stress induced by seepage disturbances	116
8.3	Experimental consideration	
8.3.1	Experimental set-up and procedure	120
8.3.2	Mean flow characteristics of seepage flow	120
8.3.3	Mean flow characteristics of main flow	121
8.3.4	Examination of induced stress	122
CHAPTER 9	TURBULENT STRUCTURE WITH TRANSPIRATION	
9.1	Introduction	124
9.2	Theoretical consideration	
9.2.1	Basic equations over permeable smooth bed	125
9.2.2	The law of the wall with transpiration	128
9.2.3	The velocity defect law with transpiration	130
9.2.4	Flow behaviours when the transpiration rate is very large	131
9.2.5	Evaluation method of the friction velocity	132
9.2.6	Some turbulence characteristics	134
9.3	Experimental consideration on mean velocity distribution	
9.3.1	Experimental set-up and procedure	137
9.3.2	Wall shear stress or friction velocity	138
9.3.3	Mean velocity distribution	139
9.3.4	Examination of the variation of flow depth in the streamwise direction (backwater curve)	142
9.3.5	Relaminarization by the strong suction	143
9.4	Experimental consideration on turbulence characteristics	
9.4.1	Reynolds stress distribution	145
9.4.2	Turbulence intensities	145
9.4.3	Spectral distribution and characteristic eddy-scale	148
9.4.4	Turbulent energy budget	149
CONCLUDING REMARKS		151

ACKNOWLEDGEMENTS	156
ACADEMIC CAREER	156

FIGURES AND TABLES (a separate volume)

Chapter 1	Introduction	1
Chapter 2	Theoretical consideration on turbulent structure	2
Chapter 3	Method of turbulence measurement and its analysis	8
Chapter 4	Experimental consideration on turbulent structure and energy budget	13
Chapter 5	Experimental consideration on mechanism of turbulence-production	30
Chapter 6	Physical model of wall turbulence	43
Chapter 7	Introduction	
Chapter 8	Interaction between main and seepage flows	50
Chapter 9	Turbulent structure with transpiration	54

--- over ---

TURBULENT STRUCTURE IN OPEN-CHANNEL FLOWS

Abstract

Turbulent transport of momentum, heat and mass dominates many of the fluid flows found in physics, engineering and the environmental sciences. Intensive research on the dynamics of the wall turbulence in boundary layer, pipe or channel, especially in an air flow, has been performed by many investigators in the last twenty years. On the other hand, in hydraulics or river mechanics, we are rather concerned about the dynamics of turbulent open-channel water flow since it dominates the turbulent friction law, turbulent diffusion problem, sediment transport in the river field, the flow characteristics near the hydraulic structures and so on. Turbulence measurements in water flow were, however, begun only eight years ago with the development of hot-film anemometers. The detailed investigations on turbulent structure in open-channel flows are still very insufficient, compared with those of air flows in boundary layer or pipe.

So, in order to make clear the turbulent structure in open-channel flows theoretically and experimentally, this thesis deals systematically with the following seven problems:

- (1) Measurements of basic quantities of turbulence
- (2) Turbulent energy budget
- (3) Structure of fluctuating Reynolds-stress
- (4) Mechanism of turbulence-production

- (5) Modelling of turbulent shear flow
- (6) Interaction between main and seepage flows
- (7) Turbulent structure with transpiration

Since it may be very difficult to completely solve these problems, we consider phenomenologically the fundamental and universal characteristics in fully developed, two-dimensional turbulent open channel flows, by making use of both the spectral and probability density functions as statistically analytic tools.

As shown in Fig. A, this thesis consists of two parts, that is: Part 1 deals with the turbulent structure over smooth and rough solid beds, and Part 2 deals with that over permeable porous bed.

Firstly, Part 1 consists of six chapters. Chapter 1 is an introduction of solid-wall turbulence. Chapter 2 deals with theoretical consideration of turbulent structure, which can offer some theoretical predictions or analytical techniques for the turbulent mechanism. Chapter 3 describes the methods of turbulence measurements in water flows, i.e. hot-film anemometer and hydrogen bubble techniques. Chapter 4 deals with the problems of (1) and (2) mentioned above. In this chapter we experimentally investigate in detail the turbulent structure in terms of long-time average. Chapter 5 deals with (3) and (4). That is, the turbulent structure in terms of short-time average or the bursting phenomenon is investigated by making use of the conditional sampling technique and flow visualization. In Chapter 6,

we propose some new physical models of wall turbulence on a basis of the knowledge systematically obtained from the above investigations, and we try to explain the bursting phenomenon or turbulence characteristics even quantitatively.

Next, Part 2 consists of three chapters. Chapter 7 is an introduction of permeable-wall turbulence. Chapter 8 deals with (6), where an interaction between main and seepage flows which occurs near the loose porous bed is considered phenomenologically. Lastly, in Chapter 9 we make clear the turbulent structure with suction or injection through the bed, and intend to grope our way towards establishment of a reasonable control of turbulent flow by such a transpiration.

Many results obtained theoretically and experimentally in Part 1 and 2 are summarized at the end of this thesis as universal conclusions of turbulent structure in open-channel flows.

The present paper is an abridged translation of the dissertation (*in Japanese*) for the degree of Dr. Eng. in Kyoto University. Some main parts of this dissertation have been already published in English in *Jour. of Fluid Mech.*, *Proc. of Japan Soc. Civil Engrs* and others, where the more detailed descriptions of these results were given.

PART 1 Turbulent structure over solid bed

Chapter 1 Introduction

Fig. 1.1 shows a brief history of researches of turbulence. The enormous materials resulting from theoretical and experimental investigations on solid-wall turbulence in air flow (boundary layer or pipe flow) have become available at present. For example, the summary of these materials is found in the well-known books written by Monin & Yaglom (1971, 1975), Tennekes & Lumley (1971), Rotta (1972), Hinze (1975) and others.

On the other hand, the sufficient materials of turbulence characteristics in open-channel water flows have not been obtained still now. It is very interesting even in practice to investigate how the turbulent structure or the turbulence-production mechanism (bursting phenomenon) in open-channel flows would be influenced by the hydraulic parameters such as Reynolds number and Froude number and the wall roughness.

Thus, in this part, some systematical measurements of turbulent open-channel flows over smooth and rough beds have been done by making use of single- and dual-sensor hot-film anemometers and hydrogen bubble tracers in order to make clear the dynamics of turbulence, from both viewpoints of energy budget (*Chapter 4*) and turbulence production mechanism (*Chapter 5*). And subsequently, a few phenomenological turbulent models (a renewal model, a Π -eddy model and a combined model) have been proposed (*Chapter 6*).

References (Chapter 1)

- 1) Rouse, H. & Ince, S. : History of hydraulics, State Univ. of Iowa 1957.
- 2) Monin, A.S. & Yaglom, A.M. : Statistical fluid mechanics, MIT Press, vol.1, 1971.
- 3) Monin, A.S. & Yaglom, A.M. : Statistical fluid mechanics, MIT Press, vol.2, 1975.
- 4) Tennekes, H. & Lumley, J.L. : A first course in turbulence, MIT Press, 1972.
- 5) Rotta, J.C. : Turbulente Strömungen, Teubner, 1972.
- 6) Hinze, J.O. : Turbulence (2-nd edi.), McGraw-Hill, 1975.

Chapter 2 Theoretical consideration on turbulent structure

2.1 Introduction

2.2 Basic equations of turbulent flow over smooth bed

2.2.1 Budget of mean-flow energy

As shown in Fig. 2.1, U , V , and W denote the components of mean velocity, and u , v , and w the velocity fluctuation, and u' , v' and w' the r.m.s. values in x - (flow directional), y - (vertical to the bed) and z - (spanwise) directions, respectively. The equations of motion are given by

$$U \frac{\partial U}{\partial x} + V \frac{\partial U}{\partial y} = F_x - \frac{1}{\rho} \frac{\partial P}{\partial x} + \frac{\partial(-\overline{u^2})}{\partial x} + \frac{\partial(-\overline{uv})}{\partial y} + \nu \frac{\partial^2 U}{\partial y^2} \dots (2.1)$$

$$U \frac{\partial V}{\partial x} + V \frac{\partial V}{\partial y} = F_y - \frac{1}{\rho} \frac{\partial P}{\partial y} + \frac{\partial(-\overline{uv})}{\partial x} + \frac{\partial(-\overline{v^2})}{\partial y} \dots (2.2)$$

Since $|U| \gg |V| \gg |W| \approx 0$ in the normal, two-dimensional flow, Eqs. (2.1) and (2.2) become

$$\frac{\partial}{\partial y} (-\overline{uv} + \nu \frac{\partial U}{\partial y}) = -gI_s \dots (2.3)$$

$$P = \rho g (h - y) \cos \theta - \rho (\overline{v^2} - \overline{v_s^2}) \dots (2.4)$$

where, h is the flow depth and $I_s \equiv \sin \theta - \cos \theta \cdot \partial h / \partial x$ is the energy gradient.

Since the wall shear stress τ_0 is defined as $\tau_0 / \rho \equiv (-\overline{uv} + \nu \partial U / \partial y)|_{y=0} \equiv U_*^2$ (U_* is the friction velocity), the Reynolds stress distribution

is given by

$$\frac{-\overline{uv}}{U_*^2} = (1 - \xi) - \frac{1}{R_*} \frac{dU^+}{d\xi} \dots (2.5)$$

where, $\xi \equiv y/h$, $U^+ \equiv U/U_*$ and $R_* \equiv hU_*/\nu \gg 1$.

From (2.3), the energy equation of mean-flow is obtained as follows:

$$\int_0^1 \left(\frac{-\overline{uv}}{U_*^2} \right) \frac{dU^+}{d\xi} d\xi + \frac{1}{R_*} \int_0^1 \left(\frac{dU^+}{d\xi} \right)^2 d\xi = \frac{U_m}{U_*} \dots (2.6)$$

where, U_m is the bulk mean velocity.

Defining $E \equiv \nu (\partial U / \partial y)^2$ (direct-dissipation of the mean flow), $P \equiv -\overline{uw} \partial U / \partial y$ (turbulence-production) and the Darcy-Weisbach's friction factor f

$$\text{i.e. } l_s \equiv (f/h) \cdot (U_m^2 / 2g) \quad \dots\dots\dots (2.7)$$

(2.6) yields

$$\int_0^1 (P+E) \frac{h}{U_*^3} d\xi = \sqrt{\frac{2}{f}} \quad \dots\dots\dots (2.8)$$

or

$$\int_0^{R_*} (P+E) \frac{\nu}{U_*^4} dy^+ = \frac{U_m}{U_*} \quad \dots\dots\dots (2.9)$$

where, $y^+ \equiv U_* y / \nu$, and the (+)-suffix denotes the dimensionless quantity by U_* and ν in the following.

Now, by assuming the Prandtl's mixing-length model, that is:

$$-\overline{uw} \equiv l^2 (dU/dy)^2 \quad \dots\dots\dots (2.10)$$

(2.5) gives

$$\frac{dU^+}{dy^+} = \frac{2(1 - y^+/R_*)}{1 + \sqrt{1 + 4l^{+2}(1 - y^+/R_*)}} \quad \dots\dots\dots (2.11)$$

, and if R_* is very large,

$$\frac{dU^+}{dy^+} = \frac{2}{1 + \sqrt{1 + 4l^{+2}}} \quad \dots\dots\dots (2.12)$$

The mixing-length $l^+ \equiv lU_*/\nu$ may be reasonably given by van Driest(1956), as follows:

$$l^+ = \Gamma \cdot \kappa y^+, \quad \Gamma \equiv 1 - \exp(-y^+/A) \quad \dots\dots\dots (2.13)$$

where κ is a Karman's constant and A is a damping factor.

When y^+ is very large, or $l^+ \gg 1$, (2.12) yields a well-known logarithmic law, i.e. $U^+ = \kappa^{-1} \ln y^+ + B$ ($l^+ \gg 1$) (2.14)

When y^+ is very small, or $l^+ \ll 1$, (2.12) yields a velocity distribution in the viscous sublayer, i.e. $U^+ = y^+$ ($l^+ \ll 1$) (2.15)

A distribution combining (2.14) and (2.15) smoothly is numerically obtained from (2.11) and (2.13) with $\kappa=0.4$ and $A=27$.

Consequently, Fig. 2.2 shows some calculated curves of Reynolds stress $-\overline{uw}/U_*^2$, the direct-dissipation $E\nu/U_*^4 \equiv E^+$ and the turbulence-production $P\nu/U_*^4 \equiv P^+$. It should be noticed that $P^+ < E^+$ when $y^+ < \delta_s^+$ and $P^+ > E^+$ when $y^+ > \delta_s^+$, where $\delta_s^+ \approx 11.6$ is a thickness of viscous sublayer.

Fig. 2.3 shows the following results, that is:

$$\phi_E(y^+) \equiv \int_0^{y^+} E^+ dy^+, \quad \phi_P(y^+) \equiv \int_0^{y^+} P^+ dy^+ \quad \dots\dots\dots (2.16)$$

where, $\phi \equiv U_m/U_*$, $R_* \equiv U_m h/\nu = \phi R_e$.

ϕ_E approaches to 9.24 at $y^+ > 30$, irrespective of the Reynolds number Re . Since (2.9) becomes

$$\sqrt{2/f} = \phi_E(R_*) + \phi_P(R_*) \quad \dots\dots\dots (2.17)$$

f can be easily calculated, and is shown in Fig. 2.4, together with the Prandtl-Karman's formula, i.e.

$$\sqrt{2/f} = 5.75 \log Re \sqrt{f/2} + 3.0 \quad \dots (2.18)$$

A good agreement between (2.17) and (2.18) should be noticed.

From the above results, the following relations can be obtained.

$$\int_0^h E dy \doteq 9.24 U_*^3, \quad \int_0^h P dy \doteq (\sqrt{2/f} - 9.24) U_*^3 \quad \dots\dots (2.19)$$

2.2.2 Budget of turbulent energy

The basic equations of turbulent components can be written:

$$U_k \frac{\partial \overline{u_i u_j}}{\partial x_k} + \overline{u_k u_j} \frac{\partial U_i}{\partial x_k} + \overline{u_k u_i} \frac{\partial U_j}{\partial x_k} - \frac{p}{\rho} \left(\frac{\partial u_i}{\partial x_j} + \frac{\partial u_j}{\partial x_i} \right) + 2\nu \left(\frac{\partial u_i}{\partial x_k} \right) \left(\frac{\partial u_j}{\partial x_k} \right) + \frac{\partial}{\partial x_k} \left[\overline{u_i u_j u_k} + (\delta_{jk} u_i + \delta_{ik} u_j) \frac{p}{\rho} - \nu \frac{\partial \overline{u_i u_j}}{\partial x_k} \right] = 0 \quad \dots\dots\dots (2.20)$$

In the flow field of Fig. 2.1, (2.20) can be simplified as follows:

$$-\overline{uw} \frac{\partial U}{\partial y} + \frac{p}{\rho} \frac{\partial \overline{u}}{\partial x} = \epsilon_1 + \frac{1}{2} \frac{\partial}{\partial y} \left(\overline{u^2 v} - \nu \frac{\partial \overline{u^2}}{\partial y} \right) \quad \dots\dots\dots (2.21)$$

$$\frac{p}{\rho} \frac{\partial \overline{v}}{\partial y} = \epsilon_2 + \frac{1}{2} \frac{\partial}{\partial y} \left(\overline{v^2 v} + 2 \frac{\overline{pv}}{\rho} - \nu \frac{\partial \overline{v^2}}{\partial y} \right) \quad \dots\dots\dots (2.22)$$

$$\frac{p}{\rho} \frac{\partial \overline{w}}{\partial z} = \epsilon_3 + \frac{1}{2} \frac{\partial}{\partial y} \left(\overline{w^2 v} - \nu \frac{\partial \overline{w^2}}{\partial y} \right) \quad \dots\dots\dots (2.23)$$

where, $\epsilon_i \equiv \nu \left\{ \left(\frac{\partial \overline{u_i}}{\partial x} \right)^2 + \left(\frac{\partial \overline{u_i}}{\partial y} \right)^2 + \left(\frac{\partial \overline{u_i}}{\partial z} \right)^2 \right\} > 0 \quad \dots\dots\dots (2.24)$

In the same manner, the equation in respect to Reynolds stress can be written:

$$-\overline{v^2} \frac{\partial U}{\partial y} + \frac{p}{\rho} \left(\frac{\partial \overline{u}}{\partial y} + \frac{\partial \overline{v}}{\partial x} \right) = 2\nu \left[\left(\frac{\partial \overline{u}}{\partial x} \right) \left(\frac{\partial \overline{v}}{\partial x} \right) + \left(\frac{\partial \overline{u}}{\partial y} \right) \left(\frac{\partial \overline{v}}{\partial y} \right) + \left(\frac{\partial \overline{u}}{\partial z} \right) \left(\frac{\partial \overline{v}}{\partial z} \right) \right] + \frac{\partial}{\partial y} \left[\overline{v^2 u} + \frac{\overline{pu}}{\rho} - \nu \frac{\partial \overline{uv}}{\partial y} \right] \quad \dots\dots\dots (2.25)$$

Denoting $q^2 \equiv u^2 + v^2 + w^2$, $\epsilon \equiv \epsilon_1 + \epsilon_2 + \epsilon_3$ (2.26)

and adding (2.21)-(2.23), the equation of turbulent energy can be obtained as follows:

$$-\overline{uv} \frac{\partial U}{\partial y} = \epsilon + \frac{\partial}{\partial y} \left\{ \frac{\overline{q^2 v}}{2} + \frac{\overline{p}}{\rho} \cdot v - v \frac{\partial}{\partial y} \left(\frac{\overline{q^2}}{2} \right) \right\} \dots (2.27)$$

With $\text{Tr} \equiv \overline{q^2 v} / 2$ (diffusion of turbulent energy) and $R \equiv \overline{pv} / \rho$ (diffusion of pressure energy), (2.27) can be also written:

$$\frac{PA}{U_*^3} = \frac{\epsilon h}{U_*^3} + \frac{\partial}{\partial \xi} \left(\frac{T_r + R}{U_*^3} \right) - \frac{1}{R_*} \frac{\partial^2}{\partial \xi^2} \left(\frac{\overline{q^2}}{2U_*^2} \right) \dots (2.28)$$

When R_* is very large, (2.28) can be approximated

$$P = \epsilon + \partial(T_r + R) / \partial y \dots (2.30)$$

From (2.19) and (2.30), the total energy loss is expressed by

$$\int_0^h (E + \epsilon) dy = U_*^2 U_m = (\tau_0 / \rho) \cdot U_m \dots (2.31)$$

Now, denoting

$$T_{r1} = \frac{\overline{u^2 v}}{2}, T_{r2} = \frac{\overline{v^2 \cdot v}}{2}, T_{r3} = \frac{\overline{w^2 \cdot v}}{2}, PV_1 = \frac{\overline{p}}{\rho} \frac{\partial u}{\partial x}, PV_2 = \frac{\overline{p}}{\rho} \frac{\partial v}{\partial y}, PV_3 = \frac{\overline{p}}{\rho} \frac{\partial w}{\partial z} \dots (2.32)$$

(2.21)-(2.25) become nearly to

$$\left. \begin{aligned} P + PV_1 &= \epsilon_1 + \partial T_{r1} / \partial y \\ PV_2 &= \epsilon_2 + \partial(T_{r2} + R) / \partial y \\ PV_3 &= \epsilon_3 + \partial T_{r3} / \partial y \end{aligned} \right\} \dots (2.33)$$

$$-\overline{v^2} \frac{\partial U}{\partial x} + \frac{\overline{p}}{\rho} \left(\frac{\partial u}{\partial y} + \frac{\partial v}{\partial x} \right) = \frac{\partial}{\partial y} \left(\overline{v^2 u} + \frac{\overline{pv}}{\rho} \right) \dots (2.34)$$

Well, since $\partial u / \partial x > 0$ correlates more strongly with $p < 0$ than $p > 0$ according to the Bernoulli's equation, it may be suggested that

$$PV_2 + PV_3 = -PV_1 > 0 \dots (2.35)$$

From (2.33)-(2.35), an internal mechanism model of turbulent energy flux may be considered, as shown in Fig. 2.5. This model suggests strongly that

- (1) $u' > v'$ and $u' > w'$ (from (2.33))
- (2) the re-distribution of turbulent energy among u' , v' and w' may occur in the smaller-scale turbulence.
- (3) thus, an isotropic approximation may be valid in the

smaller-scale turbulence, and so the turbulent dissipation is nearly given by

$$\epsilon_1 = \epsilon_2 = \epsilon_3 = \frac{\epsilon}{3} = 5\nu \overline{\left(\frac{\partial u}{\partial x}\right)^2} \dots\dots (2.38)$$

2.3 Spectral density function of turbulent energy

2.3.1 Relation between one- and three-dimensional spectra

Define three-dimensional spectrum $E(k)$ and one-dimensional spectrum $S(k)$ in the following:

$$\int_0^\infty \overline{q^2} \cdot E(k) dk = \frac{\overline{q^2}}{2} \dots\dots\dots (2.39) \quad \left\{ \begin{array}{l} \int_0^\infty u'^2 \cdot S_u(k_1) dk_1 = u'^2, \quad \int_0^\infty v'^2 \cdot S_v(k_1) dk_1 = v'^2, \\ \int_0^\infty w'^2 \cdot S_w(k_1) dk_1 = w'^2 \quad \dots\dots\dots (2.40) \end{array} \right.$$

Then, in the isotropic turbulence we can obtain

$$S_u(k_1) = \int_{k_1}^\infty \frac{E(k)}{k} \left(1 - \frac{k_1^2}{k^2}\right) dk \quad \dots (2.41)$$

$$S_v(k_1) = S_w(k_1) = \frac{1}{2} \left(S_u(k_1) - k_1 \frac{\partial S_u(k_1)}{\partial k_1} \right) \quad \dots (2.42)$$

2.3.2 Distribution of one-dimensional spectrum *)

The spectral space can be divided into three subranges, as described in the following.

(a) Productive subrange (large-scale eddy)

As shown in Fig. 2.5, there exists a strong interaction between the large-eddy and mean flow, resulting in production of turbulent energy. Its characteristic length is given by a mean-eddy scale L_x (integral scale). In this subrange, Tchen(1953) gave a -1 power law that $S_u(k) \sim k^{-1}$.

(b) Viscous subrange (small-scale eddy)

This characteristic length is given by the Taylor microscale λ or the Kolmogoroff microscale η , as follows:

$$\lambda \equiv \sqrt{15 \nu u'^2 / \epsilon} \equiv \lambda_x \equiv \left(\int_0^\infty k^2 \cdot S_u(k) dk \right)^{-1/2} \dots\dots\dots (2.43) \quad , \quad \eta \equiv (\nu^3 / \epsilon)^{1/4} \dots\dots\dots (2.44)$$

This subrange may be divided into two stages: one is the initial stage where λ is dominant (-3 power law) and another is

*) Refer to our paper published in *Proc. of JSCE, No.241, pp.155-168, 1975.*

the final stage where η is dominant (-7 power law).

(c) Inertial subrange (intermediate-scale eddy)

When the Reynolds number $R_L \equiv u' L_x / \nu$ is very large, there is an intermediate subrange between (a) and (b) ranges (see (2.52)), where the energy cascade process occurs and the $-5/3$ power law is valid:

$$S_u(k) = C u'^{-2} \cdot \epsilon^{2/3} k^{-5/3} \dots\dots\dots (2.47)$$

where, C is a Kolmogoroff's universal constant.

The above results are summarized in Table 2.1.

Well, we consider the overall distribution of spectrum. Firstly, as an interpolated relation between (a) and (c) ranges, the following Karman's formula can be here adopted.

$$S_u(k) = (2/\pi) L_x [1 + (k/k_0)^2]^{-5/4} \dots\dots\dots (2.48)$$

Denote $k_0 \equiv \alpha L_x^{-1}$, ($\alpha \sim 1$) $\dots\dots\dots (2.49)$

and, since (2.48) must coincide with (2.47) when $k \gg k_0$

$$\epsilon = K \cdot u'^3 / L_x \dots\dots\dots (2.50) \quad \text{where, } K \equiv (2/\pi C)^{3/2} \alpha^{3/2} \dots\dots\dots (2.51)$$

From (2.43), (2.44) and (2.50), the following relations are obtained.

$$L_x / \eta = \alpha^{3/2} (2/\pi C)^{3/2} R_L^{3/4}, \quad L_x / \lambda = \alpha^{3/4} / \sqrt{15} \cdot (2/\pi C)^{3/4} R_L^{1/2} \dots\dots\dots (2.52)$$

When R_L is infinitely large, $L_x \gg \lambda > \eta$ and then

$$1 \doteq \int_0^\infty \frac{2}{\pi} L_x [1 + (k/k_0)^2]^{-5/4} dk = B(1/2, 1/3) L_x k_0 / \pi$$

$$\therefore \alpha = \pi / B(1/2, 1/3) = 0.746 \dots\dots\dots (2.53)$$

where, B(m,n) is the Beta function.

Next, as an interpolated relation between (b) and (c) ranges, the following Heisenberg's formula can be also adopted.

$$\frac{q^2}{2} \cdot E(k) = \left(\frac{8}{9K_H} \right)^{2/3} \epsilon^{2/3} k^{-5/3} \left(1 + \frac{8}{3K_H^2} \frac{\nu^3}{\epsilon} k^4 \right)^{-4/3} \dots\dots\dots (2.54)$$

Since an isotropic approximation may be valid in both (b) and (c) ranges (small-scale turbulence) as mentioned previously, the following asymptotic relations are obtained by (2.41).

When $k \ll \eta^{-1}$, $S_u(k) = \frac{18}{55} \cdot \frac{1}{u'^2} \left(\frac{8\epsilon}{9K_H} \right)^{2/3} k^{-5/3} \dots\dots\dots (2.55)$

When $k \gg \eta^{-1}$, $S_u(k) = \frac{2}{63} \cdot \frac{1}{u'^2} \left(\frac{K_H \epsilon}{2\nu^2} \right)^2 k^{-7} \dots\dots\dots (2.56)$

By comparison with (2.47) and (2.55),

$$K_H = (8/9)(55C/18)^{-3/2} \dots\dots\dots (2.57)$$

Moreover, the spectrum of $\hat{k} \equiv L_x \cdot k$ must satisfy a second-order relation (dissipation spectrum), that is:

$$\int_0^{\infty} \hat{k}^2 S_u(k) \cdot L_x^{-1} d\hat{k} = (L_x/\lambda)^2 = \frac{\alpha^{5/2}}{15} \left(\frac{2}{\pi C}\right)^{3/2} R_L \dots\dots\dots (2.61)$$

Well, the overall spectral distribution can be numerically obtained by blending with (2.48) and (2.54), by using (2.41) and (2.42), as described in the following flow-chart.

(1) Calculate tentatively with $\alpha=0.746$ (Eq. (2.53))

$$S_u(k) L_x^{-1} \begin{cases} = \frac{2}{\pi} (1 + (\hat{k}/\alpha)^2)^{-5/6} ; & (0 \leq \hat{k} < 0.8 L_x \lambda^{-1}) \\ = \frac{55}{9\pi} \alpha^{5/2} \int_{\hat{k}}^{\hat{k}_{\infty}} (1 + B' x^4)^{-4/3} (x^{-8/3} - \hat{k}^2 x^{-14/3}) dx ; & (0.8 L_x \lambda^{-1} \leq \hat{k}) \end{cases}$$

where, $B' \equiv (567/55)^{-3/4} B$, $\hat{k}_{\infty} \equiv 10(L_x/\eta)$.

(2) Denoting $\int_0^{\hat{k}_{\infty}} S_u(k) L_x^{-1} d\hat{k} \equiv \beta$,
if $|\beta-1| > 0.01$, then renew α and re-calculate (1).

(3) If $|\beta-1| < 0.01$, calculate the errors of $\epsilon_s \equiv |\beta-1|$ and
 $\epsilon_d \equiv |(\lambda/L_x)^2 \int_0^{\hat{k}_{\infty}} D_u(\hat{k}) d\hat{k} - 1|$.

(4) Calculate $S_v(k)$ by using (2.42).

Fig. 2.6 shows these results obtained with $C=0.5$, which satisfy accurately (2.40) and (2.61) since $\epsilon_s \sim 10^{-3}$ and $\epsilon_d \sim 10^{-2}$ at most. Fig. 2.7 shows the energy spectrum $kS(k)$.

When \hat{k}_{50} is defined as $\int_0^{\hat{k}_{50}} S_u(k) dk \equiv 0.5$, it should be noticed that $\hat{k}_{50} \approx 1$, where the energy is dominantly contained (productive subrange).

The dissipation spectrum $D(k)=k^2 S(k)$ is also shown in Fig. 2.8.

The larger R_L is, the stronger the turbulent dissipation becomes at the higher wave number.

2.3.3 Modelling of transport of turbulent energy

Many investigators since Richardson have recognized that the turbulent energy produced in the productive subrange was transported

into the smaller-scale eddies *via* a cascade process, and eventually dissipated into heat energy. This phenomenological change process of energy may be analogous to that of 'water service', as shown in Fig. 2.9. According to this model, the rate ϵ of turbulent dissipation can be evaluated from three different methods:

(A) 'Reservoir'-method (corresponds to productive subrange)

$$\text{Use } \epsilon = K \cdot u'^3 / L_x \quad (\text{Eq. (2.50)}).$$

(B) 'Conduit'-method (corresponds to inertial subrange)

$$\text{Use } \epsilon = [u'^2 k^{3/2} S_u(k) / C]^{3/2} \quad (\text{Eq. (2.47)}).$$

(C) 'Terminal tube'-method (corresponds to viscous subrange)

$$\text{Use } \epsilon = 15 \nu u'^2 \int_0^\infty k^2 S_u(k) dk \quad (\text{Eq. (2.43)}).$$

(C)-method corresponds, so to say, to a summation of 'the terminal branch tubes'.

(B)-method corresponds, so to say, to 'a flow meter' set at any section (k). Fig. 2.10 shows an universal constant C summarized by Bradshaw(1967). From this figure, C=0.5 was here adopted. Consequently, when an existence of inertial subrange is recognized, ϵ can be easily evaluated from (B)-method.

(A)-method corresponds, so to say, to a measurement of 'outflow from the reservoir'. K can be determined from (2.51), and its results are shown in Fig. 2.11. K decreases monotonously with increase of R_L , and approaches nearly to a constant at $R_L \approx 1000$. Fig. 2.12 also shows the spectra at the lower Reynolds number, which give the values of α and K. On the other hand, Rotta(1972) obtained the values of K in the region of $R_L = 0 - 85$, in the different method with the above. His results agree well with our ones, as seen in Fig. 2.11. And, he gave the following asymptotic relations, that is :

$$K_0 \equiv \lim_{R_L \rightarrow 0} K = \frac{15 \pi}{2 R_L} \dots\dots\dots (2.62)$$

$$K_\infty \equiv \lim_{R_L \rightarrow \infty} K = 2(3\tau/2)^{3/2} (55C/18)^{-3/2}, \quad (\tau = 0.5) \dots\dots\dots (2.63)$$

(2.63) also coincides very well with our results.

2.4 Subdivision of flow field and its turbulence characteristics^{*})

2.4.1 Subdivision of open-channel flow field

Since there may exist an analogy between spectral and wall-turbulence spaces, as described in Fig. 2.13, an open-channel flow field can be also divided into three subregions (see Fig. 2.14), in the same manner as spectral space.

(1) Wall region ($y^+ \lesssim 100$)

This region corresponds to an inner layer in boundary layer, and is dominated by U_ and ν (inner parameters). As mentioned later, the bursting phenomenon occurs most remarkably in this region.*

(2) Free-surface region ($0.6 \lesssim \xi \lesssim 1.0$)

This region corresponds to an outer layer, where the turbulent characteristics are dominated by U_{max} and h (outer parameters).

(3) Equilibrium region ($100R_*^{-1} \lesssim \xi \lesssim 0.6$)

This is an intermediate region between (1) and (2) subregions, where a dynamically equilibrium state for turbulent energy budget, i.e. $P \approx \epsilon$, is nearly realized.

Well, because it may be most reasonable to choose the rate of dissipation ϵ as an essential basic quantity (see Fig. 2.9 or 2.13), we consider the turbulence characteristics in each region on a basis of the above.

2.4.2 Wall region ($y^+ \lesssim 100$)

We have confirmed experimentally that

$$\epsilon\nu/U_*^4 = A_1 \cdot (y^+)^{-1}, \quad (A_1 \text{ is constant}) \dots\dots\dots (2.64)$$

$$L_x^+ \equiv L_x U_* / \nu = A_2 \cdot (y^+)^{1/2}, \quad (A_2 \text{ is constant}) \dots\dots\dots (2.65)$$

From (2.50),

$$u'/U_* = A_3 \cdot (y^+)^{-1/6}, \quad A_3 \equiv (A_1 A_2 / K)^{1/6} \dots\dots\dots (2.66)$$

u'/U_* has a $-1/6$ power law since A_3 becomes nearly constant when R_L is very large (see Fig. 2.11).

^{*}) Refer to our paper published in *Proc. of JSCE, No.241, pp.155-168, 1975.*

Next, assuming phenomenologically that

$$\frac{u'}{U_*} = A_4 \cdot y^+ \frac{dU^+}{dy^+} \quad (A_4 \text{ is a proportional constant}) \dots\dots\dots (2.67)$$

we can also obtain from (2.66)

$$U^+ = A_5 \{ A_6 - (y^+)^{1/6} \}, \quad (y^+ > 30) \dots\dots\dots (2.68)$$

By comparison between (2.14) and (2.68),

$$A_5 \equiv 6A_3 / A_4 = 6\kappa^{-1} (y^+)^{1/6} \approx 11.4\kappa^{-1} \dots\dots\dots (2.69)$$

Thus, when $\kappa=0.4$, A_5 becomes about 28.5. Fig. 2.15 shows the curves of (2.14) and (2.68), together with the van Driest's curve by using (2.12) and (2.13). When $y^+ > 30$, these curves coincide fairly well with each other and the experimental values.

2.4.3 Free-surface region ($0.6 \leq \xi \leq 1.0$)

We have confirmed experimentally that

$$\epsilon h / U_*^3 = B_1 (\xi' + B_2) \dots\dots\dots (2.70)$$

$$L_x / h = B_3 \dots\dots\dots (2.71)$$

where, $\xi' \equiv 1 - \xi$, B_1 , B_2 and B_3 are constant.

Thus, from (2.50),

$$\frac{u'}{U_*} = \left(\frac{B_1 B_3}{K} \right)^{1/3} (\xi' + B_2)^{1/3} \dots\dots (2.72)$$

By the way, (2.13) becomes no longer valid in this region, and so by assuming that when the mean-eddy scale L_{xy}/h is constant, the mixing-length l/h also becomes constant, we can obtain from (2.11)

$$U_{\max}^+ - U^+ = B_4 \xi'^{2/3}, \quad B_4 \equiv (2/3)(l/h)^{-1} \dots\dots\dots (2.73)$$

Since the energy budget in this region can be expressed as

$T \equiv \partial T_r / \partial y \approx -\epsilon$ from (2.30), the following relation can be also obtained by assuming $T_r \equiv \overline{q^2 v} / 2 \sim U_*^3 \partial l / \partial y$ (Zagustin et al. (1969)'s hypothesis):

$$\frac{d^2(l/h)}{d\xi'^2} = -B_5 (\xi' + B_2), \quad (B_5 \text{ is constant}) \dots\dots\dots (2.74)$$

With the boundary conditions that $\xi'=0 : d(l/h)/d\xi'=0$, $\xi'=1 : l/h=0$ and $d(l/h)/d\xi'=-\kappa$,

$$l/h = (\kappa/3) \{ (1 - \xi'^3) + B_6 (1 - \xi')^2 (1 + 2\xi') \} \dots\dots\dots (2.75)$$

where, $B_5 = 2\kappa / (1 + 2B_2)$, $B_6 = B_2 / (1 + 2B_2)$.

From (2.11) and (2.75), we can approximately obtain

$$U_{max}^+ - U^+ = \frac{2}{\kappa} \left[\tanh^{-1} \xi'^{3/2} - \frac{3}{2} B_0 \left\{ \left(\frac{4\xi' + 5}{\xi' + 1} \right) \sqrt{\xi'} - 5 \tanh^{-1} \sqrt{\xi'} \right\} \right] \\ \approx \frac{2}{\kappa} \left[\tanh^{-1} \xi'^{3/2} + \frac{3}{2} B_0 \frac{\xi'^{3/2}}{\xi' + 1} \right] \quad \dots\dots\dots (2.76)$$

Fig. 2.16 shows the results of (2.75) with $\kappa=0.4$ and $B_2=0.0, 0.1$ and 0.2 , together with the following experimental formula obtained by Nikuradse:

$$l/h = 0.14 - 0.08\xi'^2 - 0.06\xi'^4 \quad \dots\dots (2.77)$$

(2.75) agrees fairly well with (2.77), and their mixing-length becomes nearly constant in the free-surface region, as described in (2.73).

Fig. 2.17 shows the distributions of velocity defect law obtained from (2.73) and (2.76), together with the numerical solution of (2.11) and (2.77). A very good agreement among them is noticeable in this free-surface region.

2.4.4 Equilibrium region ($100R_*^{-1} \lesssim \xi < 0.6$)

Although an existence of equilibrium region in a precise term (i.e. $P=\epsilon$) may not be expected when R_L is comparably small, this region becomes $\xi \lesssim 0.6$ by assuming that the turbulence may be nearly in equilibrium state if $|P - \epsilon|/\epsilon \lesssim 20\%$. Consequently, this region is expected to have a similarity law or self-consistency in the turbulent structure, in a same manner as inertial subrange.

Since its characteristic scales are y and $\sqrt{\tau/\rho}$, the dimensional analysis gives

$$\epsilon h / U_*^3 = C_1 (1 - \xi)^{3/2} \xi^{-1} \quad \dots\dots\dots (2.78)$$

Or, by using $\sqrt{\tau_0/\rho} \equiv U_*$ as a characteristic velocity scale, nearly

$$\epsilon h / U_*^3 = C_2 \xi^{-1} \quad \dots\dots\dots (2.79)$$

Because the exponent of ξ in L_x/h changes from $1/2$ to 0 in this region, we can obtain from (2.50) and (2.78):

$$\frac{u'}{U_*} \begin{cases} \sim (1 - \xi)^{1/2} \xi^{-1/6} & \text{when } L_x/h \sim \xi^{1/2} \\ \sim (1 - \xi)^{1/2} \xi^{-1/6} & \text{when } L_x/h \sim \text{const.} \end{cases} \quad \dots (2.80)$$

or from (2.50) and (2.79):

$$\frac{u'}{U_*} \begin{cases} \sim \xi^{-1/6} & \text{when } L_x/h \sim \xi^{1/2} \\ \sim \xi^{-1/6} & \text{when } L_x/h \sim \text{const.} \end{cases} \quad \dots (2.81)$$

Next, since the energy budget in this region is

$$\frac{Ph}{U_*^3} \equiv (1-\xi) \frac{dU^+}{d\xi} \approx \frac{\epsilon h}{U_*^3} ,$$

by substituting (2.78) we can obtain

$$U_N \equiv U_{max}^+ - U^+ = -C_1 [2 \{ \ln(1 - \sqrt{1-\xi}) + \sqrt{1-\xi} \} - \ln \xi] \dots\dots\dots (2.82) .$$

On the other hand, Karman obtained the following equation by choosing l and $\sqrt{\tau/\rho}$ as characteristic scales and applying a similarity law:

$$U_K \equiv U_{max}^+ - U^+ = -\kappa^{-1} \{ \ln(1 - \sqrt{1-\xi}) + \sqrt{1-\xi} \} \dots\dots\dots (2.83) .$$

And also, (2.14) of Prandtl can be extended into this region,

which results in $U_P \equiv U_{max}^+ - U^+ = -\kappa^{-1} \ln \xi \dots\dots\dots (2.84)$

Consequently, $U_N = \kappa C_1 \frac{(2U_K - U_P)}{(2-1)} \dots\dots\dots (2.85)$

Since C_1 is about 3 (see Chapter 4) and thus $\kappa C_1 \approx 1$, (2.82) can be deduced by averaging (2.83) of Karman and (2.84) of Prandtl weighted with a ratio of 2 to -1. This fact suggests that this region overlaps to some extent with the wall region. Fig. 2.18 shows U_N , U_K and U_P obtained from the above. And, their agreement is also good.

2.4.5 Overall distribution of mean velocity

Since we will deal in detail with the overall distributions of turbulence characteristics in Chapter 4, we here consider only those of mean velocity. Because a fully developed open-channel flow may be dominated by an active motion or local similarity, as will be shown in Chapter 4, the previous consideration on a basis of the mixing-length theory is still valid. So, it is an essential work to determine accurately the distribution of mixing-length. Fig. 2.19 shows the numerical solutions of (2.11) obtained by using (2.77) multiplied by the damping factor of (2.13), together with the experimental values (see Chapter 4). A good agreement between the both is noticeable. And, it is concluded that even (2.14) of Prandtl is applicable fairly accurately in $y^+ > 30$.

2.5 Turbulence characteristics over rough bed

In this section we have estimated the effect of wall-roughness upon the turbulence characteristics, by comparison with those over the smooth bed obtained in previous sections. However, some estimations obtained in this section are omitted here since the effect of wall-roughness will be in detail investigated in Chapter 4.

2.6 Mechanism of turbulence-production and structure of fluctuating Reynolds stress *)

2.6.1 Qualitative explanation of bursting phenomenon

Intensive experimental researches on the bursting phenomenon have been performed by making use of visual methods or conditional point-measurements since it was confirmed that the bursting process played an essential role for turbulence-production mechanism near the wall in a turbulent boundary layer (Kline et al. 1967, 1971), a pipe (Corino et al. 1969) or an open-channel flows (Grass 1971). They found by flow visualization that a sequence of the bursting events had a quasi-cyclic process; that is, it shows a periodic motion on the average in space and time, but not perfectly periodic at one place in time nor at one time in space. For example, Corino & Brodkey (1969) presented visual sketches of a sequence of the bursting events near the wall as shown in Fig. 2.20.

On the basis of these qualitative results, some researchers have attempted to obtain more quantitative knowledge about the structure of the Reynolds stress, i.e. turbulence-production, by using point measurements. They divided the plane of u and v into four quadrants, as shown in Fig. 2.21, in order to evaluate the contribution of the ejections and sweeps to the Reynolds stress.

This section will show that the conditional probability distribution of the Reynolds stress may be introduced theoretically by making use of the cumulant expansion method for the two variables

*) Refer to our paper published in *Jour. of Fluid Mech.*, vol. 80, pp. 99-128, 1977.

u and v, in order to predict the magnitude of the contribution to the Reynolds stress from each event.

2.6.2 Probability density function of fluctuating velocity

Denoting the joint probability function of $\hat{u} \equiv u/u'$ and $\hat{v} \equiv v/v'$ by $p(\hat{u}, \hat{v})$, its characteristic function by $\Phi(\xi, \eta)$, the moment of $\hat{u}^j \hat{v}^k$ by M_{jk} and the corresponding cumulant by Q_{jk} , the following definitions can be given :

$$\Phi(\xi, \eta) = \iint_{-\infty}^{\infty} \exp\{i(\hat{u}\xi + \hat{v}\eta)\} p(\hat{u}, \hat{v}) d\hat{u} d\hat{v}, \quad (2.90)$$

$$M_{jk} = \frac{1}{i^{j+k}} \frac{\partial^{j+k}}{\partial \xi^j \partial \eta^k} \Phi(\xi, \eta) \Big|_{\xi=\eta=0}, \quad (2.91)$$

$$Q_{jk} = \frac{1}{i^{j+k}} \frac{\partial^{j+k}}{\partial \xi^j \partial \eta^k} \ln \Phi(\xi, \eta) \Big|_{\xi=\eta=0}. \quad (2.92)$$

Expanding $\Phi(\xi, \eta)$ in a Taylor series about $\xi = \eta = 0$ yields

$$\Phi(\xi, \eta) = \sum_{n=0}^{\infty} \frac{1}{n!} \left(\xi \frac{\partial}{\partial \xi'} + \eta \frac{\partial}{\partial \eta'} \right)^n \Phi(\xi', \eta') \Big|_{\xi'=\eta'=0}. \quad (2.93)$$

Thus M_{jk} and Q_{jk} correspond to the coefficients in Taylor expansions of $\Phi(\xi, \eta)$ and $\ln \Phi(\xi, \eta)$ respectively. The relations between the moments and the cumulants are successively obtained by making use of (2.91)-(2.93).

Now, since $M_{10} = \bar{u} = 0$, $M_{01} = \bar{v} = 0$, $M_{20} = \overline{u^2} = 1$, $M_{02} = \overline{v^2} = 1$ and $M_{11} = \overline{uv}/u'v' = -R < 0$ (correlation coefficient), the following can be obtained:

$$\left. \begin{aligned} Q_{00} = 1, \quad Q_{10} = 0, \quad Q_{20} = 1, \quad Q_{11} = -R, \quad Q_{30} = M_{30}, \quad Q_{21} = M_{21}, \\ Q_{40} = M_{40} - 3, \quad Q_{31} = M_{31} + 3R, \quad Q_{22} = M_{22} - 2R^2 - 1, \dots \end{aligned} \right\} \quad (2.94)$$

Q_{jk} for $j < k$ can be obtained by merely exchanging j and k in the terms of Q_{jk} for $j \geq k$.

In turbulent phenomena the cumulants of extremely high order can usually be neglected, and even in the theory of isotropic turbulence the fourth-order cumulant terms are sometimes discarded, e.g. by Rotta (1972). This suggests that approximation by the lower-order cumulants may be valid for phenomena mainly depending upon lower-order moments, because a cumulant is considered to be a measure of the deviation from a Gaussian distribution.

Taking into account the cumulants of less than fourth order, the following Taylor series can be obtained from (2.92)-(2.94):

$$\ln \Phi(\xi, \eta) = -\frac{1}{2}(\xi^2 - 2R\xi\eta + \eta^2) + \sum_{j+k=3}^4 i^{j+k} \frac{Q_{jk}}{j!k!} \xi^j \eta^k. \quad (2.95)$$

Through an inverse transformation of (2.90) in which the terms of $\Phi(\xi, \eta)$ of less than fourth order are taken into account, $p(\hat{u}, \hat{v})$ can be written as

$$\begin{aligned} p(\hat{u}, \hat{v}) &= \frac{1}{2\pi} \iint_{-\infty}^{\infty} \Phi(\xi, \eta) e^{-i(\hat{u}\xi + \hat{v}\eta)} d\xi d\eta \\ &= G(\hat{u}, \hat{v}) + \sum_{j+k=3}^4 (-1)^{j+k} \frac{Q_{jk}}{j!k!} \frac{\partial^{j+k} G(\hat{u}, \hat{v})}{\partial \hat{u}^j \partial \hat{v}^k} \end{aligned} \quad (2.96)$$

$$\equiv G(\hat{u}, \hat{v}) \left[1 + \sum_{j+k=3}^4 \frac{Q_{jk}}{j!k!} H_{jk}(\hat{u}, \hat{v}) \right], \quad (2.97)$$

where $G(\hat{u}, \hat{v})$ is the Gaussian distribution for two variables, defined as

$$G(\hat{u}, \hat{v}) \equiv \frac{1}{2\pi(1-R^2)^{\frac{1}{2}}} \exp \left\{ -\frac{\hat{u}^2 + 2R\hat{u}\hat{v} + \hat{v}^2}{2(1-R^2)} \right\}, \quad (2.98)$$

and $H_{jk}(\hat{u}, \hat{v})$ is a Hermite polynomial in two variables.

(2.97) represents a special form of joint probability density distribution of the Gram-Charlier type. According to Frenkiel & Klebanoff (1973), the generalized Gram-Charlier distribution in the following form extended by Kampé de Fériet (1966) should be used when higher-order terms are needed:

$$p(\hat{u}, \hat{v}) = G(\hat{u}, \hat{v}) \sum_{j+k=0}^{\infty} \frac{1}{j!k!} \overline{H}_{jk}(\hat{u}, \hat{v}) H_{jk}(\hat{u}, \hat{v}), \quad (2.99)$$

where $\overline{H}_{jk}(\hat{u}, \hat{v})$ is an adjoint Hermite polynomial in two variables (see Frenkiel & Klebanoff 1973).

The probability distribution of one variable is much simpler and is derived in the same manner as (2.96):

$$p(\hat{u}) = G(\hat{v}) + \sum_{j=3}^4 (-1)^j \frac{Q_{j0}}{j!} \frac{\partial^j}{\partial \hat{u}^j} G(\hat{u}), \quad G(\hat{u}) \equiv \frac{1}{(2\pi)^{\frac{1}{2}}} \exp \left(-\frac{\hat{u}^2}{2} \right), \quad (2.100)$$

or
$$p(\hat{u}) = G(\hat{u}) \left\{ 1 + \frac{1}{8} Q_{30}(\hat{u}^3 - 3\hat{u}) + \frac{1}{24} Q_{40}(\hat{u}^4 - 6\hat{u}^2 + 3) \right\}. \quad (2.101)$$

When all cumulants Q_{jk} in (2.97) or (2.101) with $j+k \geq 3$ are equal to zero, the Gram-Charlier distribution becomes the same as the Gaussian one, and thus it may be said that Q_{jk} gives a measure of the skewness or intermittency of the distribution.

Now consider the probability distribution $p_w(w)$ of the normalized Reynolds stress $w \equiv uv/\bar{u}\bar{v}$. By a change of variables (2.97) may be reduced to

$$\begin{aligned} p_w(w) &= \int_{-\infty}^{\infty} \frac{R}{|\hat{u}|} p(\hat{u}, -Rw/\hat{u}) d\hat{u} \\ &= \frac{R}{\pi(1-R^2)^{\frac{1}{2}}} \exp \left(\frac{R^2 w}{1-R^2} \right) \int_0^{\infty} \exp \left(-\frac{\hat{u}^2 + R^2(w/\hat{u})^2}{2(1-R^2)} \right) \\ &\quad \times \left[1 + \sum_{j+k=3}^4 \frac{Q_{jk}}{j!k!} \frac{1}{2} \{ H_{jk}(\hat{u}, -Rw/\hat{u}) + H_{jk}(-\hat{u}, Rw/\hat{u}) \} \right] \frac{d\hat{u}}{\hat{u}}. \end{aligned} \quad (2.102)$$

Since H_{jk} is an odd function for when $j+k$ is odd and vice versa, the third-order cumulants in the correction term of $p_w(w)$, i.e. the second term in (2.102), vanish.

2.6.3 Conditional probability distribution of fluctuating Reynolds stress

The third-order cumulants, which are closely connected with turbulent diffusion, as will be mentioned later, are much more important quantities than the fourth-order cumulants. Because they disregarded this third-order cumulant, some previous studies such as those by Lu & Willmarth (1973) and Antonia & Atkinson (1973) could find little obvious relation between the bursting process and the probability distribution of the Reynolds stress.

From the above description, a conditional probability distribution should be introduced in order to evaluate the effect of the third-order cumulants, while, for simplicity, the fourth-order cumulants, which are less important, may be omitted.

We shall denote the probability distributions of each event shown in Fig. 2.21 by $p_1(w)$ (outward interaction), $p_2(w)$ (ejection), $p_3(w)$ (inward interaction) and $p_4(w)$ (sweep), respectively. Therefore

$$p_w(w) = p_1(w) + p_2(w) + p_3(w) + p_4(w). \quad (2.104)$$

From (2.96), $p_i(w)$ ($i = 1, \dots, 4$) can be derived by using conditional calculation. For example, $p_2(w)$ becomes

$$p_2(w) = \frac{R \exp(Rt)}{2\pi(1-R^2)^{\frac{1}{2}}} \int_0^\infty \exp\left\{-\frac{x^2 + (t/x)^2}{2}\right\} \\ \times \left[1 - \frac{1}{(1-R^2)^{\frac{1}{2}}} \{A_1 x^3 - A_1^* (t/x)^3 - A_2 x^2(t/x) + A_2^* x(t/x)^2 - A_3 x \right. \\ \left. + A_3^* (t/x)\} \right] \frac{dx}{x}, \quad (2.105)$$

where $t \equiv Rw/(1-R^2)$,

$$\left. \begin{aligned} A_1 &\equiv \frac{1}{6}Q_{30} + \frac{1}{2}RQ_{21} + \frac{1}{2}R^2Q_{12} + \frac{1}{6}R^3Q_{03}, \\ A_2 &\equiv \frac{1}{2}RQ_{30} + (R^2 + \frac{1}{2})Q_{21} + (R + \frac{1}{2}R^3)Q_{12} + \frac{1}{2}R^2Q_{03}, \\ A_3 &\equiv \frac{1}{2}Q_{30} + \frac{3}{2}RQ_{21} + (R^2 + \frac{1}{2})Q_{12} + \frac{1}{2}RQ_{03}. \end{aligned} \right\} \quad (2.106)$$

and A_i^* is A_i with Q_{jk} replaced by Q_{kj} .

Now we have the following mathematical formulae:

$$\int_0^\infty \exp\left\{-\frac{x^2 + (t/x)^2}{2}\right\} x^n (t/x)^m \frac{dx}{x} = t^m |t|^{\frac{1}{2}(n-m)} K_{\frac{1}{2}(n-m)}(|t|), \quad (2.107)$$

$$K_{\nu+1}(t) = 2\nu t^{-1} K_\nu(t) + K_{\nu-1}(t), \quad K_{-\nu}(t) = K_\nu(t), \quad (2.108)$$

where K_ν is the ν th-order modified Bessel function of the second kind. Hence substitution of (2.106)-(2.108) into (2.105) yields

$$p_2(w) = p_G(w) + \psi^-(w) \quad (w > 0). \quad (2.109)$$

In the same manner,

$$p_1(w) = p_G(w) + \psi^+(w), \quad p_3(w) = p_G(w) - \psi^+(w) \quad (w < 0), \quad (2.110)$$

$$p_4(w) = p_G(w) - \psi^-(w) \quad (w > 0), \quad (2.112)$$

where

$$p_G(w) = \frac{R}{2\pi} e^{Rt} \frac{K_0(|t|)}{(1-R^2)^{\frac{1}{2}}}, \quad (2.103)$$

$$\psi^+(w) = \frac{R}{2\pi} e^{Rt} K_{\frac{1}{2}}(|t|) \frac{|t|^{\frac{1}{2}}}{(1-R^2)^2} \left\{ (1+R) \left(\frac{S^+}{3} + D^+ \right) |t| - \left(\frac{2-R}{3} S^+ + D^+ \right) \right\}, \quad (2.113)$$

$$\psi^-(w) = \frac{R}{2\pi} e^{Rt} K_{\frac{1}{2}}(t) \frac{t^{\frac{1}{2}}}{(1+R)^2} \left\{ (1-R) \left(\frac{S^-}{3} + D^- \right) t - \left(\frac{2+R}{3} S^- + D^- \right) \right\} \quad (2.114)$$

$$\text{and } S^\pm \equiv \frac{1}{2}(S_v \pm S_u) = \frac{1}{2}(Q_{03} \pm Q_{30}), \quad D^\pm \equiv \frac{1}{2}(D_v \pm D_u) = \frac{1}{2}(Q_{21} \pm Q_{12}). \quad (2.115)$$

S_u and S_v are the skewness factors of u and v respectively, as $S_u = \overline{\hat{u}^3}$ and $S_v = \overline{\hat{v}^3}$. D_u and D_v correspond to turbulent diffusion in the x and y directions respectively, as $D_u = \overline{\hat{u} \cdot \hat{v}^2}$ and $D_v = \overline{\hat{v} \cdot \hat{u}^2}$, and here we shall call them the diffusion factors.

Using the conditional probability $p_i(w)$ ($i = 1, \dots, 4$) and (2.104), $p_w(w)$ becomes $2p_G(w)$, in which ψ^\pm disappear; then $p_w(w)$ coincides with a distribution directly derived from the Gaussian. These calculated results are shown in Fig. 2.22.

Thus it is suggested that ψ^\pm are very important terms for the sequence of the bursting process and that they are closely connected with the turbulent diffusion.

Next, taking into account the partition level H in the diagram of Reynolds stress $w = uv/\overline{uv}$ according to Lu & Willmarth (1973), as shown in Fig. 2.21(b), the contributions to the Reynolds stress can be associated with one of five events including a hole event when $|w| < H$. The hole event is labelled event 5. Then the time fraction $T_i(H)$ and the contribution to the Reynolds stress $RS_i(H)$ corresponding to each event can be represented by

$$T_i(H) = \begin{cases} \int_H^\infty p_i(w) dw & (i = 2, 4), \\ \int_{-\infty}^{-H} p_i(w) dw & (i = 1, 3), \end{cases} \quad (2.116)$$

$$T_5(H) = \int_{-H}^H p_w(w) dw = 1 - \sum_{i=1}^4 T_i(H) \quad (\text{the hole event}) \quad (2.117)$$

and

$$RS_i(H) = \begin{cases} \int_H^\infty w p_i(w) dw > 0 & (i = 2, 4), \\ \int_{-\infty}^{-H} w p_i(w) dw < 0 & (i = 1, 3), \end{cases} \quad (2.118)$$

$$RS_5(H) = \int_{-H}^H w p_w(w) dw = 1 - \sum_{i=1}^4 RS_i(H) \quad (\text{the hole event}). \quad (2.119)$$

When $H = 0$, the above equations describe the contribution of each event given by Fig. 2.21(a). When $H > 0$, it may be expected that the characteristics of each event such as skewness and intermittency can be made clear. Also, some relationships between the coherent vortex motion with turbulent production which was observed by Corino & Brodkey (1969) or Kim *et al.* (1971) through flow visualization and the data obtained in this study through point measurements may be discussed by varying H as a parameter.

2.6.4 Behaviour of velocity fluctuations with a trigger level H

It is also interesting to investigate some conditional probability distributions of u and v with a trigger level H . Denoting the probability distribution of u which produces the ejections with $w=H$ by $p_*(\hat{u}|H)$, its average value $\hat{u}_*(H)$ is given by

$$\hat{u}_*(H) = \frac{1}{p_2(H)} \cdot \int_{-\infty}^0 \hat{u} \cdot p_*(\hat{u}|H) d\hat{u} \quad \dots\dots\dots (2.120)$$

The average value $\hat{u}_s(H)$ of u which produces the sweeps with $w=H$ is also given in the same manner. Substitution of (2.97) and (2.109) into (2.120) yields

$$\hat{u}_s(H) = - \frac{\sqrt{Z} K_{\frac{1}{2}}(Z) + \delta_1(Z)}{K_0(Z)/\tau + \delta_2(Z)} \dots (2.121)$$

$$\hat{u}_s(H) = \frac{\sqrt{Z} K_{\frac{1}{2}}(Z) - \delta_1(Z)}{K_0(Z)/\tau - \delta_2(Z)} \dots (2.122)$$

where, $Z \equiv RH/\tau^2$, $\tau \equiv \sqrt{1-R^2}$

$$\begin{cases} \delta_1(Z) = - \{ (B_{01}Z + B_{02}Z^2)K_0(Z) + \\ (B_{11}Z + B_{12}Z^2)K_1(Z) \} / \tau^3 \quad \text{and} \\ \delta_2(Z) = 2\pi\phi^-(H) \cdot \exp(-RZ)/R \end{cases} \dots (2.123)$$

$$\begin{cases} B_{01} \equiv R(Q_{30} + 3Q_{12})/2 + \{(2R^2 + 1)Q_{21} + Q_{03}\}/2 \\ B_{11} \equiv (Q_{30} + 3Q_{12})/6 + R\{3Q_{21} + (3 - 2R^2)Q_{03}\}/6 \\ B_{02} \equiv R(R^2 + 3)(Q_{30} + 3Q_{12})/6 + (3R^2 + 1)(Q_{03} + 3Q_{21})/6 \\ B_{12} \equiv (3R^2 + 1)(Q_{30} + 3Q_{12})/6 + R(R^2 + 3)(Q_{03} + 3Q_{21})/6 \end{cases} \dots (2.124)$$

Lastly, the conditional probability distributions $p_s(\hat{u}|w \geq H)$ and $p_e(\hat{u}|w \geq H)$ of u which produces the ejection and the sweeps with $w \geq H$, respectively, are given in the followings by integrating (2.97) in respect of $w \geq H$:

$$p_s(\hat{u}|w \geq H) = \frac{1}{2\pi} \exp\left(-\frac{\hat{u}^2}{2}\right) \int_X^\infty (\phi_1(x) + \phi_2(x)) \exp\left(-\frac{x^2}{2}\right) dx \dots (2.125)$$

$$p_e(\hat{u}|w \geq H) = \frac{1}{2\pi} \exp\left(-\frac{\hat{u}^2}{2}\right) \int_X^\infty (\phi_1(x) - \phi_2(x)) \exp\left(-\frac{x^2}{2}\right) dx \dots (2.126)$$

where, $X \equiv R(H/|\hat{u}| - |\hat{u}|)/\tau$

$$\phi_1(x) \equiv 1 + Q_{30}\{\hat{u}^3 - 3\hat{u}(1-R^2x^2)/\tau^2\}/6 - \hat{u}(2RQ_{21} + Q_{12})(1-x^2)/2\tau^2$$

$$\phi_2(x) \equiv \hat{u}^2(RQ_{30} + Q_{21})x/2\tau + (A_1^*x^3 - A_3^*x)/\tau^3 \dots (2.127)$$

Of course, (2.125) or (2.126) coincides with (2.101) when $H \rightarrow -\infty$ ($X \rightarrow -\infty$).

References (Chapter 2)

- 1) Rotta, J. C.: Turbulente Strömungen, B. G. Teubner, 1972.
- 2) van Driest, E. R.: On turbulent flow near a wall, *J. Aeron. Sci.*, vol.23, pp.1007-1011, 1956.
- 3) Schlichting, H.: Boundary layer theory (6-th edi.), McGraw-Hill, pp.560-625, 1968.
- 4) Schubauer, G. B.: Turbulent processes as observed in boundary layer and pipe, *J. Applied Phys.*, vol.25, pp.188-196, 1954.
- 5) Tennekes, H. & Lumley, J. L.: A first course in turbulence, MIT Press, 1972.
- 6) Bradshaw, P.: 'Inactive' motion and pressure fluctuation in turbulent boundary layers, *J. Fluid Mech.*, vol.30, pp.241-258, 1967.
- 7) Hussain, A. K. M. F. & Reynolds, W. C.: The mechanics of an organized wave in turbulent shear flow, *J. Fluid Mech.*, vol.41, pp.241-258, 1970.
- 8) Batchelor, G. K.: Homogeneous turbulence, Camb. Univ. Press, 1953.
- 9) Inoue, E.: **On the structure of wind near the ground, Bull. of the National Institute of Agricultural Sciences, Ser. A, No. 2, 1952.**
- 10) Nakagawa, H., Nezu, I. & Ueda, H.: Turbulence of open channel flow over smooth and rough beds, *Proc. of JSCE*, No.241, pp.155-168, 1975.
- 11) Tchen, C. M.: On the spectrum of energy in turbulent shear flow, *Jour. of R.N.B.S.*, vol.50, pp.51-62, 1953.
- 12) Hinze, J. O.: Turbulence, McGraw-Hill, pp.451-566, 1959.
- 13) von Karman, T.: Progress in the statistical theory of turbulence, *Proc. of N.A.S.*, vol.34, pp.530-539, 1948.
- 14) Monin, A. S. & Yaglom, A. M.: Statistical fluid mechanics, MIT Press, 1971.
- 15) Bradshaw, P.: Conditions for the existence of an inertial subrange in turbulent flow, *A.R.C., R. & M.*, No.3603, 1967.
- 16) Zagustin, A. & Zagustin, K.: Analytical solution for turbulent flow in pipes, *La Houille Blanche*, No.2, pp.113-118, 1969.
- 17) Townsend, A. A.: Equilibrium layers and wall turbulence, *J. Fluid Mech.*, vol.11, pp.97-120, 1961.
- 18) Kline, S. J. *et al.* (edi.): Computation of turbulent boundary layers - - - 1968 AFOSR-IFP-Stanford Conf., vol.1, 1968.
- 19) Reichardt, H.: Vollständige Darstellung der turbulenten Geschwindigkeitsverteilung in glatten Leitungen. *ZAMM*, Bd.31, pp.208-219, 1951.
- 20) Davies, P. O. A. L. & Yule, A. J.: Coherent structures in turbulence, *J. Fluid Mech.*, vol.69., pp.513-537, 1975.
- 21) Kline, S. J., Reynolds, W. C., Schraub, F. A. & Runstadler, P. W.: The structure of turbulent boundary layers, *J. Fluid Mech.*, vol.30, pp.741-773, 1967.
- 22) Kim, H. T., Kline, S. J. & Reynolds, W. C.: The production of turbulence near a smooth wall in a turbulent boundary layer, *J. Fluid Mech.*, vol.50, pp.133-160, 1971.
- 23) Corino, E. R. & Brodkey, R. S.: A visual investigation of the wall region in turbulent flow, *J. Fluid Mech.*, vol.37, pp.1-30, 1969.
- 24) Grass, A. J.: Structural features of turbulent flow over smooth and rough boundaries, *J. Fluid Mech.*, vol.50, pp.233-255, 1971.
- 25) Brodkey, R. S., Wallace, J. M. & Eckelmann, H.: Some properties of truncated turbulence signals in bounded shear flows, *J. Fluid Mech.*, vol.63, pp.209-224, 1974.
- 26) Nakagawa, H. & Nezu, I.: Prediction of the contributions to the Reynolds stress from the bursting events in open channel flows, *J. Fluid Mech.*, vol.80, pp.99-128, 1977.
- 27) Frenkiel, F. N. & Klebanoff, P. S.: Probability distributions and correlations in a turbulent boundary layers, *Phys. of Fluids*, vol.16, pp. 725-737, 1973.
- 28) Lu, S. S. & Willmarth, W. W.: Measurements of the structure of the Reynolds stress in a turbulent boundary layer, *J. Fluid Mech.*, vol.60, pp.481-511, 1973.
- 29) Antonia, R. A. & Atkinson, J. D.: High-order moments of Reynolds shear stress fluctuations in a turbulent boundary layer, *J. Fluid Mech.*, vol.58, pp.581-593, 1973.

Chapter 3 Method of turbulence measurement and its analysis

3.1 Introduction

The method of turbulence measurements, techniques or instruments can be divided broadly into two groups: one is point-measurement that a detecting element is introduced into the flowing fluid, and another is flow visualization that a tracer or other indicator is introduced into the fluid to make the flow pattern visible. In this study, i.e. turbulence-measurements in water flow, as the former method a hot-film anemometer and as the latter method a hydrogen-bubble tracer are adopted here, respectively.

3.2 Properties of dual-sensor hot-film anemometers

3.2.1 Principle of hot-film anemometer

As shown in Fig. 3.1, in a hot-wire or hot-film anemometer two basically different methods can be applied: (a) constant-current method and (b) constant-temperature method. Since we adopted a constant-temperature anemometer manufactured by DISA, only (b)-method is considered here.

Well, an equation of heat transfer from cylindrical hot-film sensor (see Fig. 3.2) was given by Kramers:

$$N_u = 0.42 P_r^{0.2} + 0.57 P_r^{0.33} R_s^{0.5} \dots \dots \dots (3.1) \quad \text{where, } N_u \equiv hD/k, R_s \equiv UD/\nu, P_r \equiv C\rho\nu/k.$$

$$\text{Since } N_u = \frac{E_s^2/R_s}{J \cdot \pi l \cdot k (T_s - T_w)} \dots \dots \dots (3.2) ,$$

$$\text{we can obtain } E^2 - E_0^2 = A' U^{0.5} \dots \dots \dots (3.3)$$

$$A' \equiv \text{Const.} \times kl(D/\nu)^{0.5} P_r^{0.33} R_s (T_s - T_w) \dots \dots \dots (3.4)$$

$$E_0^2 \equiv \text{Const.} \times kl P_r^{0.2} R_s (T_s - T_w) \dots \dots \dots (3.5)$$

where, T_s and T_w are temperatures of sensor and water, respectively. (3.3) is an equation of calibration (U-E) in respect of a cylindrical hot-film sensor, and thus a general calibration as to any configuration of sensor (ex. see Figs. 3.3 and 3.4) can be given by

$$E^2 - E_0^2 = A' \cdot U^n \dots \dots \dots (3.6)$$

3.2.2 Directional sensitivity of hot-film sensor

We adopted a dual-sensor hot-film probe (DISA 55A89, as shown in Fig. 3.4) in order to measure the turbulence intensities, Reynolds stress and others.

Well, according to Hinze, the effective value of U can be obtained approximately from the relation: $U_i^2 = U^2 (\cos^2 \phi + k^2 \sin^2 \phi)$ (3.7)
Distinguishing the dual-sensors as shown in Fig. 3.5,

$$\phi_1 = \pi/2 - (\varphi_1 + \theta), \phi_2 = \pi/2 - (\varphi_2 - \theta) \quad \dots\dots\dots (3.8)$$

Since $\varphi_1 = \varphi_2 = \pi/4$, the following relations can be obtained from

$$(3.6) \text{ and } (3.7): \frac{(E^2 - E_o^2)}{(E^2 - E_o^2)_{\theta=0}} = \left(2 \cdot \frac{\cos^2 \phi + k^2 \sin^2 \phi}{1 + k^2} \right)^{n/2} \quad \dots\dots\dots (3.9)$$

Denoting
$$\psi_i(\theta) \equiv \left[\frac{(E_i^2 - E_{io}^2)}{(E_i^2 - E_{io}^2)_{\theta=0}} \right]^{2/n_i} \quad (i = 1, 2) \quad \dots\dots\dots (3.10)$$

$$\psi_i(\theta) = \frac{2(\cos^2 \phi_i + k_i^2 \sin^2 \phi_i)}{1 + k_i^2} \quad \text{or} \quad k_i^2 = \frac{2 \cos^2 \phi_i - \psi_i}{\psi_i - 2 \sin^2 \phi_i} \quad \dots\dots\dots (3.12)$$

..... (3.11)

An experiment of the directional sensitivity of this probe has been performed in a homogeneous water flow ($U=34.3$ cm/s, $u'/U=0.04$). Fig. 3.6 shows the experimental values, together with the curves of (3.11). And, the values of k^2 calculated by (3.12) are also shown in Fig. 3.7. From these results, the average values of k became equal to $k_1=0.12$ and $k_2=0.21$, which were of the same order to those obtained by Hinze or Champagne et al. Consequently, the cosine law, i.e. $k=0$ in (3.7), may be valid within the error of 5%.

Then, the relations between the instantaneous velocity $\tilde{u}=(\tilde{u}, \tilde{v}, \tilde{w})$ and the output voltage \tilde{E} are obtained in the followings.

From the cosine law,

$$\tilde{U}_a^2 = \frac{(\tilde{u} + \tilde{v})^2}{2} \left\{ 1 + 2 \left(\frac{\tilde{w}}{\tilde{u} + \tilde{v}} \right)^2 \right\}, \quad \tilde{U}_a^2 = \frac{(\tilde{u} - \tilde{v})^2}{2} \left\{ 1 + 2 \left(\frac{\tilde{w}}{\tilde{u} - \tilde{v}} \right)^2 \right\} \quad \dots\dots\dots (3.14)$$

Since $\tilde{u} \gg \tilde{v}, \tilde{w}$ (3.15) in two-dimensional flow,

$$\tilde{u} = (\tilde{U}_{e1} + \tilde{U}_{e2})/\sqrt{2}, \quad \tilde{v} = (\tilde{U}_{e1} - \tilde{U}_{e2})/\sqrt{2} \quad \text{where,} \quad \tilde{E}_i^2 - E_{io}^2 = A_i^2 \tilde{U}_{ei}^{n_i} \quad (i = 1, 2)$$

..... (3.16) (3.17)

3.2.3 Calibration of dual-sensor hot-film anemometer

Firstly, we examined the temperature dependence of the electric resistance of the hot-film, which results are shown in Fig. 3.8. Fig. 3.9 shows the output voltages of anemometers in the still water (i.e. $U=0$). These results agree well with (3.5), and give

$$E_{10}^2 = 0.212(33.40 - T_w), E_{20}^2 = 0.178(37.42 - T_w) \dots\dots\dots (3.18)$$

Next, some calibrations as to the mean velocity were done by using both a Pitot tube and a float in a homogeneous open-channel flow. Since $\bar{u} = U, \bar{v} = V \approx 0$, (3.16) and (3.17) become

$$E_i^2 - E_{i0}^2 = A_i' (U/\sqrt{2})^{n_i} \equiv A_i U^{n_i}, \quad A_i \equiv A_i' / 2^{n_i/2}, \quad (i = 1, 2) \dots\dots\dots (3.19)$$

Some typical results of these calibrations are shown in Fig. 3.10, which agrees fairly well with (3.19). From this figure, the exponent n_i became nearly equal to 0.5 although it changed, speaking strictly, a little with the velocity range. The values of the calibration coefficient $A(T_w)$ are also shown in Fig. 3.11.

They satisfy (3.4), and give $A_1 = 0.138(32.07 - T_w), A_2 = 0.122(35.72 - T_w) \dots\dots\dots (3.20)$.

From the above relations of (3.18)-(3.20), the calibration curves of velocity-voltage can be easily determined. For example, Fig. 3.12 shows the calibration curves of 1-st sensor as a parameter of the water temperature.

3.3 Effect of various factors on the properties of hot-film anemometer

3.3.1 Effect of the noise

Fig. 3.13 shows the data processing system constructed in this study. Consequently, it is apprehended that some noises may be involved into the analogue data of hot-film anemometers until they are converted into the digital data.

Now, if U and T_w vary infinitesimally, the output voltage E varies by $\Delta E = (\partial E / \partial U) \Delta U + (\partial E / \partial T_w) \Delta T_w \dots\dots\dots (3.21)$

When T_w is kept to be constant, (3.21) becomes

$$\frac{\Delta U}{U} = C_i \cdot \frac{\Delta E_i}{E_i}, \quad C_i \equiv \frac{2}{n_i(1 - E_{i0}^2/E_i^2)}, \quad (i = 1, 2) \dots\dots\dots (3.22)$$

C_i is the sensitivity factor of the anemometers, and Fig. 3.14 shows an example of C_i -curves calculated from (3.18)-(3.20) and (3.22). If the noise is expressed by ΔE , $\Delta E/E$ describes the noise-signal ratio of the analogue data. From this figure, $\Delta U/U$ becomes nearly equal to $(5-7)\Delta E/E$. That is, N-S ratio of even only 1% in the instruments (see Fig. 3.13) causes that of (5-7)% in the evaluation of velocity.

Thus, we made some devices to minimize the noise involved into the analogue data.

3.3.2 Effect of the water temperature changes

Since the time required for the turbulence measurement at one point is about two minutes, the water temperature changes during this one-point measurement are negligible if its temperature is nearly in the equilibrium state. But, if there are many points measured by the anemometers, the water temperature goes up a little gradually during all these measurements.

Now, when U is kept to be constant, (3.21) becomes

$$\frac{\Delta E_i}{E_i} = \frac{\Delta T_w}{2(A_i U^{n_i} + E_{i0}^2)} \left(\frac{\partial E_{i0}^2}{\partial T_w} + U^{n_i} \frac{\partial A_i}{\partial T_w} \right) \dots\dots\dots (3.23)$$

If an identical calibration curve is used in spite of the water temperature changes ΔT_w , the effect of ΔE corresponding to ΔT_w is evaluated as if the velocity has changed. That is, the following relation is obtained from (3.22):

$$\frac{\Delta U}{U} = \frac{1}{n_i A_i U^{n_i}} \left(\frac{\partial E_{i0}^2}{\partial T_w} + U^{n_i} \frac{\partial A_i}{\partial T_w} \right) < 0 \dots\dots\dots (3.24)$$

Fig. 3.15 shows the results of (3.24) calculated by using (3.18) and (3.19). Actually, the velocity is underestimated by about 20% per the increase of $\Delta T_w = 1^\circ\text{C}$ if the effect of ΔT_w on the calibration curve is neglected.

By the way, a finite differentiation of (3.17) yields

$$\frac{\Delta U}{U} \approx \frac{1}{2} \left(C_1 \frac{\Delta E_1}{E_1} + C_2 \frac{\Delta E_2}{E_2} \right), \frac{\Delta V}{U} \approx \frac{1}{2} \left(C_1 \frac{\Delta E_1}{E_1} - C_2 \frac{\Delta E_2}{E_2} \right) \dots\dots\dots (3.25)$$

Since the variation of the sensitivity factor C_i against the water temperature changes is very small as seen in Fig. 3.14, $\Delta U/U$ or $\Delta V/U$ (ex. the relative turbulence intensity u'/U or v'/U) can be evaluated fairly accurately in spite of ΔT_w .

In consideration of the above, a stable water temperature was here maintained during the operating period by circulating water throughout the day before the test began in order to diminish the effect of its changes on the hot-film as much as possible, and in result ΔT_w became within only 0.5°C at the end of all measurement tests.

Furthermore, the correction for the effect of water temperature was done by using the calibration coefficients (cf. (3.18) and (3.20)).

3.3.3 Effect of the nonhomogeneity of velocity along the sensor

When the length l of the hot-film sensor is larger than the microscale λ of turbulence, the effect of the nonhomogeneity of velocity along its sensor should not be neglected. In the same manner as the description by Hinze, the following relations as to V-type sensors (cf. Fig. 3.5) are obtained approximately:

$$\left. \begin{aligned} \bar{u}_m^2 &= \left(1 - \frac{1}{3} (\lambda/\lambda_y)^2\right) \bar{u}_t^2 + \frac{1}{4} (\lambda/\lambda_x)^2 \bar{v}_t^2 - \frac{1}{\sqrt{2}} l \frac{d(\overline{uv})_t}{dy} \\ \bar{v}_m^2 &= \frac{1}{4} (\lambda/\lambda_x)^2 \bar{u}_t^2 + \left(1 - \frac{1}{3} (\lambda/\lambda_y)^2\right) \bar{v}_t^2 - \frac{1}{\sqrt{2}} l \frac{d(\overline{uv})_t}{dy} \\ \overline{(uv)}_m &= \overline{(uv)}_t - \frac{1}{2\sqrt{2}} l \left\{ \left(1 - \frac{1}{12} (\lambda/\lambda_y)^2\right) \frac{d\bar{u}_t^2}{dy} + \left(1 - \frac{1}{12} (\lambda/\lambda_x)^2\right) \frac{d\bar{v}_t^2}{dy} \right\} \end{aligned} \right\} \dots\dots\dots (3.27)$$

where, suffixes m and t denote the measured and the true values, respectively. For example, since $|d\bar{u}_t^2/dy| \sim |d\bar{v}_t^2/dy| \sim |d(\overline{uv})_t/dy| \approx U_*^2/h$ (cf. 2.2) and our sensor has $l=1$ mm, the above effect may be within only 1% when $h=8$ cm.

3.3.4 Other effects

To diminish the effect of impurities in the water upon the characteristics of the hot-film, the suspended materials in the flow were filtered by gauzes. And, various devices have been done as to insulation badness of probe connector by the submerged water, self-vibration of the experimental channel and others.

3.4 Hydrogen-bubble technique

3.4.1 Principle of hydrogen-bubble tracer and its analysis

As shown in Fig. 3.16, a fine platinum wire of $d=50 \mu\text{m}$ diameter is stretched in the water in the direction of y - or z -axis. This wire forms the negative electrode of a pulsed D.C. circuit of (100-500) volts, where in result hydrogen bubbles with a diameter of $(0.5-1.0)d$ are produced and they form the markers for flow visualization. In order to obtain a marking in space (combined time-streak markers), the wire has short sections at nearly regular intervals (about 2 mm) coated for insulation.

Fig. 3.17 shows the data processing system for hydrogen-bubble method. Any frame in 16mm films is enlarged by the film-projector and the coordinates of some hydrogen-bubbles can be read to the limit of 0.1mm by the instrument of digital coordinator. Fig. 3.18 shows an analysis method of instantaneous velocity profile (single frame method). Denoting three bubble-points near the reference axis x_r ($x_r/d \approx 100$) by 1, 2 and 3, the following approximation is obtained:

$$u_d = \frac{(x_2 - x_1)}{\Delta T}, \quad v_d = \frac{(y_2 - y_1)}{\Delta T}, \quad u_e = \frac{(x_3 - x_2)}{\Delta T}, \quad v_e = \frac{(y_3 - y_2)}{\Delta T} \dots\dots\dots (3.28)$$

With a proportional allotment of (3.28) between d - and e -points,

$$y(i) = \frac{1}{S} \{y_d + \alpha(y_e - y_d)\}, \quad \bar{u}(i) = \frac{1}{S} \{u_d + \alpha(u_e - u_d)\}, \quad \bar{v}(i) = \frac{1}{S} \{v_d + \alpha(v_e - v_d)\} \dots\dots (3.29)$$

where, $\alpha \equiv (x_r - x_d)/(x_e - x_d)$, ΔT is the pulse-time and S is the enlargement rate of picture. Denoting the frame number by j , $y_a(i) = \frac{1}{N} \sum_{j=1}^N y(i, j)$. Then, the instantaneous velocity ($\bar{u}(i, j), \bar{v}(i, j)$) at the point of $(x_r, y_a(i))$ is obtained in the same manner as (3.29) (cf. Fig. 3.18(b)).

3.4.2 Effects of various factors upon the hydrogen-bubble method

The effects of various factors upon the hydrogen-bubble method have been investigated (ex. effects of buoyancy, wake of the wire, the read-error, response of the bubble, etc.). These results are omitted here since they are similar to those obtained by Schraub et al.

References (Chapter 3)

- 1) Hinze, J. O. : Turbulence, McGraw-Hill, pp.73-141, 1959.
- 2) Bradshaw, P. : An introduction to turbulence and its measurement, Pergamon Press, pp.85-133, 1971.
- 3) Schraub, F. A., Kline, S. J., Henry, J., Runstadler, P. W. & Littell, A. : Use of hydrogen bubbles for quantitative determination of time-dependent velocity fields in low-speed water flows, Trans. of ASME, BE, pp.429-444, 1965.

Chapter 4 Experimental consideration on turbulent structure and energy budget

4.1 Introduction

In the recent turbulence research a 'self-consistent' characteristic of turbulence has been noticed that a turbulence-characteristic may be more closely related to another turbulence-characteristic than mean-velocity one, that is, there may be a stronger interrelation among the turbulence characteristics.

In this chapter, we investigate in detail the turbulence intensities, Reynolds stress, spectral distributions, the rates of production, diffusion and dissipation of turbulence, and others in open-channel flows from the viewpoint of the self-consistency of turbulence or similarity law mentioned above, and then we make clear systematically the effects of the Reynolds number, the Froude number and the wall roughness upon these turbulent structure and the energy budget.

4.2 Experimental equipment and data analysis

Three groups of experiments on two-dimensional fully developed turbulent flow in an open channel were conducted in a tilting flume 15m long, 50cm wide and 30cm deep, as shown in Fig. 4.1. The channel slope could be changed by adjusting two jacks so that normal flow could be obtained. A few baffles and screens to prevent the occurrence of large-scale disturbances were set up at the entrance of the channel, and consequently a fully developed turbulent flow was obtained at the test section 9.5m downstream of the entrance.

As described in Table 4.1, first group (a) consisted of three different kinds of the Reynolds number $Re = U_m h / \nu$, i.e. $Re = (1.2, 2.9, 4.6) \times 10^4$, where the Froude number $Fr = U_m / \sqrt{gh}$ and the wall equivalent sand roughness $k_s^+ = k_s U_* / \nu$ were kept to be nearly constant, i.e. $Fr \approx 0.7$ and $k_s^+ \approx 0$. Second group (b) consisted of five different kinds of the Froude number ($Fr = 0.46 - 3.12$), where $Re \approx 3.2 \times 10^4$ and $k_s^+ = 0$ (smooth bed) were nearly kept. Third group (c) consisted of four different kinds of the wall roughness ($k_s^+ = 0, 9, 48, 136$), where $Re \approx 9800$ and $Fr \approx 0.16$ were nearly kept.

The three components u , v , and w of instantaneous velocity were measured by using a set of constant-temperature anemometers with a DISA type 55A89 dual-sensor hot-film probe, and a single-sensor hot-film probe (see Fig. 3.3) was used to measure only u very near the wall. Its detailed description has been already given in Chapter 3. The output signals of the anemometers were digitized by using an A-D converter (see Fig. 3.13), and then some statistical analyses were carried out by using a large digital computer, FACOM 230-75, Data Processing Center, Kyoto University.

It is important how to determine the number N of samples and the sampling frequency $f \equiv 1/\Delta t$ at any measuring point on performing analog-to-digital conversion. The maximum cutoff wave-number k_∞ is given by

$$\hat{k}_\infty \equiv L_x \cdot k_\infty \approx \frac{\pi}{\Delta T(U/\lambda)} \dots\dots\dots (4.1)$$

If \hat{k}_∞ is over about a hundred, the spectral analysis becomes possible at least to the extent of the inertial subrange, as shown in Fig. 2.6. Thus, the sampling frequency f was chosen in each run so as to satisfy this analytical condition. Since the bursting period T_B is nearly equal to $(2-3)h/U_{\max}$ as will be shown in Chapter 5, the total sampling time $T=N/f$ is given by

$$\frac{T}{T_B} \approx \frac{\pi}{(200 \sim 300)} \left(\frac{U_{\max}}{U} \right) N \sim \frac{N}{50} \dots (4.2)$$

Though the larger the sample size N is, the better the accuracy of data analysis becomes, $N=5000$ was chosen in this study because of the limitation of computer technique. Thus, this sample size ($T \approx 100T_B$) may be comparatively small but it includes the characteristics of bursting phenomenon from this data analysis.

4.3 Universal characteristics of turbulence intensities *)

It has been confirmed in our previous paper (1975) or Chapter 2 that the turbulent energy $\overline{q^2}/2$ played an essential role in the turbulent structure of an open-channel flow, and that its behaviour showed a monotonous decrease with increase of $\xi \equiv y/h$. In detail, the gradient of $\overline{q^2}$ against ξ might be nearly in proportion to itself

*) Refer to our paper published in *Proc. of JSCE, No. 261, pp. 67-76, 1977 (in Japanese), or Trans. of JSCE, vol. 10, 1979 (in English).*

$\overline{q^2}$ in the equilibrium region, as similar to the properties of the other kinds of energy such as thermal energy. Then,

$$\frac{1}{\overline{q^2}} \frac{d(\overline{q^2})}{d\xi} = \frac{d(\ln \overline{q^2})}{d\xi} \equiv -\lambda < 0 \dots (4.3)$$

The above conception may be also similar to that of Townsend(1961) or Zagustin et al.(1969). By assuming that λ is constant and applying the results of Π -eddy model proposed in Chapter 6, the following universal functions of turbulence intensities are obtained

from (4.3): $\frac{u'}{U_*} = D_1 \cdot \exp\left(-\frac{\lambda\xi}{2}\right), \frac{v'}{U_*} = D_2 \cdot \exp\left(-\frac{\lambda\xi}{2}\right), \frac{w'}{U_*} = D_3 \cdot \exp\left(-\frac{\lambda\xi}{2}\right) \dots\dots (4.7)$

where, λ and D_i ($i=1,2,3$) are the experimental constants.

In this section, we discuss experimentally the validity of (4.7) by systematically varying the Reynolds, the Froude numbers and the wall roughness (cf. Table 4.1).

4.3.1 Mean velocity distribution and friction velocity

As a result of the preliminary experiment, it was confirmed that the mean velocity over the rough bed as well as the smooth bed (cf. Fig. 2.19) satisfied very well the logarithmic law,

i.e. $U^+ = \kappa^{-1} \cdot \ln(y/k_s) + C_r(k_s^+), C_r(k_s^+) \equiv \kappa^{-1} \ln(k_s^+) + B \dots\dots\dots (2.87)$

when an origin of the y-axis was reset at a point of $k_s/4$ below the top of the roughness element.

Well, in the detailed discussion on the turbulent structure, it is a very essential work to evaluate the friction velocity U_* accurately, as mentioned in Chapter 2. There are several methods in the evaluation of U_* , that is:

(1) *Energy gradient method*

From (2.3), $U_*'' = \sqrt{ghI_s}, I_s \equiv S - dh/dx \dots\dots (4.6)$

where, S is the bed slope.

(2) *Log-law method*

The friction velocity U_*' can be estimated by using the Karman constant $\kappa=0.4$ since the mean velocity satisfies the log-law.

(3) *Reynolds-stress method*

The friction velocity U_* can be evaluated from (2.5) by using the measured Reynolds stress distribution.

(4) *Velocity gradient method*

By definition, $U_*^2 = \nu \partial U / \partial y|_{y=0}$.

(5) *Other methods*

Preston tube method, direct-measurement of wall shear stress, heat-transfer analogy method, etc.

Only (3)-method is based on the turbulence characteristics. Consequently, in consideration of the self-consistency of turbulence we could here evaluate U_* most reasonably by making use of (3) Reynolds-stress method. And, the friction velocity U_*'' , U_*' and U_* evaluated from (1)-, (2)- and (3)-methods, respectively, are summarized in Table 4.1. They agree well with each other within the error of 30%.

4.3.2 Effect of the Reynolds number on turbulence intensities

Fig. 4.2 shows the effect of the Reynolds number on u'/U_* and v'/U_* . In the region of $\xi < 0.5$ our data are in good agreement with the Laufer's data. (4.7) with $\lambda=2.0$, $D_1=2.30$ and $D_2=1.27$ can fairly well explain these experimental results. However, our data in $\xi > 0.5$ deviate over from the Laufer's data or the curves of (4.7). As will be pointed out in 4.5, this deviation may be due to a fact that the surface wave energy is included in the measured turbulent energy more or less, and that it corresponds to the inactive turbulent component defined by Bradshaw(1967). It should be noticed that near the critical-depth flow, i.e. $Fr \simeq 1$, the universal structure of turbulence may be broken down by an inactive motion such as surface wave fluctuation.

By the way, Ljatkher(1967) approximated linearly the Navier-Stokes' equation and obtained the following equations (i.e. a special case of Orr-Sommerfeld's equ.) by assuming that the effect of the Reynolds number might disappear when Re was very large (This assum-

ption may be valid, as seen in Fig. 4.2):

$$\frac{d^2 v_*}{d\xi^2} - \left\{ (kh)^2 - \frac{m(1-m)}{(1-\alpha)} \frac{1}{\xi^2} \right\} v_* = 0, \quad u_* = \frac{i}{k} \frac{dv_*}{dy} \quad \dots\dots\dots (4.8)$$

where,

$$u_* \equiv \iint_{-\infty}^{\infty} u(x, y, t) \exp -i(kx + \omega t) dx dt, \quad v_* \equiv \iint_{-\infty}^{\infty} v(x, y, t) \exp -i(kx + \omega t) dx dt \quad \dots\dots\dots (4.9)$$

(4.8) is based on an assumption that $U_c \equiv -\omega/k = \alpha U$ and $U/U_{max} = \xi^m$. Because (4.8) is the Bessel's type differential equation in respect of $v_*/\sqrt{\xi}$, its solution is expressed by a summation of modified Bessel functions. This theoretical curve is described by a broken line in Fig. 4.2, and it should be noticed that this curve agrees fairly well with (4.7). Furthermore, when the mean velocity is assumed to be nearly linear, i.e. $m=1$, a special solution of (4.8) is obtained: $v_*(k, \xi) = D(k) \cdot \exp - (kh) \xi \quad \dots\dots (4.10)$

Consequently, (4.7) can be also deduced from (4.10).

To sum up, (4.7) may be a universal function on a basis of not only the phenomenological consideration of (4.3), but also the approximation of N-S eq. of (4.8).

4.3.3 Effect of the Froude number on turbulence intensities

Fig. 4.3 shows the effect of the Froude number on the turbulence intensities. Except for Case G-2, the experimental values of u'/U_* , v'/U_* and w'/U_* show universal characteristics irrespective of Fr, and agree very well with (4.7) with $\lambda=2.0$, $D_1=2.30$, $D_2=1.27$ and $D_3=1.63$. This suggests that except for near the critical-depth flow, the active component may be more dominant than the inactive one, and thus that there may strongly exist the universality or similarity in their turbulent structure irrespective of the Reynolds and Froude numbers. We obtain from (4.7) some noticeable results that

$$v'/u' = D_2/D_1 = 0.55, \quad w'/u' = D_3/D_1 = 0.71 \quad \dots\dots\dots (4.12)$$

$$u'^2/q^2 = 0.55, \quad v'^2/q^2 = 0.17, \quad w'^2/q^2 = 0.28 \quad \dots\dots\dots (4.13)$$

irrespective of y/h . This shows that the ratios of the re-distribution of turbulent energy become nearly constant from the wall region up to the free-surface as predicted in Chapter 2 or Fig. 2.5, and that the tendency toward an isotropic turbulence, i.e. $u'=v'=w'$ may be suppressed even in the free-surface region.

Next, Fig. 4.4 shows the turbulence intensities near the wall by using y^+ . Our data of u'/U_* agree well with Laufer's data and indicate the maximum value 2.8 at $y^+ \approx 15$. Although the data of v'/U_* very near the wall could not be obtained here, they seemed to vary monotonously with y^+ (in detail, refer to Chapter 6).

From (4.7),
$$\frac{u'}{U_*} = D_1 \cdot \exp\left(-\frac{y^+}{R_*}\right), \quad \frac{v'}{U_*} = D_2 \cdot \exp\left(-\frac{y^+}{R_*}\right), \quad \frac{w'}{U_*} = D_3 \cdot \exp\left(-\frac{y^+}{R_*}\right) \dots\dots\dots (4.15)$$

(4.15) with $R_* = 600$ and 1600 is shown in Fig. 4.4, and these curves agree well with the experimental values in the region of $y^+ > 50$. By the way, Monin et al. (1971) proposed the following asymptotic relations when Re is very large: $u'/U_* \rightarrow 2.3$, $v'/U_* \rightarrow 0.9$, $w'/U_* \rightarrow 1.7$ (4.16) On the other hand, when $R_* \rightarrow \infty$ ($R_* \rightarrow \infty$), (4.15) becomes

$$u'/U_* \rightarrow 2.3, \quad v'/U_* \rightarrow 1.27, \quad w'/U_* \rightarrow 1.63 \quad \dots\dots\dots (4.17)$$

An agreement between the both is very good.

To sum up, (4.15) is very valid in $y^+ > 50$, but it is not applicable to the region of $y^+ < 50$, where a universal function will be considered anew in Chapter 6. Still, the power-type universal functions ((2.66) and (2.81)) obtained in Chapter 2 are examined in Figs. 4.3 and 4.4.

4.3.4 Effect of the wall roughness on turbulence intensities

Fig. 4.5 shows the effect of the wall roughness on the turbulence intensities. These experimental values agree well with those of Grass (1971) obtained by using the hydrogen-bubble technique. In the region of $\xi > 0.3$, this roughness effect may become fairly weak, and consequently the experimental values still coincide well with (4.7) independently of the wall roughness. It should be, however, noticed that this effect appears remarkably near the wall.

So, the experimental values near the wall are in detail shown against y^+ in Fig. 4.6. The values of u'/U_* in the wall region gradually decrease with increase of k_S^+ , but v'/U_* and w'/U_* are hardly influenced by the size of roughness element. Though the turbulence production over a smooth bed occurs mostly in a buffer-

layer $y^+ = 10-30$ by the ejections and sweeps due to the flow instability (see Chapter 5), a buffer-layer over a rough bed disappears perfectly or partly into the roughness elements, and consequently the turbulence would be produced in another way. Actually, the position $y_m^+ \approx (15-20)$ where u'/U_* attains maximum becomes under the top of roughness element when $k_s^+/4 > y_m^+$, i.e. $k_s^+ > 70$, and thus its evident maximum of u'/U_* appears no longer (see Case D-1).

A poor dependence of v'/U_* and w'/U_* on roughness may be due to their little contribution to turbulence production, so that both v' and w' seem to change monotonously with y^+ while u' shows the maximum value. Well, such an effect of the wall roughness on u'/U_* can be phenomenologically explained as follows:

As shown in Fig. 2.5, u' has a direct relation to macro-scale eddies which dominate the turbulence production. Antonia et al. (1971), Chen et al. (1974) and authors (1975) pointed out experimentally that the macro-scale L_x^+ near the wall decreased gradually with enlargement of the roughness. Then, as k_s^+ increases, A_2 in (2.65) or A_3 in (2.66) becomes smaller, and thus u'/U_* also becomes smaller. Actually, (2.66) is shown in Fig. 4.6 since it can be predicted in 4.6.4 and 4.7.1 that A_3 becomes nearly equal to 4.36 for smooth bed and 3.77 for rough bed. This result suggests strongly that the re-distribution of turbulent energy may tend toward isotropy as the macro-scale eddy decays due to the roughness.

By the way, U^+ as well as L_x^+ decreases with increase of k_s^+ , as described in (2.87). Imamoto (1971) suggested that $(u'/U_*)(U^+)^{-1/3}$ was a universal expression against y/h on a basis of a proportional relation between U^+ and L_x^+ . Now, this expression of $(u'/U_*)(U^+)^{-1/3}$ is examined against y^+ in Fig. 4.7. It should be noticed that $(u'/U_*)(U^+)^{-1/3}$ has really a universal characteristic irrespective of the wall roughness in the region of $y^+ < 70$ where its effect on u'/U_* appears remarkably as mentioned the above. Furthermore, this universal function (a thick line in Fig. 4.7) will be investigated in Chapter 6.

4.4 Relative turbulence intensity and Reynolds stress

4.4.1 Relative turbulence intensity u'/U

The characteristics of only u'/U are investigated here since v'/U and w'/U are easily evaluated from (4.12).

Fig. 4.8 shows the values of u'/U obtained by varying only the Reynolds number Re . In $\xi < 0.1$, u'/U decreases remarkably with increase of Re , but in $\xi > 0.1$ this effect of Re becomes weaker. And, such a characteristic is also seen in the experimental curves obtained by Laufer(1951) and Blinco et al.(1971). Now, the following relation can be obtained from (2.14) and (4.7):

$$\frac{u'}{U} = \frac{2.3 \exp(-\xi)}{\kappa^{-1} \ln \xi + A(R_*)} \quad , \quad A(R_*) \equiv \frac{1}{\kappa} \ln R_* + 5.5 \quad \dots\dots\dots (4.18)$$

The curves of (4.18) with $\kappa=0.4$, $R_*=600$ and 2000 agree well with the experimental values in $\xi > 0.1$ (see Fig. 4.8) though (4.18) is invalid very near the wall.

Next, Fig. 4.9 shows the values of u'/U obtained by varying only the Froude number Fr . In spite of the wide variation of Fr , the experimental values get nearly on a single curve, and thus they show a good agreement with (4.18) except for very near the wall.

Lastly, Fig. 4.10 shows the values of u'/U obtained by varying only the wall roughness. Of course, the relative turbulence intensity increases, especially very remarkably near the wall, with enlargement of the roughness size. Now, From (2.87) and (4.7)

we obtain

$$\frac{u'}{U} = \frac{2.3 \exp(-\xi)}{\kappa^{-1} \ln \xi - \{\kappa^{-1} \ln(k_s/\lambda) - C_r(k_s^+)\}} \quad \dots\dots\dots (4.19)$$

As shown in Fig. 4.10, the curves of (4.19) explain fairly well the effect of the roughness.

4.4.2 Reynolds stress distribution

The measurement of Reynolds stress in a water flow was just realized only eight years ago by McQuivey et al.(1969) who used a 'yawed film' technique of single-sensor. On the other hand, we measured the Reynolds stress by making use of a dual-sensor hot-film (cf. Chapter 3).

Fig. 4.11 shows the values of Reynolds stress obtained at each group in Table 4.1. They show a universal distribution independently of the Reynolds, the Froude numbers and the wall roughness.

Now, from (2.5) and (2.14) we obtain
$$\frac{-\overline{uv}}{U_*^2} = (1-\xi) - \frac{1}{\kappa R_* \xi} \dots\dots\dots (4.20)$$

(4.20) coincides fairly well with the measured values.

In other words, this fact confirms the validity of (3)-method in the evaluation of U_* mentioned in 4.3.1. Still, since $-\overline{uv}$ very near the free surface became negative value in the case of supercritical flow (Case G-3, -4, -5), the flow depth h_g at which $-\overline{uv} = 0$, was adopted here ($h_g/h = 0.9$ for Case G-5).

4.4.3 Correlation coefficients of Reynolds stress

A correlation coefficient of Reynolds stress is defined as $R = -\overline{uv}/u'v'$, which is a measure indicating its self-consistency of turbulence or similarity.

Fig. 4.12 shows the values of R obtained at each group, i.e. (a), (b) and (c) in Table 4.1. In the wall region and the free-surface region respectively, R increases and decreases monotonously with y/h , while in the equilibrium region it remains nearly constant, i.e. $R \approx 0.4$. The comparison with previous data in boundary layer and pipe flows shown in Fig. 4.12 indicates that R displays the universal characteristics, irrespective of the flow conditions and the roughness. Now, such a curve of R can be predicted from

(4.7) and (4.20), as follows:
$$R \equiv \frac{-\overline{uv}}{u'v'} = \frac{(1-\xi) - (\kappa R_* \xi)^{-1}}{2.92 \exp(-2\xi)} \dots (4.21)$$

As shown in Fig. 4.12, (4.21) has a good agreement with the experimental values though there is an application limit in this equation.

Next, $R_q \equiv -\overline{uv}/q^2$ is another coefficient indicating a correlation between the Reynolds stress and turbulence, and its experimental values are also shown in Fig. 4.13. These variations are similar to those of R in Fig. 4.12. That is, the value of R_q in the equilibrium region becomes nearly constant, i.e. $R_q = 0.12 - 0.16$, which corresponds to the value ($R_q = 0.15$) in the boundary-layer

calculation developed by Bradshaw et al.(1967).

More, from (4.7) and (4.20), we also obtain

$$R_q \equiv \frac{-\overline{uv}}{q^2} = \frac{(1-\xi) - (\kappa R_* \xi)^{-1}}{9.56 \exp(-2\xi)} \dots\dots\dots (4.22)$$

(4.22) explains fairly well the experimental values, as seen in Fig. 4.13.

4.5 Effect of the surface wave on turbulent structure

According to the conception of 'active-inactive motions' proposed by Bradshaw(1967), the active part is responsible for Reynolds shear stress, while the inactive part does not contribute essentially to this shear stress. The former shows a universal characteristic or local similarity of turbulence, while the latter contributes to the transfer of a scalar quantity such as turbulent energy and consists of a lower frequency part (a larger-scale eddy). Actually, our data of Reynolds stress in Fig. 4.11 have shown fairly well a universal characteristic, while the turbulence intensities near the critical-depth flow have shown some deviations from the universal function of (4.7), as pointed out in Figs. 4.2 and 4.3. This fact suggests strongly that the effect of surface wave near the critical-depth flow upon its turbulent structure may be due to an inactive part. So, the validity of this suggestion is examined in the following on a basis of the measurement of both surface-wave and wall-pressure fluctuations.

4.5.1 Analysis of surface-wave fluctuations

The surface-wave fluctuation h' was measured by a resistance-type wave amplitude instrument, where two fine nickel wires of 0.1mm diameter were stretched parallel to the y-axis in the water in the same manner as the case of hydrogen-bubble wire. The hydraulic conditions of this experiments (Group W) are those over the smooth bed varying only the Froude number, as indicated in Table 4.2.

Fig. 4.14 shows the intensity $\sqrt{h'^2}$ of surface-wave fluctuation and its relative intensity $\sqrt{h'^2}/h$. The values of both $\sqrt{h'^2}$ and $\sqrt{h'^2}/h$ increase rapidly with Fr and reach maximum near the critical-

depth, i.e. $Fr=1$, and then decrease with Fr in the supercritical flow. Such a so-called resonant behaviour near the critical-depth may be due to an inactive motion, as mentioned later.

By the way, the equation of free surface pattern can be linearly approximated and in result it becomes

$$(1 - \beta F_r^2) \frac{\partial^2 h'}{\partial x^2} - 2\beta \frac{F_r^2}{U_m} \frac{\partial^2 h'}{\partial x \partial t} - \left(\frac{F_r}{U_m}\right)^2 \frac{\partial^2 h'}{\partial t^2} - \frac{NS}{h} \frac{\partial h'}{\partial x} - \frac{2S}{U_m h} \frac{\partial h'}{\partial t} = 0 \quad \dots (4.23),$$

where, S is the bed slope, β is the Boussinesq coefficient and N is the hydraulic exponent ($N = 7/3 + (1 + 2h/B)^{-1}$, B is the channel width).

Assuming $h' = H \cdot \exp i(kx - \omega t)$ and $\omega \equiv kV_w + i\tilde{\omega}$ (4.24),

$$(4.23) \text{ gives } \left(\frac{\tilde{\omega}}{kU_m}\right)^2 = \frac{(N - 2\phi)(1 - F_r^2(\beta - 2\phi + \phi^2))}{F_r^2(4\beta - N - 2\phi)} \geq 0 \quad \dots (4.25)$$

where, $V_w/U_m \equiv \phi$.

So, the existence conditions of the small amplitude wave of (4.24)

are given by $\phi = N/2$, $\phi = 2\beta - N/2$ (4.26) $\phi = \beta \pm \sqrt{\beta(\beta - 1) + F_r^{-2}}$ (4.27)

On the other hand, eliminating ϕ from (4.23) and (4.24),

$$\frac{\tilde{\omega}h}{U_m} = \frac{S(kh)^2}{8} \frac{F_r^2(N^2 - 4\beta N + 4\beta) - 4}{(kh)^2 F_r^2 [\beta(2\beta - 1)F_r^2 + 1] + S^2} \quad \dots (4.28)$$

Consequently, denoting $F_{r,c} = ((N/2)^2 + \beta - \beta N)^{-1/2}$... (4.29),

the wave of (4.24) becomes stable for $F_r < F_{r,c}$, and unstable for

$F_r > F_{r,c}$. Fig. 4.15 shows a diagram of existence and stability of

the small disturbances, that is, the curves of (4.26), (4.27) and

(4.29) using $\beta=1.02$ and $N=10/3$. From this diagram, the critical-

depth flow (the celerity ϕ of its wave is zero, i.e. $F_r = \beta^{-1/2} \approx 1$ from

(4.27)) becomes stable because $Fr,c=1.6$. Unfortunately, this

small amplitude theory cannot explain the resonant behaviour in

Fig. 4.14. Well, it has been observed since Boussinesq that the

'undular hydraulic jump'-like surface wave occurred near the critical

depth flow. So, such a low-frequency undulation may have a strong

correlation with the inactive part of turbulence, which will be

investigated furthermore.

Also, we examined the ratio Ω of the surface-wave fluctuation energy

to the turbulent energy, i.e. $g \equiv \frac{(\rho/2)gh^2}{\int_0^h (\rho/2)q^2 dy} \dots\dots\dots (4.30)$

Applying (4.7), (4.30) yields $g = \left(\frac{U_m}{4.13U_*}\right)^2 \cdot \frac{1}{F_r^2} \left(\frac{\sqrt{k'^2}}{h}\right)^2 \dots\dots (4.31)$

As shown in Fig. 4.14, the variation of Ω vs. Fr is similar to that of the surface-wave fluctuation intensity. And, we understand that the surface-wave fluctuation energy becomes in same order of the turbulent energy near the critical-depth flow.

Next, the spectral analysis of the surface-wave fluctuation was done by making use of the F.F.T. method (the sample size N was chosen N=4096), and its raw results were smoothed by a digital triangular filter, and then they were normalized by $\overline{h'^2}$.

Consequently, these analysis of the frequency spectrum F(f) satisfied within errors of 2-3% the normalized condition that $\int_0^\infty F(f) df = 1$.

Now, these results of F(f) are shown in Fig. 4.16 as a parameter of Fr. When Fr is so small as (1) or (2) shown in Fig. 4.16, F(f) has an evident peak at $f_m=2-3$ (Hz), and for $f > f_m$, it seems to satisfy the -5 power universal law obtained by the wind-wave theory, that is: $F(f) = a \left(\frac{g}{\sqrt{k'^2}}\right)^2 f^{-5} \dots\dots\dots (4.32)$

Such a good agreement with a universal function of (4.32) may be due to the active part (cf. Fig. 4.14). With increase of Fr (3), (4), (5), the energy transfer from the higher frequency into the lower one occurs remarkably, and consequently the lower frequency part of F(f) becomes more dominant near the critical-depth flow. On the other hand, in the supercritical flow (6, 7, 8), the higher frequency part of F(f) becomes more dominant again. Hence, this fact suggests strongly that a lower frequency undulation occurs really near the critical-depth and thus that its flow is dominated by the inactive part, as pointed out previously.

4.5.2 Analysis of wall-pressure fluctuations

A pressure tap of 1mm diameter was set flush on the smooth bed in the center of the channel and its wall-pressure fluctuation p was

measured by using a gauge-type pressure transducer. The hydraulic conditions of this experiments (Group P) are indicated in Table 4.2.

Fig. 4.17 shows the intensity $p' \equiv \sqrt{\overline{p'^2}}$ of wall-pressure fluctuation and its relative intensity p'/P ($P \equiv \rho gh$, see (2.4)). The variation of p' vs. Fr is similar to that of the surface-wave fluctuation intensity. That is, p' shows an evident maximum near the critical-depth. By the way, the dominant terms of the pressure equation

$$\text{are given by } \bar{\nabla}^2 \left(\frac{p}{\rho U_*^2} \right) = -2 \frac{\partial U^+}{\partial \xi} \cdot \frac{\partial (v/U_*)}{\partial (x/h)} \dots (4.33)$$

where, $\bar{\nabla}^2$ is the dimensionless Laplacian by h .

If the turbulent structure is dominated by the active part, the universal expressions of $U^+ = \text{fun.}(\xi, R_e)$ and $v'/U_* = D_2 \cdot \exp(-\xi)$, become valid, and consequently the following universal function is also obtained

$$\text{from (4.33): } p'/\rho U_*^2 \equiv p'/\tau_0 = G(\xi, R_e) \dots (4.34)$$

$$\text{or, } \frac{p'}{P} = F_r^2 \left(\frac{U_*}{U_m} \right)^2 \cdot G(0, R_e) = \text{fun.}(R_e) \cdot F_r^2 \dots (4.35)$$

Although the friction velocity U_* in this experiments was evaluated from (4.6), it could be concluded from Fig. 4.18 that its values were fairly accurate (a thick line in Fig. 4.18 is given from (2.7), as follows: $U_* \text{ (cm/sec)} = k \cdot F_r^{2/3}$, $k \equiv (f/2)^{1/2} (g \nu R_e)^{1/3}$ (4.36)

Now, Fig. 4.17 also shows the values of p'/τ_0 using this friction velocity U_* . As Fr increases, p'/τ_0 deviates gradually from a universal value $G(0, R_e)$ and reaches maximum at $Fr \approx 0.8$. For $Fr > 0.8$, p'/τ_0 decreases monotonously with Fr and approaches again to $G(0, R_e)$ at $Fr \approx 2.5$. This fact confirms that such a deviation from $G(0, R_e)$ may be caused by the inactive part whose contribution is most remarkable near the critical-depth, especially on the side of subcritical range. Also, it has been recognized really that the universal value $G(0, R_e)$ contributed by the active part was a function of only the Reynolds number. For example, according to the Corcos (1964)' data (see Fig. 8.10), $p'/\tau_0 \equiv G(0, R_e) = 2.5$ at $Re = 3 \times 10^4$. Actually, our data of p'/τ_0 in the open-channel flow where $|Fr-1|$ is large and thus the active part is dominant, tend to approach to this universal value.

Next, the frequency spectra of wall-pressure fluctuations were obtained in the same manner as 4.5.1, and they were shown in Fig. 4.19. Unfortunately, the resonant phenomenon of the diaphragm in the pressure transducer occurred at about 5 Hz, and consequently these spectral distributions were quite inaccurate. However, the values of spectra in $f < 5$ Hz may be reliable, and so Fig. 4.19 shows clearly that the lower-frequency part of $F(f)$ becomes more dominant near the critical-depth (ex. ⑤, ⑥), as similar to Fig. 4.16. This fact also indicates evidently the existence of the inactive motion near the critical-depth.

4.6 Spectral distribution of velocity fluctuation and characteristic eddy-scale *)

4.6.1 Wave-number spectrum of each velocity component

Since it is very difficult to measure directly the wave-number spectrum $S(k)$ introduced in Chapter 2, $S(k)$ must be even now estimated from the frequency spectrum $F(f)$ by applying the Taylor's frozen-turbulence hypothesis, i.e. $\partial A / \partial t = -U \partial A / \partial x$ (4.37), where A is the transferable quantity. As its application criterion, Lin(1953) gave the following relations:

$$\frac{(\overline{du/dt})^2 / \{U^2 (\overline{\partial u / \partial x})^2\}}{\approx 5 (u'/U)^2 \dots (4.38)} \quad \text{and} \quad |v \partial U / \partial y| \ll |U \partial u / \partial x| \dots (4.39)$$

(4.38) is satisfactory with errors of 5% in the region of $\xi \geq 0.1$ for the smooth bed since $u'/U \leq 0.1$ (see Figs. 4.8-4.10).

Next, applying that $U/U_{max} = \xi^{1/7}$ and $L_x/\lambda = \sqrt{\xi}$ (see 4.6.4), (4.39) becomes $ky \gg (1/7)$ or $kL_x \gg (7\sqrt{\xi})^{-1}$ (4.40)

Judging from (4.38) and (4.40), the validity of (4.37) may become worse close to the wall. However fortunately, according to many recent researches cited by Monin et al.(1975), the frozen-turbulence approximation (4.37) may be applicable fairly accurately except for the productive subrange, i.e. $kL_x \leq 1$. Then, the following transformation can be applicable: $S(k) = (U/2\pi) \cdot F(f)$, $k = 2\pi f/U$ (4.41)

Now, Fig. 4.20 shows an example of spectral distributions $S(k)$ of each velocity component which were estimated by using (4.41)

*) Refer to our paper published in *Proc. of JSCE, No.241, pp.155-168, 1975.*

from $F(f)$ obtained in the same manner (F.F.T. method) as Fig. 4.16. Judging from this figure, the sampling number N was reasonably chosen $N=4096$. Firstly, the distribution of $S_u(k)$ satisfies fairly well the results summarized in Table 2.1. Since the Reynolds number Re is comparatively small, the inertial subrange may be so narrow (cf. (2.52)) as to detect its existence or the local isotropy exactly. However, the $-5/3$ power law is really satisfactorily recognized, and thus the phenomenological model of Fig. 2.9 becomes here applicable. Although the observed values in the lower frequency spectrum may not be conclusive because of the analytic limitation of (4.40), they agree fairly well with the Karman's interpolated formula (2.48). And thus, we could not here detect the multi-structure of spectrum, i.e. the occurrence of a few kinds of cascade process among the different scales, whose occurrence has been reported in the field experiments such as the atmospheric turbulence, the ocean or river turbulence. This may be due to only a single influx of external energy, i.e. an order-scale of L_x or h (mean-velocity scale): see Fig. 2.9.

Next, as to $S_v(k)$ and $S_w(k)$, an evident existence of the $-5/3$ power law cannot be recognized in Fig. 4.20. Now, $S_v(k)$ or $S_w(k)$ for a small-scale eddy ($kL_x \gg 1$) calculated from each power law of $S_u(k)$ in Table 2.1 by using (2.42) is given by a dotted line in Fig. 4.20. Compared with the observed values, isotropy can be recognized in the viscous subrange, as predicted in Chapter 2.

4.6.2 Spectral distribution normalized by L_x

In order to investigate systematically the spectral distributions on the different flow conditions, it is necessary to normalize them by a suitable characteristic scale. As this scale, L_x (macro-scale) or η (micro-scale) is usually chosen. Here, we adopted L_x because of an easy comparison with the theoretical results obtained in 2.3.

Now, assuming that (2.48) is valid up to $k=0$, we can obtain

$$L_x = (\pi/2) S_u(0) \dots\dots\dots (4.42)$$

However, for the present, (4.42) is considered to be a rough estimate because of (4.40). And, all the analyzed results were plotted by making use of X-Y plotter in the computer center, in the manner as described in Fig. 4.21.

Fig. 4.22 shows the spectral distributions at the typical measured points of each region for the smooth bed. Since $R_* \approx R_L$ is nearly equal to 500, the theoretical curve calculated with $R_L=500$ in 2.3.2 is described by a thick line in Fig. 4.22. Although the effect of the noise involved may appear in the higher wave-number part of $L_x \cdot k \geq 70$, this observed spectral distributions show a universal characteristic and agree well with the theoretical curve throughout the subranges. The results for the rough bed shown in Fig. 4.23 are also similar to those for the smooth bed. In this manner, all the results for the lower-velocity group, i.e. (c)-group in Table 4.1 showed a good agreement with the theoretical curve.

Next, Fig. 4.24 shows the spectral distributions near the wall ($\xi \approx 0.18$) and near the free-surface ($\xi \approx 0.75$) for the higher-velocity group, i.e. (b)-group in Table 4.1. Although the observed values fall on a universal curve irrespective of Fr , they indicate some systematic deviation from the theoretical curve calculated with $R_L=2000$. But, since the existence of the $-5/3$ power law is still recognized, the above deviation may be due to the inaccurate value of L_x . So, we correct the value of L_x in the following.

From (2.47), $r_m \equiv C (\epsilon L_x / u'^3)^{2/5} = (S_u(k) / L_x) \cdot (k L_x)^{3/5}$ (4.43)

From (2.50), $r_t \equiv C (\epsilon L_x / u'^3)^{2/5} = C \cdot K^{2/5}$ (4.44)

If the value of L_x is accurate, γ_m must coincide with γ_t . So, if the value γ_m measured from Fig. 4.24 is different from the theoretical value γ_t , L_x is corrected in the following so that γ_m coincides with γ_t : $\hat{L}_x \equiv L_x \cdot (r_t / r_m)^{5/2}$ (4.45)

By the way, while C is nearly equal to 0.5 (cf. Fig. 2.10), K is a function of R_L as shown in Fig. 2.11. From Fig. 4.25 which re-plotted the variation of K , we obtain a simply approximated function:

$$K = K_\infty + 3.98 R_L^{-1/2} , K_\infty = 0.691 \quad \text{..... (4.46)}$$

Now, the spectral distributions normalized by using \hat{L}_x corrected in this manner (see Fig. 4.21) are replotted in Fig. 4.26. Actually, such corrected distributions show a good agreement with the theoretical curves with $R_L=1000$ or 2000 in the inertial subrange whose observed values are most reliable. And, (a)-group in Table 4.1 also showed the similar results.

To sum up, all these data have confirmed that the inertial subrange where the $-5/3$ power law was valid had the universal characteristics irrespective of the Reynolds, the Froude numbers and the wall roughness.

4.6.3 Local isotropy and dissipation spectrum

Fig. 4.27 (a) and (b) show the spectrum $S_v(k)$ for the smooth and the rough beds, respectively. $S_v(k)$ as well as $S_u(k)$ becomes universal fairly well when it is normalized by L_x . The agreement with the theoretical curve obtained in 2.3 is very good in the range of $L_x \cdot k \geq 30$ for the smooth bed and $L_x \cdot k \geq 20$ for the rough bed.

This fact suggests that the isotropic relation, i.e. a local isotropy may be fairly valid in the viscous subrange and that the tendency toward isotropy may be a little stronger for the rough bed than the smooth bed. This suggestion may not be contradictory to the results obtained in 4.3 (e.g. Fig. 4.6).

Next, although the spectrum $S_{uv}(k)$ of the Reynolds stress is zero for any wave-number k in the strictly isotropic turbulence, it is essential to $S_{uv}(k) \neq 0$ in the shear flow. Fig. 4.28 shows the co-spectra $S_{uv}(k)$ of $-\overline{uv}$ obtained by F.F.T. method. Though there are fairly large scatters in the observed values, it can be recognized that $S_{uv}(k)$ becomes smaller than $S_u(k)$ in the range of $L_x \cdot k \geq 30$. This result also suggests that the tendency toward isotropy appears in this viscous subrange.

Lastly, the dissipation spectrum $D_u(k) \equiv k^2 S_u(k)$ is shown in Fig. 4.29, together with the theoretical curves. Up to the inertial subrange (the increasing part of $D_u(k) \sim k^{1/3}$), the observed values agree very well with the theoretical curve. And also, in the viscous subrange

an agreement between the both is comparatively good although the data in this range may be little accurate.

4.6.4 Characteristic eddy-scales and their relations

Fig.4.30 shows the macro-scale L_x evaluated from (4.42) and its corrected value \hat{L}_x by using (4.45), which were measured by a single-sensor hot-film. McQuivey et al.(1969) also evaluated L_x from (4.42), while Raichlen(1967) evaluated it on a basis of the Dryden's formula, i.e. $S_u(k) = (2L_x/\pi) \cdot [1 + (L_x \cdot k)^2]^{-1}$ (4.47)

The both methods are almost identical. Evidently, the scatters in the corrected values \hat{L}_x are very less than those in the values L_x . From this figure, the following relations are obtained irrespective

of Fr: $\hat{L}_x/h = B \cdot \xi^{1/2}$, ($\xi \leq 0.6$) (4.48), $\hat{L}_x/h = B_3$, ($\xi \geq 0.6$) (4.49)

where, the universal constants B and B_3 are both nearly equal to unity. And, they confirm the validity of the theoretical consideration in 2.4.

Fig. 4.31(a) shows the data measured by a dual-sensor hot-film, and of course they agree very well with the data measured by a single one. Consequently, the data very close to the wall can be complemented by using a single-sensor hot-film. Now, the effect of roughness upon L_x was investigated in Fig. 4.31(b). As expected previously, this effect appears evidently near the wall of $\xi \leq 0.1$. We(1975) has already confirmed that the data of L_x^+ satisfied well (2.65) and then gave $A_2 = 31$ (for smooth bed) and 20 (for rough bed). Such a characteristic that L_x decreases with enlargement of the roughness have also already reported by Engelund(1969), Antonia et al.(1971), Chen et al.(1974) and others. On the other hand, the roughness effect becomes weaker over the equilibrium region, and then it is considered that the universal functions (4.48) and (4.49) are satisfactory in this region. Since the turbulent dissipation ϵ_h/U_*^3 is expressed by the universal function $\phi(\xi)$ irrespective of even the roughness as pointed out later, (2.50) becomes

$$L_x/h = K \cdot (u'/U_*^3) \cdot \phi^{-1}(\xi) \dots\dots\dots (4.50)$$

From (4.7), $(L_x/h)K^{-1}$ is finally a function of only ξ . Consequently, adopting $B=1.0$ for the higher velocity group, then (4.46) gives

$B = 1.1$ for the lower velocity group. These result explains well the variations in Figs. 4.30 and 4.31 (or see Fig. 4.34).

Next, the micro-scale λ_x defined as $\lambda_x \equiv u' / \sqrt{(\partial u / \partial x)^2}$ can be evaluated from the following three methods.

- (1) *Spectrum method* : Evaluation from the dissipation spectrum $D_u(k)$, i.e. $\lambda_x = \left[\int_0^{k_m} D_u(k) dk \right]^{-1/2}$.
- (2) *Probability method* : Evaluation from the r.m.s.-value of $\partial u / \partial t$ (or $\Delta u / \Delta t$) by using (4.37).
- (3) *Zero-crossing method* : Assuming that u and $\partial u / \partial t$ are independent Gaussian, λ_x is evaluated from $\lambda_x = U / \pi N$, where N is the count number of the zero-crossing (i.e. $u=0$).

The superiority among their methods has been already examined in our previous paper(1975), and consequently the spectrum method was adopted here. Fig. 4.32 (a) and (b) show the micro-scale λ_x observed in the higher and the lower velocity groups, respectively. From (2.52), (4.7) and (4.48), the theoretical relation is obtained:

$$\frac{\lambda}{h} = c_1 \cdot \xi^{1/4} \exp\left(\frac{\xi}{2}\right), \quad c_1 \equiv \sqrt{\frac{15 B}{2.3 K R_*}} \quad \dots\dots\dots (4.51)$$

As for the higher velocity group ($Re \approx 3 \times 10^4$), approximating that $\lambda_x = \lambda$ (this approximation is fairly valid since the local isotropy may exist in the viscous subrange, see 4.6.3), the curve of (4.51) calculated with $B=1.0$ and $R_*=1600$ is shown in Fig. 4.32 (a). But, our observed data deviate over in parallel from this theoretical curve. This is caused by a fact that the spectral analysis in the viscous subrange could be hardly done for the higher velocity group as shown in Fig. 4.26. The deviation in the Raichlen's(1967) data may be also due to this reason. On the other hand, the Laufer's(1954) data in air flow are close to the theoretical curve because he sufficiently obtained the dissipation spectrum up to the fairly higher frequency, i.e. $f_\infty = 5-7$ kHz. As for the lower velocity group ($Re \approx 1 \times 10^4$), the observed values obtained by author and McQuivey et al.(1969) show a comparatively good agreement with (4.51) using $B=1.1$ and $R_*=600$ since their dissipation spectra were analyzed up to the viscous subrange (see Fig. 4.29). Still, the better agreement with the observed data in the free-surface

region is obtained if (4.49) is reasonably used instead of (4.48) in (4.51). To sum up, it should be noticed that the micro-scale λ_x satisfies fairly well the 1/3 power law, i.e. $\lambda_x/h = c_2 \epsilon^{1/3}$ (4.52), while the macro-scale L_x satisfies the 1/2 power law.

Next, the values of L_x/λ_x are shown in Fig. 4.33. (2.52) and (4.46) yield

$$\frac{L_x}{\lambda} = \sqrt{\frac{KR_L}{15}} = \sqrt{\frac{R_L}{15} (K_* + 3.98 R_L^{-1/2})} \dots\dots\dots (4.53)$$

The observed values for the lower velocity group are close to the theoretical curve (4.53), while those for the higher velocity group deviate below from this curve since λ_x was overestimated.

Lastly, the relations among the characteristic eddy scales L_x , λ_x and η are shown in Fig. 4.34. That is, from (4.7) and (4.48),

$$R_L/R_* = 2.3 \sqrt{\epsilon} \exp(-\epsilon) \dots\dots\dots (4.54)$$

and from (2.44),

$$\eta/h = R_*^{-3/4} (\epsilon h/U_*^3)^{-1/4} = K^{-1/4} R_L^{-3/4} \cdot (L_x/h) \dots\dots\dots (4.55)$$

The characteristic scale decreases monotonously with decrease of y/h due to the wall restraint. It is recognized that the effect of the wall restraint may become weaker for the smaller-scale, and consequently L_x , λ and η yield the 1/2, 1/3 and (1/4-1/6) power laws, respectively. Another noticeable characteristic is that the ratio of macro-scale to micro-scale becomes larger as the Reynolds number R_* or R_L is larger (compare the curves of $R_*=600$ and 1600 in Fig. 4.34). This means that the inertial subrange exists more wide as the Reynolds number is larger. However, judging from Fig. 4.34, to the extent of the Reynolds number in our experiments, both L_x/λ and λ/η are at most in one order, where the strict existence of the inertial subrange cannot be expected as pointed out previously.

4.7 Turbulent energy budget in open-channel flow

4.7.1 Turbulent energy dissipation

We(1975) have already examined the superiority among three kinds of the evaluation method of dissipation ϵ proposed in 2.3.3. To be brief, the accurate values of L_x and λ_x cannot be easily obtained, especially in very large Reynolds number, as have been pointed out in Figs. 4.30 and 4.32. Consequently, both (A) and (C) methods seem

to be rough estimation. On the other hand, because the $-5/3$ power law was recognized clearly in every spectral distribution (see 4.6), it can be concluded that the (B)-method, i.e. (2.47), is most reliable. This conclusion is also given by Grant et al.(1962), Bradshaw (1967), Lawn(1971) and others.

Now, Fig. 4.35 (a) and (b) show the dimensionless distributions of turbulent energy dissipation $\epsilon h/U_*^3$ evaluated from (2.47) for the higher and lower velocity groups, respectively. The observed values of $\epsilon h/U_*^3$ in both groups indicate a similar variation, that is a universal distribution irrespective of the Reynolds, the Froude numbers and the wall roughness. Above all, it should be noticed that the effect of roughness upon $\epsilon h/U_*^3$ is much smaller than upon u'/U_* or L_x/h .

Well, the following universal functions were given in Chapter 2:

$$\epsilon v/U_*^4 = A_1(y^+)^{-1} \quad (\text{wall region}) \dots\dots\dots(2.64)$$

$$\epsilon h/U_*^3 = C_1(1-\xi)^{3/2} \xi^{-1} \quad (\text{equilibrium region})\dots\dots\dots(2.78)$$

$$\epsilon h/U_*^3 = B_1(\xi' + B_2) \quad (\text{free-surface region})\dots\dots\dots(2.70)$$

The curve of (2.78) with $C_1=3.0$ is shown by a thin line ② in Fig. 4.35, and really it agrees well with the observed values in the equilibrium region. Also, the curve of (2.70) with $B_1=5$ and $B_2=0.1$

shows a good agreement with the observed values in the free-surface region. Although the theoretical results in Chapter 2 are valid in this manner, it is more desirable to obtain the overall universal function of $\epsilon h/U_*^3$ from the same reason as the discussion of overall spectral distribution in 2.3.2. For this purpose, by using (4.7) as u'/U_* and (4.48) as L_x/h , we can obtain from (2.50)

$$\frac{\epsilon h}{U_*^3} = K(R_L) \cdot \frac{12.2 \exp(-3\xi)}{B \sqrt{\xi}} \dots(4.56)$$

B is equal to 1.0 and 1.1 for the higher velocity group($R_* = 1600$) and the lower one ($R_* = 600$), respectively. $K(R_L)$ is determined from (4.46) and (4.54), and then the curve of (4.56) is indicated by a thick line ① in Fig. 4.35. Throughout the flow field except for very near the wall, (4.56) coincides very well with the observed values. Moreover, the curves of (4.56) for both groups become nearly identical

because of the small variation of K vs. R_L (see Fig. 2.11), and this shows the independence of the dissipation $\epsilon h/U_*^3$ on the Reynolds number, as mentioned above.

Next, Fig. 4.36 shows the dimensionless distributions of dissipation $\epsilon^+ \equiv \epsilon \nu / U_*^3$ in the wall region. Although we here could not obtain the data in the viscous sublayer, Laufer(1954) succeeded in the measurement very near the wall in air pipe flow, i.e. $y^+ \leq 10$, and hence his data are replotted in Fig. 4.36. The observed values of ϵ^+ also show well a universal characteristic. That is, they attain the maximum near the sublayer edge $\delta_s^+ \approx 10$, and then decrease monotonously with increase of y^+ . The theoretical curves of (4.56) and (2.78) are indicated in Fig. 4.36 by solid lines ① and ②, respectively. The observed values show a better agreement with (2.78) than (4.56) because (4.7) or (4.56) becomes inapplicable near the wall of $y^+ \leq 50$, as mentioned in 4.3.3. On the other hand, when R_* is very large, (2.78) becomes nearly equal to (2.64) in the wall region, and thus it is confirmed that the dissipation ϵ^+ over the sublayer edge can be given by (2.64) or (2.78), namely the -1 power law of y^+ . Then, A_1 becomes nearly equal to $C_1 = 3.0$.

4.7.2 Production and diffusion of turbulent energy

The turbulent energy production $P \equiv -\overline{uv} \partial U / \partial y$ is easily obtained from the measured Reynolds stress and mean velocity distributions. Over the equilibrium region, the theoretical distribution is given from (2.14) and (4.20), as follows:
$$\frac{P h}{U_*^3} = \left(1 - \xi - \frac{1}{\kappa R_* \xi}\right) (\kappa \xi)^{-1} \dots (4.57)$$

The observed values of P and its theoretical curve of (4.57) are both shown in Figs. 4.38 and 4.40, as mentioned later.

It is necessary for the explanation of the turbulence production mechanism to investigate the distribution of its production $P^+ \equiv P \nu / U_*^3$ in the wall region. However, since P^+ in this region could not be measured, only its theoretical curve calculated from (2.5), (2.12) and (2.13) (after van Driest) was plotted by a broken line ③ in Fig. 4.36. The variation of P^+ is similar to that of ϵ^+ .

In detail, the turbulent production P , the turbulent dissipation ϵ and the direct-dissipation E are nearly equal to each other at the sublayer edge $y^+ \approx 10$ (cf. 2.2.1 or Fig. 2.2). In the sublayer ($y^+ \leq 10$), they show $E > \epsilon > P$, i.e. the deficiency of turbulent energy. In the buffer layer ($10 \leq y^+ \leq 30$), they show $P > \epsilon$, i.e. the sufficiency of turbulent energy. And, in the log region ($y^+ > 30$, see Fig. 2.15), they show $P \approx \epsilon$, i.e. the equilibrium state of turbulent energy.

Next, we consider the turbulent energy diffusion $T_r \equiv \overline{q^2 v} / 2$. Although the correlation between v and w could not be measured in our experiments, the following approximation may be valid, because $\overline{w^2 v} \approx \overline{v^2 v}$ according to Laufer's experimental results:

$$T_r \equiv \frac{\overline{q^2 v}}{2} \approx \overline{(u^2/2 + v^2) v} \dots\dots\dots (4.59)$$

Fig. 4.37 shows the observed values of T_r evaluated from (4.59) for the both groups. Although there are some scatters in the data of Fig. 4.37(a), our data show a universal distribution in spite of the wide variation of Fr , and they agree well with Lawn's data. According to Lawn and author, the effect of the Reynolds number upon T_r/U_*^3 is also very small (Laufer's data may be inaccurate in this respect). On the other hand, the effect of the roughness upon T_r/U_*^3 appears evidently near the wall, as seen in Fig. 4.37(b). That is, as the roughness becomes larger, the maximum value of T_r decreases gradually and its distribution becomes flatter. In this manner, T_r/U_*^3 becomes nearly universal in respect of the Reynolds and Froude numbers, while it is evidently influenced near the wall by the roughness. So, because the diffusion T_r will have a close connection with the turbulence-production mechanism, as predicted in 2.6, the effect of the roughness upon this mechanism will be in detail investigated in Chapter 5.

Incidentally, the diffusion T_r in the free surface region can be expressed by a universal function since the roughness effect may disappear. Then, from Zagustin's hypothesis and (2.75), we can obtain

$$\frac{T_r}{U_*^3} \equiv \left(\frac{B_1}{B_5}\right) \frac{d\ell}{dy} = \left(\frac{B_1}{B_5}\right) \kappa \ell' (\ell' + 2B_6(1 - \ell')) \dots\dots\dots (4.60)$$

Since $B_1=5$ and $B_2=0.1$ as mentioned in 4.7.1, (4.60) yields

$$T_r/U_*^3 = \epsilon' (5\epsilon' + 1)/2 \dots\dots\dots (4.61)$$

Of course, (4.61) satisfies the relation that $T \equiv \partial T_r / \partial y = -\epsilon$ in the free-surface region. The curve of (4.61) is shown by a solid line ③ in Fig. 4.37. Actually, it has a good agreement with the observed values in this region.

4.7.3 Turbulent energy budget

Since the turbulent production P , the dissipation ϵ and the diffusion $T \equiv \partial T_r / \partial y$ were obtained in the previous section, the relationship among them, i.e. the turbulent energy budget can be considered here.

According to the theoretical results in 2.2, when R_* is very large, the turbulent energy equation in the main flow region is given by

$$\frac{Ph}{U_*^3} = \frac{\epsilon h}{U_*^3} + \frac{\partial}{\partial \xi} \left(\frac{T_r}{U_*^3} \right) + \frac{\partial}{\partial \xi} \left(\frac{R}{U_*^3} \right) \dots\dots\dots (4.62)$$

Since it is very difficult to directly measure the pressure energy diffusion $R' \equiv \partial R / \partial y$, we here estimate R' from (4.62), that is:

$$R' = P - \epsilon - T \dots\dots\dots (4.63)$$

Fig. 4.38 shows the turbulent energy budget over the smooth bed. It indicates the similar characteristics as Laufer's results about the pipe flow experiments. In the region of $\xi \leq 0.7$, the production P becomes nearly equal to the dissipation ϵ . Consequently, the transport of kinetic energy T plays only secondary role in the turbulence behaviours and is nearly balanced by the transport of pressure energy R' . Since for $\xi > 0.7$ the production P and the pressure diffusion R' are scarcely recognized, the dissipation ϵ is nearly balanced by the transport of kinetic energy T .

From (4.62) and these experimental results,

$$0 \equiv \int_0^h (P - \epsilon) dy \doteq \underbrace{\int_0^{y_1} (P - \epsilon) dy}_{\text{Wall Region}} + \underbrace{\int_{y_1}^{y_2} (P - \epsilon) dy}_{\text{Equi. Re.}} + \underbrace{\int_{y_2}^h T dy}_{\text{Free-Surface Region}}$$

That is,
$$\int_0^{y_1} (P - \epsilon) dy \doteq \int_{y_2}^h (-T) dy > 0 \dots\dots\dots (4.64)$$

(4.64) concludes that the energy excess range where $P > \epsilon$ exists near the wall, while the energy deficiency range where $\epsilon > P \approx 0$

exists near the free surface. Between two ranges there exists the intermediate range where the energy flows under a dynamically equilibrium state so that $P \approx \epsilon$, as already shown in Fig. 2.13.

By the way, from (2.28), the turbulent energy equation in the wall region is given by
$$\frac{P\nu}{U_*^4} = \frac{\epsilon\nu}{U_*^4} + \frac{T\nu}{U_*^4} + \frac{R'\nu}{U_*^4} - \frac{\partial^2}{\partial y^{+2}} \left(\frac{\overline{q^2}}{2U_*^2} \right) \dots\dots\dots (4.65)$$

Expanding the velocity in a Taylor series about $y^+=0$ yields

$$\frac{\overline{q^2}}{2U_*^2} = \frac{1}{2} \left\{ \left(\frac{\partial u^+}{\partial y^+} \right)_0^2 + \left(\frac{\partial w^+}{\partial y^+} \right)_0^2 \right\} y^{+2} + o(y^{+3}) \dots\dots\dots (4.67)$$

Since $\sqrt{(\partial u^+/\partial y^+)^2} \approx 0.3$ and $\sqrt{(\partial w^+/\partial y^+)^2} \approx 0.1$ according to Hinze(1975), (4.67) becomes
$$\overline{q^2}/2U_*^2 \approx 0.05 y^{+2} + o(y^{+3}) \dots\dots\dots (4.68)$$

Consequently, the rate $V_T \equiv -\partial^2(\overline{q^2}/2U_*^2)/\partial y^{+2}$ of work by the viscous stress becomes nearly equal to $V_T \approx -0.1$ very close to the wall. Thus, V_T in the wall region must not be neglected because it is of the same order as the production P^+ or the dissipation ϵ^+ , as seen in Fig. 4.36.

Fig. 4.39 replots the turbulent energy budget in the wall region, where the values of P , ϵ , T and V_T were obtained by Laufer(1954). P is roughly balanced by ϵ . The sum of T and V_T is roughly balanced by R' . In detail, the sublayer ($y^+ < 10$) is the deficiency range ($P < \epsilon$) of the turbulent energy. The buffer layer ($10 < y^+ < 30$) is its excess range ($P > \epsilon$), and the log region ($y^+ > 30$) is its equilibrium range ($P \approx \epsilon$), as mentioned previously. The excess turbulent energy in the buffer layer is transported into the sublayer by the pressure diffusion ($R' < 0$), and also into the free-surface region by the kinetic energy diffusion ($T < 0$). Consequently, the turbulent budget among them balances itself.

Next, Fig. 4.40 shows the turbulent energy budget over the rough bed. Although this budget relation over the rough bed is nearly similar to that over the smooth bed, the roughness effect appears in the diffusion terms T and R' near the wall. Though the turbulence production mechanism over the rough bed is, at present, still unknown, its mechanism may be quite different from that over the smooth bed, since the buffer layer (the excess range of the turbulent energy) exists no longer over the rough bed. A clue to make clear

its mechanism will be given in Chapter 5.

Lastly, Fig. 4.41 shows the relationship between the production P and the dissipation ϵ . Although there are a little scatters in the observed values, the values of $|P-\epsilon|/\epsilon$ become nearly equal to 0.2 in the equilibrium region, and then in the free-surface region they increase up to 1.0, i.e. $P \approx 0$. The curve ① in Fig. 4.41 which was calculated from (4.56) and (4.57), agrees well with the observed values, and thus it explains well the relationship between P and ϵ .

References (Chapter 4)

- 1) Raichlen, F. : Some turbulence measurements in water, Proc. of ASCE, EM-2, pp.73-97, 1967.
- 2) McQuivey, R. S. & Richardson, E. V. : Some turbulence measurements in open-channel flow, Proc. of ASCE, HY-1, pp.209-223, 1969.
- 3) Imamoto, H. : Hydraulic studies on turbulence in open-channel flow, Doctral thesis presented to Kyoto University, 1971 (in Japanese).
- 4) Blinco, P. H. & Partheniades, E. : Turbulence characteristics in free surface flows over smooth and rough boundaries, J. Hydraulic Research, vol.9, pp.43-69, 1971.
- 5) Nakagawa, H., Nezu, I. & Ueda, H. : Turbulence of open channel flow over smooth and rough beds, Proc. of JSCE, No.241, pp.155-168, 1975.
- 6) Townsend, A. A. : Equilibrium layers and wall turbulence, J. Fluid Mech., vol.11, pp.97-120, 1961.
- 7) Laufer, J. : The structure of turbulence in fully developed pipe flow, NACA, TR-1174, 1954.
- 8) Bradshaw, P. : 'Inactive' motion and pressure fluctuations in turbulent boundary layer, J. Fluid Mech., vol.30, pp.241-258, 1967.
- 9) Nakagawa, H. & Nezu, I. : On a new eddy model in turbulent shear flow, Proc. of JSCE, No.231, pp.61-70, 1974.
- 10) Ljatkher, V. M. : Calculation of spectra of turbulent pulsations in uniform flows, Proc. of 12-th Cong. of IAHR, vol. 2, B-3, 1967.
- 11) Smutek, R. : Discussion on 'Measurement of turbulence in water' by Richardson et al., Proc. of ASCE, HY-1, pp.519-523, 1969.
- 12) Monin, A. S. & Yaglom, A. M. : Statistical fluid mechanics, MIT Press, vol.1, pp.257-416, 1971.
- 13) Grass, A. J. : Structural features of turbulent flow over smooth and rough boundaries, J. Fluid Mech., vol.50, pp.233-255, 1971.
- 14) Chen, C. K. & Roberson, J. A. : Turbulence in wakes of roughness elements, Proc. of ASCE, HY-1, pp.53-67, 1974.
- 15) Antonia, R. A. & Luxton, R. E. : The response of a turbulent boundary layer to a step change in surface roughness, J. Fluid Mech., vol.48, pp.721-761, 1971.
- 16) Engelund, F. : Dispersion of floating particles in uniform channel flow, Proc. of ASCE, HY-4, pp.1149-1162, 1969.
- 17) Laufer, J. : Investigation of turbulent flow in a two-dimensional channel, NACA, TR-1053, 1951.
- 18) Bremhorst, K. & Walker, T. B. : Spectral measurements of turbulent momentum transfer in fully developed pipe flow, J. Fluid Mech., vol.61, pp.173-186, 1973.
- 19) Hinze, J. O. : Turbulence (2-nd edi.), McGraw-Hill, pp.586-770, 1975.
- 20) Corcos, G. M. : The structure of turbulent pressure field in boundary layer flows, J. Fluid Mech., vol.18, pp.353-378, 1964.
- 21) Monin, A. S. & Yaglom, A. M. : Statistical fluid mechanics, MIT Press, vol.2, pp.337-652, 1975.
- 22) Lin, C. C. : On Taylor's hypothesis and the acceleration terms in the Navier-stokes equation, Quar. of Applied Math., vol.x, pp.295-306, 1953.
- 23) Bradshaw, P. : Conditions for the existence of an inertial subrange in turbulent flow, A.R.C., R. & M., No.3603, 1967.
- 24) Grant, H. L., Stewart, R. W. & Moilliet, A. : Turbulence spectra from a tidal channel, J. Fluid Mech., vol.12, pp.241-268, 1962.
- 25) Townsend, A. A. : The structure of turbulent shear flow, Camb. Univ. Press, 1956.
- 26) Lawn, C. J. : The determination of the rate of dissipation in turbulent pipe flow, J. Fluid Mech., vol.48, pp.477-505, 1971.

Chapter 5 Experimental consideration on mechanism of turbulence production

5.1 Introduction

The physics of wall-turbulence have now been established in at least a qualitative sense through experiments and refined data analysis, as pointed out by Mollo-Christensen(1971). Kline et al.(1967) and Kim et al.(1971) discovered the bursting phenomenon, in which ejections played a predominant role, by making visual studies of the mechanism of turbulence production by the hydrogen-bubble technique. Also, Corino & Brodkey(1969) and Grass(1971) found by flow visualization that sweeps are prominent near the wall. This suggests that sweeps may be as important as ejections for turbulence production. This was verified by Nychas et al.(1973) and Offen & Kline(1974,-75).

On the basis of these qualitative results, some researchers (Lu & Willmarth 1973, Brodkey et al. 1974, etc.) have attempted to obtain more quantitative knowledge about the structure of the Reynolds stress, i.e. turbulence production, by using point measurements.

In this chapter, we also experimentally investigate the mechanism of turbulence production in open-channel flows by means of both conditional point-measurements and flow visualization, on the basis of the theoretical predictions of 2.6 and the previous results mentioned above.

5.2 Probability distributions of the velocity fluctuations and the instantaneous Reynolds stress *)

5.2.1 Probability density function of velocity and its higher moments

The data plotted in Fig. 5.1 are the probability densities measured in each region of turbulent flow over a smooth bed. Data were sampled by dividing the region $-3 < \hat{u}, \hat{v} < 3$ into 40 cells, where $\hat{u} \equiv u/u'$ and $\hat{v} \equiv v/v'$. When the skewness factor S and the flatness factor F are given, the Gram-Charlier distribution (2.96) is determined by using the following relations from (2.94):

$$\left. \begin{aligned} Q_{30} = S_u &\equiv \overline{\hat{u}^3}, & Q_{03} = S_v &\equiv \overline{\hat{v}^3} \\ Q_{40} = F_u - 3 &\equiv \overline{\hat{u}^4} - 3, \\ Q_{04} = F_v - 3 &\equiv \overline{\hat{v}^4} - 3 \end{aligned} \right\} \dots\dots\dots (5.1)$$

*) Refer to our paper published in *Jour. of Fluid Mech.*, vol. 80, pp. 99-128, 1977.

Now, the experimental values of S and F for u and v are shown in Fig. 5.2, together with data obtained in a boundary layer by Gupta & Kaplan(1972) and in an oil flow by Kreplin(1973, quoted in Eckelmann 1974). Owing to the deficiency of measurements in the vicinity of the wall, it is difficult to make a definite remark about the difference in the values of these quantities in free-surface flow and in boundary-layer flow. But, except for the free-surface region, a good agreement between the two may be observed. In the free-surface region both $|S|$ and $|F|$ have their maximum values, while they increase monotonously in the outer layer of the boundary-layer flow. This discrepancy may be due to the presence of large-scale intermittency in the boundary-layer flow.

It is noteworthy that S_u and S_v are almost symmetrical with respect to each other about the axis $S=0$ (Gaussian) for any value of y^+ , and change sign at $y^+ \approx 10$. Also, Fig. 5.2 suggests that the Gram-Charlier distribution should be taken into account in both the wall and the free-surface regions because the deviation from the Gaussian distribution becomes larger in these regions.

The theoretical curves of the probability density given by (2.96) were calculated by using the measured values of S and F (Fig. 5.2), and are shown in Fig. 5.1. Despite some scatter in the observed data, the actual phenomena can be fairly well explained by the Gram-Charlier distribution. Though the fourth-order distribution is in better agreement with the experimental results than the third-order one, the difference between the two does nothing to change the essential characteristics of the distribution. In the wall and equilibrium regions over the viscous sublayer, i.e. $y^+ \geq 10$, the third-order distribution seems to be sufficiently accurate. But it is better to consider the fourth-order distribution for the free-surface region, because the deviation from the observed values becomes comparatively large. Like S_u and S_v , shown in Fig. 5.2, the distributions of $p(\hat{u})$ and $p(\hat{v})$ indicate nearly symmetrical deviation to the positive and negative sides of the zero axis respectively; $p(\hat{u})$ having its maximum

value on the positive side and its longer tail on the negative side, and vice versa for $p(\hat{v})$.

The above description of the flow over the smooth bed applies in the case of the rough beds too. The values of the fourth- and fifth-order moments are shown in Fig. 5.3, as well as the data obtained by Lawn(1971). In the wall and equilibrium regions, the fourth-order moments hardly deviate from the Gaussian distribution and thus the third-order distribution may be valid in these regions. In the free-surface region, however, the third-order approximation may yield significant errors because of a considerable deviation from the Gaussian distribution.

Judging from Fig. 5.3, the fifth-order moment widely deviates from Gaussian value, $M_{50} \neq 0$. The following can be deduced in the same way as (2.94): $Q_{50} = M_{50} - 10 M_{30} \dots\dots\dots (5.2)$

The values of M_{50} calculated from (5.2) by setting Q_{50} equal to zero are shown in Fig. 5.3, and they agree fairly well with the observed values. This is the reason why the higher-order cumulants can be neglected as described in 2.6. Since all the odd-order moments of a Gaussian distribution are equal to zero, it is suggested that the third-order Gram-Charlier distribution should replace the Gaussian one. Also, it seems that in the wall region the fifth-order moment (in general, odd-order moments) is influenced by the roughness, which will be discussed later in detail.

5.2.2 Probability density function of instantaneous Reynolds stress

The observed values of the probability density function $p_w(w)$ of the Reynolds stress in each flow region are indicated in Fig. 5.4, as an example of the flow over a smooth bed. The fluctuating Reynolds stress $w (= uv/\overline{uv})$ was sampled by divided $-6 < w < 8$ into 40 cells. The sums of the values of $p_w(w)$ in the ranges $w < -6$ and $w > 8$ respectively are plotted on the broken lines in Fig. 5.4. Since $p_w(w) = 2p_G(w)$ as indicated by (2.103) and (2.104), $p_w(w)$ was calculated by using the values of R given in Fig. 4.12, and the resulting curves are shown as solid lines in Fig. 5.4. Good agreement

between the theoretical and experimental values was obtained, especially in the equilibrium region, and any small discrepancy between the two was due to a large deviation of the fourth-order moments from Gaussian as shown in Fig. 5.3. Consequently, the unconditional probability distribution $p_w(w)$ of Reynolds stress can be represented by one directly derived from a Gaussian distribution with high accuracy, as verified by Lu & Willmarth(1973) and Antonia & Atkinson(1973).

It may be noted from Fig. 5.4 that the probability distribution of values of uv has a very sharp peak at $w=0$ and a very long tail extending to large values of $|w|$. In a theoretical equation $p_w(w)$ becomes infinite at $w=0$ because $K_0(0) = \infty$ and becomes larger on the positive side of the curve than on the negative side because $\bar{w} = \int_{-\infty}^{\infty} wp_w(w) dw = 1$. Consequently, it can be suggested that almost all of the events occur with small values of $|w|$ but sometimes an event occurs with a very large value of $|w|$. Hence, we can conclude that the instantaneous Reynolds stress might have marked intermittency.

In order to investigate this characteristic in detail, the observed values of the skewness factor S_{uv} and the flatness factor F_{uv} of w are shown in Fig. 5.5, together with data obtained by Antonia & Atkinson(1973). Provided that $Q_{jk} = 0$ for $j+k \geq 5$, S_{uv} and F_{uv} can be evaluated in terms of the lower moments in the same way as in (2.94):

$$S_{uv} = \frac{1}{(M_{22} - R^2)^{\frac{3}{2}}} \{M_{30}M_{03} + 9M_{12}M_{21} + 3(M_{31} + M_{13}) + 2R(5R^2 - 3M_{22} + 9)\}, \quad (5.3)$$

$$F_{uv} = \frac{1}{(M_{22} - R^2)^2} \{M_{40}M_{04} + 16M_{31}M_{13} + 24(M_{21}M_{03} + M_{12}M_{30}) + 18(M_{22}^2 + 2M_{21}^2 + 2M_{12}^2) - 30R^2M_{22} + 12R(M_{31} + M_{13} - 9M_{21}M_{12} - M_{30}M_{03}) - 3(R^4 + 24R^2 + 6)\}. \quad (5.4)$$

The theoretical values of S_{uv} and F_{uv} were calculated from (5.3) and (5.4) by using the experimental values of the moments as indicated in Fig. 5.5. The calculated values are in comparatively good agreement with the observed ones. Some of the discrepancy in the F_{uv} (8-th order moment of u or v) diagram may be due to the error introduced by neglecting the higher-order cumulants.

As previously mentioned, the difference between the third-order distribution and the fourth-order one is not large. Both S_{uv} and

F_{uv} show a gradual variation with y/h up to the equilibrium region (that is, $S_{uv} \approx -2$, $F_{uv} = 10 \sim 20$ in this region), similar to the distribution of the higher-order moments shown in Fig. 5.3, but in the free-surface region they increase abruptly and then decrease towards the surface. Although good agreement between the behaviour of S_{uv} and F_{uv} in open-channel flow and in boundary-layer flow can be seen up to the equilibrium region, some discrepancies similar to those in Fig. 5.2 are evident in the free-surface region corresponding to the outer layer. Since the absolute values of S_{uv} and F_{uv} are comparatively large in the free-surface region, the strong asymmetry and intermittency in the Reynolds-stress fluctuations may appear, as inferred from Fig. 5.4.

The effect of roughness on S_{uv} and F_{uv} seems to appear only in the wall region, so that their values for the rough beds become smaller than those for the smooth bed. This means that the profile of the $p_w(w)$ distribution is not so slender and the intermittency of the Reynolds-stress fluctuations is smaller in case of a rough bed.

5.2.3 Conditional probability distribution of instantaneous Reynolds stress

As mentioned in 2.6, $p_w(w)$ cannot describe the characteristics of each event separately, because some of the terms corresponding to different events may balance each other as indicated by (2.104). Thus, the conditional probability density functions $p_i(w)$ ($i=1-4$) expressed by (2.109)-(2.112) should be considered in order to discuss the contribution of each event to the Reynolds stress. This can be done by determining both the skewness factor S and the diffusion factor D connected with u and v , and their observed values for smooth and rough beds are shown in Fig. 5.6, together with data for a pipe flow obtained by Lawn(1971). Although the diffusion factor is smaller than the corresponding skewness factor, both curves are qualitatively similar and have the following characteristics. First, the relation between D_u and D_v resembles that between S_u and S_v , for example the D_u curve is almost the reflexion of the D_v curve in the zero

axis. Also, $S_u < 0$, $S_v > 0$ and $D_u < 0$, $D_v > 0$ except in the immediate vicinity of the wall. Another characteristic seen in Fig. 5.6 is the remarkable effect of roughness in the vicinity of the wall. In case of the smooth bed, S and D both vary so gradually that they remain nearly constant when y/h is below the equilibrium region. For a rough bed, the absolute values of S and D decrease towards the wall so rapidly that they become zero at $y/h \sim 0.1$ and then, changing sign, increase upon approaching the wall. These trends are shown by the dashed lines in Fig. 5.6. Since in the middle of the equilibrium region the values of S and D for a rough bed always coincide with those for a smooth bed, it can be concluded that roughness has an effect on the values of S and D in this region at least.

Although there is a close resemblance between our curves and Lawn's for a smooth bed, the difference in magnitude over the whole depth between the two may be caused by the difference in data processing. As mentioned by Frenkiel & Klebanoff (1967), the analog method used by Lawn cannot be expected to obtain such accurate values of the higher-order moments as the digital procedure adopted here.

S^+ , D^+ , S^- and D^- can be evaluated from (2.115) for the values of S and D obtained above and are shown in Fig. 5.7. Judging from (2.115) and the symmetry between S_u and S_v , and D_u and D_v in Fig. 5.6, S^+ and D^+ will reduce to nearly zero, and S^- and D^- will reduce to S_v and D_v , respectively. The roughness effect is marked for S^- and D^- up to the equilibrium region, while neither S^+ nor D^+ displays this effect because of cancellation of the roughness terms.

In the same manner, Fig. 5.8 shows the results obtained for the higher-velocity group in Table 4.1 (b). From Figs. 5.7 and 5.8, the following characteristics can be obtained:

- (1) S^+ , S^- , D^+ and D^- show a close universality irrespective of Fr and Re .
- (2) S^- and D^- near the wall are influenced remarkably by the wall roughness.
- (3) Both S^- and D^- show a similar variation. Consequently, D^-/S^- becomes roughly equal to 0.7.

(4) Both S^+ and D^+ become nearly equal to zero, though the approximation of $S^+ \approx 0$ is worse than that of D^+ .

Next, by substituting the values of S^+ , D^+ , S^- and D^- into (2.109) - (2.112) with the Bessel function $K_{1/2}(t)$ equal to $(\pi/2t)^{1/2} e^{-t}$, the conditional probability distributions of the Reynolds stress can be obtained. An example of the calculated distribution for each event is presented in Fig. 5.9. The probability distribution at the point $y/h=0.193$ in the equilibrium region over a smooth bed is represented in terms of $|w|p(w)$. Similar figures have been obtained in the other regions and for rough beds. These theoretical results agree very well with the observations by Brodkey et al. (1974, Fig. 9).

In Fig. 5.9 both the ejection and the sweep events exhibit much larger values and much longer tails than the interaction events, which implies that the ejection and sweep events have much greater intermittency. Despite having a smaller maximum, the curve of the ejection events has larger values than that of the sweep events beyond $w \approx 5$, so that it may be expected that ejections make the greatest contribution to the Reynolds stress. Since $|w|p_1(w)$ is similar to $|w|p_4(w)$ while $|w|p_2(w)$ is similar to $|w|p_3(w)$, the characteristics of these events mainly depend upon the sign of u . This gives theoretical support to the observation by Brodkey et al. (1974) that the bursting process may be governed by the fluctuating velocity u rather than by v . The fact that $wp_4(w)$ in Fig. 5.9 takes small negative values for large values of w is unreasonable, and therefore the sweep events cannot be represented accurately by (2.112) in this range of w . This negative $p_4(w)$ would probably be corrected by considering terms of higher than third order which have been described earlier. Thus the discrepancy between the experimental results and the theoretical values predicted by the third-order approximation will become larger near the free surface, where S_{uv} and F_{uv} are large.

5.3 Internal structure of Reynolds stress and mechanism of turbulence-production *)

5.3.1 Internal structure of Reynolds stress

As defined in 2.6, the fraction of time $T_i(H)$ and the contribution to the Reynolds stress $RS_i(H)$ corresponding to each event in the flow over a smooth bed are shown in Figs. 5.10 (a), (b) and (c) for a typical point in the wall, equilibrium and free-surface regions respectively. Theoretical curves were obtained from (2.116)-(2.119), while our experimental data were analysed by almost the same method of conditional sampling as that used by Lu & Willmarth(1973):

$$T_i(H) = \lim_{T \rightarrow \infty} \frac{1}{T} \int_0^T I_i(t, H) dt \approx \frac{1}{N} \sum_{j=1}^N \{I_i(t, H)\}_j \dots\dots\dots (5.5)$$

$$RS_i(H) = \frac{1}{uv} \lim_{T \rightarrow \infty} \frac{1}{T} \int_0^T u(t) v(t) I_i(t, H) dt \approx \frac{1}{N} \sum_{j=1}^N \{w(t) I_i(t, H)\}_j \dots\dots (5.6)$$

where
$$I_i(t, H) \equiv \begin{cases} 1 : |w(t)| > H \text{ and the point } (u, v) \text{ in the } i\text{-th quadrant,} \\ 0 : \text{otherwise} \end{cases}$$

$$\text{As for the hole event } (i=5), \quad T_5(H) = 1 - \sum_{i=1}^4 T_i(H), \quad RS_5(H) = 1 - \sum_{i=1}^4 RS_i(H) \dots\dots\dots (5.7)$$

In the wall region (Fig. 5.10 a) and the equilibrium region (Fig. 5.10 b), the agreement between the experimental data and the predicted values is fairly good over a wide range of hole size H , so that it may be expected that the third-order probability distribution represents the correct picture for a sequence of bursting processes. In the free-surface region(Fig. 5.10 c), however, a discrepancy between the two appears for large values of H , owing to the neglect of higher-order terms.

Although the time occupied for $H < 1$ amounts to about a half of the total time, the corresponding contribution to the Reynolds stress is only a few percent, which suggests that $w(t)$ has a large intermittency. Though the inward interaction shows slightly larger values than the outward interaction, they both become negligibly small at $H \approx 5$, and consequently the negative contribution to the Reynolds stress disappears. The sweep event decreases rapidly with H and beyond

*) Refer to our paper published in *Jour. of Fluid Mech.*, vol. 80, pp. 99-128, 1977.

$H \approx 10$ only the ejection event contributes to the Reynolds stress, while the time occupied by this event is very short. From this, it may be inferred that the ejection event may arise in the form of a very sharp pulse, which agrees well with the results obtained by Corino & Brodkey(1969), Kim et al.(1971) or Grass(1971) by means of flow visualization. The correlations in magnitude among the four events are invariant over the whole depth. In particular, the fact that $T_2 < T_4$ and $RS_2 > RS_4$ for small values of H implies that the ejection event is more intensive than the sweep event in this range.

A typical example of the conditional probability distribution of the Reynolds stress in the flow over a rough bed is presented in Fig. 5.11, together with the experimental results. Since the roughness effect appears predominantly in the wall region as indicated in Chapter 4, only the structure of the Reynolds stress in this region is discussed here; it was verified that the structure in the other regions was almost the same as that for a smooth bed, shown in Fig. 5.10. The agreement between the theoretical curves and the experimental values is fairly good. It is noteworthy that the relations between the magnitudes of the ejection and the sweep and between the magnitudes of the inward and the outward interactions become the reverse of those for a smooth bed, because of the negative values of S^- and D^- . This result will be discussed in detail later.

5.3.2 Relative intensity of the different events

In order to describe clearly the relation between the sequence of the bursting process and the Reynolds stress, it is necessary to investigate the relative intensity of each event at $H=0$. Fig. 5.12 (a) and (b) show the distributions of the Reynolds stress contributed by each event *vs.* y/h for the smooth and rough beds respectively. Experimental results for a smooth boundary layer by Lu & Willmarth(1973) and for a smooth oil channel by Brodkey et al.(1974) are also shown. It is very interesting that the observed values completely agree with the curves calculated from (2.118) over the whole depth, irrespective of the roughness size. This implies that the theore-

tical considerations in 2.6 may be able to explain the bursting phenomenon in some detail for both rough and smooth beds.

In case of the smooth bed, there exists the relation $ejection > sweep > inward\ interaction \geq outward\ interaction$ within the observed range of y/h . The difference between the two interactions, however, is almost negligibly small, because $S^+ \approx D^+ \approx 0$ on the basis of the symmetry between S_u and S_v and between D_u and D_v . In the wall region the intensities of all events decrease with increasing y/h , and good agreement was obtained between our results and those by Brodkey et al. (1974). Although the values of the ejection given by Lu & Willmarth (1973) agree well with our data, the values of the sweep show some differences. This discrepancy will be discussed later, with the characteristic quantities in the wall region represented by a y^+ parameter.

Next, in the equilibrium region, the intensity of each event is nearly constant irrespective of y/h . Since in this region a dynamic equilibrium exists between the turbulence production and dissipation, and a similarity in turbulent structure exists independently of external boundary conditions (cf. Chapter 4), it is expected that the bursting process and the accompanying turbulence production may attain a stable equilibrium state in this region, resulting in almost constant intensity for each event. The rates of intensity contributed by ejections and sweeps are about 75% and 60% respectively, and the excess Reynolds stress balances the sum of the negative rates contributed by the inward and outward interactions. Similar characteristics were verified by point measurements by Lu & Willmarth or Brodkey et al. and by flow visualization by Corino & Brodkey (1969) or Kim et al. (1971).

In the free-surface region the relative intensity of each event rapidly increases with y/h . Near the free surface both ejections and sweeps show a positive stress rate of over 100%, while the negative stress brought about by the interactions increases to such an extent that the differences between the positive stress and the negative stress are equal to the net Reynolds stress, whose absolute value,

however, becomes very small, i.e. $-\overline{uv} \approx 0$.

The relations between the intensities of each event in case of the rough beds and the smooth bed are almost the same, as shown in Fig. 5.12 (b), so that we can confirm the observation by Grass(1971) that both ejections and sweeps exist irrespective of the roughness conditions. But, in the range from the wall to the middle of the equilibrium region, where the roughness effect on the turbulent structure appears (cf. Chapter 4), some differences in the intensity profiles for the rough and smooth beds can be observed. It is noteworthy that, contrary to the case of a smooth bed, the intensity of ejections decreases towards the wall to become nearly equal to that of the sweeps at $y/h \approx 0.1$, and sweeps may become more intense than ejections in the vicinity of the wall as was observed by Grass(1971) using the hydrogen bubble technique. This fact that both ejections and sweeps, which are the predominant events in the bursting phenomenon, may be greatly affected by the roughness condition is very important and will be discussed in detail later.

In the same manner, Fig. 5.13 shows the contributions to Reynolds stress from the different events for the higher-velocity group experiments. In spite of the wide variation of Fr , the values of each RS_i coincide fairly well with each other, and also they agree well with the theoretical curves and the observed values of Fig. 5.12 (a).

Next, the fractions of time occupied by each event on the smooth and rough beds are shown in Figs. 5.14 (a) and (b), respectively, together with the theoretical curves calculated from (2.116). Unlike RS_i , the magnitude of the fraction of time T_i satisfies the relation sweep > ejection > outward-interaction \geq inward-interaction. Also, these results agree very well with those obtained by Brodkey et al.(1974). Each fraction of time is nearly constant irrespective of y/h except in the free-surface region, that is, T_2 or T_4 and T_1 or T_3 become roughly equal to 30% and 20%, respectively. On the other hand, the fractions of time for all events tend to approach a definite value on the free surface. It may be seen from this characteristic as well

as that of RS_i that the bursting process near the free surface may consist of smoother and more isotropic events.

Lastly, the turbulent energy production $P = -\overline{uv} \partial U / \partial y$ is plotted vs. the flow depth in Fig. 5.15. The positive and negative time-average production P_p and P_n , respectively, are given by

$$P_p = (RS_2 + RS_4)P, \quad P_n = -(RS_1 + RS_3)P \quad \dots\dots\dots (5.8)$$

Of course, $P = P_p - P_n$ is the net production. The contribution of negative production to the net production is comparatively small up to the equilibrium region, but in the free-surface region it becomes of the same order as that of the net production though its absolute value is very small. It can be concluded, therefore, that the energy interchange from turbulence to the mean flow should not be neglected in the free-surface region. This property has been suggested by Hino et al. (1975) in an oscillating pipe flow, too.

5.3.3 Mechanism of turbulence-production in the wall region and its prediction

Since the turbulence occurs almost in the ejection and sweep events and moreover most remarkably near the wall, we investigate the contributions of the ejection and sweep in this region.

Fig. 5.16 shows the distributions of RS_i and T_i for the ejection and sweep in the wall region, whose data were obtained in the experiment Case A-1 ($R_* = 600$). Also, the results obtained by Brodkey et al. ($R_* = 195$) and Lu & Willmarth ($R_* = 1800$) are shown in Fig. 5.16. Except for the outer layer ($y^+ \sim R_*$), a good agreement among these data is recognized, and thus the following universal characteristics are obtained. Firstly, for the wall and equilibrium regions, i.e. $30 \leq y^+ \leq 0.6R_*$, RS_i and T_i become nearly constant. That is, according to our experimental data,

$$\left. \begin{aligned} T_2 &\approx 0.29 \pm 0.012, & T_4 &\approx 0.34 \pm 0.008 \\ RS_2 &\approx 0.77 \pm 0.029, & RS_4 &\approx 0.57 \pm 0.029 \end{aligned} \right\} \quad \dots\dots\dots (5.9)$$

Figs. 4.39 & 4.41 and (5.9) suggest strongly that when the turbulent structure is in equilibrium state and thus its similarity is expected, the ejection and sweep motions also show a stable behaviour and

consequently their contributions may become constant irrespective of y^+ . This essential characteristics should be taken into account in modelling the turbulence, which will be considered in Chapter 6.

Next, it should be noticed that the relation in magnitude between the ejection and sweep may reverse at $y^+ \approx 10$, which corresponds to the edge of the viscous sublayer. That is, in the sublayer the sweeps may become more dominant than the ejections. Actually, because the sublayer is the range of the deficiency of turbulent energy, as mentioned in 4.7, the sweep motion ($u > 0$, $v < 0$) may play an important role in this energy transfer.

Well, such an important fact that the mechanism of turbulence-production becomes different at the edge of sublayer, i.e. $y^+ \approx 10$, can be well explained by the theory of 2.6, as follows: Firstly, we assume that even in the region of $y^+ < 20$,

- (1) R becomes nearly constant. Actually, $R \approx 0.36$ according to Eckelmann(1974).
- (2) $S^+ \approx 0$ and $S^- \approx S_v \approx -S_u$, judging from Fig. 5.2.
- (3) $D^+ \approx 0$ and $D^-/S^- \approx 0.7$, as inferred from 5.2.3.

On the basis of the above assumption, RS_4/RS_2 and T_4/T_2 can be predicted from (2.116) and (2.118) as a function of S^- , and then their calculated results are shown in Figs. 5.17 and 5.18, respectively. Here, Fig. 5.2 gives that S^- becomes positive for $y^+ > 10$, while S^- becomes negative for $y^+ < 10$. Consequently, Fig. 5.17 indicates that $RS_4/RS_2 < 1$ when $y^+ \geq 10$, while $RS_4/RS_2 > 1$ when $y^+ \leq 10$. Near the edge of sublayer, the magnitude of the ejection and sweep becomes nearly equal to one another. In the same way, $T_4/T_2 > 1$ for $y^+ \geq 10$, while $T_4/T_2 < 1$ for $y^+ \leq 10$. Certainly, these predicted results explain well the characteristics of the observed values shown in Fig. 5.16.

5.3.4 Effect of wall roughness upon bursting events

The ratio RS_4/RS_2 of the Reynolds stress of a sweep to that of an ejection is plotted in Fig. 5.19, for each degree of roughness, with the results obtained by Wallace et al.(1972), Lu & Willmarth(1973)

and Brodkey et al.(1974). In our experiments, for $y^+ > 100$ and case of a smooth bed RS_4/RS_2 remains nearly constant, the Reynolds stress of sweeps being about 70% of that of the ejections, showing a good agreement with data by other investigators. For $y^+ < 100$, our values increase towards the wall like those of Wallace et al.(1972) or Brodkey et al.(1974), while the values by Lu & Willmarth(1973) show the reverse tendency, decreasing towards the wall. Lu & Willmarth suggested that this discrepancy might be due to the difference in the Reynolds number. However, from Fig. 5.17 it can be seen that RS_4/RS_2 may rather increases towards the wall because S^- is considered to decrease as it approaches the wall because of the variation of the skewness factor S shown in Fig. 5.2. Compared with Fig. 5.19, the calculated curves represent well the experimental results in the wall region. The fact that the contribution of sweeps becomes larger than that of the ejections as the wall is approached is also suggested by the results obtained by Zarič(1972). Judging from the above, a tendency for the values of RS_4/RS_2 in the vicinity of the wall to decrease towards the wall, as indicated by Lu & Willmarth, seems to be incorrect.

Our data show that in the wall region the values of RS_4/RS_2 increase in proportion to the roughness scale, while in the outer part of the wall region the roughness effect diminishes with increasing y^+ and the same turbulent structure as in the flow over a smooth bed is seen in Fig. 5.19. This roughness effect on the Reynolds stress is due to the variation of the skewness factor S and the diffusion factor D with roughness. As shown in Fig. 5.20, S^- and D^- both decrease with increasing roughness in the range from the wall to the middle of the equilibrium region, which results in the increase of RS_4/RS_2 shown in Fig. 5.17. Thus the experimental results shown in Fig. 5.19 can be reasonably explained.

Defining $T_r = \overline{q^2 v} / 2U_*^3$ as the turbulent energy transport (see Eq.(4.59)), the following equation can be derived:

$$T_r = \frac{1}{2} \left(\frac{u'}{u_*'} \right) \left(\frac{u'}{U_*} \right)^3 \left\{ Q_{21} + 2 \left(\frac{u'}{u_*'} \right)^2 Q_{03} \right\} \quad \dots\dots\dots (5.10)$$

Since $Q_{21} \approx D^-$, $Q_{03} \approx S^-$ and $v'/u' = 0.55$ (Eq. (4.12)), (5.10) is reduced to the following, independent of the roughness condition:

$$T_r \approx 0.28 (u'/u_*')^3 (D^- + 0.6 S^-) \approx 0.36 (u'/u_*')^3 S^- \quad \dots\dots\dots (5.11)$$

Fig. 5.20 shows the values of Tr calculated from (5.10) using the measured velocity fluctuations. As mentioned in 4.7.2, the roughness effect is marked on this kind of figure. We can see from (5.11) that Tr depends upon the values of D^- and S^- and so it decreases with increasing roughness. Since $\partial Tr / \partial y$ is directly involved in the turbulent energy budget as the term representing turbulent energy diffusion (see 2.2.2), it is expected that the bursting corresponding to the ejection or sweep motion is closely connected with the turbulent energy budget in the form of the turbulent diffusion.

5.3.5 Behaviour of velocity fluctuations when turbulence occurs

It is an essential work how to connect the knowledge of bursting events obtained by point-measurements with that obtained by visual methods. Since the level H is expected to fulfill the function of a filter by which the ejection motion can be detected from the ejection event signals, as pointed out in 2.6, we here examine this suggestion in the following.

An example of the conditional probability distributions of u , i.e. $p_e(\hat{u} | w > H)$ and $p_s(\hat{u} | w > H)$ calculated from (2.125) and (2.126) as well as those of v is shown in Fig. 5.21. When $H \approx 5$ is chosen, almost all the events are contained in the range of $w \geq -H$ (see Fig. 5.10), and consequently $p_e(\hat{u})$ or $p_s(\hat{u})$ coincides with the unconditional probability distribution $p(\hat{u})$ shown in Fig. 5.1. In comparison with the sweep event, the ejection event has a contribution from the larger values of $|u|$ and $|v|$ when H is large. That is, the correlation between $u < 0$ and $v > 0$ becomes larger in the stronger ejection.

Fig. 5.22 shows the distributions of the average values $\hat{u}_e(H)$ and $\hat{u}_s(H)$ of u/u' when the magnitude w of the ejection and sweep, respec-

tively, just attains the level H , together with the theoretical curves calculated from (2.121) and (2.122). Although there is a little difference between the observed and theoretical values owing to using the digital signals of $w(t)$, agreement between the two is comparatively good. Of course, $\hat{u}_e < 0$ and $\hat{u}_s > 0$, and the larger H is, the more intensive the velocity fluctuations accompanied with turbulence-production become. At $H \approx 5$ where the interaction events almost disappear, Fig. 5.22 indicates that $\hat{u}_e = -1.0 \sim -1.5$ and $\hat{u}_s = 1.0 \sim 1.5$.

Well, since a coherent motion of bursting phenomenon is visualized in a form of the streamwise velocity fluctuation $u(t)$ instead of the Reynolds stress fluctuation $w(t)$, a trigger level u_L is set for $u(t)$. Then, denoting $t=0$ when $|u(t)/u'|$ crosses a special trigger level u_L in an increasing direction, $w(t)$ in the ejection or sweep event has been ensemble-averaged. Fig. 5.23 shows the behaviours of the ensemble averaged ejections and sweeps with three cases of trigger levels; $u_L = 0.5, 1.0$ and 1.5 , in the wall region. The existence of the coherent motion is not recognized at $u_L = 0.5$, but if u_L is set at 1.0 , $w(t)$ has a large peak immediately after $\hat{u}(t)$ reaches a level of -1.0 or 1.0 , and a larger peak appears at $u_L = 1.5$. In the same manner, Fig. 5.24 shows the behaviours of the ejection motion in the equilibrium region. Setting $u_L = 1.0 \sim 1.5$, for $d|u|/dt > 0$ the turbulence occurs immediately after $|u|$ attains the u_L , while for $d|u|/dt < 0$ immediately before $|u|$ attains the u_L . Fig. 5.25 shows the results obtained in the free-surface region. $w(t)$ in this region shows apparently more enlarged and chaotic behaviour because $-\overline{uv}$ becomes nearly equal to zero. The fact that the ejection or the sweep motions can be detected in $w(t)$ when $u_L \geq 1.0$, agrees well with the point-measurement data given by Lu & Willmarth(1973). Since $u_L = 1.0 \sim 1.5$ corresponds roughly to $H \approx 5$ judging from Fig. 5.22, the energetic ejection or sweep motions which can be observed visually (see Fig. 2.20 or Fig. 5.39), would be able to be detected from the conditionally sorted signals $w(t)$ when H is set at about 5.

5.4 Periodic characteristics of the bursting phenomenon*)

5.4.1 Brief recapitulation of the bursting period obtained previously Kline et al.(1967), Corino & Brodkey(1969), Kim et al.(1971), Nychas et al.(1973), Offen & Kline(1974, -75) and others found by flow visualization that a sequence of the bursting events had a quasi-cyclic process. That is to say, it shows a periodic motion on the average in space and time, but not perfectly periodic at one place in time nor at one time in space. For example, Corino & Brodkey pointed out in Fig. 2.20 that there were variations of the sequence, and that all of the steps did not appear all the time or in the exact fashions described, but on the average it proceeded.

Thus, in order to reveal the governing parameters of the bursting phenomenon, it is necessary to investigate its periodic characteristics. The visual method whereby the bursting period is determined by counting the frequency of occurrences of the coherent motions near the wall visualized on high-speed movie films, is simple and plain. However, it needs laborious work and more or less involves subjective judgement. On the other hand, some researchers as well as the author have shown that the existence of a sequence of bursting events such as ejections, sweeps and interactions can be also detectable even in the fluctuating velocity signals obtained by hot-wire or hot-film anemometers when a conditional sampling technique is reasonably used. If it is, therefore, possible to establish a reasonable criterion for discriminating the ejections or the sweeps from these velocity signals, the bursting period can be also evaluated easily from the data analysis of point-measurement signals by using a high-speed digital computer. Of course, these results should be compared with the visual data, since it may be fairly difficult to detect accurately the coherent motions extending in space only by one or a few hot-films.

Firstly, Rao et al.(1971) estimated the mean bursting period \bar{T}_B from the single-hot-wire signals of $u(t)$ in a boundary layer by using

*) Refer to our paper published in *Memoirs of Faculty of Engineering, Kyoto University*, vol. 40, part 4, 1978.

a special criterion for discrimination. They proposed the following experimental results.

$$\bar{T}_B U_*^2 / \nu = 0.65 R_\theta^{0.73} \dots\dots\dots (5.12) \quad \text{and} \quad \bar{T}_B U_{\max} / \delta_* \approx 32 \dots\dots\dots (5.13)$$

where, R_θ is defined as $R_\theta \equiv U_{\max} \theta / \nu$, δ_* is the displacement thickness and θ is the momentum thickness. They found that the mean bursting period could scale with outer rather than inner parameters, as shown in (5.12) and (5.13), and that the probability distribution of the bursting period might be log-normal.

Next, Kim et al. (1971) found that when the auto-correlation of $u(t)$ reached the re-rise maximum, the lag time τ_0 agreed fairly well with the bursting period evaluated from the visual data. Consequently, they suggested that τ_0 could be regarded as a bursting period \bar{T}_B . By these means, Laufer & Narayanan (1971) evaluated the mean period of the bursting phenomenon near the viscous sublayer in a boundary layer, and verified that (5.12) was valid and could be reduced to the following equation by assuming the 1/7-power velocity law:

$$\bar{T}_B U_{\max} / \delta \approx 5 \dots\dots\dots (5.14)$$

where δ is the boundary layer thickness.

Consequently, (5.12), (5.13) and (5.14) are almost the same. ($\bar{T}_B U_{\max} / \delta$ becomes nearly equal to 4 from (5.13) since δ / δ_* for the 1/7-power velocity law.) Also, the dependency of the bursting period upon the outer parameter (U_{\max} and δ) is confirmed.

However, Lu & Willmarth (1973) pointed out that these criteria had something unreasonable, and proposed another method described as follows. The fluctuating signals $w'(t) = -uv/u'v'$ of the Reynolds stress were used as a detection of the coherent motions. The mean period \bar{T}_e of the ejection motion was evaluated from $w'(t)$ in the ejection event, when the discrimination level was set at the value of (4.0~4.5) where the sweeps almost disappeared. The mean period \bar{T}_s of the sweep motion was also evaluated in the same manner. Their results agreed fairly well with the visual data, or (5.14), and this evaluation method might become more reasonable than previous methods.

Indeed, Sabot & Comte-Bellot(1976) evaluated the bursting period in a pipe flow by this method.

In the light of the above, the present study is to propose another reasonable evaluation method of the bursting period, and investigate the periodic characteristic of the bursting phenomenon in open channel flows.

5.4.2 Discrimination criterion and definition of bursting period

The instantaneous Reynolds-stress signals $w(t)=uv/\overline{uv}$ are reasonably used as discriminating information, since they are directly related to the mechanism of turbulence-production, namely the bursting phenomenon. Now, $w(t)$ is conditionally divided into four events: $w_1(t)$ when $u>0$ and $v>0$, $w_2(t)$ when $u<0$ and $v>0$, $w_3(t)$ when $u<0$ and $v<0$ and $w_4(t)$ when $u>0$ and $v<0$. Obviously, $w(t)=w_1(t)+w_2(t)+w_3(t)+w_4(t)$.

Two typical examples of the conditionally sampled signals $w_2(t)$ in the ejection event are shown in Fig. 5.26. It is confirmed that the Reynolds stress fluctuations $w(t)$ are very intermittent, and especially that the ejections and sweeps generate turbulence violently in the form of a very sharp pulse, as mentioned in previous section.

The hole size H for the division of the bursting events is introduced as a discrimination level of the ejection or sweep motions. Assuming that each motion with a certain level H occurs when $|w_1(t)|$ reaches or exceeds level H , its mean period T_i ($i=1-4$) is obtained by counting the number N_i of the occurrences in the total observing time T , as follows: $T_i(H)=T/N_i$ ($i=1,2,3,4$)

For example, Fig. 5.27 shows the variation of the mean period $T_2(H)$ (or \hat{T}_e) of an ejection event normalized by outer parameters (U_{max} and h) for a smooth bed. Since T_2 is a monotonously increasing function of H , the mean period \overline{T}_e of the ejection motion which can be observed visually, that is, an event (5) in Fig. 2.20, cannot be determined from Fig. 5.27 without providing a discrimination criterion. According to the Lu & Willmarth method, as mentioned previously, $\overline{T}_e U_{max}/h$ becomes (4-10) since the level H is about 10, at which the contributions of the sweeps almost disappears. This range of \overline{T}_e is too large to know the effects of hydraulic parameters such as Re , Fr

and the wall roughness upon the bursting period systematically.

Now, it may be noticed in Figs. 5.27 and 5.28 that T_2 shows a nearly linear increase with H when $H \leq 5$, and a more remarkable increase when $H > 5$ although the slope of $T_2(H)$ increases more or less continuously. This tendency of $T_2(H)$ may be related to the fact that the interaction events scarcely contribute to the production of Reynolds stress when level H reaches about 5. This suggests that the ejection signals $w_2(t)$ or the sweep signals $w_4(t)$ with $H \leq 5$ contain a part of the interaction motions corresponding to the events (1)-(4) in Fig. 2.20. This suggestion might be also inferred from the results of a conditional sampling technique, as already shown in 5.3.5.

From the above phenomenological considerations, the contributions of the interaction motions should be removed from the sequence of the bursting process in order to evaluate the period of only the ejections or sweeps. However, there is at present quite a lack of knowledge about the contributions of the interaction-like motions which may be contained in the signals of $w_2(t)$ or $w_4(t)$. Hence, we now propose a tentative assumption that the interaction-like contributions may be of the same order as those of the interaction event signals $w_1(t)$ or $w_3(t)$, since the contributions of $|w_1(t)| \leq 5$ might be roughly equal to each other, owing to a detection of old-born or new-born small bursting motions. By assuming that the number N_{in} of occurrences of these interaction-like motions with a level of H is roughly given by an average of those of two interaction events: that is, $N_{in} = (N_1 + N_3)/2$, the revised bursting period is defined as follows:

$\hat{T}_2 \equiv T / (N_2 - N_{in})$ for ejections, $\hat{T}_4 \equiv T / (N_4 - N_{in})$ for sweeps.
 $\hat{T}_2 U_{max} / h$ is shown against H in Fig. 5.29 ($(\hat{T}_e - \hat{T}_{in})$ denotes \hat{T}_2) for the case corresponding to Fig. 5.27. When H is small, $\hat{T}_2 U_{max} / h$ is large owing to the strong cancellation effect of the interaction-like motions, as mentioned above. Because the interaction-like motions disappear gradually as H increases, this cancellation effect becomes weaker, and consequently \hat{T}_2 approaches T_2 . Thus, we try to tentatively define the mean period of the ejections \bar{T}_e and the sweeps \bar{T}_s

as the minimum value of $\hat{T}_2(H)$ and $\hat{T}_4(H)$, respectively, because it may be considered that the interaction-like contributions almost disappear at this minimum point. Since the minimum value $\hat{T}_2(H)$ or $\hat{T}_4(H)$ remains stationary even when H varies to some extent, \bar{T}_e or \bar{T}_s can be determined uniquely, and therefore this evaluation method may be well-defined as compared with previous methods.

5.4.3 Bursting period and its probability characteristics

The evaluated values of \bar{T}_e and \bar{T}_s for the smooth and rough beds are shown in Fig. 5.30, normalized by the outer parameters. Since the auto-correlation $R_u(\tau)$ has a second-mild maximum, as shown in Fig. 5.31, the bursting period \bar{T}_B was also evaluated by Kim et al's method, although it was difficult to evaluate \bar{T}_B accurately, except when near the wall. The values of \bar{T}_e had a good agreement with those of \bar{T}_B , as seen in Fig. 5.30. Therefore, our tentative evaluation method of the bursting period seems to be fairly reasonable. *)

In the same manner, Fig. 5.32 shows the data obtained in the higher-velocity group. Although there are some scatterings in these data, $\bar{T}_e U_{\max}/h$ and $\bar{T}_s U_{\max}/h$ are approximately constant for any y/h , irrespective of the hydraulic conditions. That is,

$$\frac{\bar{T}_e \cdot U_{\max}}{h} \simeq \frac{\bar{T}_s \cdot U_{\max}}{h} \simeq (1.5-3.0) \quad \dots\dots (5.15)$$

(5.15) shows the same order as (5.14) or Lu & Willmarth's results in a boundary layer, though a quantitative comparison among these data cannot be done reasonably because of the differences of the flow conditions and the evaluation methods. It should be noticed that the ejection period \bar{T}_e becomes nearly equal to the sweep period \bar{T}_s , as pointed out by Lu & Willmarth. This means that there exists, on an average, at least one each of ejection and sweep motions in a bursting process. Consequently, the bursting period \bar{T}_B can be identi-

*) Furthermore, we (Sympo. Dynamic Flow Measurements 1978) just now propose another different evaluation method whereby the ejection period \bar{T}_e is determined at the level $H=H_{0.5}$ where $RS_2(H_{0.5})=0.5 \times RS_2(H=0)$. Since the interaction events almost disappear at the $H_{0.5}$, this new method also gives the nearly same results as the above, i.e. (5.15).

fied with the ejection or sweep one, $\bar{T}_e \approx \bar{T}_s \approx \bar{T}_B$.

From the previous and present investigations, it may be concluded that the bursting period in the wall and equilibrium regions of open channel flows can scale with the outer parameters (U_{max} and h) rather than the inner parameters (U_* and v/U_*), irrespective of Re , Fr and the wall roughness. This is also supported by the noticeable fact that the wall roughness scarcely influences the bursting period, while this effect can be noticed clearly in the bursting process near the wall as pointed out in 5.3.4.

Furthermore, Fig. 5.33 shows the trigger levels H_e and H_s of ejection and sweep, respectively, at which the bursting period was evaluated (cf. Fig. 5.27). Fig. 5.33 gives that $H_e \approx (3-6)$ and $H_s \approx 3$, whose values, in fact, correspond roughly to the level at which the interaction motions nearly disappear. Also, Fig. 5.34 shows the levels \hat{u}_e and \hat{u}_s corresponding to H_e and H_s , respectively. These data give that $\hat{u}_e \approx -1.4$ and $\hat{u}_s \approx 1.3$, at which the ejection and sweep motions can be surely detected, as judging from Figs. 5.23-5.25.

Next, the probability distribution $p_T(T)$ of the bursting period T will be discussed *). The experimental values of $p_T(T)$ can be easily obtained from Fig. 5.26, since H_e and H_s have already determined in Fig. 5.34. According to the suggestion of Rao et al. (1971), the data of the probability distribution of $\log(T/\bar{T})$ have been plotted in a normal-probability paper of Fig. 5.35. Also, Fig. 5.36 shows the normalized probability distributions $\sigma_0^{-1} \log(T/T_0)$ for smooth and rough beds, where $\log T_0 \equiv \overline{\log T}$, $\sigma_0 \equiv \{(\overline{(\log T/T_0)^2})^{1/2}$. The straight line described in this figure is a log-normal distribution which is written by

$$p_T(T) = \frac{(\log e)}{\sqrt{2\pi} \sigma_0 T} \exp \left\{ -\frac{1}{2} \left(\frac{1}{\sigma_0} \log T/T_0 \right)^2 \right\} \dots\dots\dots (5.16)$$

Though there is a little scattering in our hot-film data, these data have a good agreement with (5.16), as well as the visual data obtained by Kim et al. (1971). Consequently, it is confirmed that the

*) When it isn't necessary to distinguish between the ejection period T_e and the sweep period T_s , these suffixes will be omitted in the following explanations. That is, $\bar{T} \approx \bar{T}_e \approx \bar{T}_s \approx \bar{T}_B$.

probability of the bursting period can be described approximately by a log-normal distribution, i.e. (5.16), irrespective of Re, Fr and the wall roughness.

Then, the following equation can be obtained easily from (5.16):

$$\int_0^{\infty} T^i \rho_T(T) dT = T_0^i \cdot \exp\left(\frac{i^2}{2K^2}\right), \quad K \equiv (\log \epsilon) / \sigma_0 \quad \dots\dots\dots (5.17)$$

Denoting $T_B = \bar{T}$, $\sigma_B \equiv (\overline{(T-\bar{T})^2})^{1/2}$ and $\psi \equiv \sigma_B / T_B$,

$$\left. \begin{aligned} \sigma_0 &\equiv (\log \epsilon) / K = (\log \epsilon) \sqrt{\ln(1+\psi^2)} \\ T_0 &\equiv \tau T_B, \quad \gamma \equiv (1+\psi^2)^{-1/2} \end{aligned} \right\} \quad \dots\dots\dots (5.18)$$

Thus, if the mean value T_B and its coefficient ψ of variation are known, (5.16) can be determined as a probability distribution of the bursting period. The experimental values of ψ for the ejection period are shown in Fig. 5.37, and similar results have been also obtained for the sweep period. As concerns our hot-film data, the values of ψ near the wall are nearly constant, i.e. $\psi \approx 1.0 \sim 1.5$, while the visual data of kim et al. show $\psi \approx 0.5$. At present, though it is difficult to explain the cause of this difference between the hot-film and visual data, the former may be apt to be accompanied by a kind of unevenness involved in the point-measurements of the coherent motions which extent in space. Consequently, the hot-film data are probably evaluated larger than the visual data.

5.5 Internal structure of bursting phenomenon

5.5.1 Dependence of the bursting phenomenon upon the inner and outer parameters

For the present, from the previous and present experimental data, we can approve the opinion that the bursting period may be controlled by the outer rather than the inner parameters. Consequently, the turbulent structure in the wall region of an open-channel flow may be characterized not only by the inner parameter (see Chapters 2 and 4), but also by the outer parameter that characterizes the free-surface regions, which have been already recognized in a boundary layer flow.

Now, the streamwise, the vertical and the transverse spatial scales of this coherent motion are denoted by λ_1 , λ_2 and λ_3 , respectively. Since the mean streamwise spatial scale $\bar{\lambda}_1$ is nearly equal to $T_B U_c$, where U_c is the convection velocity and $U_c \approx U_m \approx 0.9 U_{max}$, it becomes from (5.15) as $\bar{\lambda}_1/h \approx 1.5 \sim 3.0$ (in open channel) (5.23), as well as $\bar{\lambda}_1/\delta \approx 4$ in a boundary layer, as shown by Hinze(1975). The mean vertical spatial scale $\bar{\lambda}_2$ is considered to be below the wall region thickness, i.e. $\bar{\lambda}_2^+ < 100$. In particular, it is suggested from the visual observation (cf. Fig. 2.20) that $\bar{\lambda}_2^+ \leq 50$, where the coherent motions appear most violently. The mean transverse spatial scale $\bar{\lambda}_3$ may be able to be identified with the spacing between the high and low speed streaks which were found by Kline et al.(1967). It was confirmed by our visual observations (see the next section) that

$$\bar{\lambda}_3^+ \equiv \bar{\lambda}_3 U_* / \nu \approx 100 \text{ (5.24)}$$

in open channels, which coincided with the data in boundary layers.

From the results obtained above, it is deduced that a typical eddy with coherent motions near the wall may depend upon both the inner and outer parameters. Consequently, the eddy model qualitatively described by Hinze(1975) in Fig. 6.6 may fairly reasonably explain the mechanism of the bursting phenomenon, as will be shown later. Furthermore, by hydrogen-bubble method(Fig.3.16) we have also found a log-normal distribution of the probability of λ_3^+ , as shown in Fig. 5.38. That is, the probability distribution $p_\lambda(\lambda_3^+)$ satisfied very well the following equation, independently of y^+ .

$$p_\lambda(\lambda_3^+) = \frac{(\log e)}{\sqrt{2\pi} \sigma_\lambda \lambda_3^+} \exp \left\{ -\frac{1}{2} \left(\frac{1}{\sigma_\lambda} \log \lambda_3^+ / \lambda_{30}^+ \right)^2 \right\} \text{ (5.25)}$$

From (5.16) and (5.25), it seems that the bursting phenomenon has self-consistently the characteristic of a log-normal distribution while it is controlled by both the inner and outer parameters. Hence, a closer interrelation between the wall and the free-surface regions in an open-channel corresponding to the inner and the outer layers in a boundary layer is suggested more than had been previously expected.

Incidentally, Laufer & Narayanan(1971) deduced that the bursting phenomenon near the wall might be caused by the bulge motions near

the boundary layer edge, but we cannot find any bulge motions in an open-channel flow. We infer here that there may exist a close relation between the bursting mechanism and the breakdown mechanism of the largest-scale eddy with scale L_0 . If the Strouhal similarity might be valid for both mechanisms, the following relation could be obtained.

$$T_B U_{\max}/h \approx (St_K)^{-1} (L_0/h) \dots\dots\dots (5.20)$$

where, St_K is the Strouhal number and it may be now tentatively roughly equal to 0.2, with an assumption that the breakdown of this eddy would be roughly similar to that of the Karman-vortex. Then, (5.20) may coincide roughly with (5.14) or (5.15) since $L_0 \approx 0.8$ (see Fig. 4.30).

5.5.2 Further suggestions on bursting phenomenon

It may be fairly well asserted from the visual and hot-film measurements that the breakdown of the largest-scale eddy is intermittent, and then generates most of the turbulent energy or the Reynolds stress (cf. Figs. 2.5 & 2.9). On the other hand, as indicated by Sandborn (1959), the breakdown of the smallest-scale eddy is also intermittent, and then dissipates most of the turbulent energy.

Among the evaluation methods of the bursting period mentioned previously, the methods of Rao et al. (1971) and Ueda & Hinze (1975) are based on a microscale intermittency, while the methods of Kim et al. (1971), Lu & Willmarth (1973), the present author as well as the visual method are based on a macroscale intermittency. Since almost the same characteristics of the bursting period have been evaluated from these two different methods, it is inferred that the breakdown of a macroscale eddy may have a close relation and interaction with that of a microscale eddy, and that the turbulent structure may be essentially characterized by both the macro- and micro-scales. Consequently, an energy cascade process in which the turbulent energy of macroscale eddies is gradually transferred to that of microscale eddies, would be more complicated than we have previously understood.

Now, assuming that there exists a self-similarity in the breakdown of eddies of this cascade process, log-normal characteristics of the bursting process or the coherent motion reported here could be

explained by the eddy model of Gurvich & Yaglom(1967). Thus, it is suggested that the bursting phenomenon may be closely related to the breakdown mechanism of both the macro- and micro-scale eddies.

By the way, some researchers have already found that there existed also the high and low speed streaks, whose spacing is nearly equal to $2h$, on the free surface of an actual river, that is to say, the boil phenomenon. Therefore, although the scale between the bursting and the boil phenomena is quite different when the Reynolds number is very large, the both phenomena are very similar to one another. Hence, we may be able to expect the possibility of an interrelation between the both phenomena, and furthermore we are now investigating the spatial structure of bursting phenomenon by obtaining the conditional spatial correlations in order to make clear the above suggestions.

5.6 Visual observations of bursting phenomenon *)

5.6.1 Instantaneous velocity profiles in vertical plane

The velocity profiles of the lower-velocity group in Table 4.1(c) were visualized by the hydrogen-bubble method in order to obtain the distinct pictures. The time-lines of hydrogen bubbles were photographed by the 16mm high-speed cine-camera. Fig. 5.39 shows some typical photographic illustrations of the ejection and sweep motions for the rough bed (Case D-1). The pictures of No.1 - 4 indicate the ejection motions, while the pictures of No.5 - 9 indicate the sweep motions. For example, the picture of No.1 probably shows the first stage of the bursting, where a low-speed streak is lifted from the wall. The picture of No.2 probably shows the oscillatory motion in the streamwise direction, and then the violent burst or breakup occurs in No.3 picture. These pictures of three stages of the bursting motion agree very well with Kim et al's observations. Also, the ejection motion may occur more violently than sweep motion does.

By means of the method described in 3.4.1, the instantaneous velo-

*) Refer to our paper (*Visualization of wall turbulence in open-channel flow by hydrogen-bubble method*) published in 5-th Sympo. on Flow Visualization, ISAS Univ. of Tokyo, pp.47-50, 1977.

city profiles (\tilde{u} , \tilde{v}) were analyzed, and some examples of these data for the smooth bed are shown in Fig. 5.40, together with the mean velocity distribution $U(y)$ described by a thick solid line. Since according to (5.15) the bursting period in this case is nearly equal to $T_B \approx (1.5 \sim 3.0)h/U_{max} \approx (1 \sim 1.5)$ sec., the eight successive pictures in Fig. 5.40 (a) & (b) are expected to show one sequence of the bursting process. The low-speed part ($u = \tilde{u} - U < 0$) tends to be surely lifted up and ejected from the wall.

In order to examine the behaviours of the low-speed and the high-speed parts, we have performed the conditionally ensemble average of the instantaneous velocity (\tilde{u} , \tilde{v}), in the same manner as Grass(1971) did. The total successive pictures of 160 frames were divided into 8 groups; that is, one group consisted of 20 successive frames, whose elapsed time T_G was 3.7 seconds (cf. Fig. 5.40). Thus, it is expected that each group contains at least one bursting process or the coherent motion, since the value of T_G is larger than the mean bursting period T_B . The frames of picture where the velocity \tilde{u} indicated the maximum or the minimum at any measured point P_i ($i=1 - 12$) were chosen from each group, and then these instantaneous velocity profiles were ensemble averaged. Figs. 5.41 and 5.42 show the conditionally averaged instantaneous velocity profiles at instants when \tilde{u} became minimum and maximum at any point P_i , respectively. As seen in Fig. 5.41, the low-speed part drew black has a strong correlation with $\tilde{v} > 0$, and surely it shows the ejection motion. In the same manner, Fig. 5.42 shows the sweep motion. The both figures indicate that the liftup- ejection motions may exist up to the further region from the wall, compared with the sweep motions. This suggests a possibility of the interrelation between the ejection (bursting) and the boil phenomena, as mentioned previously.

5.6.2 Instantaneous velocity profiles in horizontal plane

A fine platinum wire was stretched in the direction of z-axis in the water flume (8.5m long, 30cm wide, 30cm deep), and the instantaneous velocity profiles in the horizontal plane were visualized

(see Fig. 3.16). Figs. 5.43 & 5.44 show some typical photos of these profiles obtained for three different kinds of the Reynolds number, i.e. $Re = 340, 1600$ and 5100 .

Firstly, at $Re=340$ (Fig. 5.43 A), the time-lines are scarcely agitated, and consequently the flow becomes laminar. As for the flow of $Re=1600$, the flow near the free surface $\xi=0.7$ (see Fig. 5.43 B) are still nearly laminar, while the high and low speed streaks appear remarkably near the wall $y^+=22$ (Fig. 5.43 C). Five successive pictures of Fig. 5.43 C show that the high and low speed streaks have fairly variations in both the streamwise space and the time. Although the behaviours of the coalescence and division of these streaks are very complicated, the mean spacing between the high and low speed streaks surely satisfies (5.24); that is $\lambda_3^+ \approx B_*/5 = R_*/110$, and also its probability distribution satisfies (5.25), as shown in Fig. 5.38.

Lastly, Fig. 5.44 shows some photos obtained by varying the height y^+ for $Re=5100$. The picture of No.1 indicates the velocity profile in the viscous sublayer, i.e. at $y^+=5$, and the velocity certainly fluctuates even in the sublayer, as have been already pointed out by Einstein et al.(1956). At $y^+=10$ and 15 , the high and low speed streaks are observed most clearly, whose spacing becomes equal to $\lambda_3^+ \approx B_*/15 = R_*/3 = 100$, too. However, as y^+ increases, the streaks intend to become weaker and also its spacing may become larger (see our paper described in the margin of p. 82). At present, it is quite unknown whether this is due to the fact that the bursting phenomenon may become weaker near the free surface or this may indicate an interrelation with the boil phenomenon. Thus, we are now performing the further detailed researches about these things.

References (Chapter 5)

- 1) Davies, P. O. A. L. & Yule, A. J. : Coherent structures in turbulence, J. Fluid Mech., vol.69, pp.513-539, 1975.
- 2) Mollo-Christensen, E. : Physics of turbulent flow, AIAA J., vol.9, pp.1217-1228, 1971.
- 3) Kline, S. J., Reynolds, W. C., Schraub, F. A. & Runstadler, P. W. : The structure of turbulent boundary layers, J. Fluid Mech., vol.30, pp.741-773, 1967.
- 4) Willmarth, W. W. & Lu, S. S. : Structure of the Reynolds stress near the wall, J. Fluid Mech., vol.55, pp.65-92, 1972.
- 5) Wallace, J. M., Eckelmann, H. & Brodkey, R. S. : The wall region in the turbulent shear flow, J. Fluid Mech., vol.54, pp.39-48, 1972.
- 6) Nychas, S. G., Hershey, H. C. & Brodkey, R. S. : A visual study of turbulent shear flow, J. Fluid Mech., vol.61, pp.513-540, 1973.

- 7) Offen, G. R. & Kline, S. J. : Combined dye-streak and hydrogen-bubble visual observation of a turbulent boundary layer, *J. Fluid Mech.*, vol.62, pp.223-239, 1974.
- 8) Lu, S. S. & Willmarth, W. W. : Measurements of the structure of the Reynolds stress in a turbulent boundary layer, *J. Fluid Mech.*, vol.60, pp.481-511, 1973.
- 9) Brodkey, R. S., Wallace, J. M. & Eckelmann, H. : Some properties of truncated turbulence signals in bounded shear flows, *J. Fluid Mech.*, vol.63, pp.209-224, 1974.
- 10) Nakagawa, H. & Nezu, I. : Prediction of the contributions to the Reynolds stress from the bursting events in open-channel flows, *J. Fluid Mech.*, vol.80, pp.99-128, 1977.
- 11) Frenkiel, F. N. & Klebanoff, P. S. : Probability distributions and correlations in a turbulent boundary layer, *Phys. of Fluids*, vol.16, pp.726-737, 1973.
- 12) Bayazit, M. : Free surface flow in a channel of large relative roughness, *J. Hydraulic Research*, vol.14, pp.115-126, 1976.
- 13) Gupta, A. K. & Kaplan, R. E. : Statistical characteristics of Reynolds stress in a turbulent boundary layer, *Phys. of Fluids*, vol.15, pp.981-985, 1972.
- 14) Antonia, R. A. & Atkinson, J. D. : Higher-order moments of Reynolds shear stress fluctuations in a turbulent boundary layer, *J. Fluid Mech.*, vol.58, pp.581-593, 1973.
- 15) Lawn, C. J. : The determination of the rate of dissipation in turbulent pipe flow, *J. Fluid Mech.*, vol.48, pp.477-505, 1971.
- 16) Corino, E. R. & Brodkey, R. S. : A visual investigation of the wall region in turbulent flow, *J. Fluid Mech.*, vol.37, pp.1-30, 1969.
- 17) Kim, H. T., Kline, S. J. & Reynolds, W. C. : The production of turbulence near a smooth wall in a turbulent boundary layer, *J. Fluid Mech.*, vol.50, pp.133-160, 1971.
- 18) Grass, A. J. : Structural features of turbulent flow over smooth and rough boundaries, *J. Fluid Mech.*, vol.50, pp.233-255, 1971.
- 19) Zarič, Z. : Analyse statistique de la turbulence près d'une paroi par échantillonnage conditionnel, *Comptes Rendus*, t-269, Série-A, pp.513-515, 1972.
- 20) Echelmann, H. : The structure of the viscous sublayer and the adjacent wall region in a turbulent channel flow, *J. Fluid Mech.*, vol.65, pp.439-459, 1974.
- 21) Rao, K. N., Narasimha, R. & Narayanan, M. A. B. : The 'bursting' phenomenon in a turbulent boundary layers, *J. Fluid Mech.*, vol.48, pp.339-352, 1971.
- 22) Lu, S. S. & Willmarth, W. W. : Measurement of the mean period between bursts, *Phys. of Fluids*, vol.16, pp.2012-2013, 1973.
- 23) Laufer, J. & Narayanan, M. A. B. : Mean period of the turbulent production mechanism in a boundary layer, *Phys. of Fluids*, vol.14, pp.182-183, 1971.
- 24) Hinze, J. O. : *Turbulence* (2-nd edi.), McGraw-Hill, pp.586-770, 1975.
- 25) Clark, J. A. & Markland, E. : Flow visualization in turbulent boundary layers, *Proc. of ASCE*, HY-10, pp.1653-1664, 1971.
- 26) Gupta, A. K., Laufer, J. & Kaplan, R. E. : Spatial structure in the viscous sublayer, *J. Fluid Mech.*, vol.50, pp.493-512, 1971.
- 27) Sandborn, V. A. : Measurements of intermittency of turbulent motion in a boundary layer, *J. Fluid Mech.*, vol.6, pp.221-240, 1959.
- 28) Ueda, H. & Hinze, J. O. : Fine-structure turbulence in the wall region of a turbulent boundary layer, *J. Fluid Mech.*, vol.67, pp.125-143, 1975.
- 29) Mollo-Christensen, E. : Intermittency in large-scale turbulent flows, *Annu. Review of Fluid Mech.*, vol.5, pp.101-118, 1973.
- 30) Gurvich, A. S. & Yaglom, A. M. : Breakdown of eddies and probability distribution for small-scale turbulence, *Phys. of Fluids*, vol.10, pp. S59-S65, 1967.
- 31) Einstein, H. A. & Li, H. : The viscous sublayer along a smooth boundary, *Proc. of ASCE*, EM-2, pp.1-27, 1956.

Chapter 6 Physical model of wall turbulence

6.1 Introduction

Even before the existence of the bursting phenomenon was discovered clearly by Kline et al.(1967), there had been already several attempts to describe the mechanism of the turbulence production near the wall by suitable turbulence eddy models, among which a horseshoe vortex model proposed by Theodorsen(1955) and a renewal model of the viscous sublayer proposed by Einstein & Li(1956) should be still noteworthy, as mentioned in the following.

Willmarth & Tu(1967) proposed an 'average model of vortex line' (see Fig. 6.1) in order to qualitatively explain the pressure-velocity correlations near the wall, from which the existence of the bursting phenomenon might be inferred. Next, Kline et al.(1967) offered an eddy model (see Fig. 6.2) by which the mechanism of wall-turbulence production could be reasonably explained. Both of these eddy models are very similar to Theodorsen's horseshoe vortex model. We can recognize for the present that such an eddy model might be most suitable for a qualitative explanation of the bursting process. As a fact, Black(1968) formulated this horseshoe vortex model phenomenologically (see Fig. 6.3), after which he could successfully explain several turbulence characteristics quantitatively. For example, it is noticed that this model can reasonably explain the cyclic development and breakdown of the primary motion, as shown in Fig. 6.4. Also, Yokoshi(1970) tried to explain the turbulent structure of an actual river by using the horseshoe vortex model (see Fig. 6.5) and he suggested that a boil phenomenon in the river would be caused by this eddy.

In order to quantitatively describe the turbulent structure in the equilibrium region, we(1974) also proposed a Π -eddy model whereby a horseshoe vortex model was simplified by assuming that some of the horseshoe vortices in the wall region, as shown in Fig. 6.6, survived without the vortex-breakdown during their development, even in the region of $y^+ > 100$, and also attained the equilibrium state of turbu-

lent energy, which will be described in detail in the next section. It is considered that Hinze's (1975) eddy model shown in Fig. 6.6 summarizes reasonably the previous eddy models mentioned above, on a basis of the new knowledges of the bursting phenomenon.

In the light of the above, the present study is to propose three different kinds of turbulent eddy model in order to explain the turbulence characteristics or the bursting phenomenon quantitatively. As shown in Fig. 6.7, the Π -eddy model is firstly proposed in the equilibrium region. Next, a renewal model is proposed in the wall region of $y^+ < 50$, where the bursting phenomenon occurs remarkably and its horseshoe vortex is under development, that is, a non-equilibrium state. Lastly, a combined model is tentatively proposed in order to connect the Π -eddy model with the renewal model near the edge of the wall region.

6.2 Π -eddy model *)

6.2.1 Constitution of a Π -eddy model and its formulation

Due to the fact that a horseshoe vortex model proposed already by Theodorsen and other researchers is fairly reasonable in qualitative aspects, as mentioned above, this horseshoe vortex model is accepted as an original eddy model in the following discussions. But, since it is fairly difficult to obtain exact expression of the horseshoe vortex model in order to discuss quantitatively its behaviours, a simplified eddy model which has the angular vortex lines as described in Fig. 6.8 may be considered here. As the vortex line of this simplified eddy model has a Π -shape, this model may be called 'a Π -eddy model'.

Now, a particular eddy is considered in the moving coordinates with the convective velocity U_c of its eddy, as shown in Fig. 6.8. A rectangular vortex line $ABCD$ which has an angle of inclination θ toward the x-axis is assumed for two-dimensional turbulent shear

*) Refer to our paper (*On a new eddy model in turbulent shear flow*) published in *Proc. of JSCE*, No.231, pp.61-70, 1974.

flow. Its legs AB and CD are in a plane parallel to the x - y plane, and its top BC is parallel to the z -axis. The condition $\theta=0$ may represent an incipient stage of the Π -eddy which coincides with a hairpin eddy or an attached eddy on the wall. However, since the incipient stage of the Π -eddy or the horseshoe vortex is very complicated because of the non-equilibrium state (cf. Fig. 6.7), an equilibrium condition under which the Π -eddy is lifted up from the bottom and fully developed is considered here. That is to say, some of the horseshoe vortices in the wall region survive without the vortex breakdown during their development, even in the region of $y^+ > 100$, and then they attain the equilibrium state in the turbulent structure, as mentioned in Chapters 4 and 5. Since $AB \gg BC$ because of $BC^+ \approx \lambda_3^+ \approx 100$ (cf. Fig. 6.6), the contribution of the vortex BC to the turbulent structure can be ignored except that the vortex BC will suffer the lift force. The vortex tubes AB and CD may be reasonably assumed to have an elliptical cross section with a long radius a in the x -direction and a short radius b in the z -direction, since they are distorted by the vortex-stretching effect. Consequently, it can be assumed that the primary motion of the Π -eddy describes an elliptic steady circulation with angular velocity ω in the vortex axis.

From the above assumptions, the motion of any Π -eddy is formulated as follows:

$$\left. \begin{aligned} \tilde{x}(t) &= \tilde{x}_0(t) - a \cos \omega t \cdot \sin \theta \\ \tilde{y}(t) &= \tilde{y}_0(t) + a \cos \omega t \cdot \cos \theta \\ \tilde{z}(t) &= \tilde{z}_0(t) + b \sin \omega t \end{aligned} \right\} \dots\dots (6.1)$$

where, the wave-sign and dot-sign denote the moving coordinates and the time differential ($=d/dt$), respectively. Of course, $\dot{\tilde{x}} = u$, $\dot{\tilde{y}} = v$ and $\dot{\tilde{z}} = w$ since $U \approx U_c$. $(\tilde{x}_0, \tilde{y}_0, \tilde{z}_0)$ is an arbitrary coordinates on the rotating axis in the vortex tube, and its velocity $u_0 \equiv (\dot{\tilde{x}}_0, \dot{\tilde{y}}_0, \dot{\tilde{z}}_0)$ is probably much smaller than that of the elliptic motion, since the Π -eddy attains the equilibrium state. That is to say, the Π -eddy consists of a primary motion with an elliptic steady circulation in the vortex axis, and a secondary motion, i.e. the overall deformation motion of the eddy, with a perturbation of its vortex tube due to the vortex-stretching effect.

By the way, since this secondary motion distorts the length l ($\equiv AB \equiv CD$) of the legs and the inclination angle θ , it is very difficult to determine the velocity U_0 of the secondary motion accurately. So, the following simplified formulation is considered here. The Π -eddy is surely influenced by the vortex-stretching since there is the velocity shear $\partial \hat{U} / \partial y = \partial U / \partial y$ even though the relative velocity $\hat{U} \equiv U - U_c$ is very small. Then, the equilibrium Π -eddy $ABCD$ is infinitesimally perturbed to $AB'C'D$ by this vortex-stretching effect, as shown in Fig. 6.9 (consequently, $\dot{z}_0 \equiv 0$). The head BC suffers the lift force L and the drag force D . So long as the Π -eddy under the equilibrium condition does not instantaneously disappear by the stretching, some apparent resistances F must be thought to work upon AB and CD of the eddy against the forces of L and D , which probably result from complex interactions between the mean flow and turbulence.

Now, describing the vortex tube BC as a circular cylinder with a radius R and a length l_1 , the following equation can be obtained from Fig. 6.9.

$$\left. \begin{aligned} -\rho\pi R^2 l_1 \Delta \ddot{x} - (\Delta F \cos \theta + F \sin \theta \cdot \Delta \theta) + \Delta D &= 0 \\ -\rho\pi R^2 l_1 \Delta \ddot{y} - (\Delta F \sin \theta - F \cos \theta \cdot \Delta \theta) + \Delta L &= 0 \end{aligned} \right\} \dots\dots\dots (6.2)$$

where, the drag force $D = \rho C_d R l_1 \hat{U}^2$ and the lift force $L = \rho C_l R^2 l_1 \omega \hat{U}$. Since the apparent resisting force F may have a strong correlation with the length l of the vortex tube AB , F is simply assumed to be linear with l , i.e. $\Delta F \equiv k \Delta l$ (where k is a proportional constant). The equations of vorticity and mass conservation are given, respectively, by $S\omega \equiv \Gamma$ (constant) and $\rho S l \equiv \text{constant}$ (6.3)

where S denotes a cross sectional area of the vortex ($S = \pi a b$).

Also, from Fig. 6.9, the followings are obtained :

$$\Delta x = \Delta l \cos \theta - l \sin \theta \cdot \Delta \theta \quad \text{and} \quad \Delta y = \Delta l \sin \theta + l \cos \theta \cdot \Delta \theta \quad \dots\dots\dots (6.4)$$

From the above equations, the following differential equations are obtained by adopting only the first order of the perturbations.

$$\begin{pmatrix} \Delta \ddot{l} \\ \Delta \ddot{\theta} \end{pmatrix} = - \begin{pmatrix} A & B \\ C & D \end{pmatrix} \begin{pmatrix} \Delta l \\ \Delta \theta \end{pmatrix} \quad \dots\dots\dots (6.5)$$

The coefficients A , B , C and D are fairly complicated. However, when the relative velocity \hat{U} is approximated to be equal to zero

according to Favre et al's(1967) or Sternberg's(1967) experimental data, these coefficients become as follows:

$$\left. \begin{aligned} A &= \frac{k}{\rho \pi R^2 \ell_1} - \frac{C_f}{\pi} \omega \sin^2 \theta \frac{dU}{dy} & C &= -\frac{C_f}{\pi} \omega \sin \theta \cos \theta \frac{dU}{dy} \\ B &= -\frac{C_f}{\pi} \omega \ell \sin \theta \cos \theta \frac{dU}{dy} & D &= -\frac{C_f}{\pi} \omega \ell \cos^2 \theta \frac{dU}{dy} \end{aligned} \right\} \dots\dots\dots (6.6)$$

Consequently, the secondary motion $u_0 \equiv (\Delta \dot{x}, \Delta \dot{y}, 0)$ can be predicted from (6.5). Considering that the apparent resisting force is included only in the term A, it is suggested that a perturbation along a vortex line may be represented by $\Delta \dot{z}$. So, θ is assumed to be independent of time t for simplifying the following analysis.

Then, from (6.1)-(6.6),

$$\left. \begin{aligned} u(t) &= a \omega \sin \omega t \sin \theta + A_0 \omega_0 \cos(\omega_0 t + \delta) \cos \theta \\ v(t) &= -a \omega \sin \omega t \cos \theta + A_0 \omega_0 \cos(\omega_0 t + \delta) \sin \theta \\ w(t) &= b \omega \cos \omega t \end{aligned} \right\} \dots\dots\dots (6.7)$$

where,

$$\omega_0 = \sqrt{\frac{k}{\rho \pi R^2 \ell_1} - \frac{C_f}{\pi} \omega \sin^2 \theta \frac{dU}{dy}} \dots\dots\dots (6.8)$$

and, A_0 and δ are constants.

(6.7) are the basic equations of the Π -eddy model, whose first and second terms describe the primary and secondary motions, respectively. It is noticed that for larger velocity gradient dU/dy or larger angular velocity ω the vortex line may be more easily raised with a longer period of the perturbation and in an extreme case the Π -eddy may be broken down by quick stretching without any vibration. However, it is difficult to evaluate the actual value of ω_0 at present.

6.2.2 Turbulence intensities and Reynolds stresses evaluated by a Π -eddy

Assuming that the direct correlation between the primary and secondary motions is negligible, i.e. $\omega \gg \omega_0$, the turbulence intensities and Reynolds stresses contributed by any Π -eddy can be evaluated from (6.7), as follows:

$$\left. \begin{aligned}
 \overline{u^2} &= (a\omega)^2 \frac{\sin^2 \theta}{2} + (A_0 \omega_0)^2 \frac{\cos^2 \theta}{2} \\
 \overline{v^2} &= (a\omega)^2 \frac{\cos^2 \theta}{2} + (A_0 \omega_0)^2 \frac{\sin^2 \theta}{2} \\
 \overline{w^2} &= \frac{(b\omega)^2}{2}
 \end{aligned} \right\} \dots (6.9)$$

$$\left. \begin{aligned}
 \overline{uv} &= -\frac{1}{2} \{ (a\omega)^2 - (A_0 \omega_0)^2 \} \sin \theta \cos \theta \\
 \overline{uw} &= 0 \\
 \overline{vw} &= 0
 \end{aligned} \right\} (6.10)$$

(6.10) obviously indicates that there is no correlation between u and w and between v and w , which coincides with the characteristics of two-dimensional shear flow. Since $0 \leq \theta \leq \pi/2$ and $-\overline{uv} > 0$, (6.10) gives $(a\omega)^2 \geq (A_0 \omega_0)^2$ (6.11)

Of course, (6.11) indicates that the contribution of the secondary motion is smaller than that of the primary motion. Also, the correlation coefficient R is given by

$$R = \frac{(a^2 \omega^2 - A_0^2 \omega_0^2) \sin \theta \cos \theta}{\sqrt{\{(a\omega)^2 \sin^2 \theta + (A_0 \omega_0)^2 \cos^2 \theta\} \{(a\omega)^2 \cos^2 \theta + (A_0 \omega_0)^2 \sin^2 \theta\}}} \dots (6.12)$$

Obviously, (6.12) evaluates $0 < R < 1$, which also agrees with the turbulence characteristics. Next, from (6.9), the following can be obtained:

$$\overline{u^2} - \overline{v^2} = \frac{1}{2} \{ (a\omega)^2 - (A_0 \omega_0)^2 \} \{ \sin^2 \theta - \cos^2 \theta \} \dots (6.13)$$

Since $u'^2 > v'^2$ in the actual turbulent shear flow (see Chapter 4), almost all of Π -eddies must satisfy the relation that $u^2 > v^2$. Consequently, almost all of Π -eddies have to be applicable in the following range of the inclination angle:

$$\frac{\pi}{4} \leq \theta < \frac{\pi}{2} \dots (6.14)$$

6.2.3 Spectral density functions of energy

The above investigation has been limited only to a specified eddy element, but the characteristics of turbulence as a whole contributed by all of the eddies should be made clear. In order to attain this purpose, the conception of energy spectrum about eddy scale \mathcal{L} must be introduced in the same manner as Chapter 2, together with adoption of space wave number in Eulerian expression instead of the above Lagrangian form.

Although a part of the primary motions may produce turbulence

due to the interaction with the mean flow, it is considered that almost of the primary motions in the equilibrium region have a turbulence cascade process where a larger scale eddy successively transports its turbulent energy into a smaller scale eddy, because in this region there exists an equilibrium state of the turbulent energy and any eddy element satisfies the similarity law, as shown in Figs. 2.9 & 2.13.

Here, we adopt Heisenberg's concept of the effective viscosity in the cascade process, as follows. Since the effective viscosity ν_T of any Π -eddy is given by $L^2\omega$, it can be adopted that $\nu_T = (a^2 + b^2)\omega/2$ in terms of its average. When the effective viscous force against the primary motion can be approximated to be equal to $4\pi\nu_T\mathcal{V}$ by application of Oseen's law for a circular cylinder (where, \mathcal{V} is the representative velocity of a Π -eddy), a rate W of work done by the mean effective viscosity of eddy against the eddy motion can be given by $4\pi\nu_T\mathcal{V}^2$. Adopting $v^2 \equiv (\bar{u}^2 + \bar{v}^2 + \bar{w}^2)/3$, the following is obtained.

$$W \sim 4\pi \cdot \frac{(a^2 + b^2)\omega}{2} \cdot \frac{(\bar{u}^2 + \bar{v}^2 + \bar{w}^2)}{3} \dots\dots (6.15)$$

According to Heisenberg's concept, the transport T of energy in the cascade process is equal to the rate of work per unit volume, i.e. $T = W/(\pi ab \cdot l)$. Also, the transport T is equal to its final dissipation rate ϵ , as shown in Fig. 2.9. Assuming that the contribution of the secondary motion may be negligible in this cascade process because of $a\omega \gg A_0\omega_0$, the following equation can be obtained from (6.9) and (6.15).

$$\epsilon \equiv \frac{K \cdot (1 + e^2)^2}{3e} a^2 \omega^3 \dots\dots\dots (6.16)$$

where, $e \equiv b/a < 1$ and K is a constant introduced for uncertainty in the above assumptions ($K = O(1)$).

Next, since the one-dimensional wave number k in the x -direction is given by $k = \pi \sin \theta / a$ (see our paper 1974), (6.16) becomes

$$\omega^2 = \frac{(3e/K)^{2/3}}{(1+e^2)^{4/3}} (\pi \sin \theta)^{-4/3} \epsilon^{2/3} k^{4/3} \dots (6.17)$$

By the way, in the range ($k_0 \leq k \leq k_\infty$) where the cascade process exists, the Reynolds similarity is valid, and furthermore the turbulent structure itself has a similarity in the equilibrium region, which is the same conception as 'self-similarity' mentioned in 5.5. Consequently, the ratio ϵ may be regarded as constant because the shape of any Π -eddy is similar to each other.

Therefore, a spectrum density function $G(k)$ of ω^2 will be obtained for $k_0 < k < k_\infty$:

$$G(k) \equiv \frac{d\omega^2}{dk} = \frac{4}{3} \frac{(3\epsilon/K)^{2/3}}{(1+\epsilon^2)^{1/3}} (\pi \sin\theta)^{-1/3} \epsilon^{2/3} k^{-1/3} \dots\dots\dots (6.18)$$

Now, on the assumption that ω_0 is so inappreciable compared with ω in the cascade process, the spectra of turbulence intensities can be written, as follows:

$$\left. \begin{aligned} \overline{u^2}(k) &= \frac{\sin^2\theta}{2} \left(\frac{\pi}{k} \sin\theta\right)^2 G(k) \equiv E_u(k) \\ \overline{v^2}(k) &= \frac{\cos^2\theta}{2} \left(\frac{\pi}{k} \sin\theta\right)^2 G(k) \equiv E_v(k) \\ \overline{w^2}(k) &= \frac{\epsilon^2}{2} \left(\frac{\pi}{k} \sin\theta\right)^2 G(k) \equiv E_w(k) \end{aligned} \right\} \dots\dots\dots (6.19)$$

That is,

$$\left. \begin{aligned} E_u(k) &= \frac{2}{3} \frac{(3\pi\epsilon/K)^{2/3}}{(1+\epsilon^2)^{1/3}} (\sin\theta)^{5/3} \epsilon^{2/3} k^{-5/3} \\ E_v(k) &= \frac{2}{3} \frac{(3\pi\epsilon/K)^{2/3}}{(1+\epsilon^2)^{1/3}} (\sin\theta)^{2/3} (\cos\theta)^2 \epsilon^{2/3} k^{-5/3} \\ E_w(k) &= \frac{2}{3} \frac{\epsilon^2(3\pi\epsilon/K)^{2/3}}{(1+\epsilon^2)^{1/3}} (\sin\theta)^{2/3} \epsilon^{2/3} k^{-5/3} \end{aligned} \right\} \dots\dots\dots (6.20)$$

(6.20) shows that each spectral density function is in proportion to the $-5/3$ power of k in the cascade process ($k_0 \leq k \leq k_\infty$), which surely coincides with the local isotropic theory proposed by Kolmogoroff (cf. Section 2.3).

Lastly, denoting $k_0 \equiv b^{-1} > a^{-1}$, the contribution of the secondary motion should not be neglected in the range of $k = a^{-1} < k_0$. Then, since the Π -eddy may be just before the breakdown by the vortex-stretching, the cross section of its vortex tube will be extremely distorted. Consequently, assuming $\epsilon^2 \ll 1$, (6.3) and (6.16) give $\epsilon \sim \epsilon^{-1} a^2 \omega^3 \sim \epsilon^{-2} \omega^2 \Gamma$. Therefore, from (6.9),

$$E_u(k) \sim (\epsilon \Gamma^{-1} k_0^{-2}) k^{-1}, \quad E_v(k) \sim (\epsilon \Gamma^{-1} k_0^{-2}) k^{-1}, \quad E_w(k) \sim (\epsilon \Gamma^{-1} k_0^{-4}) k \quad \dots\dots\dots (6.21)$$

(6.21) indicates that $E_u(k)$ satisfies the -1 power law in the productive subrange ($k \leq k_0$), whose result also coincides with Tchen's results and the experimental data obtained in Chapter 4.

However, $E_v(k)$ and $E_w(k)$ obtained from (6.21) are incorrect. This is probably due to the fact that the modelling of the secondary motion has been too simplified. In particular, the incorrectness in $E_w(k)$ may have been caused by an assumption that the vortex stretching affects never the spanwise components.

6.2.4 Comparison of turbulence intensities with the experimental data

In order to evaluate the turbulence intensities u' , v' and w' from (6.20), the ratio e and the inclination angle θ must be known. Firstly, since e is constant in any Π -eddy, it will be related to the mean eddy scales L_x in the x-direction and L_z in the z-direction. Because L_z/L_x is equal to 0.5 in an isotropic turbulence of $e \equiv 1$, it may be estimated that $e \approx 2(L_z/L_x)$ in a shear turbulence. According to Laufer's (1951) experiment for a two-dimensional channel flow, it was shown that the value of L_z/L_x became about 0.3 independently of y/h . Consequently, we can here adopt $e=0.6$.

Next, it is more difficult to evaluate the inclination angle θ accurately, because θ may be different more or less for each eddy size. Since the time-space correlations may show the maximum in an identical eddy, θ will be roughly estimated from these maximum correlation distributions. Fig. 6.10 shows the data of θ for mean eddy size summarized by Sternberg (1967). According to this figure, θ increases remarkably from about 20 degrees at the edge of the viscous sublayer, and it attains about 40 degrees at the edge of the wall region ($y=15$ mm), and more it becomes over 45 degrees in the equilibrium region. This fact agrees very well with (6.14) evaluated by the Π -eddy model. However, the maximum inclination angle θ_{\max}

which a Π -eddy can hold is quite unknown at present.

Well, the actual turbulence in the equilibrium region is probably contributed uniformly from all eddies of $\pi/4 \leq \theta \leq \theta_{\max}$. That is to say, it is assumed here that the results of (6.20) averaged uniformly in the range of $\pi/4 \leq \theta \leq \theta_{\max}$ are observed actually.

For example, when θ_{\max} is chosen as the upper limit value in theory, i.e. $\theta_{\max} = \pi/2$, the followings can be obtained:

$$\left. \begin{aligned} E_u(k) &= 2.295 K' \epsilon^{2/3} k^{-5/3} \\ E_v(k) &= 0.476 K' \epsilon^{2/3} k^{-5/3} \\ E_w(k) &= 2.774 \epsilon^2 K' \epsilon^{2/3} k^{-5/3} \end{aligned} \right\} \dots\dots\dots (6.22)$$

where,
$$K' \equiv \left[\frac{\epsilon}{K(1 + \epsilon^2)^2} \right]^{2/3}$$

As mentioned in Chapter 2, $C \equiv 2.295K'$ is a universal constant which is nearly equal to 0.5 (see Fig. 2.10). Then, by using $e=0.6$, K becomes equal to 3.19. The turbulence intensities u' , v' and w' are approximately evaluated from (6.22), as follows:

e.g.
$$u'^2 = \int_{k_0}^{k_\infty} E_u(k) dk = \frac{3}{2} C \epsilon^{2/3} (k_0^{-2/3} - k_\infty^{-2/3}) \dots\dots\dots (6.23)$$

By using $e=0.6$, the following relations are obtained.

$$\frac{v'}{u'} = 0.46, \quad \frac{w'}{u'} = 0.66 \dots\dots\dots (6.24)$$

In the same manner as the above, the results calculated by varying θ_{\max} as a parameter are shown in Fig. 6.11. Well, Fig. 6.12 replots the experimental data of v'/u' and w'/u' obtained in Chapter 4. When θ_{\max} is chosen as 78 degrees, (6.20) or Fig. 6.11 gives

$$\frac{v'}{u'} = 0.55, \quad \frac{w'}{u'} = 0.69 \dots\dots\dots (6.25)$$

In the equilibrium region ($0.064 \leq y/h \leq 0.6$ for the higher-velocity group, and $0.16 \leq y/h \leq 0.6$ for the lower-velocity group), (6.25) coincides very well with the experimental values, that is, (4.12). Also, K becomes equal to 2.73, whose value is consistent with $K=O(1)$ in (6.16). However, in the wall region $y/h \leq 0.1$ for the lower-velocity group, (6.25) cannot explain the experimental data. Consequently, the π -eddy model is not applicable to the region of $y^+ \leq 50$.

To sum up, the Π -eddy model can explain fairly well the macro structure of turbulence in the equilibrium region. Since this region is scarcely influenced by the outer boundary conditions and consequently it has a dynamic equilibrium state or self-similarity, that is, a self-consistency of turbulence, the turbulence intensities are given by the followings, as mentioned in 4.3.

$$u'/U_* = D_1 \cdot \epsilon^{-\xi}, \quad v'/U_* = D_2 \cdot \epsilon^{-\xi}, \quad w'/U_* = D_3 \cdot \epsilon^{-\xi} \quad \dots\dots\dots(6.26)$$

Thus, (6.26) may be considered to be a conclusion obtained from a Π -eddy model. The vortex tube of the Π -eddy has a cross section distorted by about 60% in the mean flow direction, and keeps uniformly an inclination angle developing up to about 80 degrees.

6.3 Renewal model *)

6.3.1 Formulation of a renewal model

In modelling the wall region, we consider an idealized model of the bursting process, which is called a renewal model, because it is most essential to take account of its periodic characteristics.

We can divide a period T of the bursting phenomenon into two duration intervals: one is the built-up or developing duration T_1 , and the other is the breakdown duration T_2 of the coherent vortex motion, that is, $T = T_1 + T_2$. The ejection motion occurs in the breakdown duration T_2 , and both the sweep and the interaction motions occur in the built-up duration T_1 , since the former is swept literally by the latter and a new horseshoe vortex is born again. For convenience, the beginning of a sweep motion is here denoted as $t=0$, and then a sequence of the bursting process is considered to be a cyclic motion of sweep-interaction-ejection-sweep.

Let $\tilde{U}_1 \equiv (\tilde{u}_1, \tilde{v}_1)$ and $\tilde{U}_2 \equiv (\tilde{u}_2, \tilde{v}_2)$ be the instantaneous velocities during T_1 and T_2 , respectively. The eddy-viscosity might be infinitely smaller in the built-up duration and infinitely larger in the

*) Refer to our paper (*Bursting phenomenon near the wall in open channel flow and its simple mathematical model*) just published in *Memoirs of Faculty of Engineering, Kyoto University*, vol.40, part 4, 1978.

breakdown duration than the molecular-viscosity since much of the Reynolds stress is generated by the breakdown of the horseshoe vortex, i.e. ejection motion. Consequently, assuming that the non-linear coupling effect and the pressure fluctuation effect are negligible during the built-up time, the Navier-Stokes equation which controls the coherent motion in this duration can be approximated by using the boundary layer theory since $\lambda_2^+ < \lambda_3^+ < \lambda_1^+$ (see 5.5.1), as follows:

$$\frac{\partial \tilde{u}_1}{\partial t} = \nu \frac{\partial^2 \tilde{u}_1}{\partial y^2} \dots\dots\dots (6.27)$$

The boundary conditions are

$$y=0 : \tilde{u}_1=0 , \quad y \rightarrow \infty : \tilde{u}_1=U_0 \quad \dots\dots\dots (6.28)$$

where U_0 is the main stream velocity outside the wall region.

Since the distorted velocity distribution of an ejection motion may be swept due to the stress-relieved mechanism and restored to a uniformly accelerated velocity, as observed in Figs. 2.20 & 5.40, the initial condition can be idealized by

$$t=0 : \tilde{u}_1=U_0 (y>0) \quad \dots\dots\dots (6.29)$$

Then, the solution of (6.27) with the conditions of (6.28) and

$$(6.29) \text{ reads } \tilde{u}_1 = \frac{2U_0}{\sqrt{\pi}} \int_0^\theta e^{-x^2} dx \equiv U_0 \operatorname{erf} \theta \quad \dots\dots (6.30)$$

where, $\theta \equiv y/(2\sqrt{\nu t})$ and $\operatorname{erf} \theta$ is the error-function of θ .

(6.30) was firstly obtained by Einstein & Li(1956), and it forms the origin of the present model. On the other hand, Black(1968) adopted Coles' logarithmic law, i.e. $\tilde{u}_1=U_* (\kappa^{-1} \ln y^+ + 5.1)$ as the initial condition of (6.27), and then he obtained a more complicated solution than (6.30). Though this initial condition seems to be more suitable for the actual phenomenon than (6.29), as seen from Figs. 2.20 & 5.40, we do not adopt the Black solution here because it is too intricate to go on calculating further.

Now, making the axis transformation to $\partial/\partial t = -U_c \partial/\partial x$ (Taylor's frozen turbulence hypothesis, see (4.37)) where U_c is the convection velocity of a horseshoe vortex, and using the equation of continuity, we can obtain

$$\tilde{v}_1 = - \int_0^y \frac{\partial \tilde{u}_1}{\partial x} dy = - \frac{1}{\alpha} \sqrt{\frac{\nu}{\pi t}} \{1 - \exp(-\theta^2)\} \quad \dots\dots\dots (6.31)$$

where, $\alpha \equiv U_c/U_0$ is equal to (0.7 - 0.8) according to the previous experiments (see Hinze's book 1975).

Next, because the mechanism of the vortex-breakdown is not sufficiently evident, $\tilde{U}_2 = (\tilde{u}_2, \tilde{v}_2)$ is evaluated here by introducing a simplified idea. It is considered that $\beta \equiv T_2/T_1$ is infinitesimal, i.e. $\beta \ll 1$, since the vortex-breakdown or the ejection motion occurs in very short time, as shown in Fig. 5.26. Then, $\tilde{u}_1(t=T_1)$ is renewed into $\tilde{u}_1(t=T) \equiv \tilde{u}_1(t=0)$ in a very short time. Consequently, the average of both $\tilde{u}_1(t=T_1)$ and $\tilde{u}_1(t=T)$ can be represented as $\tilde{u}_2(T_1 \leq t \leq T)$. We can also obtain $\bar{v}_2 = -\bar{v}_1/\beta$ since the average vertical velocity $V \equiv \bar{v} = (T_1 \bar{v}_1 + T_2 \bar{v}_2)/T$ must always be zero in an open channel flow. Furthermore, \tilde{v}_2 may be closely identified with \bar{v}_2 for $\beta \ll 1$. Then, $\bar{v}_2 \equiv -\bar{v}_1/\beta \quad \dots\dots\dots (6.32)$

From the above simplification, the following relations can be obtained by using $\beta \ll 1$.

$$\left. \begin{aligned} U \equiv \bar{u} &= \frac{1}{T} \left(\int_0^{T_1} \tilde{u}_1 dt + \int_{T_1}^T \tilde{u}_2 dt \right) \equiv \frac{1}{T} \int_0^T \tilde{u}_1 dt \\ V \equiv \bar{v} &= 0 \end{aligned} \right\} \quad \dots\dots\dots (6.33)$$

$$\left. \begin{aligned} u'^2 &\equiv \overline{(\tilde{u} - U)^2} \equiv \frac{1}{T} \int_0^T \tilde{u}_1^2 dt - U^2 \\ v'^2 &\equiv \overline{(\tilde{v} - V)^2} \equiv \frac{1}{(1+\beta)} \left\{ \frac{1}{T_1} \int_0^{T_1} \tilde{v}_1^2 dt + \frac{1}{\beta} (\bar{v}_1)^2 \right\} \end{aligned} \right\} \quad \dots\dots\dots (6.34)$$

$$\bar{u}\bar{v} = \overline{(\tilde{u}_1 - U) \cdot \tilde{v}_1} + \beta \overline{(\tilde{u}_2 - U) \cdot \tilde{v}_2} / (1 + \beta) \quad \dots\dots\dots (6.35)$$

The second term of (6.35) is the Reynolds stress which is generated by an ejection motion, and is given by $\overline{(\tilde{u}_2 - U) \cdot \tilde{v}_2} \equiv (\tilde{u}_1(t=T_1) - \tilde{u}_1(t=T)) \cdot \tilde{v}_2$ because this Reynolds stress is equal to the momentum change of \tilde{u} which is transferred by $\tilde{v}_2 > 0$ during the period of breakdown.

Then,

$$\bar{u}\bar{v} = \frac{1}{(1+\beta)} \left\{ (\bar{u}_1 \bar{v}_1 - \bar{u}_1 \cdot \bar{v}_1) + \bar{v}_1 \cdot (\tilde{u}_1(t=T) - \tilde{u}_1(t=T_1)) \right\} \quad \dots\dots\dots (6.35)'$$

Since $U_*^2 \equiv \nu \overline{(\partial \tilde{u} / \partial y)}_{y=0}$, we can also obtain from (6.30)

$$U_*^2 \equiv \nu \frac{1}{T} \int_0^T \left(\frac{\partial \tilde{u}_1}{\partial y} \right)_{y=0} dt = \frac{2}{\sqrt{\pi}} U_0 \sqrt{\frac{\nu}{T}} \dots \dots \dots (6.36)$$

6.3.2 Further consideration of renewal model by taking account of the probability distribution of bursting period

The above results represent the turbulent characteristics during one bursting period T. However, in order to obtain the actual turbulent characteristics, as compared with the experiments, the probability distribution of T should be taken into account.

Then, the friction velocity (6.36) by using (5.16)-(5.18)

becomes as follows:
$$U_*^2 = \int_0^\infty \left(\frac{2}{\sqrt{\pi}} U_0 \sqrt{\frac{\nu}{T}} \right) p_T(T) dT = \frac{2}{\sqrt{\pi}} U_0 \sqrt{\frac{\nu}{T_B}} \cdot r^{-3/4} \dots \dots \dots (6.37)$$

Also, by doing the variable transformation of $s \equiv \log(T/T_0)/\delta_0$,

(6.33) becomes
$$U^+ \equiv U_0^+ \phi(y^+) = U_0^+ \int_{-\infty}^\infty G(s) ds \int_0^1 \text{erf}(\theta) d\tau \dots \dots \dots (6.38)$$

where, $G(s) = \frac{1}{\sqrt{2\pi}} \exp(-s^2/2)$, and θ reads $\theta \equiv \frac{y}{2\sqrt{\nu t}} = \frac{\sqrt{\pi}}{4} r^{1/4} \frac{y^+}{U_0^+} \frac{1}{\sqrt{10} \sigma_0^s \cdot \tau}$.

In the same manner, we can obtain from (6.34) and (6.35)':

$$\left(\frac{u'}{U_*} \right)^2 = U_0^{+2} \int_{-\infty}^\infty G(s) ds \int_0^1 \{ \text{erf}(\theta) \}^2 d\tau - U^{+2} \dots \dots \dots (6.39)$$

$$\left(\frac{v'}{U_*} \right)^2 = \frac{r^{1/2}}{(1+\beta)(2\alpha U_0^+)^2} \left[\int_{-\infty}^\infty \frac{G(s)}{10 \sigma_0^s} ds \int_0^1 \frac{(1 - \exp(-\theta^2))^2}{\tau} d\tau + \frac{1}{\beta} \psi(y^+) \right] \dots \dots (6.40)$$

$$\begin{aligned} \frac{-\bar{u}v}{U_*^2} &= \frac{r^{1/4}}{(1+\beta) \cdot 2\alpha} \left[\left\{ \int_{-\infty}^\infty \frac{G(s)}{\sqrt{10} \sigma_0^s} ds \int_0^1 \frac{(1 - \exp(-\theta^2)) \cdot \text{erf}(\theta)}{\sqrt{\tau}} d\tau - \phi(y^+) \cdot \psi(y^+) \right\} \right. \\ &\quad \left. + \psi(y^+) \cdot \left\{ 1 - \text{erf} \left(\frac{\sqrt{\pi}}{4} r^{1/4} \frac{y^+}{U_0^+} \right) \right\} \right] \dots \dots (6.41) \end{aligned}$$

where, $\psi(y^+) \equiv \int_{-\infty}^\infty \frac{G(s) ds}{\sqrt{10} \sigma_0^s} \int_0^1 \frac{(1 - \exp(-\theta^2))}{\sqrt{\tau}} d\tau$

Lastly, the bursting period T_B is obtained from (6.37),

as follows:
$$\frac{T_B U_*^2}{\nu} = \frac{4r^{-3/2}}{\pi} U_0^{+2} \dots \dots \dots (6.42)$$

PART 2 Turbulent structure over permeable bed

Chapter 7 Introduction

In Part 1 we have investigated theoretically and experimentally the problems (1)-(5) mentioned previously (see page 1), which are very basic and important in turbulence research of two-dimensional solid open-channel flows. However, various turbulent phenomena which often appear in hydraulic engineering and environmental sciences are very complicated, and then even in two-dimensional open-channel flows the following boundary conditions are furthermore added to the flow dealt with in Part 1.

- (1) A seepage flow exists under the porous bed. Consequently, an interaction with main and seepage flows cannot be neglected in open-channel flow.
- (2) Suction or injection exists steadily through the porous bed. Consequently, the turbulent structure may be varied essentially.
- (3) The bed surface is discontinuous, uneven or wavy.
- (4) The bed is moving sand surface. Consequently, an interaction between flow and moving bed should be considered (Sediment transport by turbulent flow).
- (5) Suspended materials exist in open-channel flow. Consequently, the turbulent structure may be varied essentially.

In this part, we investigate the turbulent structures with boundary conditions of (1) and (2) in Chapter 8 and Chapter 9, respectively, and we consider the fundamental characteristics of turbulence over a permeable bed, by comparing with the results obtained over a solid bed (Part 1).

Chapter 8 Interaction between main and seepage flows *)

8.1 Introduction

When the bed permeability is small enough to neglect the effect of seepage flow under the bed, the main flow shows the characteristics over a solid rough bed, which have been already discussed in Part 1. When the effect of seepage flow on the main flow cannot be neglected, there exists a hydrodynamic interaction between them through the porous bed. Compared with solid rough bed, the momentum exchange becomes more active, and consequently an additional shear stress will be produced by this interaction. For example, Lovera et al.(1969) reported that the friction-factor of flat permeable bed in a natural river was much larger than that of rough bed given by Nikuradse. Also, Monin et al.(1971) pointed out that similar phenomenon was observed in the wind flow over a vegetated ground. These additional stress may be caused by an interaction between main and seepage flows.

The seepage flow near the pore surface is excited to be turbulent by the pressure fluctuations of main flow. Otherwise, the seepage flow becomes laminar and Darcy law is applicable. Then, there is an analogy between smooth and permeable flow fields, as shown in Fig.8.1. That is, the viscous sublayer is also disturbed by the pressure fluctuations of main flow, as have been mentioned in 4.7.3. Consequently, an additional shear stress is probably induced in the main flow by the disturbed seepage flow.

To sum up, there exists a hydrodynamic interaction mechanism between main and seepage flows, as shown in Fig. 8.2. This chapter deals with these feed-back systems, in order.

*) Refer to our paper published in *Proc. of JSCE, No.244, pp.81-90, 1975 (in Japanese), or Trans. of JSCE, vol.7, pp.201-204, 1976 (in English).*

8.2 Theoretical consideration

8.2.1 Basic equations of seepage flow

The local velocity v_p in the porous media must obey the following Navier-Stokes equation.

$$\frac{\partial v_p}{\partial t} = F - \nabla \left(\frac{\bar{p}}{\rho} \right) + \nu \nabla^2 v_p - (v_p \cdot \nabla) v_p \quad \dots\dots\dots (8.1)$$

where, F is the volume force, $\bar{p} = p + p'$ is the instantaneous pressure.

But, as shown in Fig. 8.3, it is impossible to evaluate the local velocity v_p , and moreover in practice it is better to substitute a nominal velocity, i.e. seepage velocity q for this local velocity.

That is,

$$q = \frac{1}{s} \int_s v_p ds \equiv n \langle v_p \rangle \quad \dots\dots\dots (8.2)$$

where, n is the porosity of the medium. $\langle \rangle$ denotes the sectional average on s .

Well, the following empirical descriptions are assumed to be valid. The viscous friction is a linear term, as follows:

$$\nu \langle \nabla^2 v_p \rangle \equiv - \frac{\nu}{K} q \quad \dots\dots\dots (8.3)$$

The inertial friction is a nonlinear term, as follows:

$$\langle (v_p \cdot \nabla) v_p \rangle \equiv \frac{C}{\sqrt{K}} |q| q \quad \dots\dots\dots (8.4)$$

where, K is the intrinsic permeability of the medium, and C is a experimental constant.

Defining the Reynolds number $R_K \equiv \sqrt{K} |q| / \nu$ of seepage flow as the ratio of (8.4) to (8.3), Eq.(8.1) is approximated as follows:

$$\frac{1}{n} \frac{\partial q}{\partial t} = F - \nabla \left(\frac{\bar{p}}{\rho} \right) - \frac{\nu}{K} [1 + CR_K] q \quad \dots\dots\dots (8.5)$$

(8.5) is applied to a permeable open-channel flow field, as shown in Fig. 8.4. Then, denoting one-dimensional seepage flow $q = (q_m + q_x, q_y, q_z)$, where q_m is the mean velocity and q_x, q_y and q_z are the fluctuating velocities, the basic equations of mean velocity are given by

$$y\text{-component : } P = \rho g \cos \theta \cdot (h - y) \dots\dots\dots (8.6)$$

$$x\text{-component : } (1 + CR_K) q_m = (Kg/\nu) I_e \dots\dots\dots (8.7)$$

I_e is the hydraulic gradient of porous media and it coincides with the energy gradient of main flow (see page 6). R_K is nearly equal to $R_K \approx \sqrt{K} q_m / \nu$.

$$\text{When } R_K \ll 1/C, \quad q_m = (Kg/\nu) I_e \dots\dots\dots (8.8)$$

$$\text{When } R_K \gg 1/C, \quad q_m = (\sqrt{K} C \cdot g I_e)^{1/2} \dots\dots\dots (8.9)$$

(8.8) is Darcy law, which is applicable in the laminar region. On the other hand, (8.9) is applicable in the turbulent region. Thus, C is a measure of nonlinear term. According to the experimental results by Arbhahirama et al. (1973), C is approximately given by $C = 100 (d_m \sqrt{n/K})^{-1.5}, (20 < d_m \sqrt{n/K} < 80) \dots\dots\dots (8.10)$

where, d_m is the particle mean diameter of porous media.

Next, in the same manner as 2.2, the basic equations of fluctuating components are given from (8.5)-(8.7), as follows:

$$\left. \begin{aligned} \frac{\partial q_x}{\partial t} &= -n \frac{\partial}{\partial x} \left(\frac{p}{\rho} \right) - a_1 q_x \\ \frac{\partial q_y}{\partial t} &= -n \frac{\partial}{\partial y} \left(\frac{p}{\rho} \right) - a_2 q_y \end{aligned} \right\} \dots\dots\dots (8.11)$$

$$\text{where, } a_1 \equiv (n\nu/K)(1 + 2CR_K), \quad a_2 \equiv (n\nu/K)(1 + CR_K) .$$

From the equation of continuity,

$$\nabla^2 (p/\rho) = - \frac{C q_m}{\sqrt{K}} \frac{\partial q_x}{\partial x} \dots\dots\dots (8.12)$$

On the other hand, the primary terms of pressure equation of the main flow is also given by

$$\nabla^2 (p/\rho) = - 2 \frac{\partial U}{\partial y} \frac{\partial v}{\partial x} \dots\dots\dots (8.13)$$

(8.12) is very similar to (8.13). In other words, the external force term of pressure fluctuations in the main flow is $(\partial U / \partial y) (\partial v / \partial x)$, while its term in the seepage flow is $(q_m / \sqrt{K}) (\partial q_x / \partial x)$. These external terms are both very similar.

8.2.2 Analysis of turbulent fluctuations of seepage flow

We consider the turbulent fluctuations of seepage flow excited by the pressure fluctuation p_0 on the boundary ($y=0$) of main flow (see Fig. 8.1 (b)). That is, the boundary conditions of seepage flow are assumed as follows:

$$p = R_e \{ \sqrt{2} \tilde{p}_0' \exp i(kx + \omega t) \} \equiv p_0 \quad , \quad \text{at} \quad y=0 \quad \dots\dots\dots (8.14)$$

$$q_y = 0 \quad , \quad \text{at} \quad y = -h_p \quad \dots\dots\dots (8.15)$$

where, $\text{Re}\{ \}$ denotes the real part of $\{ \}$. \tilde{p}_0' ($\equiv \sqrt{\tilde{p}_0'^2}$) is the r.m.s. value of pressure fluctuations in the main flow. h_p is the thickness of porous media, at which the turbulent flow is attenuated and becomes laminar, as mentioned previously. Then, on these boundary conditions, (8.11)-(8.12) are easily solved, as follows: ($-h_p \leq y \leq 0$)

$$p = R_e \left\{ \frac{\sqrt{2} \tilde{p}_0' \cosh \beta(h_p + y)}{\cosh(\beta h_p)} \exp i(kx + \omega t) \right\} \quad \dots\dots\dots (8.16)$$

$$q_x = R_e \left\{ -i \frac{nk}{(\alpha_1 + i\omega)} \cdot \frac{\sqrt{2}(\tilde{p}_0'/\rho) \cosh \beta(h_p + y)}{\cosh(\beta h_p)} \times \exp i(kx + \omega t) \right\} \quad \dots\dots (8.17)$$

$$q_y = R_e \left\{ -\frac{nk^2}{(\alpha_1 + i\omega)\beta} \cdot \frac{\sqrt{2}(\tilde{p}_0'/\rho) \sinh \beta(h_p + y)}{\cosh(\beta h_p)} \times \exp i(kx + \omega t) \right\} \quad \dots\dots (8.18)$$

where, $\beta^2 \equiv k^2(\alpha_2 + i\omega)/(\alpha_1 + i\omega)$.

By using the relation of $\overline{q_x^2} = \frac{1}{2} [\overline{\tilde{q}_x \tilde{q}_x^*} + R_e \{ \overline{\tilde{q}_x^2} \}] = \frac{1}{2} \overline{\tilde{q}_x \tilde{q}_x^*}$

(\tilde{q}_x and \tilde{q}_x^* are complex conjugates), the following approximations are obtained in the region very close to the porous boundary, i.e.

$$0 \sim |y| \ll h_p \quad \overline{q_x^2} = \frac{n^2 k^2}{(\alpha_1^2 + \omega^2)} (\tilde{p}_0'/\rho)^2 \quad \dots\dots\dots (8.19)$$

$$\overline{q_y^2} = \frac{n^2 k^2}{\sqrt{(\alpha_1^2 + \omega^2)(\alpha_2^2 + \omega^2)}} (\tilde{p}_0'/\rho)^2 \dots\dots (8.20)$$

(8.19) and (8.20) are also derived by Chu et al.(1972), on the different boundary condition from (8.15).

Next, since (8.19) and (8.20) are a contribution of a disturbed eddy with scale (k, ω) , the contributions of all eddies are here considered by introducing two-side normalized spectral distribution $\Phi_p(k, \omega)$ of the pressure fluctuations, in the same manner as 6.2.3.

That is, $\bar{p}_0^2(k, \omega) = \rho_0^2 \Phi_p(k, \omega)$ and $\int_{-\infty}^{\infty} \int_{-\infty}^{\infty} \Phi_p(k, \omega) dk d\omega = 1$ (8.21)

Then, the turbulence intensities q'_x and q'_y near the porous boundary are given by

$$q_x'^2 = \iint_{-\infty}^{\infty} \frac{p_0'^2}{\rho_x^2} dk d\omega = \frac{n^2}{\rho^2} \iint_{-\infty}^{\infty} \frac{p_0'^2 k^2}{\alpha_1^2 + \omega^2} \times \Phi_p(k, \omega) dk d\omega \dots\dots\dots (8.22)$$

$$q_y'^2 = \iint_{-\infty}^{\infty} \frac{p_0'^2}{\rho_y^2} dk d\omega = \frac{n^2}{\rho^2} \iint_{-\infty}^{\infty} \frac{p_0'^2 k^2}{\sqrt{(\alpha_1^2 + \omega^2)(\alpha_2^2 + \omega^2)}} \Phi_p(k, \omega) dk d\omega \dots\dots\dots (8.23)$$

Also, the normalized spectral functions Φ_x and Φ_y of q_x and q_y , respectively, are given by

$$\Phi_x(k, \omega) = \left(\frac{p_0'}{\rho q_x}\right)^2 \frac{n^2 k^2}{\alpha_1^2 + \omega^2} \Phi_p(k, \omega) \dots\dots\dots (8.24)$$

$$\Phi_y(k, \omega) = \left(\frac{p_0'}{\rho q_y}\right)^2 \frac{n^2 k^2}{\sqrt{(\alpha_1^2 + \omega^2)(\alpha_2^2 + \omega^2)}} \times \Phi_p(k, \omega) \dots\dots\dots (8.25)$$

Consequently, if $\Phi_p(k, \omega)$ is known, the spectra of seepage fluctuations are easily obtained. However, it is at present difficult to directly evaluate Φ_p over a permeable rough bed. Thus, we here estimate the function of Φ_p from the results of solid-wall turbulence obtained by Willmarth et al. (1962) and Corcos (1964).

According to Corcos, the following relations are satisfied.

$$\Phi_p(k, \omega) = \frac{U_c}{|\omega|} \phi(\omega) E_0(\mu + 1) \dots\dots\dots (8.26)$$

$$E_0(\mu + 1) \equiv \frac{1}{\pi} \int_0^{\infty} A(t) \cos t(\mu + 1) dt \dots\dots\dots (8.27)$$

where, $t \equiv \omega \xi / U_c$, $\mu \equiv k U_c / \omega$, ξ is the lag distance. $A(t)$ is the ratio of amplitude defined as $A(t) \equiv |\Gamma(\xi, \omega)| / \phi(\omega)$, $\Gamma(\xi, \omega)$ is the cross-spectrum, and $\phi(\omega)$ is the auto-correlation spectrum.

Of course, if the frozen turbulence hypothesis of Taylor is exactly valid, $A(t)$ becomes equal to unity. Then, (8.26) and (8.27) become $\Phi_p(k, \omega) = \phi(\omega) \delta(1 + \omega / k U_c)$, $\delta(\omega)$ is the delta function.

or $\Phi_p(-\omega / U_c, \omega) = \phi(\omega) \dots\dots\dots (8.28)$

That is to say, the disturbances of (8.14) are perfectly coherently convected with the velocity $U_c = -\omega / k$.

Now, assuming that the auto-correlation has an exponential type, we obtain

$$\phi(\omega) = \frac{1}{2\pi} \int_{-\infty}^{\infty} \exp(-|\tau|/\mathfrak{Z}) e^{-i\omega\tau} d\tau = \frac{\mathfrak{Z}}{\pi(1+\mathfrak{Z}^2\omega^2)} \dots\dots\dots (8.29)$$

where, \mathfrak{Z} is the integral time scale.

Next, Fig. 8.5 shows the experimental values of $A(t)$ obtained by Willmarth et al. and Corcos. In the same manner as (8.29), the fitting function of $A(t)$ is firstly assumed to be an exponential type. That is, $A(t) = e^{-b_1 t}$ (b_1 is an experimental constant) ... (8.30)

Then,

$$E_0(\mu+1) = \frac{1}{\pi} \frac{b_1}{b_1^2 + (\mu+1)^2} \dots\dots\dots (8.31)$$

However, the calculated values of q'_x and q'_y using (8.22), (8.23) and (8.31) are divergent, because the higher wave number components of (8.31) are too large. (Same example appears in (2.43) by using (4.47).) Hence, it may be better to use the following fitting function which satisfies the condition of $A'(0)=0$, since (8.28) of the frozen turbulence is probably valid when t is very small.

$$A(t) = \frac{1}{1+(b_2 t)^2} \quad (b_2 \text{ is an experimental constant}) \dots(8.32)$$

Then,

$$E_0(\mu+1) = \frac{1}{2b_2} \exp\left(-\frac{1}{b_2} |\mu+1|\right) \dots (8.33)$$

From (8.29) and (8.33), (8.26) becomes

$$\phi_p(k, \omega) = \frac{U_c \mathfrak{Z}}{2\pi b_2 |\omega| (1+\mathfrak{Z}^2\omega^2)} \times \exp\left(-\frac{1}{b_2} \left|\frac{U_c k}{\omega} + 1\right|\right) \dots (8.34)$$

Consequently, from (8.22) and (8.23), we can obtain

$$q_x'^2 = n^2 \left(\frac{p_0'}{\rho}\right)^2 \frac{2b_2^2 + 1}{U_c^2} \cdot \frac{1}{\alpha_1' + 1} \dots\dots\dots (8.35)$$

$$q_y'^2 = n^2 \left(\frac{p_0'}{\rho}\right)^2 \frac{2b_2^2 + 1}{U_c^2} \frac{2\alpha_1'}{\pi(\alpha_1'^2 - 1)} \times [K_1 + (\epsilon^2 - 1)K_3] \dots\dots\dots (8.36)$$

where, $\alpha_1' \equiv \alpha_1 \mathfrak{Z}$, $\alpha_2' \equiv \alpha_2 \mathfrak{Z}$. K_1 and K_3 are the elliptic functions of Legendre-Jacobi type, which are defined as follows:

$$K_1 = \int_0^1 \frac{dx}{\sqrt{(1-x^2)(1-k^2x^2)}} \quad \text{and} \quad K_3 = \int_0^1 \frac{dx}{(x^2 - \epsilon^2)\sqrt{(1-x^2)(1-k^2x^2)}}$$

where, $\epsilon^2 = \alpha_1'^2 / (\alpha_1'^2 - 1) > 0$, $k^2 = 1 - \alpha_2' / \alpha_1' > 0$

If (8.30) is used instead of (8.32), $2b_2$ in the denominator of (8.45) is replaced only by πb_1 .

Where, $I \equiv \int_0^\infty \frac{dt}{\sqrt{(a_1'^2 + t)(a_2'^2 + t)(1+t)}}$, which is easily integrated as follows:

(i) $a_1' \geq a_2' > 1$ (When $1 > a_1' > a_2'$, the lower sign is used)

$$I = \pm \frac{2}{\sqrt{\beta_1 \beta_2}} \ln \left| \frac{a_1' \sqrt{\pm \beta_2} + a_2' \sqrt{\pm \beta_1}}{\sqrt{\pm \beta_1} + \sqrt{\pm \beta_2}} \right|$$

(ii) $a_1' > 1 > a_2'$

$$I = \frac{2}{\sqrt{-\beta_1 \beta_2}} \left\{ \tan^{-1} \left(\frac{a_1'}{a_2'} \sqrt{-\frac{\beta_2}{\beta_1}} \right) - \tan^{-1} \sqrt{-\frac{\beta_2}{\beta_1}} \right\}$$

(iii) $a_1' \geq a_2' = 1$ (When $1 = a_1' \geq a_2'$, α_1' is replaced by α_2' .)

$$I = 2/(a_1' + 1)$$

where, $\beta_1 \equiv a_1'^2 - 1$, $\beta_2 \equiv a_2'^2 - 1$.

(8.46)

Fig. 8.9 shows the coefficient I as a function of α_1' with parameter of $\gamma \equiv \alpha_2/\alpha_1$. Of course, the larger the permeability K becomes (or the smaller α_1' becomes), the larger the coefficient I becomes, and consequently the larger induced stress is generated.

Well, the mean velocity distribution of the main flow is given by the velocity defect law, as follows:

$$\frac{U - U_{max}}{U_\infty} = \frac{1}{\kappa} \ln \left(\frac{y + \delta}{h + \delta} \right) \dots \dots \dots (8.47)$$

where, δ is the experimental constant which corresponds to the 'displacement height' of roughness elements (It has been discussed in 2.5.) Assuming that (8.47) is valid up to the position of $y=0$, we can obtain $(dU/dy)_{y=0} = U_\infty/\kappa\delta$ \dots \dots \dots (8.48).

Next, according to many previous experimental results, the wall-pressure intensity p_0' is proportional to the wall shear stress τ_0 . That is, $p_0' = a \tau_0$ \dots \dots \dots (8.49)

where, the coefficient a is a function of the wall roughness k_S^+ and the Reynolds number Re , i. e. : $a = G(Re, k_S^+)$ from (4.34).

The integral time scale \bar{Z} can be approximately given by $\bar{x} \sim 0.4 h / U_0$, since $U_c \bar{x}$ is nearly equal to the macroscale L_x in the main flow *).

From the above considerations, we can obtain the following formula which estimates the induced stress τ_i .

$$\frac{\tau_i}{\tau_0} \approx \frac{0.4 a^2}{\pi(2b_2)} \cdot A_m \cdot \left(\frac{\pi^2 l}{h \xi_0} \right) \left(\frac{U_c}{U_0} \right)^3 \dots\dots\dots (8.50)$$

where, $\xi_0 = \delta / h$.

Fig. 8.5 gives that $b_1 = 0.12$ or $b_2 = 0.16$, and thus $\pi b_1 = 0.38$ or $2b_2 = 0.32$, which are not quite different from each other.

Fig. 8.10 shows the observed values of the coefficient a by Corcos, as a function of Re for the case of smooth bed. According to the experimental results by Willmarth et al., the value of a for the rough bed is by (1.2 - 1.4) times as large as that for the smooth bed. Since our porous roughness is still larger than the roughness of Willmarth et al., we tentatively adopt the values of a for the smooth bed (Corcos) multiplied by 1.4 times, which are shown by a curve in Fig. 8.10.

When the values of a , b_1 or b_2 are reasonably determined, the validity of the estimated formula of (8.50) can be investigated experimentally by measuring the velocity characteristics of main and seepage flows.

*) L_x in the porous-wall turbulence may be the nearly same as that in the rough-wall turbulence. Then, since $L_x/h \approx 0.6\sqrt{F}$ from Fig.4.31, the macroscale in the main flow is given as follows:

$$\bar{L}_x/h \equiv \int_0^1 L_x/h d\xi \approx 0.4 \quad \therefore U_c \bar{x} \sim \bar{L}_x \sim 0.4 h$$

8.3 Experimental consideration

8.3.1 Experimental set-up and procedure

As shown in Fig. 8.11, the glass beads of diameter $d_m=1.25$ cm were set homogeneously on the smooth bed of our open-channel (see Fig. 4.1) for about 10 m distances between the test section. The interval of 1 m long downstream from the test section was covered with a very thin rough-plate (C in Fig. 8.11), by which the main and seepage flows were perfectly separated. Hence, the quantities of main and seepage flows were separately measured by a triangular weir and a flow bucket, respectively. The channel slope and the valve (A) were adjusted so that the main flow might become fully developed and normal. Next, the valve (B) was adjusted so that there might not exist any suction or injection through the porous boundary, that is, (8.7) might be satisfied.

The experiments of three groups have been performed. First group was a solid rough bed, which was made by densely setting the roughness elements by one stratum (Case D, cf. Table 4.1 (c)). Second group was a dense porous bed, which was made by fairly densely setting the roughness elements by three strata (Case E). Then, the thickness h_p of this porous media was nearly equal to 3.4 cm. Lastly, third group was a loose porous bed, which was made by loosely setting the porous elements by five strata (Case F). Then, h_p was also nearly equal to 3.4 cm.

8.3.2 Mean flow characteristics of seepage flow

The porosity n of the media was easily determined by the number density of porous elements, in result $n=0.39$ (Case E) and $n=0.54$ (Case F).

Next, Fig. 8.12 shows the relationship between the seepage velocity q_m and the hydraulic gradient I_e which was determined by 17 manometers. Then, the permeability K and the coefficient C were determined so that (8.7) might coincide with the experimental values. These data are shown in Table 8.1. Surely, a good

agreement between the experimental values and (8.7) is confirmed in Fig. 8.12.

Now, defining the friction factor f_K of seepage flow as follows: $l_s \equiv f_K \cdot (2/\sqrt{K}) \cdot (q_m^2/2g)$ (Darcy-Weisbach type, cf. (2.7)), (8.7) becomes $f_K = R_K^{-1} + C$ (8.51)

Fig. 8.13 shows the relationship between R_K and f_K . Of course, (8.8) becomes $f_K = R_K^{-1}$ (laminar region, Darcy law), while (8.9) becomes $f_K = C$ (turbulent region). As seen in Fig. 8.13, our experiments correspond to the transition region where (8.51) is applicable.

8.3.3 Mean flow characteristics of main flow

In order to evaluate only the effect of the induced stress which is generated on the porous boundary, the hydraulic conditions should be given that the Reynolds number Re and the Froude number Fr are kept to be constant (cf. 4.2). In this study, we have carried out the experiments of three different kinds of Re and Fr for each Case, i.e. Run 1, Run 2 and Run 3. These hydraulic data for experiments are shown in Table 8.2.

Well, the wall shear stress τ_0 or the friction velocity U_* should be evaluated as accurately as possible, since the induced stress is probably not so large. Although the evaluation method of U_* has been already discussed in 4.3.1, (2) log-law method should not be adopted here. It's because the Karman constant κ is not necessarily equal to $\kappa=0.4$. Actually, Chu et al. (1973) have obtained $\kappa=0.27$ in a permeable air pipe flow.

Therefore, we have evaluated the values of U_* from (3) Reynolds-stress method. Fig. 8.14 shows an example of the distribution of Reynolds stress which was measured over the permeable porous bed by the dual-sensor hot-film anemometer. Although there is some scattering of the measured data near the

bed because of the local effect of the roughness elements, these values of $-\overline{uv}/U_*^2$ agree fairly well with (4.20). Consequently, we can conclude that the Reynolds-stress method adopted here is reasonably valid.

Next, Fig. 8.15 shows the velocity defect law of the main flow. A good agreement between the observed values and (8.47) is surely recognized. Consequently, the values of U_0 and (8.48) are reasonably evaluated from (8.47).

In Table 8.2 which summarizes the above results, it should be noticed that the Karman constant κ tends to decrease as the porous bed becomes looser. Well, it is well-known that the Karman constant can be varied by the outer conditions. For example, these phenomena have been observed in flows with suspended materials, with suction or injection (see next chapter) or with loose boundaries. Ippen(1971) pointed out that the Karman constant is varied by the boundary conditions near the bed. That is to say, the Karman constant may decrease as the momentum exchange of turbulence becomes more active near the bed, and vice versa.

8.3.4 Examination of induced stress

The induced stress can be evaluated experimentally by the following method. In the Case D where the seepage flow is negligible, the induced stress is equal to zero, and hence only the wall shear stress τ_0' occurs over the solid rough bed. Next, in the Case E and F where the effect of seepage flow is expected to appear sufficiently, the contribution of the induced stress τ_i is contained in the total wall shear stress τ_0 which is actually observed. Consequently, it is considered that the total wall shear stress τ_0 can be composed of the addition of the wall shear stress τ_0' generated by the wall roughness and the induced stress τ_i generated by the seepage disturbances.

Then,
$$\frac{\tau_i}{\tau_0} = \frac{\tau_0 - \tau_0'}{\tau_0} = \frac{U_*^2 - U_*'^2}{U_*^2} \dots\dots\dots (8.52)$$

The experimental values of the induced stress τ_i evaluated from (8.52) are shown in Table 8.3. The contribution of the induced stress is equal to (5 - 7)% (dense boundary: Case E) and (12 - 14)% (loose boundary: Case F) of the total wall shear stress.

We can here evaluate the coefficient A_m of (8.50) from the above experimental values and (8.50). These calculated values of A_m are also shown in Table 8.3. Although there is some scattering in these data, A_m is nearly equal to constant, that is: its average value is $A_m=0.15$ (from $b_1=0.12$) or $A_m=0.13$ (from $b_2=0.16$).

By the way, Phillips(1967) has evaluated $A_m=0.12$ with deviation of 5% from the jet experiments performed by Townsend, and then he has predicted that the same order value as $A_m=0.12$ could be obtained even if Phillips theory of (8.41) were applied to the other kinds of shear flows.

Consequently, so far as our experimental results are concerned, the prediction of Phillips is valid even in the flow over permeable porous bed. In other words, we can explain fairly successfully the hydrodynamic interaction between main and seepage flows by application of Phillips theory. However, since the estimation formula of (8.50) has some assumptions and experimental constants, the universal conclusion on the induced stress cannot be obtained at present. Further investigations should be carried out in a vegetated open-channel flow, a mountainous river with large relative roughness k_s/h and others, where the interaction between main and seepage flows may occur strongly.

References (Chapter 8)

- 1) Lovera, F. & Kennedy, J. F. : Friction-factors for flat-bed flows in sand channels, Proc. of ASCE, HY-4, pp.1227-1234, 1969.
- 2) Monin, A. S. & Yaglom, A. M. : Statistical fluid mechanics, MIT Press, vol.1, pp.257-327, 1971.
- 3) Miles, J. W. : On the generation of surface waves by shear flows, J. Fluid Mech., vol.3, pp.185-204, 1957.
- 4) Phillips, O. M. : The maintenance of Reynolds stress in turbulent shear flow, J. Fluid Mech., vol.27, pp.131-144, 1967.
- 5) Chu, Y. & Gelhar, L. W. : Turbulent pipe flow with granular permeable boundaries, Ralph M. Parsons Labo., MIT, Report No.148, 1972.
- 6) Arbbahirama, A. & Dinoy, A. A. : Friction factors and Reynolds number in porous media flow, Proc. of ASCE, HY-6, pp.901-911, 1973.
- 7) Corcos, G. M. : The structure of turbulent pressure field in boundary layer flows, J. Fluid Mech., vol.18, pp.353-378, 1964.
- 8) Willmarth, W. W. & Wooldridge, C. E. : Measurements of the fluctuating pressure at the wall beneath a thick turbulent boundary layer, J. Fluid Mech., vol.14, pp.187-210, 1962.
- 9) Lighthill, M. J. : Physical interpretation of the mathematics theory of wave generation by wind, J. Fluid Mech., vol.14, pp.385-398, 1962.
- 10) Ippen, A. T. : A new look at sedimentation in turbulent streams, Jour. of BSCE, vol.58, pp.131-163, 1971.

Chapter 9 Turbulent structure with transpiration*)

9.1 Introduction

In the last thirty years intensive theoretical and experimental research on the turbulent structure with suction or injection ('Transpiration' is a general term for them) has been performed mainly in the fields of aeronautical, mechanical or chemical engineering, in order to establish a practical interest of the control of turbulent flows by suction or injection. For example, the control of flow separation by suction has interested in boundary layer flows, i.e. influence of transpiration on friction factor. Also, the thermal protection by injection has interested in pipe flow, i.e. influence of transpiration on heat-mass transfer.

In the 1950's, Rubesin(1954), Dorrance et al.(1954), Clarke et al.(1955), Black et al.(1958), Dutton(1958) and others proposed the law of the wall, i.e. 'bilog-law' of mean velocity distribution in a transpired boundary layer, although their theoretical and experimental research was still insufficient. In the early 1960's Stevenson(1964), Tennekes(1965), Torii et al.(1965), Mickley et al.(1965) and others tried to establish the velocity defect law and the similarity law with transpiration. In the later 1960's, Kays' group of Simpson et al.(1969) and Julien et al.(1971) and other groups investigated the accelerated turbulent boundary layer with uniform or distributed transpiration.

All the above research is concerned mainly with the mean velocity characteristics in turbulent boundary layer or pipe flow with

*) We have just recently published two papers which deal with these topics in more detail. Paper(I): 'Turbulent structure in permeable open-channel flows with transpiration', *Proc. of JSCE, No.285, pp.45-56, 1979 (in Japanese) or to be published in Trans. of JSCE, 1979 (in English)*. Paper(II): 'Structure of instantaneous Reynolds stress over a permeable open-channel with suction or injection', *Memoirs of Faculty of Engineering, Kyoto University, vol.41, part 3, 1979*. We supplement this chapter by these papers, if necessary. S-symbol is denoted here for supplement.

transpiration. However, the recent research or new intention is probably concerned with the turbulence characteristics with transpiration and the influence of transpiration on the wall-turbulence mechanism or bursting phenomenon. For example, refer to the papers by Andersen et al.(1975)(boundary layer), Schildknecht et al.(1975)(pipe flow) and present authors(1975)(open-channel).

In order to examine the effect of suction or injection on the turbulent structure in open-channel flow, the present chapter firstly establishes the evaluation method of the friction velocity and makes clear systematically the mean velocity distribution, including even the case of strong suction or injection at which relaminarization or separation phenomenon may occur, respectively. Next, the turbulence characteristics such as turbulence intensities, spectral distribution, turbulent energy budget and so on are investigated.

9.2 Theoretical consideration

9.2.1 Basic equations over permeable smooth bed

As shown in Fig. S1, we consider for simplification, (1) fully developed, two-dimensional flow ($W=0$), (2) the transpiration velocity v_0 is given uniformly through the porous smooth bed and it is very small than the main velocity ($U \gg V \sim v_0$), and (3)

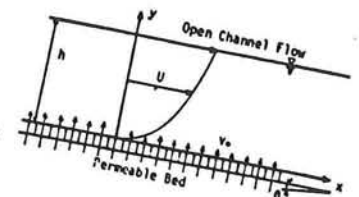


Fig.S1 Open-channel flow over permeable smooth bed

when $v_0=0$, the flow is normal, while even when $v_0 \neq 0$, the flow is quasi-normal. Then, on the boundary condition that $V=v_0$ at $y=0$, the equation of continuity becomes as follows:

$$V = v_0 - \int_0^y \left(\frac{\partial U}{\partial x} \right) dy \quad \dots \dots \dots (9.1)$$

Since (2.4) is still valid because of (2), the following equation for the shear stress $\tau(y)$ is obtained from (2.1) by using (2.4) and (9.1).

$$\frac{\tau}{\rho} = \frac{\tau_0}{\rho} - gI_0 y + v_0 U + \Psi(y) \quad \dots\dots\dots (9.2)$$

where, $\Psi(y) \equiv \frac{d}{dx} \int_0^y U^2 dy - U \frac{d}{dx} \int_0^y U dy \quad \dots\dots\dots (9.3)$

On the boundary condition that $\tau=0$ at $y=h$, (9.2) becomes

$$\tau/\rho = U_*^2(1-\xi) + v_0(U - \xi U_{max}) + \{\Psi(y) - \xi\Psi(h)\} \quad \dots\dots\dots (9.4)$$

$$U_*^2 \equiv \tau_0/\rho = gI_0 h - \frac{d}{dx} \int_0^h U^2 dy \quad \dots\dots\dots (9.5)$$

and $\xi \equiv y/h$.

The second and third terms of (9.4) are the additional ones caused by transpiration v_0 . Of course, when $v_0=0$ (solid bed), these terms become equal to zero, and then (9.4) coincides with (2.5).

In order to evaluate the advection term $\Psi(y)$, we assume that there may exist a similarity law of the mean velocity, that is:

$$U/U_{max} = \eta(y/h) \quad \dots\dots\dots (9.6)$$

Now, denoting that

$$\left. \begin{aligned} Q_1 &\equiv \frac{1}{U_{max}} \frac{d}{dx} (U_{max} h) \\ Q_2 &\equiv \frac{1}{U_{max}^2} \frac{d}{dx} (U_{max}^2 h) \\ \theta_1(\xi) &\equiv \int_0^\xi \eta d\xi \\ \theta_2(\xi) &\equiv \int_0^\xi \eta^2 d\xi \end{aligned} \right\} \dots\dots\dots (9.7),$$

(9.3) becomes $\Psi(y) \equiv \{Q_2 \theta_2(\xi) - Q_1 \eta(\xi) \theta_1(\xi)\} U_{max}^2 \quad \dots\dots\dots (9.8).$

From (9.1) and (9.7), $Q_1 = \frac{v_0}{U_{max} \theta_1(1)}$, $Q_2 = 2Q_1 - \frac{dh}{dx} \quad \dots\dots\dots (9.9).$

By using (9.9), (9.5) can be written as follows:

$$\frac{dh}{dx} = \frac{\sin \theta - (U_*^2/gh) - 2\alpha(v_0 U_m/gh)}{\cos \theta - \alpha F_r^2} \quad \dots\dots\dots (9.10).$$

where, $\alpha \equiv \theta_2(1)/(\theta_1(1))^2$ is the momentum correction coefficient, which becomes equal to $\alpha=1.016$ when the 1/7-power velocity law is applicable, i.e. $\eta \equiv \xi^{1/7}$. $F_r \equiv U_m/\sqrt{gh}$ is the Froude number.

(9.10) is the equation for back-water curves (flow depth profile) in a transpired open-channel flow. When $v_0=0$ (solid bed), (9.10) becomes $U_*^2 = gh_0 \sin \theta$, since the normal flow depth h_0 is formed (where, U_* is the friction velocity when $v_0=0$).

Substituting (9.9) and (9.10) for (9.8), we can obtain

$$\tau^+ \equiv \frac{\tau}{\rho U_*^2} = (1-\xi) + v_0^+ (U^+ - \xi U_{\max}^+) + \phi(\xi) \quad \dots \quad (9.11).$$

The correction term $\phi(\xi) \equiv \Psi^+(\xi) - \xi \cdot \Psi^+(1)$ is calculated as follows: *)

$$\Psi^+(\xi) = \frac{1}{(\cos \theta - \alpha F_r^2)} \left\{ \left(\frac{F_r}{\theta_1(1)} \right)^2 \left(1 - \frac{1}{\Omega} \right) + \frac{2 v_0^+ U_{\max}^+}{\theta_1(1)} \right\} \theta_1(\xi) - \frac{v_0^+ U_{\max}^+}{\theta_1(1)} \cdot \eta \cdot \theta_1(\xi) \quad \dots \quad (9.12)$$

where, $\Omega \equiv (U_*/U_{*0})^2 = \tau/\tau(v_0=0)|_{\xi=0}$ and the (+)-suffix denote the dimensionless quantity by U_* and v , as mentioned previously. Consequently, when the mean velocity distribution $\eta(\xi)$ is known, the correction term $\phi(\xi)$ can be easily evaluated. For example, when the 1/7-power velocity law is applicable, (9.12) becomes for $Fr \ll 1$, as follows: $|\phi(\xi)| = (7/9) |v_0^+ U_{\max}^+ \xi (\xi^{2/7} - 1)| \leq 0.072 v_0^+ U_{\max}^+$, which is fairly small *).

Then, $\tau/\rho \doteq U_*^2 (1 - \xi) + v_0 (U - \xi U_{\max}) \quad \dots \quad (9.15)$

Hence, it is suggested from (9.15) that when injection is given through the permeable bed ($v_0 > 0$), the friction velocity U_* decreases and in an extreme case it will show separation of the flow ($U_* = 0$). However, when suction is given, the friction velocity U_* increases and also the velocity gradient, i.e. the shear stress near the wall increases.

*) If we notice the experimental fact that the gradient of the shear stress at the free surface ($y=h$) is seldom affected by the moderate rate of transpiration, i.e.

$$\frac{d\tau}{dz} \Big|_{\xi=1} = \frac{d\tau(v_0=0)}{dz} \Big|_{\xi=1} = -\rho U_{*0}^2 \quad \dots \quad (9.13),$$

then we can obtain

$$\Psi^+(\xi) = \frac{1}{(1 - \theta_1(1))} \left\{ \left(1 - \frac{1}{\Omega} \right) + \frac{v_0^+ U_{\max}^+}{\theta_1(1)} \right\} \theta_1(\xi) - \frac{v_0^+ U_{\max}^+}{\theta_1(1)} \eta \cdot \theta_1(\xi) \quad (9.14).$$

The difference between (9.12) and (9.14) is negligible in the subcritical flow ($Fr \ll 1$).

Ω becomes nearly equal to zero at $\beta \approx 0.3$, where a separation of the flow may appear. On the other hand, Ω increases for suction, and thus the velocity gradient $dU/dy|_{y=0} = U_*^2/\nu$ also increases. The curves of $v_o^+ = \beta/\sqrt{\Omega}$ vs. β show the characteristics that v_o^+ increases rapidly for injection, while it approaches about -0.1 for suction, where a relaminarization may occur.

Fig. 9.5 shows the relationship between $f = f_o \Omega$ and Re , as a parameter of the transpiration rate $\beta \equiv v_o/U_{*o}$. Of course, when $\beta = 0$ (solid bed), the curve of f vs. Re coincides with Fig. 2.4. f increases for suction, while f decreases rapidly for injection, and such a characteristic is very similar to the friction factor C_f in boundary layer.

Well, we have already established the evaluation method of the friction velocity U_{*o} for a solid bed, as described in 4.3.1. Therefore, when U_{*o} is known, the friction velocity $U_* \equiv \sqrt{\Omega} U_{*o}$ can be easily determined by (9.37) for any transpiration rate $\beta \equiv v_o/U_{*o}$. We call it the β - Ω method.

9.2.6 Some turbulence characteristics

(1) Reynolds stress distribution

When the correction term $\Phi(\xi)$ in (9.11) is negligible, the Reynolds stress is given by

$$\frac{-\overline{uv}}{U_*^2} = (1 - \xi) + v_o^+(U^+ - \xi U_{\max}^+) - \frac{dU^+}{dy^+} \dots \dots \dots (9.39).$$

Fig. 9.6 shows the curves of the Reynolds stress $-\overline{uv}/U_*^2$ which were calculated from (9.18) and (9.39) with the transpiration rate of $v_o^+ = -0.1 \sim 0.1$, for the case of $R_* = 500$ and 2000. The curves of $-\overline{uv}/U_*^2$ for injection increase similarly as compared with solid bed ($v_o = 0$), while they decrease similarly for suction.

However, in order to examine the absolute effect of transpiration on the Reynolds stress, U_* should be replaced by U_{*o} as a characteristic velocity scale, since U_* itself is varied by v_o .

Hence, as a parameter of $\beta \equiv v_o/U_{*o}$ for any Re , Ω is calculated from (9.37), and then $-\overline{uv}/U_{*o}^2$ is calculated from (9.39) with $R_* = \sqrt{f/2} Re$ and $v_o^+ = \beta/\sqrt{\Omega}$. An example of these results is plotted for $Re = 5 \times 10^4$ in Fig. 9.7. The absolute values of the Reynolds stress increase with an enlargement of injection, while they decrease with an enlargement of suction. It should be noticed that these variation characteristics are contrary to those of $U_*^2 = (-\overline{uv} + \nu \partial U / \partial y)_{y=0}$. In other words, U_* increases for suction because the increase of the viscous stress is larger than the decrease of the Reynolds stress, and vice versa for injection.

Surely, as seen in Fig. 9.6 or 9.7, the Reynolds stress in the main region shows nearly a linear distribution, which confirms the validity of (9.31). Now, defining $\gamma \equiv -\overline{uv}/(-\overline{uv})_o$, we can obtain from 9.2.5, as follows: $r \approx \Omega + \phi = \Omega + \beta(25 + \sqrt{2/f_o}) \dots\dots (9.40)$. In contrast with the ratio Ω of the wall shear stress, γ increases for injection, while γ decreases for suction. At $\beta \approx -0.1$ ($v_o^+ \approx -0.08$), γ becomes equal to zero, which means that the production of Reynolds stress in the main region is almost suppressed to change into insufficient turbulent state, i.e. relaminarization, as pointed out previously.

By the way, the more accurate examination so that the correction term $\Phi(\xi)$ was taken into account, is given in Paper (I) and (II). However, its basic results are the same as the above.

(2) Turbulent energy budget

The turbulent energy production P is given by

$$\frac{P_h}{U_*^3} = R_* \left(\frac{-\overline{uv}}{U_*^2} \right) \left(\frac{dU^+}{dy^+} \right) \dots\dots\dots (9.41).$$

Fig. 9.9 shows the absolute variations of P which were calculated from (9.41) by using (9.18) and (9.39). Except for near the wall, the turbulent production P also increases with an enlargement of injection, while it decreases with an enlargement of suction.

On the other hand, the opposite variation characteristics appear near the wall. It's because the Reynolds stress increases for injection, while the viscous stress increases for suction, as compared with no-transpiration ($v_0=0$).

Well, in the same manner as (2.27), the equation of turbulent energy with transpiration is given by

$$P = \epsilon + \frac{\partial}{\partial y} \left\{ \left(\frac{\overline{q^2}}{2} + \frac{p}{\rho} \right) \nu - \nu \frac{\partial}{\partial y} \left(\frac{\overline{q^2}}{2} \right) \right\} + U \frac{\partial}{\partial x} \left(\frac{\overline{q^2}}{2} \right) + \nu \frac{\partial}{\partial y} \left(\frac{\overline{q^2}}{2} \right) \dots (9.42).$$

Since the advection term (the 4-th and 5-th terms) is the same order as $\nu_0 \partial/\partial y (\overline{q^2}/2)$, (9.42) can be approximated when R_* is large, as follows:

$$P = \epsilon + \frac{\partial}{\partial y} \left\{ \frac{\overline{q^2}}{2} (\nu + \nu_0) + \frac{p\nu}{\rho} \right\} \dots (9.43).$$

By newly defining the turbulent diffusion T_T as $T_T \equiv \overline{(\nu + \nu_0)q^2/2}$, (9.43) coincides with (2.30). Although (9.42) or (9.43) is not directly examined in this chapter, it is suggested that T_T/U_*^3 may be the same order as $(1+4\beta)$, since $\overline{q^2}/2U_*^2 \lesssim 4$ and $\overline{q^2}\nu/2U_*^3 \lesssim 1$ (see Chapter 4). Consequently, the dissipation ϵ may be mainly balanced by the production P , although the diffusion $\partial T_T/\partial y$ may increase with an enlargement of injection because of $(\partial \overline{q^2}/\partial y) \nu_0 < 0$, and vice versa for suction (cf. Fig. 4.38). This suggests strongly that except for very near the wall, there may not be a drastic change in the transpired turbulent structure, as compared with the solid-turbulence.

In the same manner as 2.2.1, the absolute variations of the production P and the direct-dissipation E are given by

$$\left. \begin{aligned} P_0^+ &\equiv P\nu/U_*^4 = P^+ \cdot \Omega^2 \\ E_0^+ &\equiv E\nu/U_*^4 = E^+ \cdot \Omega^2 \\ y_0^+ &\equiv y U_*^3/\nu = y^+/\sqrt{\Omega} \end{aligned} \right\} \dots (9.44).$$

Fig. 9.10 shows the results of (9.44) near the wall. The total energy loss \mathcal{E} of mean flow is given from (9.22) and (9.39), as follows:

$$\mathcal{E} = \int_0^A (E + P) dy = U_*^2 U_m + \frac{\nu_0}{2} \left\{ U_m^2 - \left(\frac{U_*}{\kappa} \right)^2 \right\} \dots (9.45).$$

(9.45) corresponds to (2.8) or (2.9). Defining $\zeta \equiv \bar{\epsilon}/\epsilon_0$ (where $\bar{\epsilon}_0$ is the value at $v_0=0$), (9.45) becomes

$$\zeta = \Omega + \frac{1}{2} \beta \sqrt{\frac{f_0}{2}} \left\{ \left(\frac{2}{f_0} \right) - \frac{\Omega}{\kappa^2} \right\} \dots\dots\dots (9.46)$$

where, $\kappa^{-1} \equiv 2.5 (1 + 9.2 \beta / \sqrt{\Omega})$.

The values of ζ are shown in Fig. 9.8. For the moderate transpiration of $|\beta| < 0.1$, ζ is nearly equal to constant, irrespective of v_0 and Re.

From Fig. 9.10 and the characteristic of $\zeta \approx 1$, it is considered that in the case of injection the increase of the turbulent production is nearly balanced by the decrease of the direct-dissipation, and vice versa in the case of suction. Also, it should be noticed that such a relationship between P and E changes inversely at the edge of viscous sublayer, i.e. $y_0^+ \approx 10$.

9.3 Experimental consideration on mean velocity distribution

9.3.1 Experimental set-up and procedure

Fig. 9.11 (a) shows the experimental set-up in which the recirculating tilting flume is 15 m long, 50 cm wide and 30 cm deep. About 9 m downstream from the channel entrance, an apparatus of transpiration flow was set up (see Fig. 9.11 (b)), whose porous plate made of sintered plastics of 0.65 mm diameter was 104 cm long, 49 cm wide and 1.5 cm thick. In order to uniformly give any transpiration velocity v_0 , a buffer zone made of glass beads and eight orifices of 25 mm diameter were set in the transpiration tank, as shown in Fig. 9.11 (b). Through the preliminary experiments, it was recognized that a fully developed turbulent flow was obtained at the test section 84 cm downstream from the upstream edge of the porous plate.

The mean velocity distributions were measured in detail by a single-sensor hot-film anemometer (DISA 55A83, see Fig. 3.3).

Four kinds of experiments were performed (Case H-1, H-2, H-3 and H-4), as described in Table 9.1. Case H-1 and H-4 were the most important experiments, which correspond to Case A-1 and G-1 in Table 4.1, respectively. In the case of H-1, H-2 and H-3, two injections and two suction were given. In the case of H-4, three injections and three suction were given. The maximum quantity Q_t of these transpirations was less than the 10% of the main flow quantity Q .

By the way, we (Paper(I)) have recently carried out the re-experiments in which the more transpiration rates were given, as described in Table S1. This chapter is supplemented by these results of Table S1, if necessary, in the following sections.

Table S1 Hydraulic data for experiments with suction or injection

Case	$v_0=0$ (Without transpiration flow **** Run 1)							
	h (cm)	U_n (cm/sec)	U_{s0} (cm/sec)	R_{s0} $=U_{s0}h/\nu$	Re $=U_n h/\nu$	Fr $=U_n/\sqrt{gh}$	S slope	Q (l/sec)
H-1	8.02	15.1	0.804	609	1.15×10^4	0.17	0.08×10^{-4}	6.05
H-2	4.25	28.3	1.369	564	1.16	0.44	5.71	6.00
H-3	3.40	35.4	1.907	614	1.14	0.61	12.84	6.02

$v_0 \neq 0$ (With transpiration flow)											
Case H-1											
Run	15	14	13	9	8	1	4	5	10	11	12
U_w	1.760	1.585	1.316	1.146	0.980	0.804	0.641	0.523	0.373	0.271	0.193
β	-0.243	-0.202	-0.137	-0.094	-0.050	0.0	0.049	0.089	0.148	0.198	0.249
v_w^+	-0.111	-0.102	-0.084	-0.066	-0.041	0.0	0.062	0.136	0.319	0.589	1.036
Q_t/Q	-12.6%	-10.5	-7.1	-4.9	-2.6	0.0	2.5	4.6	7.7	10.2	12.9

Case H-2					Case H-3					
Run	9	8	1	4	5	8	7	1	4	5
U_w	2.066	1.684	1.369	1.062	0.799	2.307	2.166	1.907	1.509	1.147
β	-0.111	-0.052	0.0	0.056	0.111	-0.047	-0.031	0.0	0.051	0.104
v_w^+	-0.074	-0.042	0.0	0.072	0.189	-0.039	-0.027	0.0	0.065	0.172
Q_t/Q	-9.9%	-4.6	0.0	5.0	9.9	-5.8%	-3.8	0.0	6.3	12.8

9.3.2 Wall shear stress or friction velocity

Fig. 9.12 and Fig. S3 show an example of the measured values of mean velocity, U/U_{max} vs. y/h . For injection, the lower velocity region is lifted up from the wall, while for suction the higher velocity region is attracted toward the wall. Surely, the effect of transpiration on the

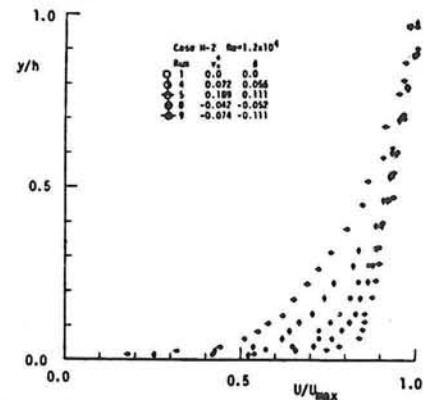


Fig. S3 Mean velocity distribution with suction or injection

turbulent structure is recognized remarkably near the wall, even when $\beta \equiv v_o/U_{*o}$ is below ± 0.1 .

Well, in our previous research (this doctoral dissertation, 1977), the friction velocity U_* could be evaluated by the extended methods of (2) and (3) in 4.3.1. In the (2) log-law method, the friction velocity U_* was determined by (9.22), where the Karman constant κ was given by (9.24). On the other hand, in the (3) Reynolds-stress method, the friction velocity \hat{U}_* was determined by comparing (9.39) with the measured Reynolds stress distributions.

Fig. 9.13 shows the results evaluated by both these methods. In this experiments, they agree with each other within the error of $|U_* - \hat{U}_*|/\hat{U}_* \leq 15\%$. Fig. 9.14 shows the variation of U_* vs. β , together with the theoretical curves of (9.37). Also, a good agreement between the experimental and theoretical values is recognized in Fig. 9.14.

In the consideration of the above, we could conclude in Paper (I) that the β - Ω method described in 9.2.5 is the most reasonable and the easiest for evaluation of U_* , because (9.37) is really valid. The values of U_* described in Table S1 were determined by this β - Ω method.

9.3.3 Mean velocity distribution

Fig. 9.15 shows the dimensionless mean velocity distribution $U^+ = U/U_*$ in the case of H-1 and H-4 (old data). These experimental values agree fairly well with the theoretical curves of (9.18) or the bilog-law of (9.21).

Now, Fig. S5 shows the dimensionless mean velocity distribution with injection in the case of H-1 (new data). Run 1 is a case without transpiration, i.e. $v_o=0$, whose data coincide very well with the well-known law of the wall proposed by van Driest or the Prandtl-Karman log-law. The experimental values with injection also show a good agreement with the theoretical curves of (9.18)

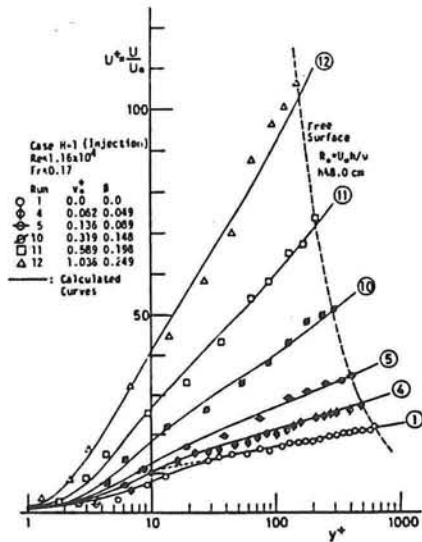


Fig.S5 Dimensionless mean velocity distribution U^+ with injection (Case H-1) (the law of the wall)

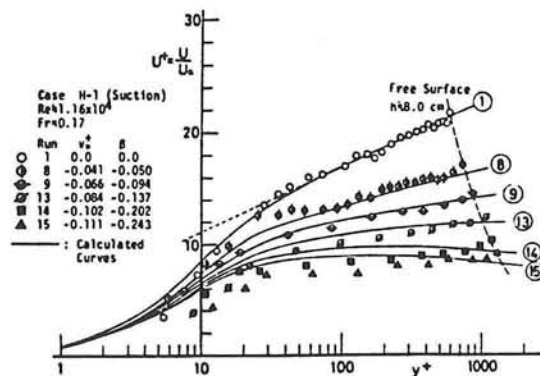


Fig.S6 Dimensionless mean velocity distribution U^+ with suction (Case H-1) (the law of the wall)

throughout the whole region from the bed up to the free surface. That is to say, it is confirmed that the mixing-length model of (9.17) is valid even in the case of an open-channel flow with injection. Above all, even in the case of the large injection rate $v^+ \approx 1$ where separation characteristics may appear, a good agreement is recognized. Also, an examination of validity of (9.32) is shown in Fig. 9.16. Surely, (9.32) agrees fairly well with the observed values. Then, it is obtained that $\kappa_0 = 0.33$, whose value is less than $\kappa_0 = 0.4$. The value of D^* shows a decrease with an enlargement of injection, as predicted from (9.33).

On the other hand, Fig. S6 shows the mean velocity distribution U^+ with suction obtained at the same hydraulic condition as Fig. S5. It should be noticed that, although the agreement between the observed and the calculated values is still good at the moderate suction rate, the disagreement between them appears in larger suction rates such as Run 14 and Run 15.

In the same manner, Fig. S7 shows the mean velocity distribution for Case H-2 (new data). The experimental values also show a very good agreement with the theoretical curves of (9.18) throughout the whole region. For Case H-3, a good agreement between them was recognized, too.

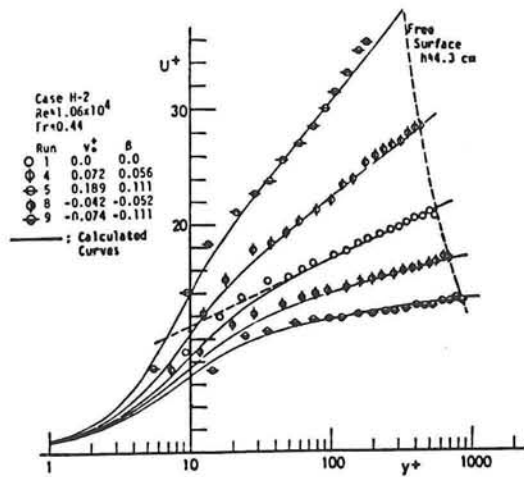


Fig.S7 Dimensionless mean velocity distribution with suction or injection (Case H-2)

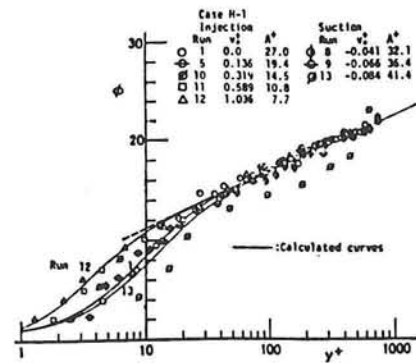


Fig.S8 Bilog-law of mean velocity

Fig. 9.17 shows the bilog-law for Case H-1 (old data). Fig. S8 also shows it for Case H-1 (new data). In Run 14 ($v_o^+ = -0.102$) and Run 15 ($v_o^+ = -0.111$), the experimental values of ϕ can't be calculated because $(v_o^+ U^+ + 1) < 0$. The data in Run 13 ($v_o^+ = -0.084$) don't also agree with the theoretical curves derived from the mixing-length model, i.e. the bilog-law. On the other hand, the experimental values in all runs of injection and some runs of the moderate suction of $|v_o^+| \leq -0.08$ agree very well with the bilog-law. Above all, it should be noticed that ϕ vs. y^+ is a universal curve in the region of $y^+ \geq 30$ irrespective of transpiration, as described by (9.21).

Lastly, we examine the expression of $|v_o^+ U^+|$ vs. $|v_o^+ y^+|$ which was proposed by Tennekes (1965), on the basis of a similarity law. Fig. 9.18 shows the values of $|v_o^+ U^+|$ for suction, by a semi-log plot. The solid curve in Fig. 9.18 is the curve of (9.20). As $|v_o^+ y^+|$ becomes smaller, the values of $|v_o^+ U^+|$ approach the curve of (9.20), which confirms the existence of the viscous sublayer with suction. Tennekes proposed the following formula for the 'moderate' suction rate of $-0.1 < v_o^+ < -0.04$.

$$|v_o^+ U^+| = C_1 \ln |v_o^+ y^+| + C_2 |v_o^+|, \quad (-0.1 < v_o^+ < -0.04) \quad \dots \dots (9.47)$$

He obtained $C_1=0.06$ and $C_2=11$ in a transpired boundary layer. As seen in Fig. 9.18, (9.47) also shows a good agreement with our experimental values, from which $C_1=0.05$ and $C_2=12$ are obtained. It is also confirmed that (9.47) agrees fairly well with (9.22) at the 'moderate' suction rate, and then κ becomes equal to $\kappa=-v_0^+/C_1$.

On the other hand, although the Tennekes expression is still unknown for injection, Fig. 9.19 shows the values of $v_0^+U^+$ for injection, tentatively by a log-log plot. Then, the following relation may be satisfied.

$$v_0^+U^+ = C_3 \cdot (v_0^+ y^+)^n \quad (v_0^+ > 0) \quad \dots\dots\dots (9.48)$$

From Fig 9.19, $n=1/7$ and $C_3=15.7$ are obtained. Hence, it is understood that the 1/7-power velocity law is valid for injection.

9.3.4 Examination of the variation of flow depth in the streamwise direction (backwater curve)

In order to conclude more clearly the validity of bi-log law when $v_0^+ > -0.084$ which was shown in the previous section, the friction velocity U_* should be evaluated independently of the β - Ω method, since the β - Ω method itself was derived from the bilog-law. This examination

can be done by (1) the variation of dh/dx and (2) the Reynolds stress distribution. Of course, these (1) and (2) correspond to the methods of (1) and (3) in 4.3.1, respectively. The Reynolds stress distribution will be described later.

Now, Fig. S9 shows the experimental values of $\Delta h \equiv (h-h_0)$ for each run of Case H-1. As mentioned frequently, it may be impossible to determine U_* accurately from these data of Δh by using (9.10). On the contrary, we here calculate the values of $\partial\Delta h/\partial x$

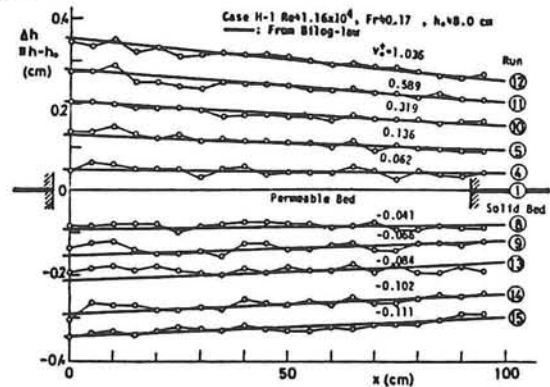


Fig.S9 Variation of flow depth with suction or injection

from (9.10) by using U_* evaluated by the β - Ω method. These calculated values are shown by solid line in Fig. S9.

Although there is some scattering in the observed data, they agree fairly well with the calculated curves of (9.10). Consequently, we can surely conclude the validity of the β - Ω method and the bilog-law.

9.3.5 Relaminarization by the strong suction

From the above consideration, it has been clarified that the mean velocity distribution in an open channel with transpiration except for the strong suction satisfies the bilog-law or the mixing length model fairly well throughout the flow depth. On the contrary, as the suction rate becomes stronger, the main flow cannot keep the fully developed turbulent state any longer and consequently a relaminarization may occur, as mentioned previously. It is well known that such a relaminarization also occurs in a boundary layer with a strongly favourable pressure gradient ($dp/dx < 0$, Fig. 9.3). Hence, it is desirable to explain these relaminarization phenomena systematically.

By the way, Huffman et al. (1972) pointed out that the outer boundary conditions such as transpiration and pressure gradient, affected the inner layer primarily via the shear stress gradient $\partial\tau/\partial y$ in the inner layer. In the same manner as they did, the average value of $\partial\tau/\partial y$ over the wall region of $0 \leq y^+ \leq \delta^+ = 100$ is now defined by $\langle \partial\tau/\partial y \rangle$. Then, the following relation is obtained from (9.11).

$$-\left\langle \frac{\partial\tau^+}{\partial y^+} \right\rangle = -\frac{v_*^+ U^+(\delta^+)}{\delta^+} + \frac{1 + v_*^+ U_{max}^+}{R_*} - \frac{\phi(\delta^+)}{\delta^+} \dots \dots \dots (9.49)$$

Fig. S10 shows the curves of (9.49) for various Froude numbers.

Although the detailed discussion is omitted here (see Paper(I)), the

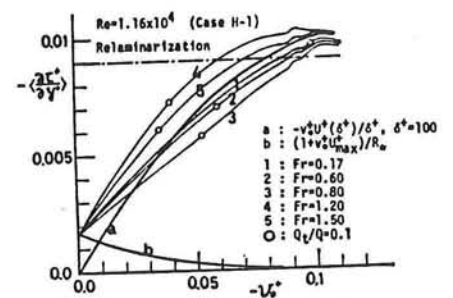


Fig.S10 Average gradient of the shear stress S10

critical value $v_0^+ \approx -0.085$ for relaminarization corresponds to $\langle \partial \tau^+ / \partial y^+ \rangle \approx -0.009$ in the case of small Froude number.

On the other hand, Patel et al. (1968) also discovered that the relaminarization of accelerated turbulent flow occurred at a critical value of shear stress gradient, independently of overall Reynolds number. That is, when the shear stress could be described by

$$\tau = \tau_0 + \alpha y \quad \dots (9.50),$$

then its critical value was given by a parameter of $A_r \equiv \nu \alpha / \rho U_*^3 = -0.009$. This value is equal to $\langle \partial \tau^+ / \partial y^+ \rangle_c \approx -0.009$, which is very remarkable.

Next, Fig. S11 shows the relation of the damping factor A^+ against $-\langle \partial \tau^+ / \partial y^+ \rangle$ in an open channel, which was calculated by (9.18), (9.19) and (9.49) for four kinds of Reynolds numbers. Fig. S11 also shows the observed values in wall jet, closed channel and boundary layer, which were cited by Huffman et al. (1972). It should be noticed that A^+ increases rapidly at the critical value of $\langle \partial \tau^+ / \partial y^+ \rangle = -0.009$. Thus, the viscous effect becomes very remarkably, that is, the relaminarization may occur. When $v_0 = 0$ (solid bed),

(9.49) becomes $-\langle \partial \tau^+ / \partial y^+ \rangle = 1/R_*$. Hence, if $\langle \partial \tau^+ / \partial y^+ \rangle_c \approx -0.009$, R_{*c} becomes equal to 111 or $Re_{*c} = 111(U_m/U_*) \approx 2000$, whose value corresponds to the critical Reynolds number for the solid bed.

Lastly, Fig. S12 shows the relation of A^+ vs. v_0^+ , together with the experimental curves obtained in a transpired boundary layer. The damping factor A^+ decreases with an enlargement of injection,

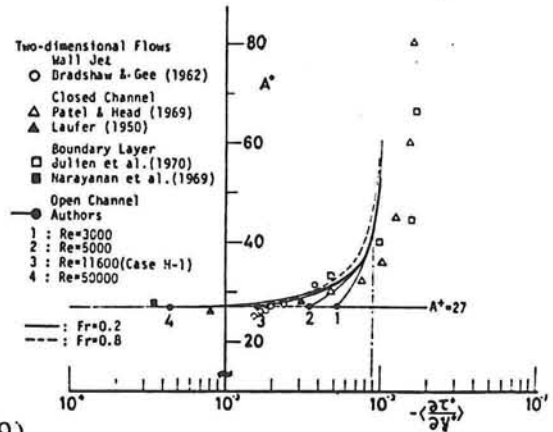


Fig.S11 Relation of A^+ vs. $-\langle \partial \tau^+ / \partial y^+ \rangle$

S11

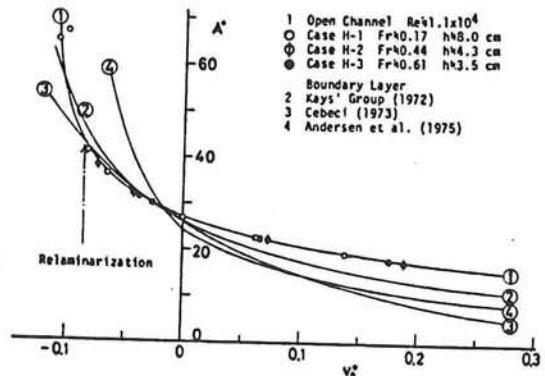


Fig.S12 Variation of A^+ against v_0^+

S12

while it increases rapidly with an enlargement of suction.

The experimental curve of (1) for an open channel is nearly given by

$$A^+ \begin{cases} = 27/(1+4.1 v_0^+) & (v_0^+ < 0) \\ = 27/(1+2.7 v_0^+) & (v_0^+ > 0) \end{cases} \dots\dots\dots (9.51).$$

9.4 Experimental consideration on turbulence characteristics

9.4.1 Reynolds stress distribution

Fig. 9.20 shows the distributions of the Reynolds stress for Case H-1 and H-4 (old data), which were measured by dual-sensor hot-film anemometers in the same manner as Part 1. Although there is comparatively large scattering in the measured data, they show a fairly good agreement with the theoretical curves of (9.15).

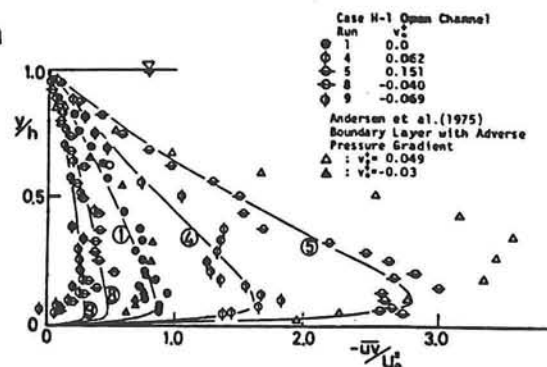


Fig.S13 Reynolds stress distribution
S13

Fig. S13 also shows the distribution of the Reynolds stress for Case H-1 (new data), together with the theoretical curves of (9.11), which is more exact than (9.15). Surely, the experimental values agree fairly well with the theoretical curves, though there is some deviation near the wall for suction. This deviation may have been caused by the partially suppressed turbulence and the experimental error. Actually, the more detailed examination of the Reynolds stress characteristics is given in Paper (II).

9.4.2 Turbulence intensities

Fig. 9.21 shows the turbulence intensity u'/\hat{U}_* for Case H-1 and H-4 (old data). Fig. 9.22 and 9.23 show the turbulence intensities v'/\hat{U}_* and w'/\hat{U}_* , respectively, for Case H-1 (old data). Also, Fig. S14 (a), (b) and (c) show the values of u'/U_* , v'/U_* and w'/U_* , respectively, for Case H-1 (new data and replotting of old data). Since these turbulence intensities are varied nearly

Acknowledgements

The author wishes to express his foremost acknowledgement to Dr. Hiroji Nakagawa, Hydraulics Professor of Civil Engineering, Kyoto University, whose invaluable guidance, patience and encouragement made this work possible. Thanks are also extended to some graduate students in our hydraulics laboratory for their aid in the performance of the experiments

Academic career

During 1967-1971, I studied Civil Engineering in Kyoto University. During 1971-1976, I researched Hydraulics in the master and doctor courses of graduate school in Kyoto University.

On January 23, 1978, I obtained Doctor of Engineering in Kyoto University.

At the present (July, 1979), I am a lecturer in Civil Engineering of Kyoto University.

On July 30, 1979

Iehisa NEZU
Iehisa Nezu
Kyoto, JAPAN

TURBULENT STRUCTURE IN OPEN-CHANNEL FLOWSCONTENTS
(FIGURES AND TABLES)

	<i>Page</i>
PART 1 TURBULENT STRUCTURE OVER SOLID BED	
<i>Chapter 1</i> Introduction	1
<i>Chapter 2</i> Theoretical consideration on turbulent structure	2
<i>Chapter 3</i> Method of turbulence measurement and its analysis	8
<i>Chapter 4</i> Experimental consideration on turbulent structure and energy budget	13
<i>Chapter 5</i> Experimental consideration on mechanism of turbulence-production	30
<i>Chapter 6</i> Physical model of wall turbulence	43
PART 2 TURBULENT STRUCTURE OVER PERMEABLE BED	
<i>Chapter 7</i> Introduction	
<i>Chapter 8</i> Interaction between main and seepage flows	50
<i>Chapter 9</i> Turbulent structure with transpiration	54

TURBULENT STRUCTURE IN OPEN-CHANNEL FLOWS

Part 1 Turbulent structure over solid bed

Chapter 1 Introduction

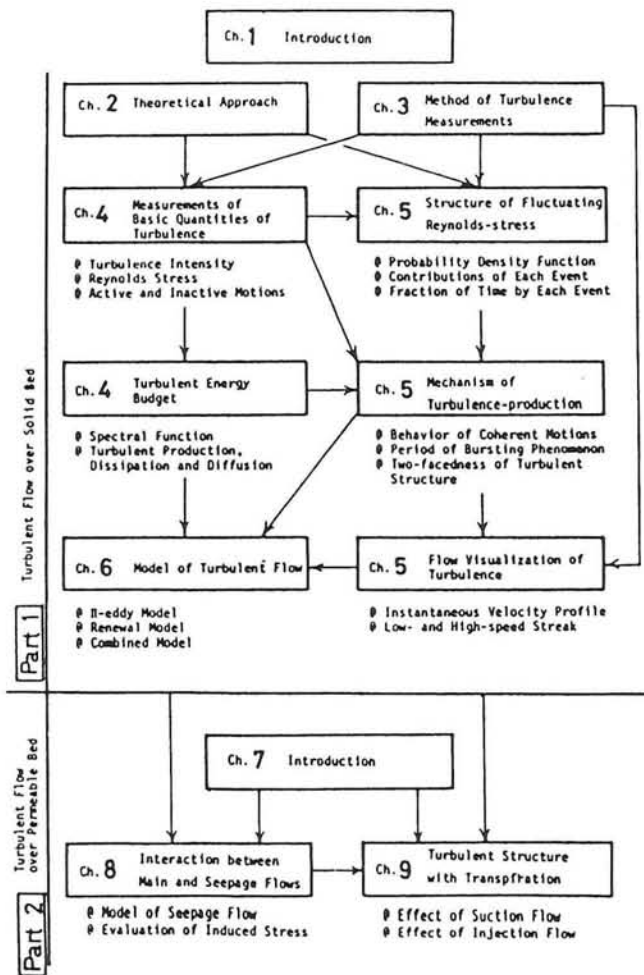


Fig. A Intention of this paper and its construction.

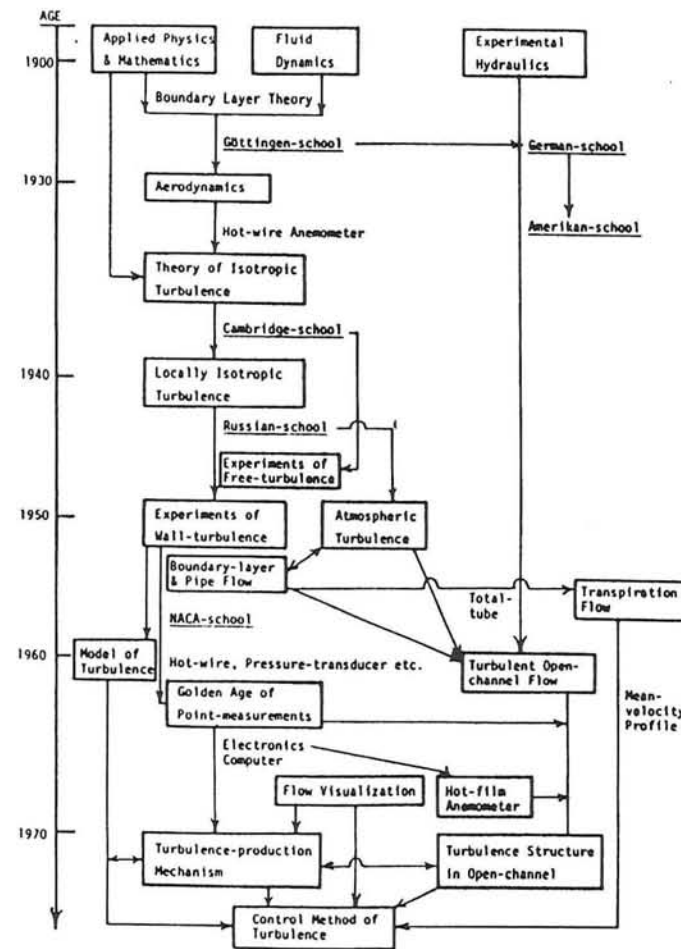


Fig. 1.1 History of researches of turbulence.

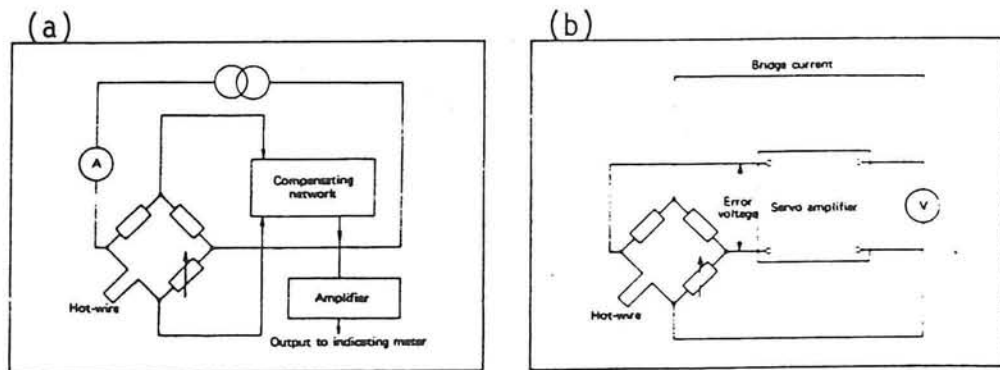


Fig. 3.1 (a) constant-current and (b) constant-temperature anemometers.

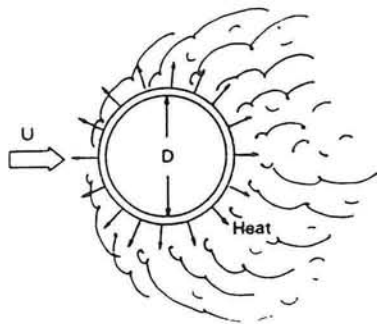
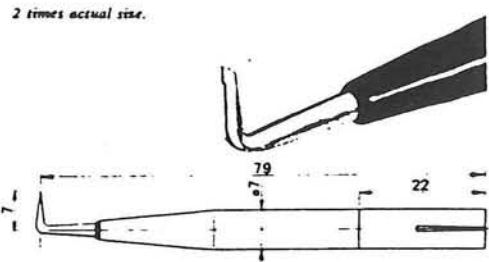


Fig. 3.2 Heat transfer from cylindrical hot-film sensor.



DISA 55A83

Fig. 3.3 Single-sensor hot-film probe (DISA-made).

DUAL-SENSOR HOT-FILM PROBES DISA 55A89

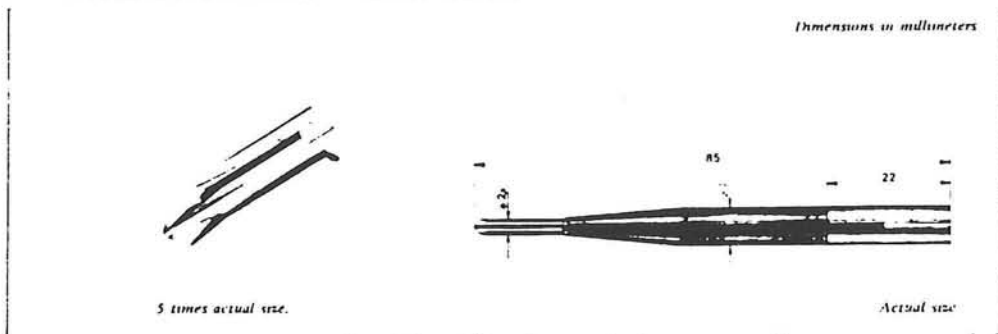


Fig. 3.4 Dual-sensor hot-film probe (DISA-made).

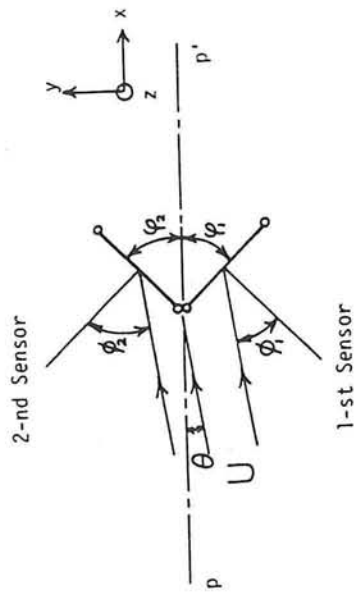
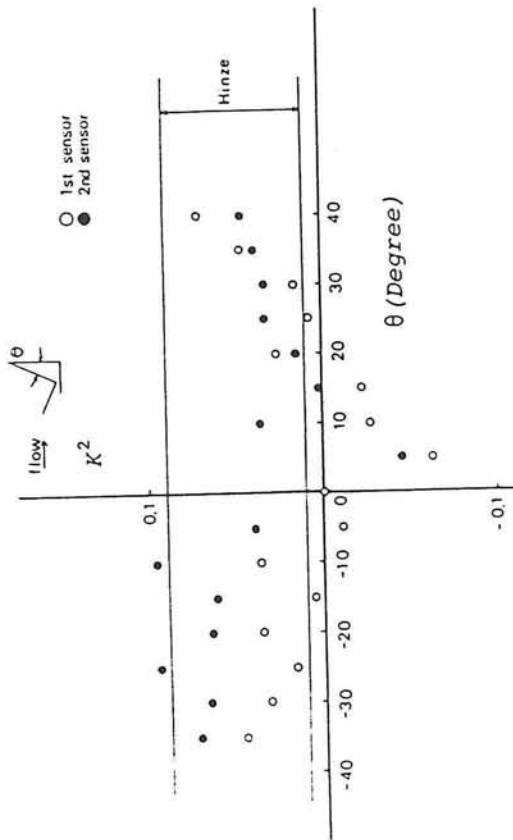


Fig. 3.5 Effect of flow direction on V-type sensors.

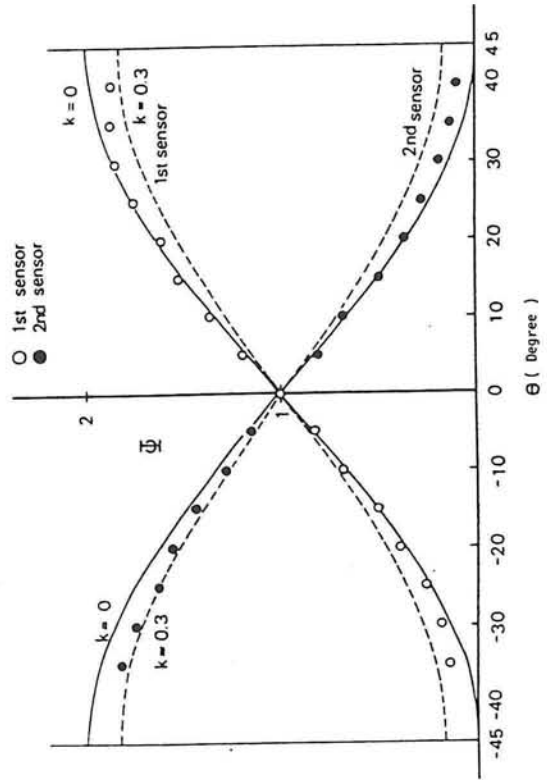


Fig. 3.6 Directional sensitivity of dual-sensors $\psi(\theta)$.

Fig. 3.7 Directional sensitivity factor k .

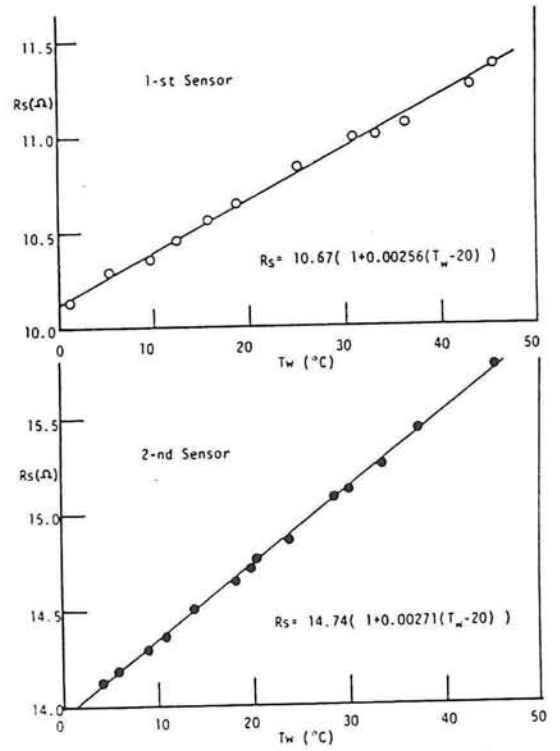


Fig. 3.8 Temperature characteristics of resistance of each sensor.

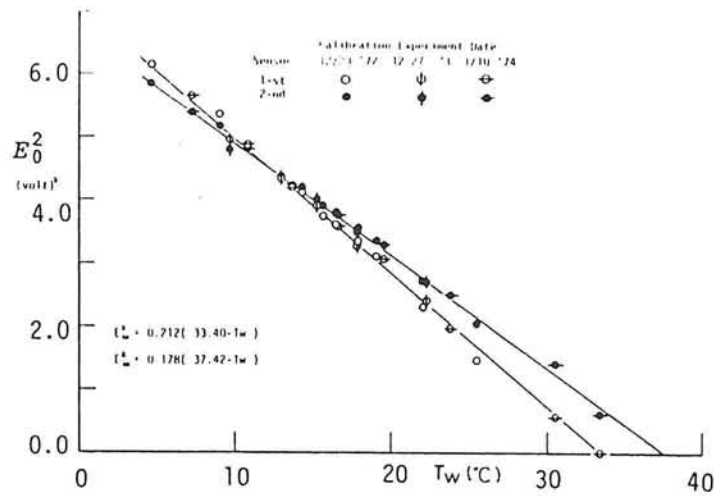


Fig. 3.9 Output voltages of anemometers in still water.

10

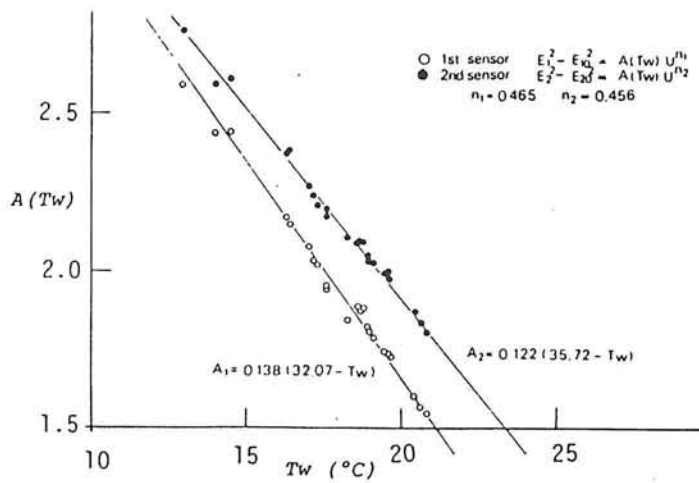


Fig. 3.11 Temperature characteristics of calibration coefficient $A(T_w)$.

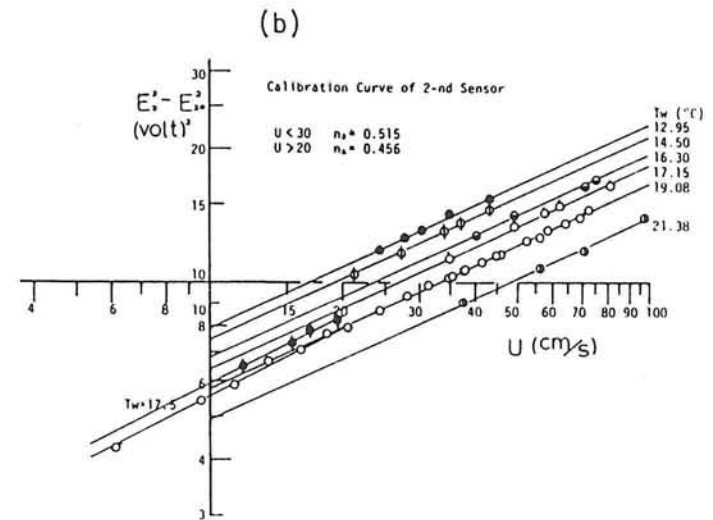
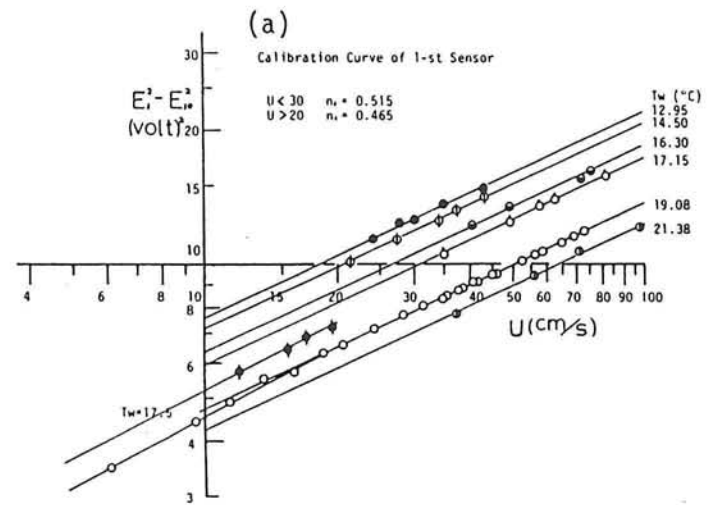


Fig. 3.10 Calibration curves of dual-sensor.

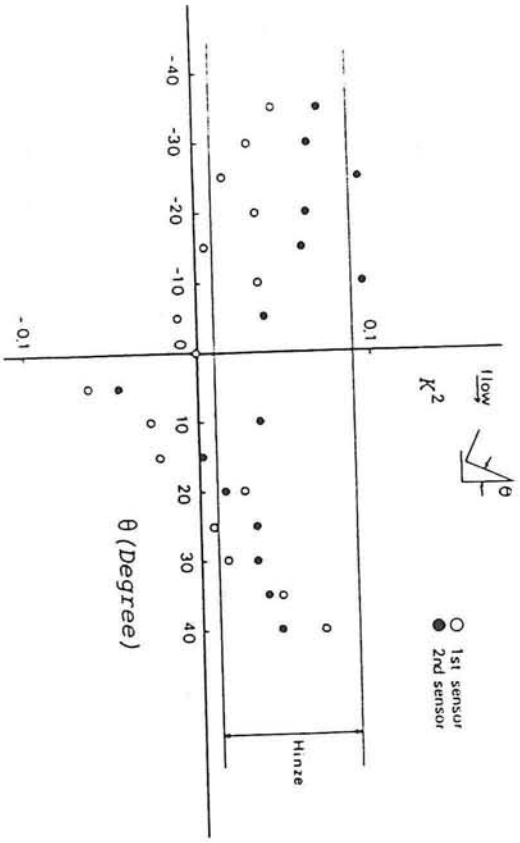


Fig. 3.5 Effect of flow direction on V-type sensors.

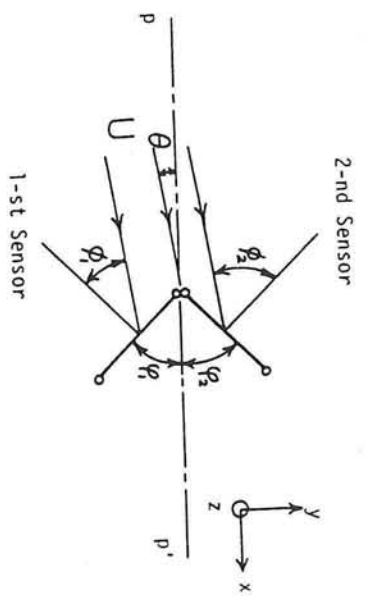


Fig. 3.7 Directional sensitivity factor k .

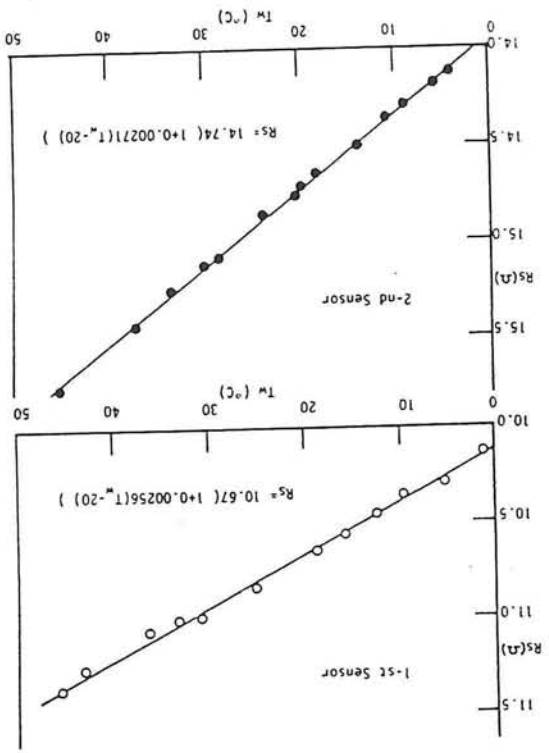


Fig. 3.8 Temperature characteristics of resistance of each sensor.

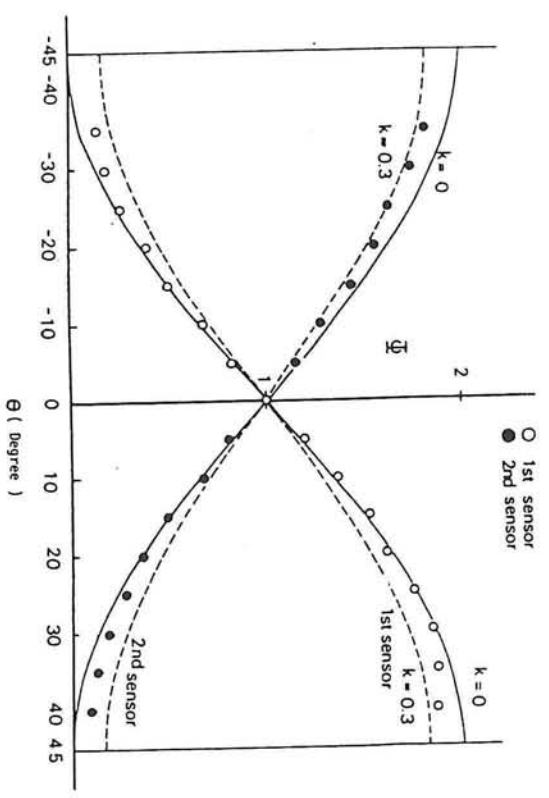


Fig. 3.6 Directional sensitivity of dual-sensors $\psi(\theta)$.

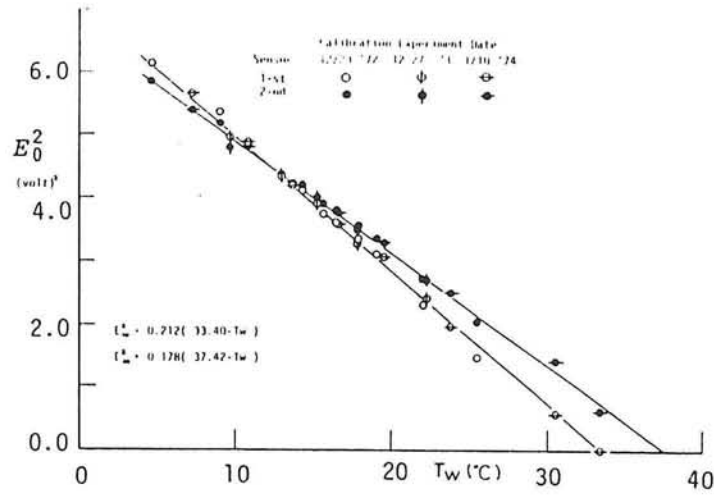


Fig. 3.9 Output voltages of anemometers in still water.

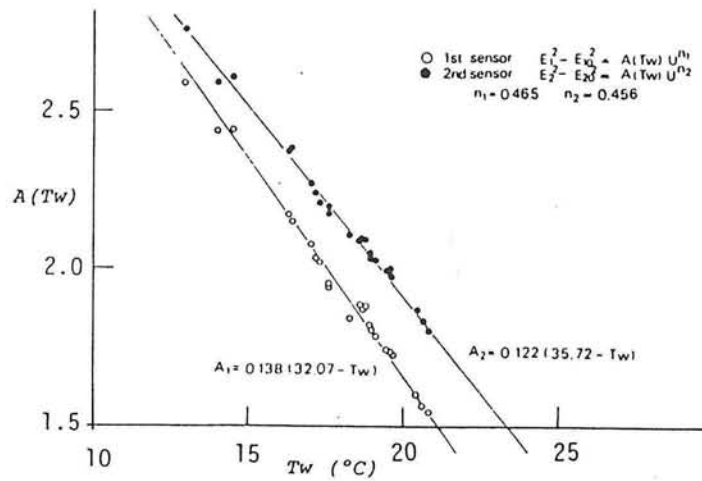


Fig. 3.11 Temperature characteristics of calibration coefficient $A(T_w)$.

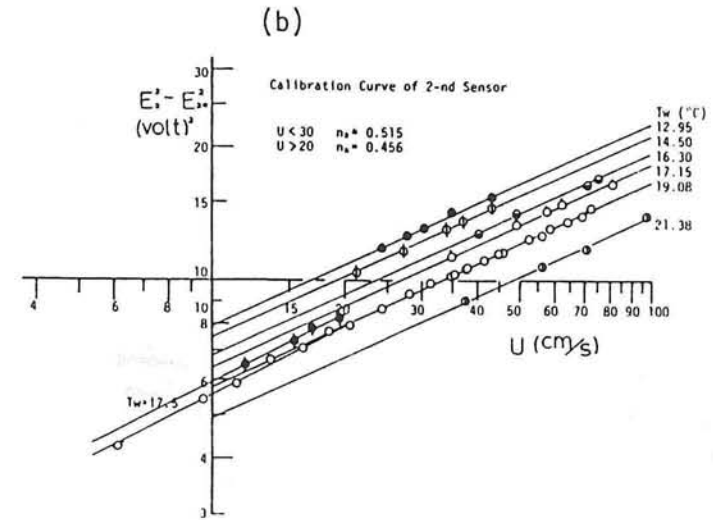
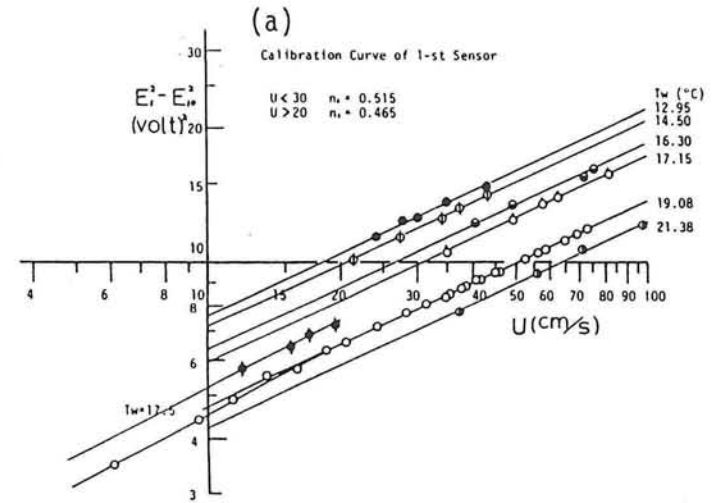


Fig. 3.10 Calibration curves of dual-sensor.

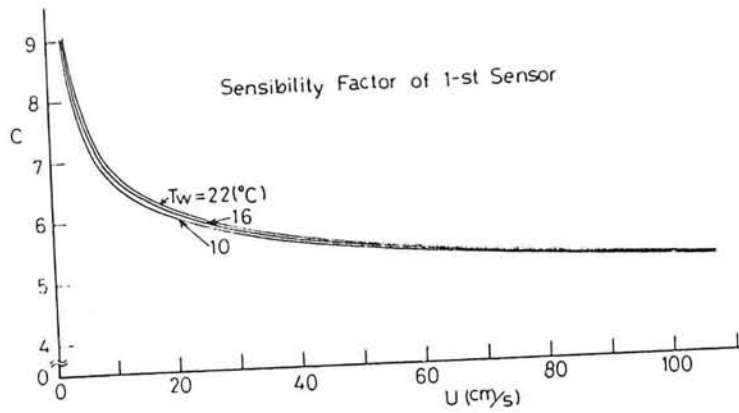
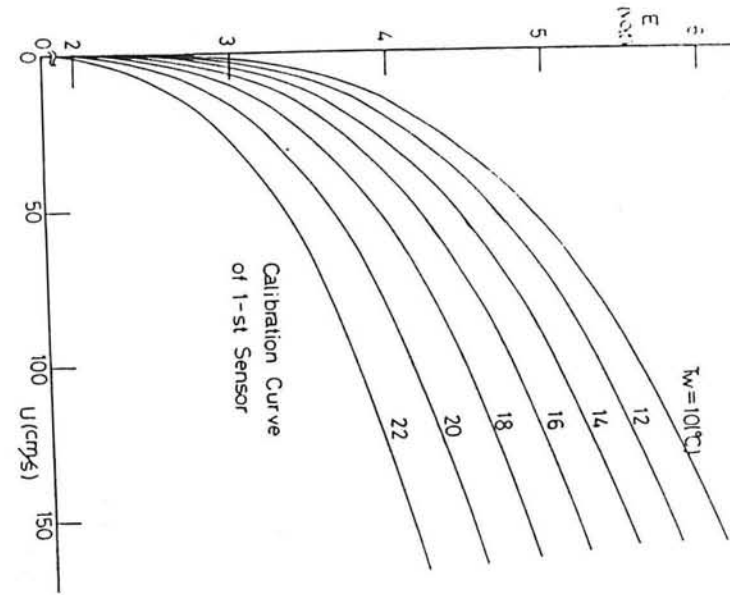


Fig. 3.14 Sensitivity factor c of 1-st sensor.

Fig. 3.12 Calculated calibration curves of 1-st sensor.



11

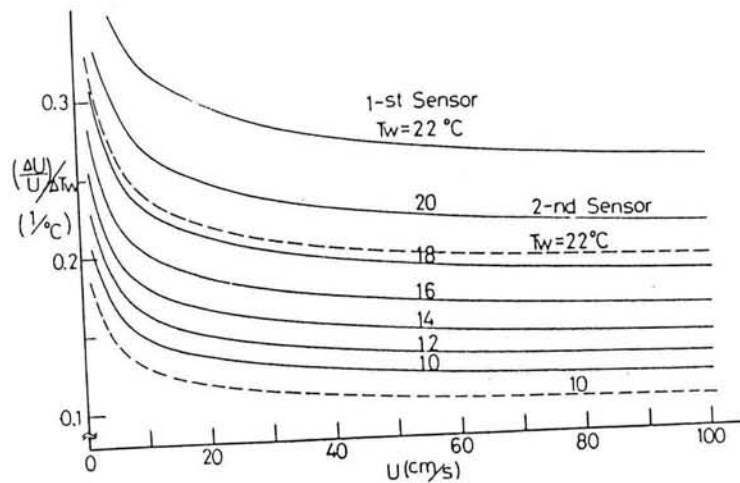


Fig. 3.15 Temperature sensitivity of hot-film sensors.

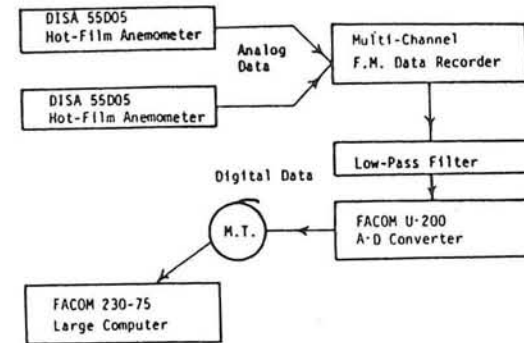


Fig. 3.13 Data processing system of point-measurements.

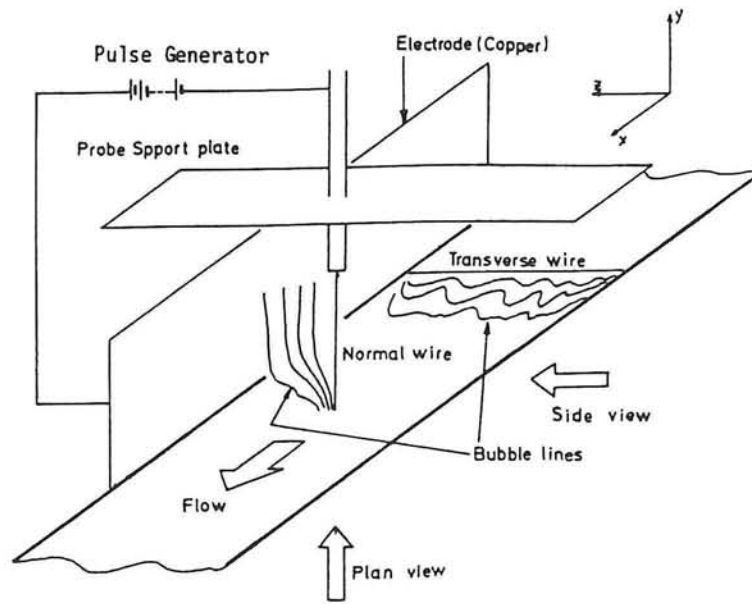


Fig. 3.16 Flow visualization system (orientation of H_2 -bubble wires and camera views).

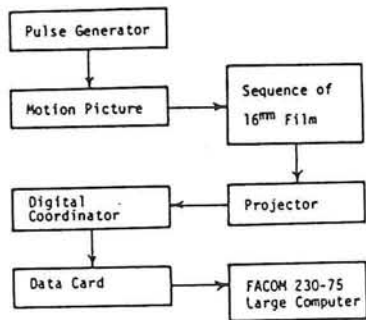


Fig. 3.17 Data processing system of hydrogen-bubble method.

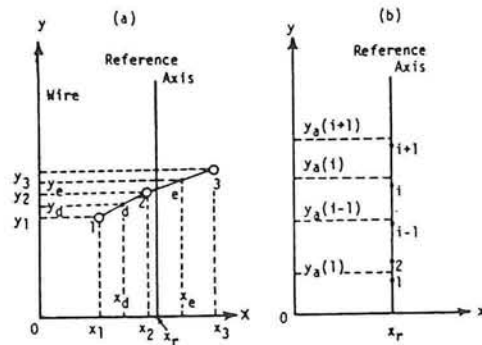


Fig. 3.18 Analysis method of instantaneous velocity profile.

Chapter 4 Experimental consideration on turbulent structure and energy budget

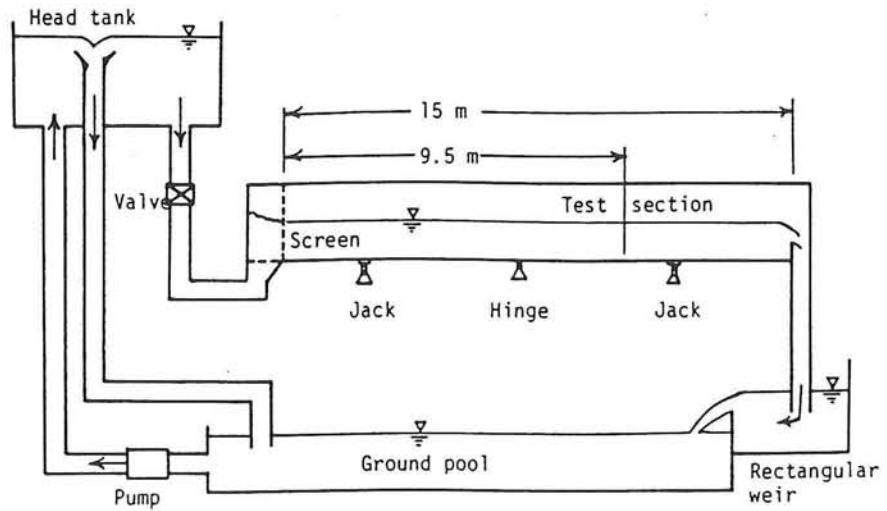


Fig. 4.1 15m recirculating tilting experimental flume.

(a) Hydraulic conditions that the Froude number is nearly constant (Smooth bed).

Case	h (cm)	U_{max} (cm/s)	U_m (cm/s)	U_* (cm/s)	U_*' (cm/s)	U_*'' (cm/s)	R_* $\times 10^3$	Re $\times 10^4$	Fr	Slope S $\times 10^{-4}$	Q (l/s)	T_w ($^{\circ}C$)
A-3	3.14	46.1	40.7	2.206	2.152	2.132	0.643	1.18	0.733	14.8	6.4	17.18
A-5	5.99	60.0	53.8	2.485	2.485	2.507	1.33	2.89	0.703	10.7	16.1	15.75
A-6	8.00	67.0	60.1	2.638	2.638	2.732	2.03	4.62	0.689	9.5	24.1	18.60

(b) Hydraulic conditions that the Reynolds number is nearly constant (Smooth bed).

G-1	8.01	48.3	40.1	2.152	2.468	1.896	1.63	3.03	0.455	4.58	16.1	17.78
G-2	5.49	73.2	58.5	3.138	3.808	3.177	1.76	3.23	0.798	18.8	16.1	20.51
G-3	4.14	101.8	77.2	3.748	4.954	3.856	1.59	3.27	1.21	36.6	16.0	21.27
G-4	3.15	118.6	101.2	4.711	5.462	5.180	1.49	3.19	1.82	86.9	15.9	20.35
G-5	2.20	169.4	144.8	6.162	9.066	7.950	1.39	3.27	3.12	293.0	15.9	21.43

U_*' = by Reynolds stress, U_*'' = by Log-law, $U_*'' = \sqrt{ghS}$

(c) Hydraulic conditions that the Reynolds and the Froude numbers are nearly constant.

Case	h (cm)	U_{max} (cm/s)	U_m (cm/s)	U_* (cm/s)	U_*' (cm/s)	U_*'' (cm/s)	R_* $\times 10^2$	Re $\times 10^4$	Fr	S $\times 10^{-4}$	Q (l/s)	T_w ($^{\circ}C$)	k_s^+
A-1	7.77	16.8	14.8	0.810	0.810	0.790	5.98	1.09	0.170	0.80	5.8	18.35	~0
B-1	7.94	17.7	15.5	0.895	0.895	0.938	5.66	0.98	0.175	1.13	6.1	11.35	9
C-1	7.83	15.7	13.2	0.989	0.989	0.999	7.37	0.98	0.150	1.23	5.2	17.95	48
D-1	7.63	17.2	13.9	1.267	1.336	1.416	8.32	0.86	0.160	2.77	5.3	12.30	136

Table 4.1 Summary of hydraulic data for experiments.

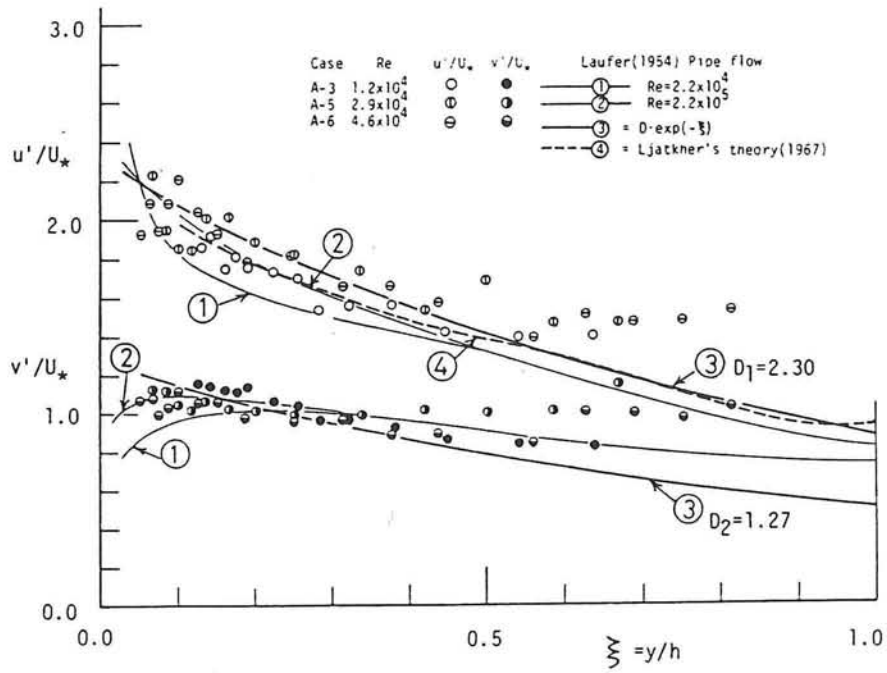


Fig. 4.2 Effect of the Reynolds number on turbulence intensities.

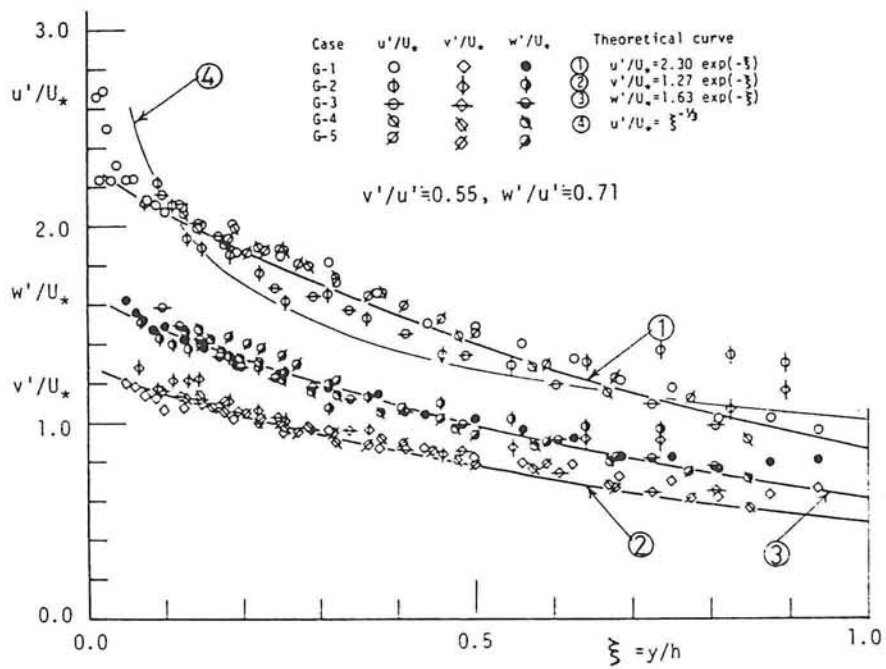


Fig. 4.3 Effect of the Froude number on turbulence intensities.

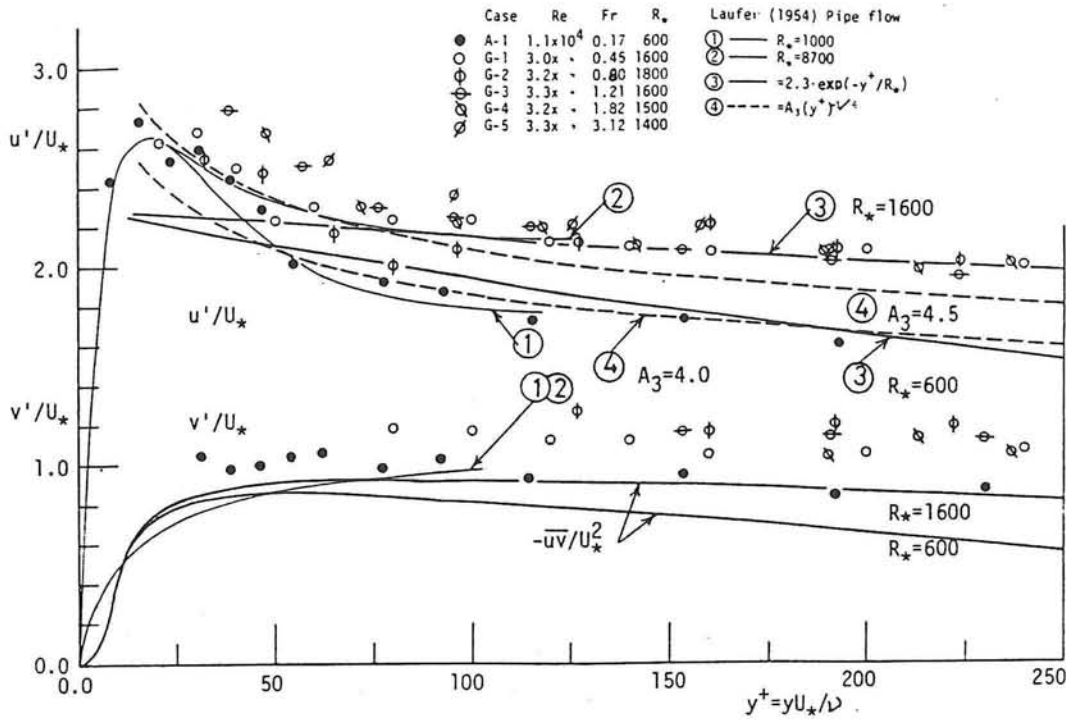


Fig. 4.4 Effect of the Froude number on turbulence intensities near the wall.

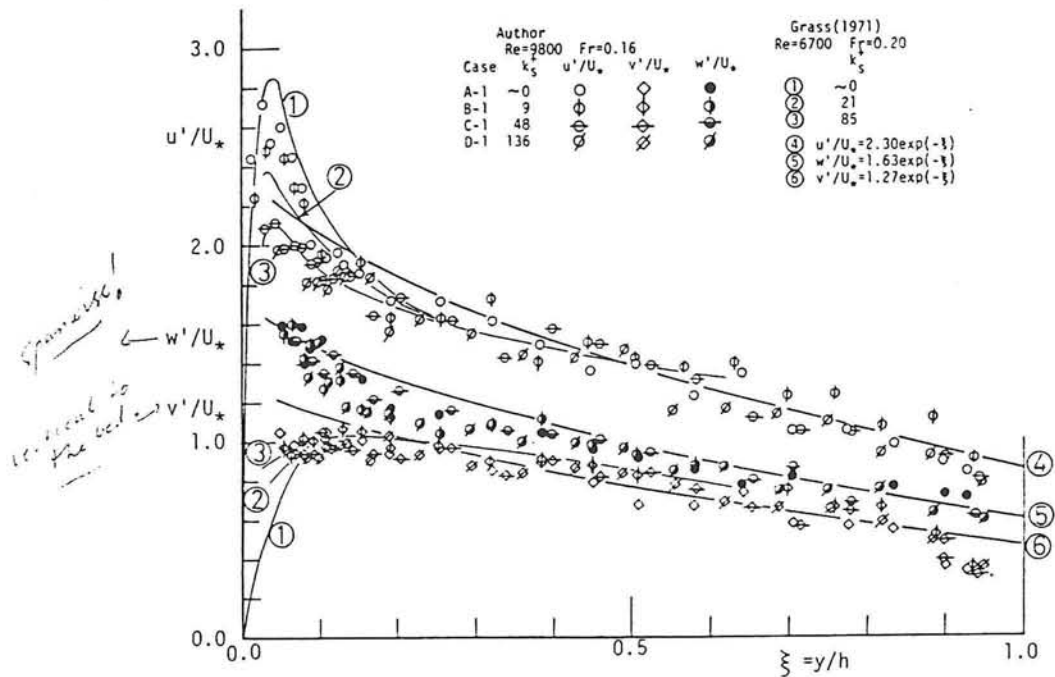


Fig. 4.5 Effect of the roughness on turbulence intensities.

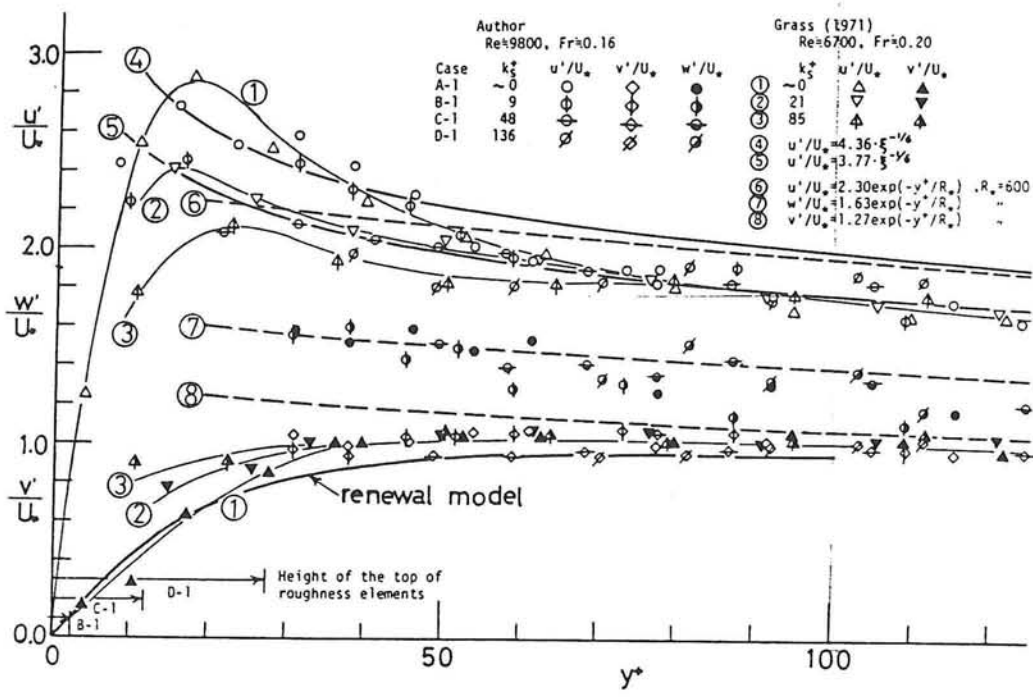


Fig. 4.6 Effect of the roughness on turbulence intensities in the wall region.

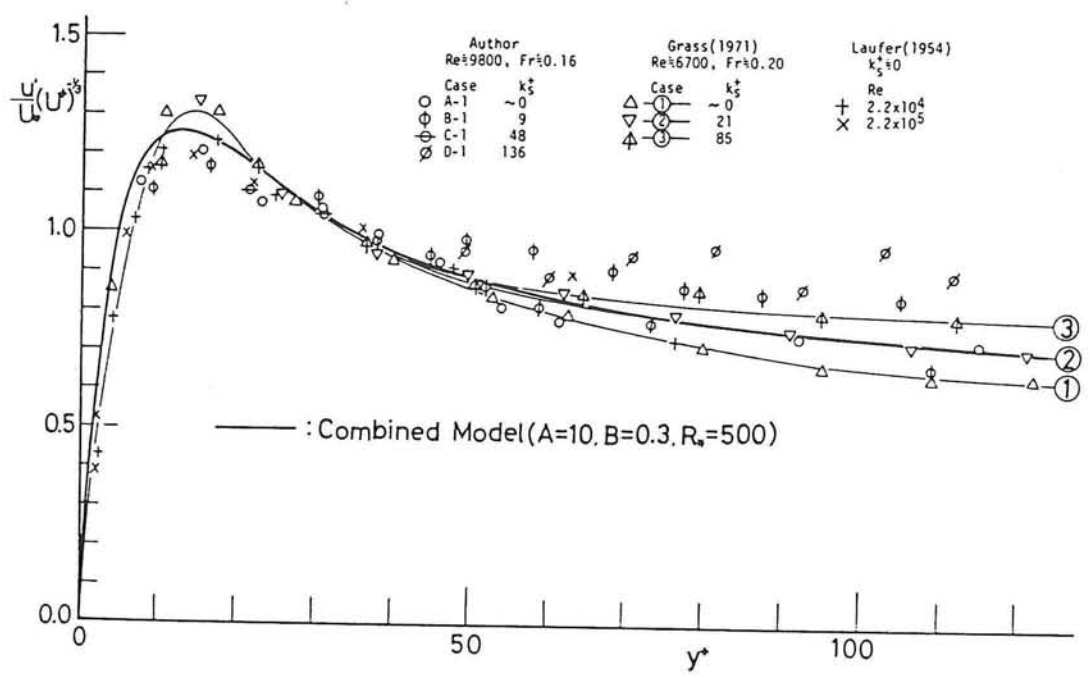


Fig. 4.7 Universal distribution of $(u'/U_*) (u^*)^{-1/3}$ in the wall region.

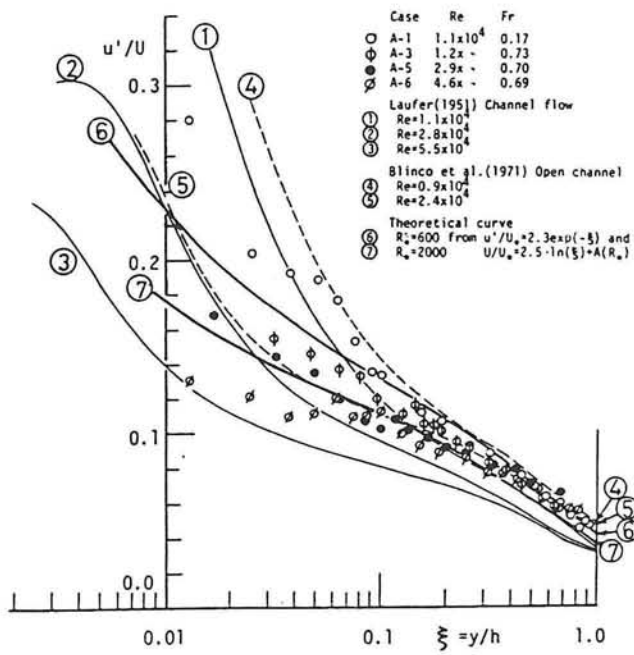


Fig. 4.8 Relative turbulence intensity u'/U (effect of Re).

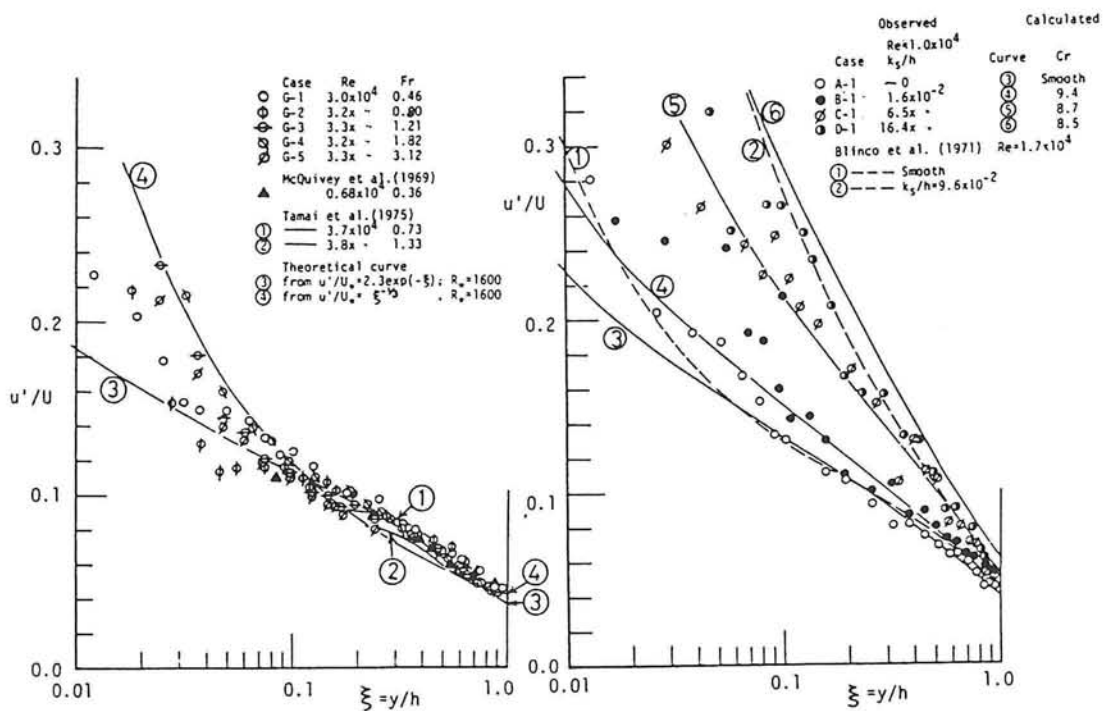


Fig. 4.9 Effect of Fr on u'/U .

Fig. 4.10 Effect of roughness on u'/U .

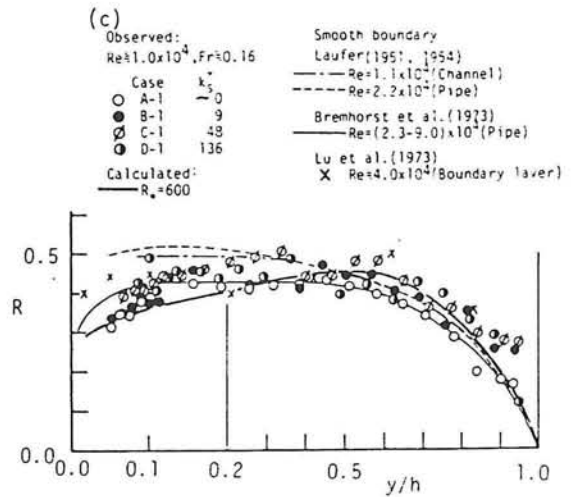
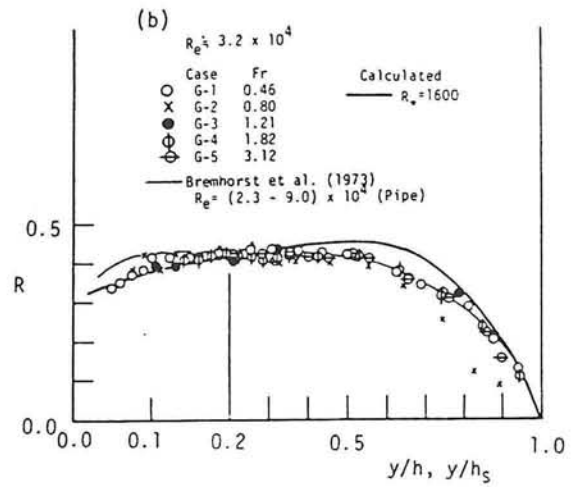
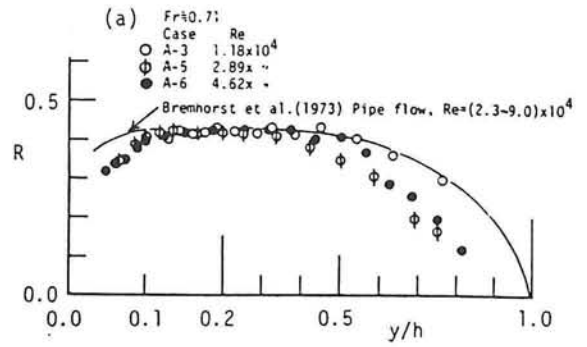
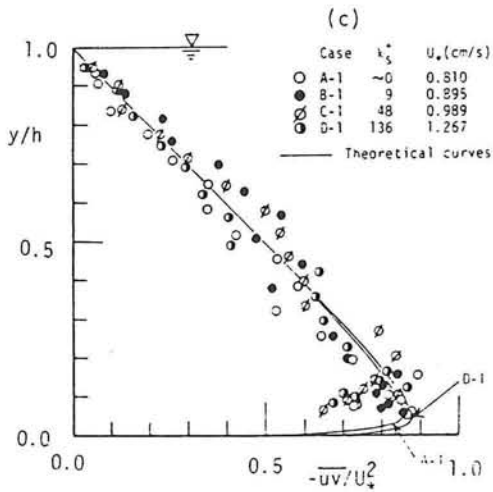
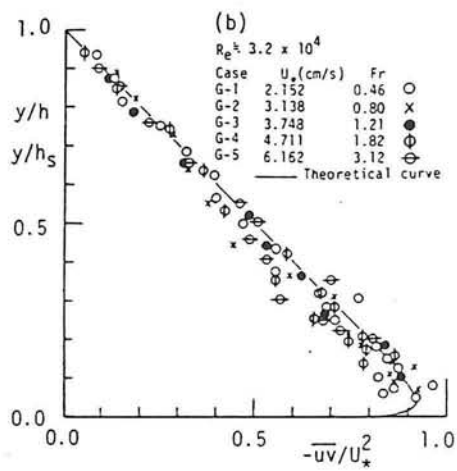
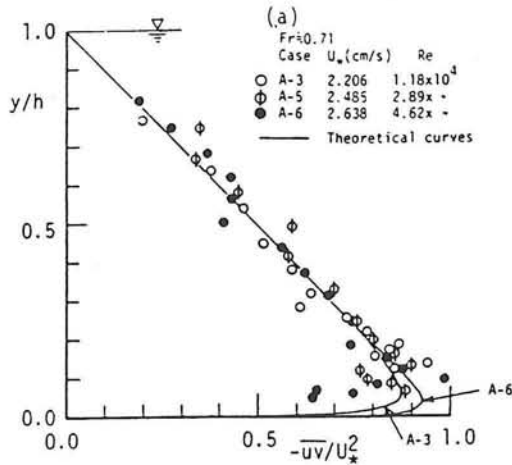


Fig. 4.11 Distribution of Reynolds stress $-\overline{uv}/U_*^2$.

Fig. 4.12 Coefficient of correlation $R = -\overline{uv}/u'v'$.

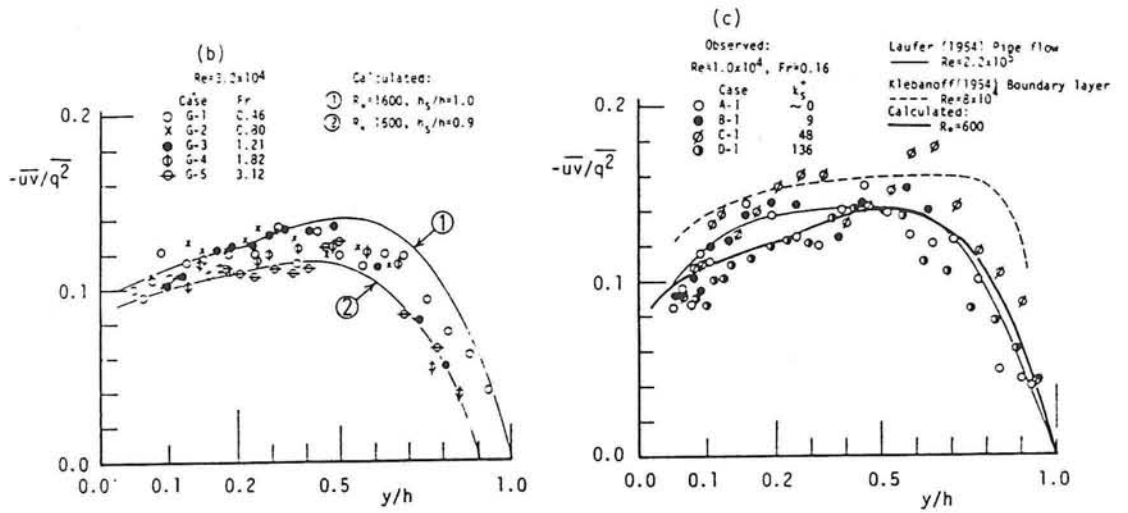


Fig. 4.13 Ratio $-\overline{uv}/q^2$ of Reynolds stress to turbulent energy.

Group P : Wall Pressure Fluctuations							Group W : Surface Wave Fluctuations						
Case	h (cm)	U_{max} (cm/sec)	U_m (cm/sec)	U''_* (cm/sec)	Re $\times 10^4$	Fr	Case	h (cm)	U_{max} (cm/sec)	U_m (cm/s)	U''_* (cm/s)	Re $\times 10^4$	Fr
P-1	8.11	49.20	39.64	1.908	3.20	0.445	W-1	7.92	51.82	40.95	1.885	3.13	0.465
P-2	7.02	57.04	45.76	2.303	3.18	0.552	W-2	7.22	55.47	45.12	2.336	3.13	0.536
P-3	6.16	63.16	52.09	2.558	3.17	0.670	W-3	6.37	68.80	50.20	2.601	3.11	0.635
P-4	5.85	66.78	54.72	2.913	3.14	0.723	W-4	5.57	72.68	57.57	2.842	3.08	0.779
P-5	5.73	76.81	55.96	3.246	3.09	0.747	W-5	5.29	69.15	59.71	3.119	3.04	0.829
P-6	5.21	81.69	61.33	3.444	3.12	0.858	W-6	5.28	80.48	60.89	3.786	3.19	0.846
P-7	4.58	85.79	69.89	3.525	3.16	1.043	W-7	4.24	97.80	75.16	3.902	3.16	1.166
P-8	4.02	96.34	79.91	3.560	3.11	1.273	W-8	3.48	107.49	91.57	4.590	3.24	1.568
P-9	3.82	100.91	83.94	3.704	3.17	1.372	W-9	2.98	117.05	107.32	5.038	3.28	1.986
P-10	3.39	111.47	94.09	4.530	3.13	1.632							
P-11	3.06	122.20	103.98	5.107	3.06	1.898							
P-12	2.51	154.03	127.61	6.837	3.13	2.573							

Table 4.2 Summary of hydraulic data for Group-P and -W.

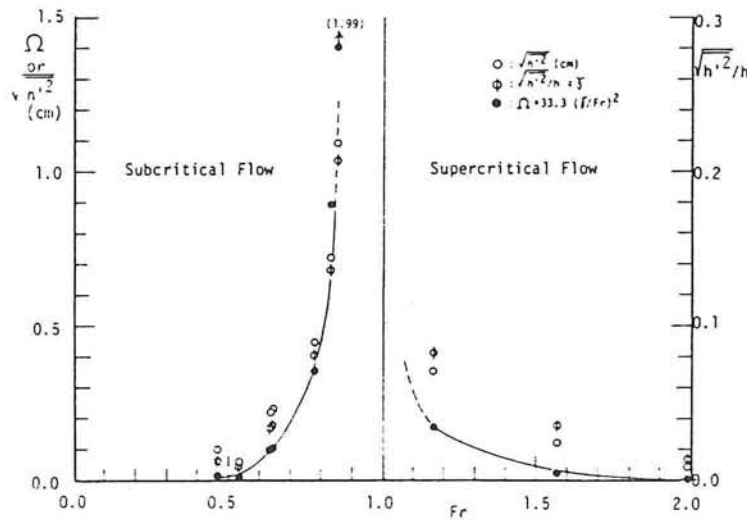


Fig. 4.14 Intensity of surface wave fluctuations.

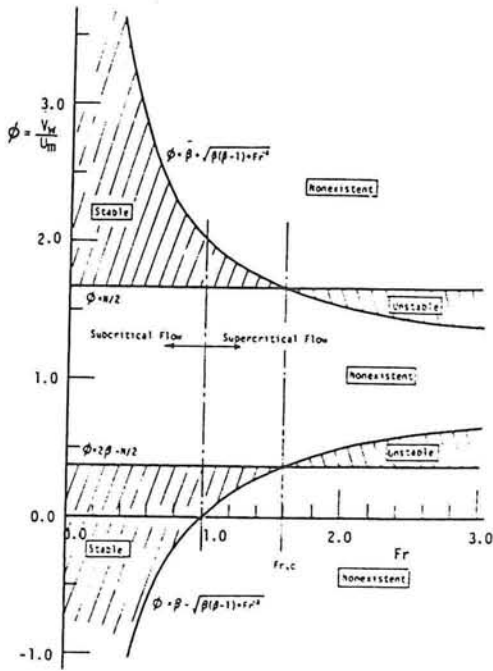


Fig. 4.15 Diagram of existence and stability of small disturbances.

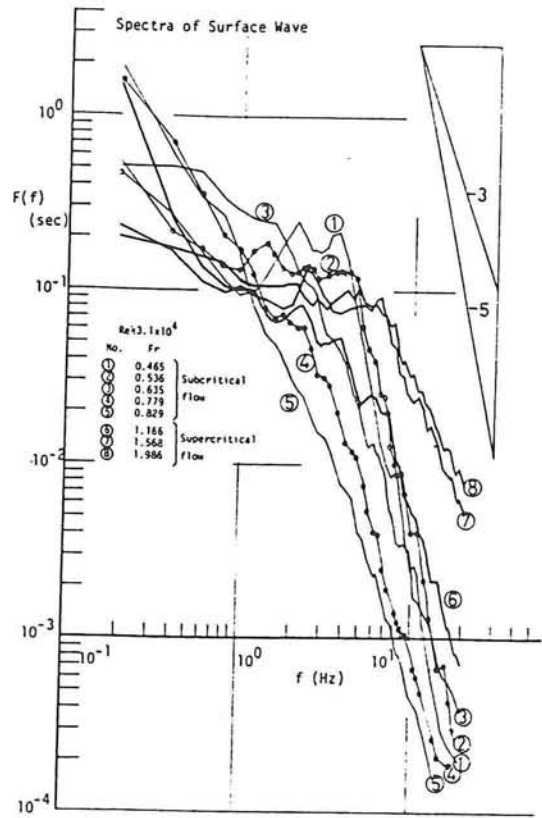


Fig. 4.16 Frequency spectra of surface wave fluctuations.

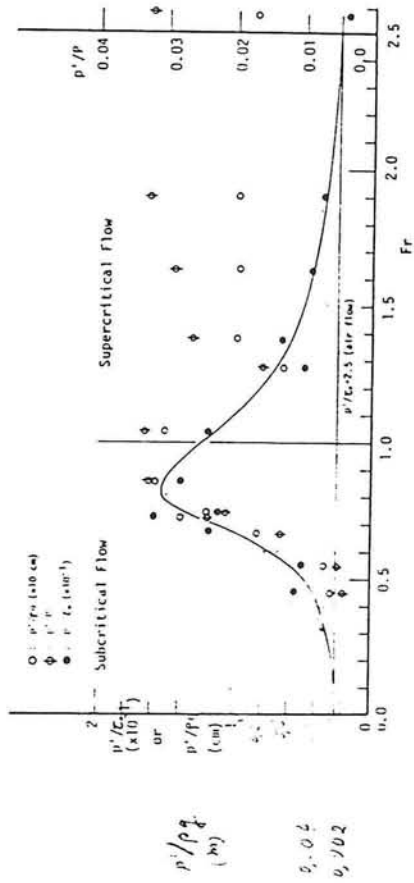


Fig. 4.17 Intensity of wall pressure fluctuations.

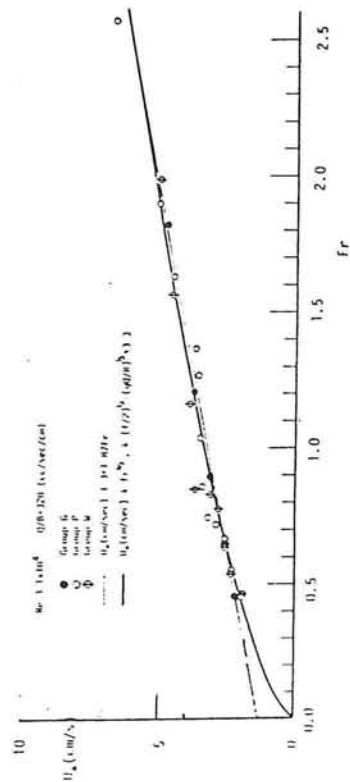


Fig. 4.18 Variation of friction velocity u_* with Froude number Fr .

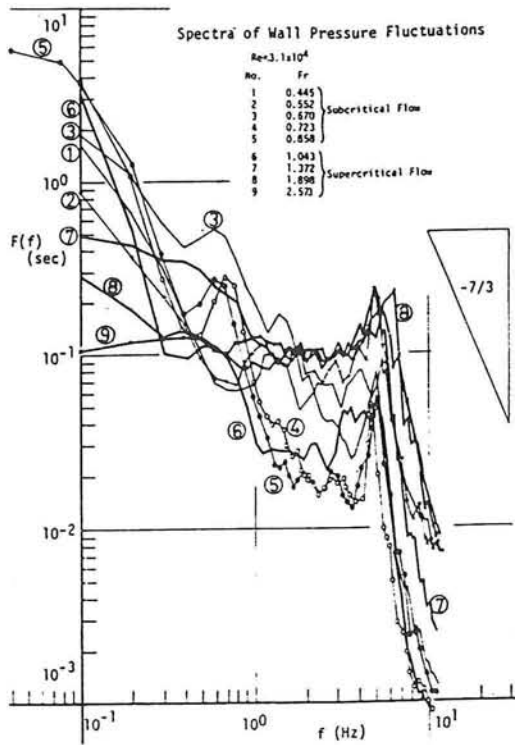


Fig. 4.19 Frequency spectra of wall pressure fluctuations.

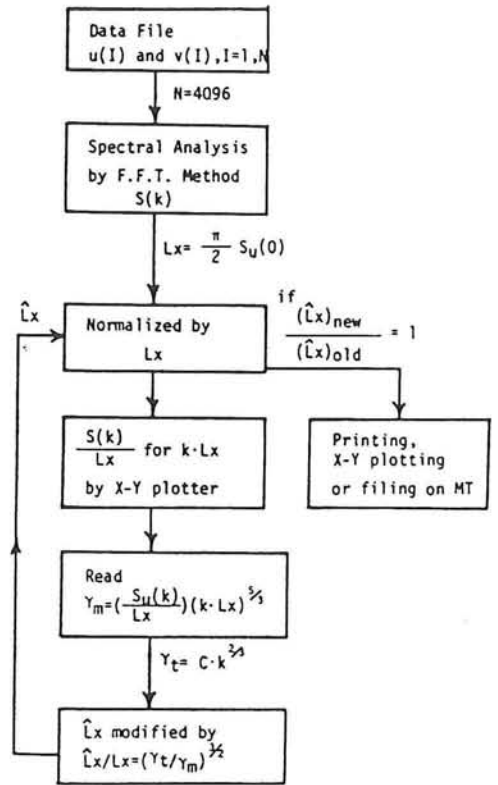


Fig. 4.21 Flow chart of spectral analysis.

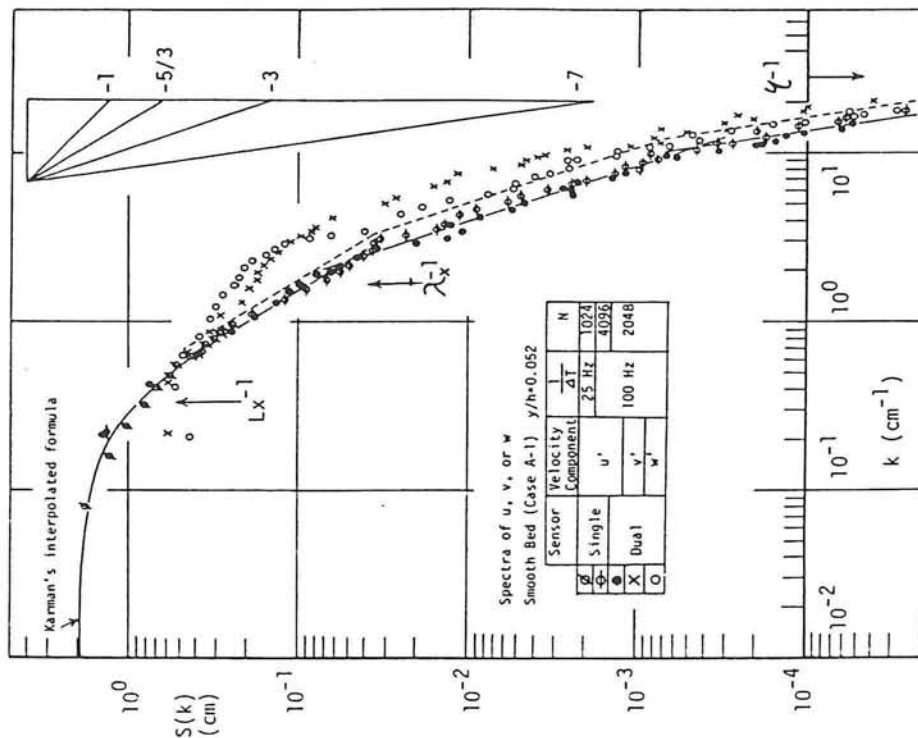


Fig. 4.20 An example of spectra $S_u(k)$, $S_v(k)$ and $S_w(k)$.

$$S_u = \frac{U^2}{2\pi} F(f)$$

$$k = \frac{2\pi f}{U} \quad (\text{m}^{-1})$$

22

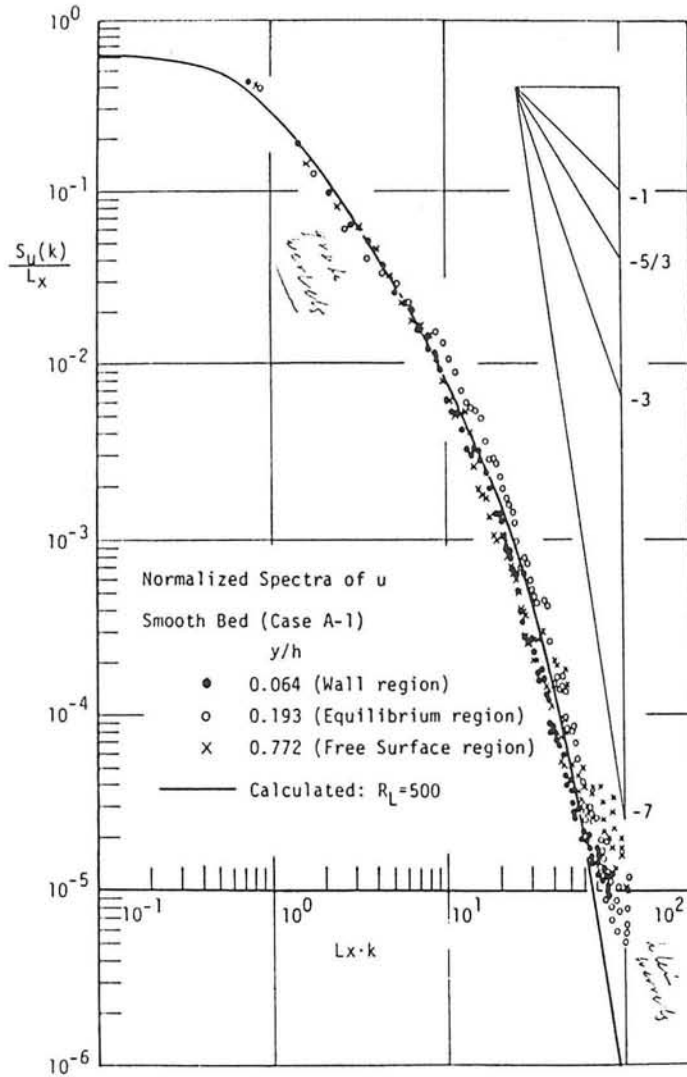


Fig. 4.22 Spectral distributions normalized by L_x for smooth bed (Case A-1).

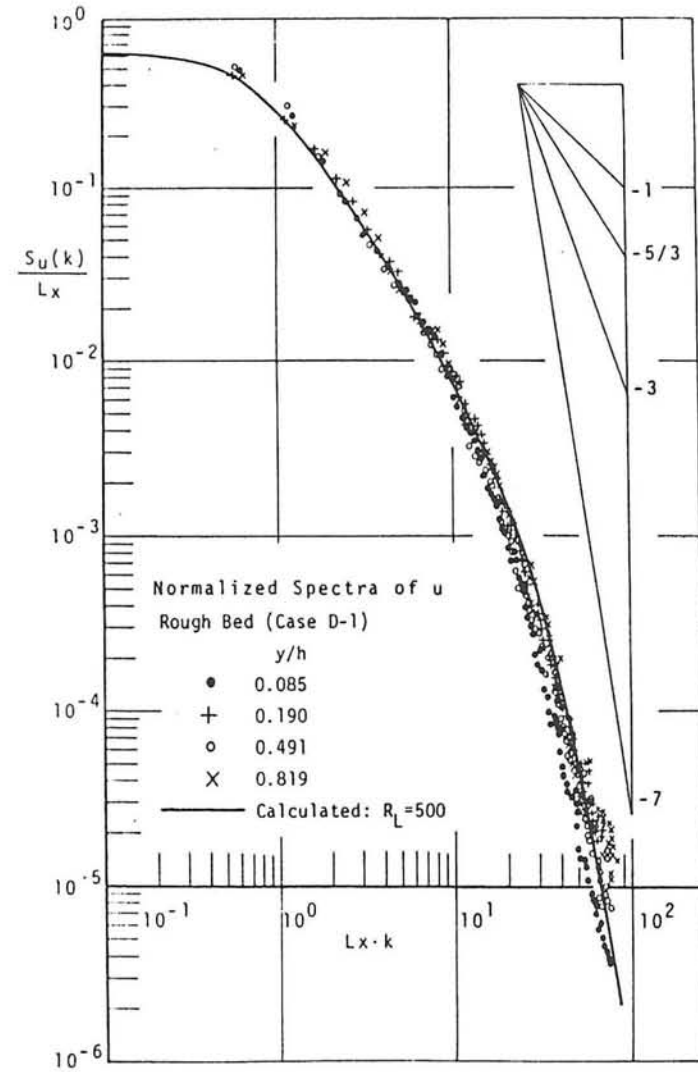


Fig. 4.23 Spectral distributions normalized by L_x for rough bed (Case D-1).

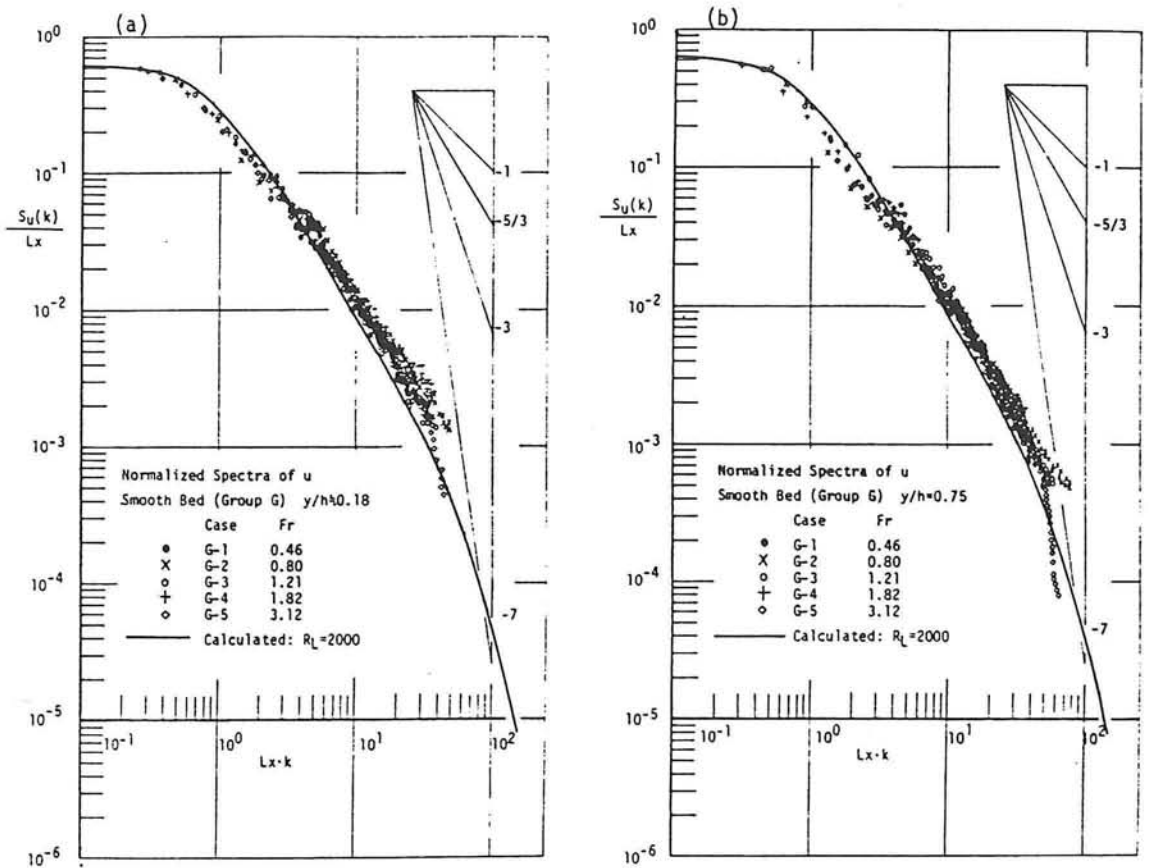


Fig. 4.24 Spectral distributions normalized by L_x (higher-velocity group).

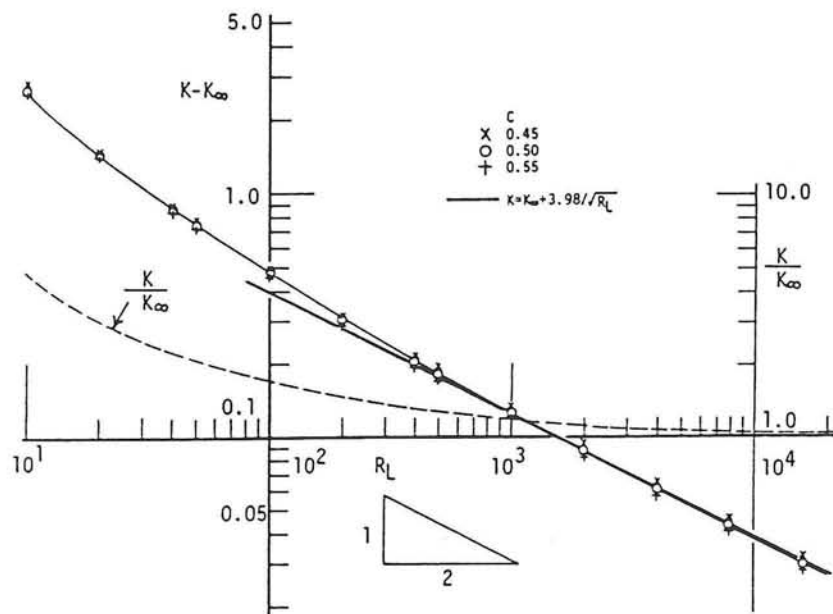


Fig. 4.25 Relations between K and R_L .

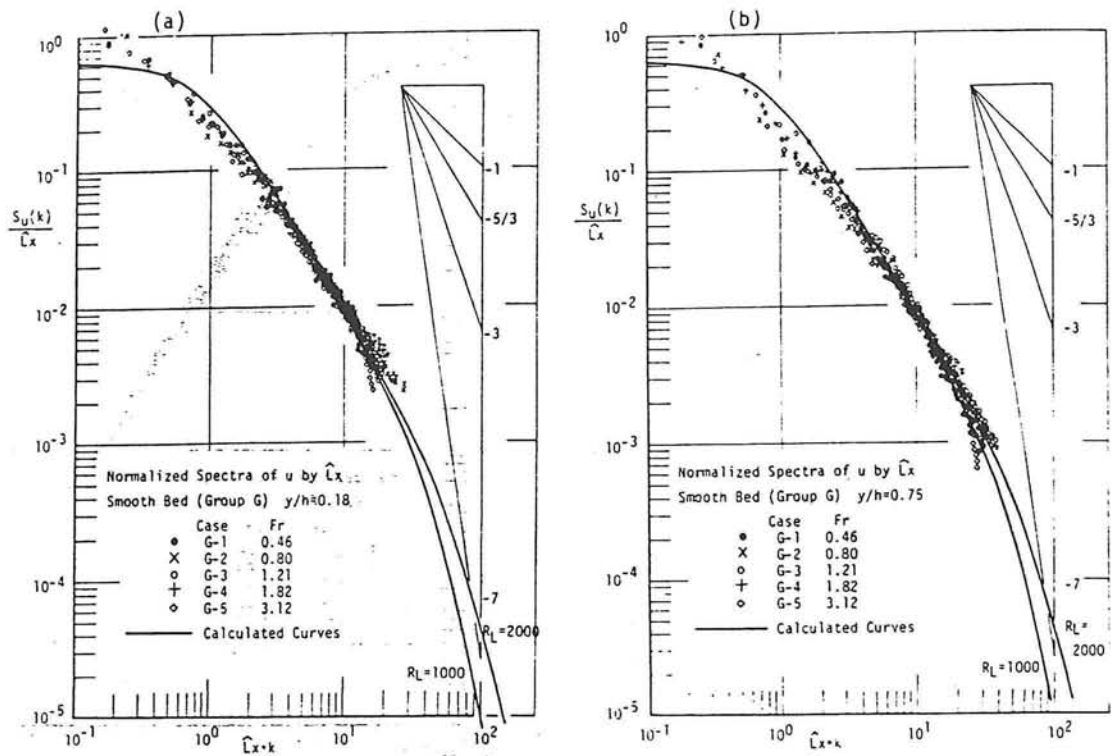


Fig. 4.26 Spectral distributions normalized by corrected \hat{L}_x .

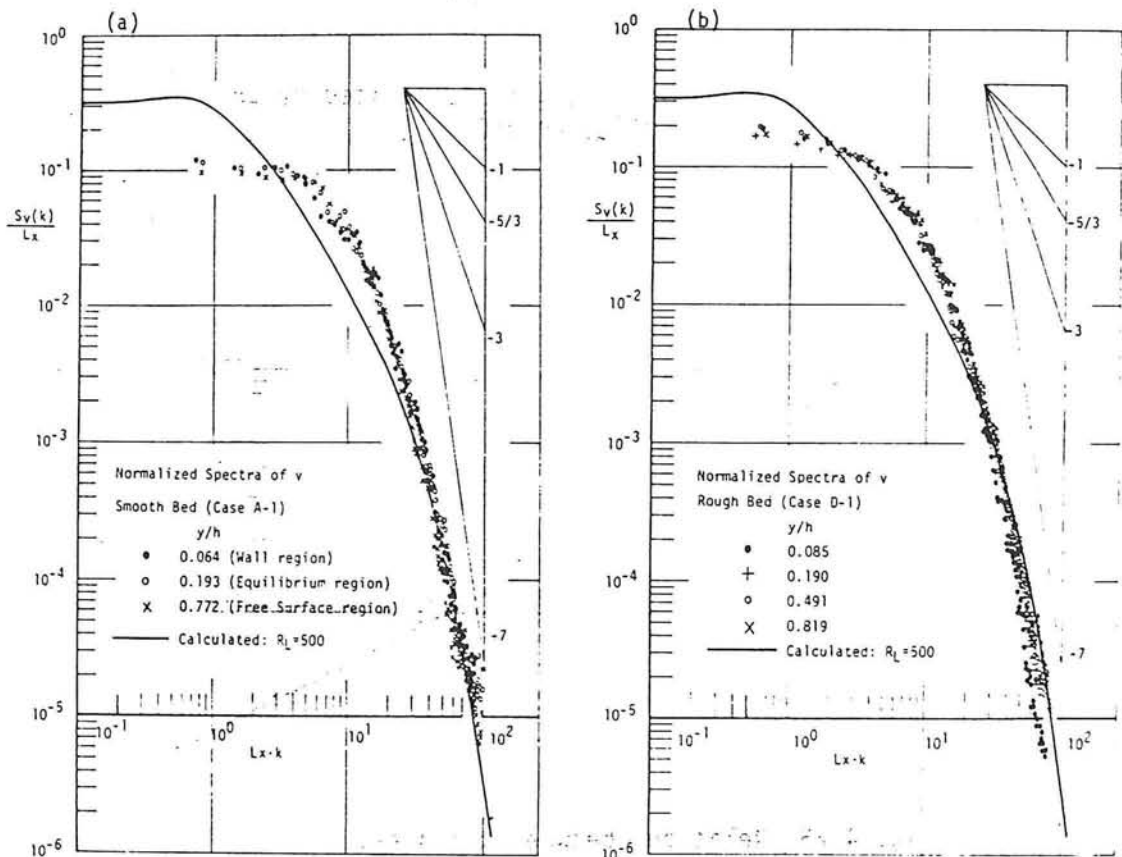


Fig. 4.27 Normalized spectra $S_v(k)/Lx$ of v .

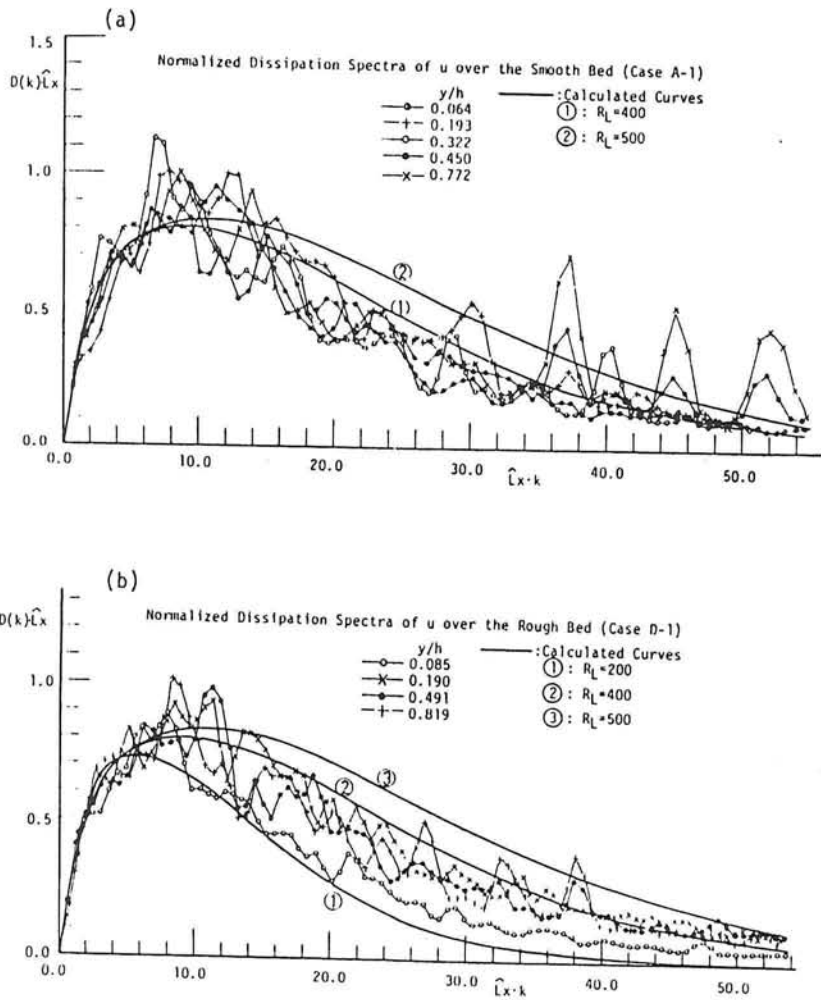
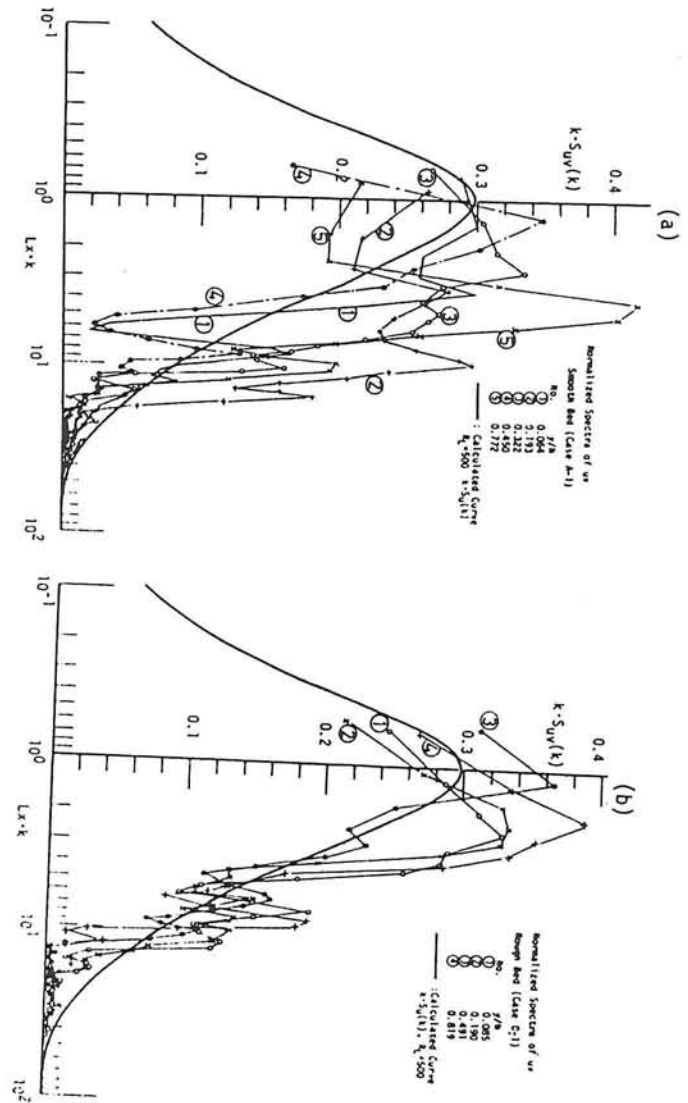


Fig. 4.29 Dissipation spectra $D_u(k)$ of u .

Fig. 4.28 Co-spectra $S_{uv}(k)$ of $-uv$.



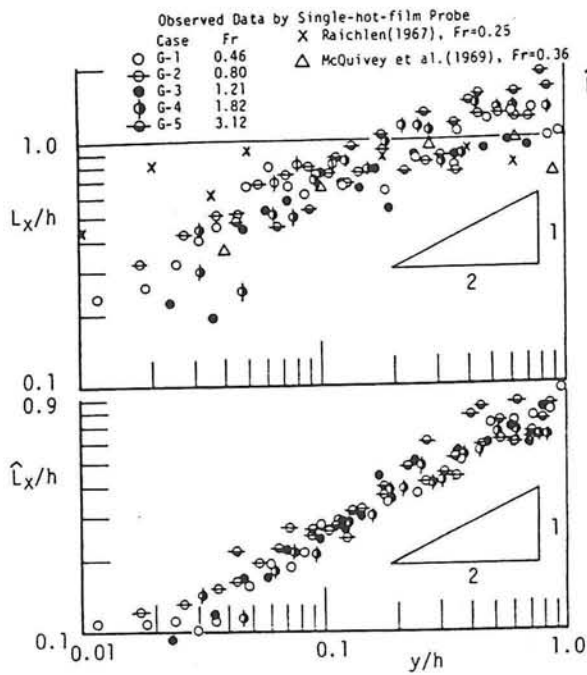


Fig. 4.30
 Distributions of macro-scale L_x
 before and after correction.

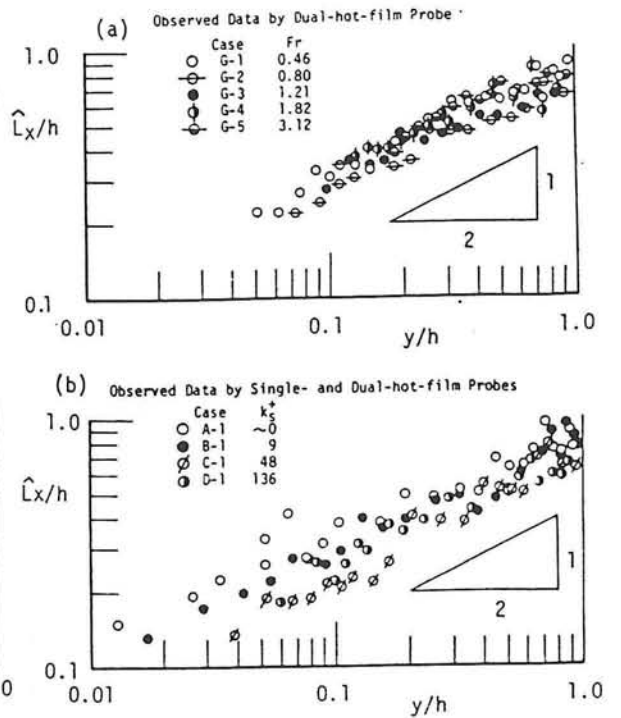


Fig. 4.31
 Distributions of corrected
 macro-scale \hat{L}_x .

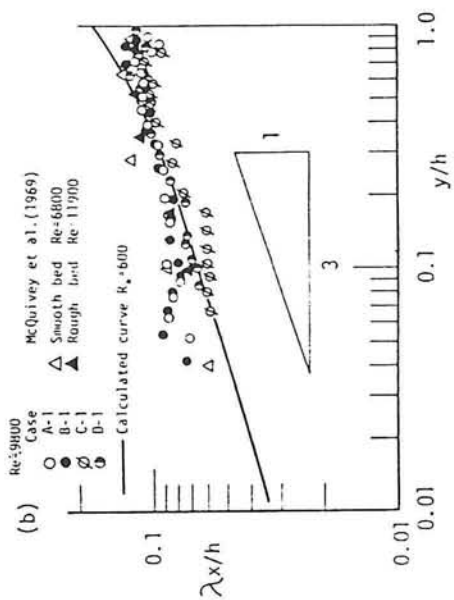
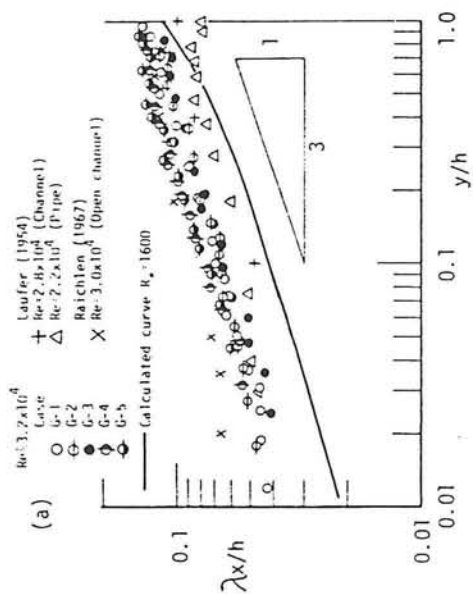


Fig. 4.32 Distributions of
 Taylor's micro-scale λ_x .

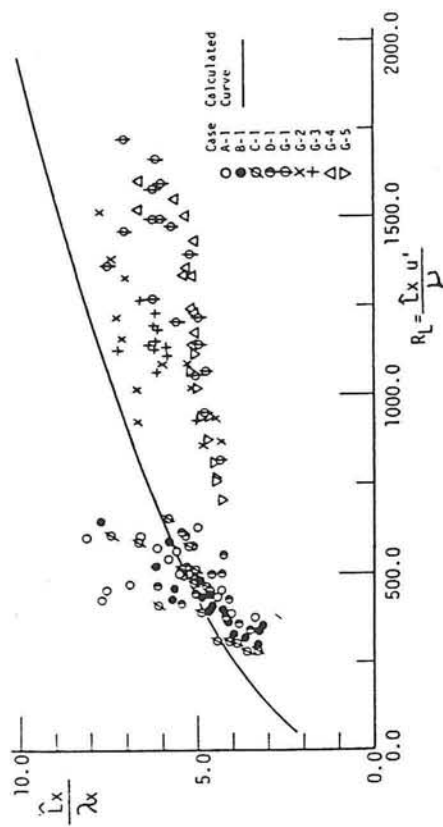


Fig. 4.33 Relation between Lx/λ and R_L .

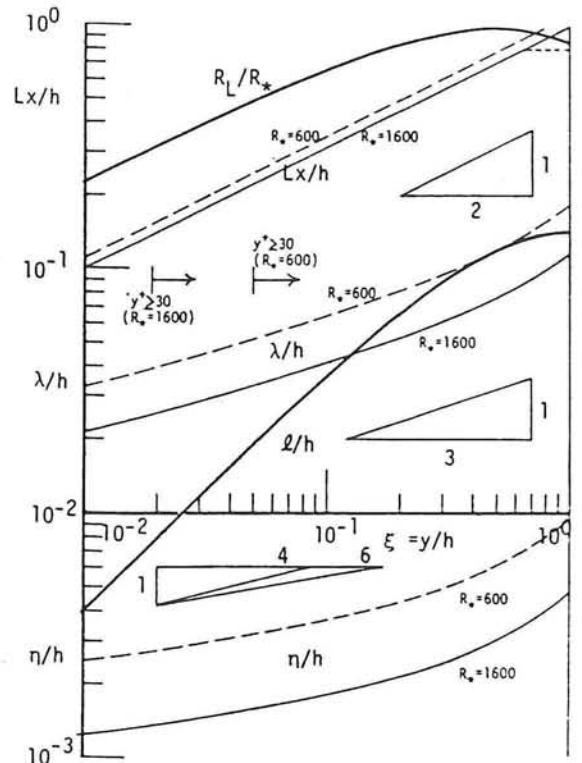


Fig. 4.34 Relations among the characteristic scales.

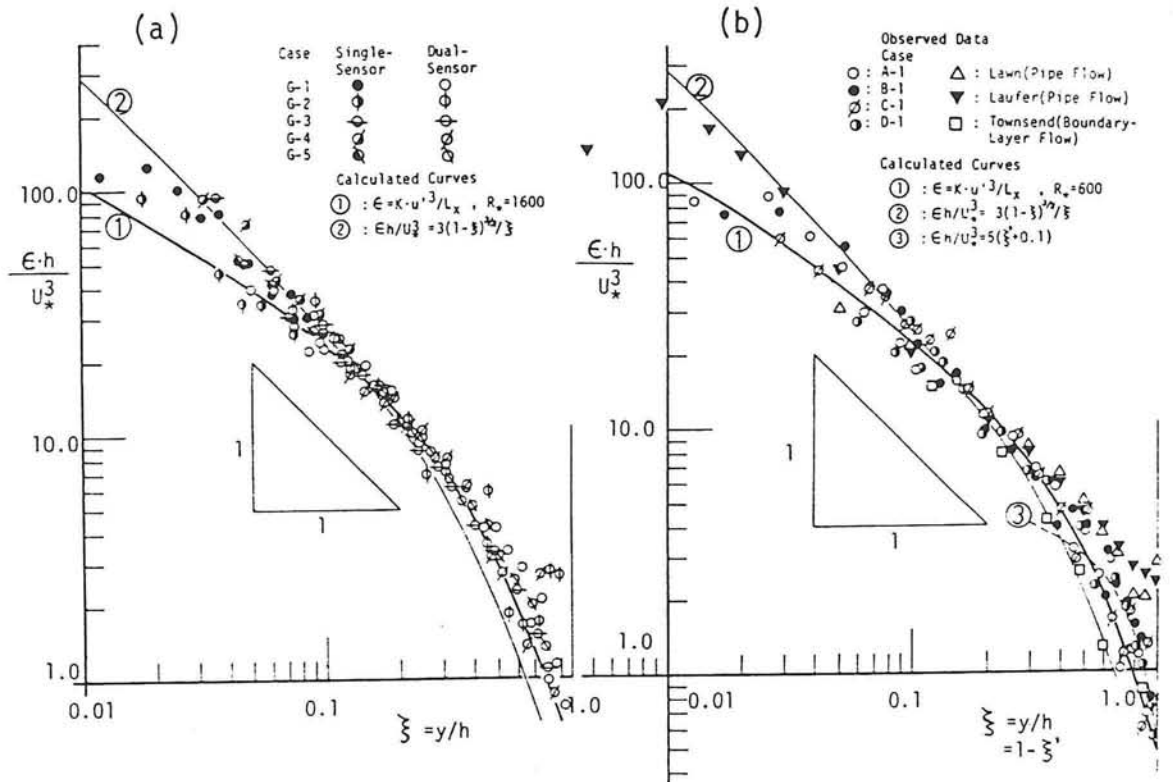


Fig. 4.35 Distributions of turbulent energy dissipation $\epsilon h/U_*^3$.

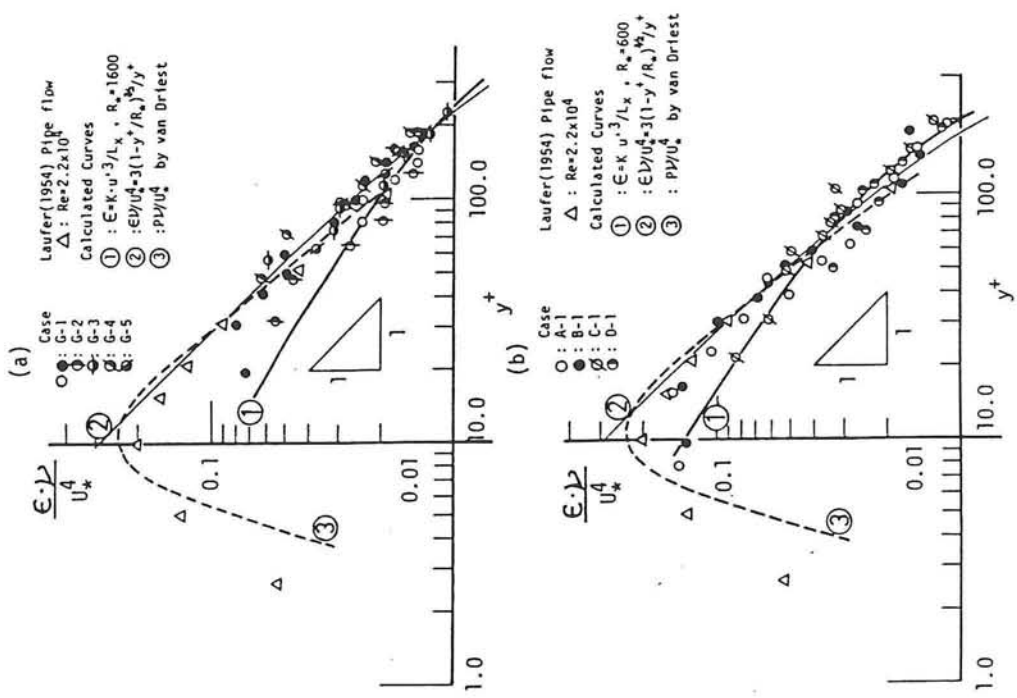


Fig. 4.36 Turbulent energy dissipation $\epsilon v / u_*^4$ in wall region.

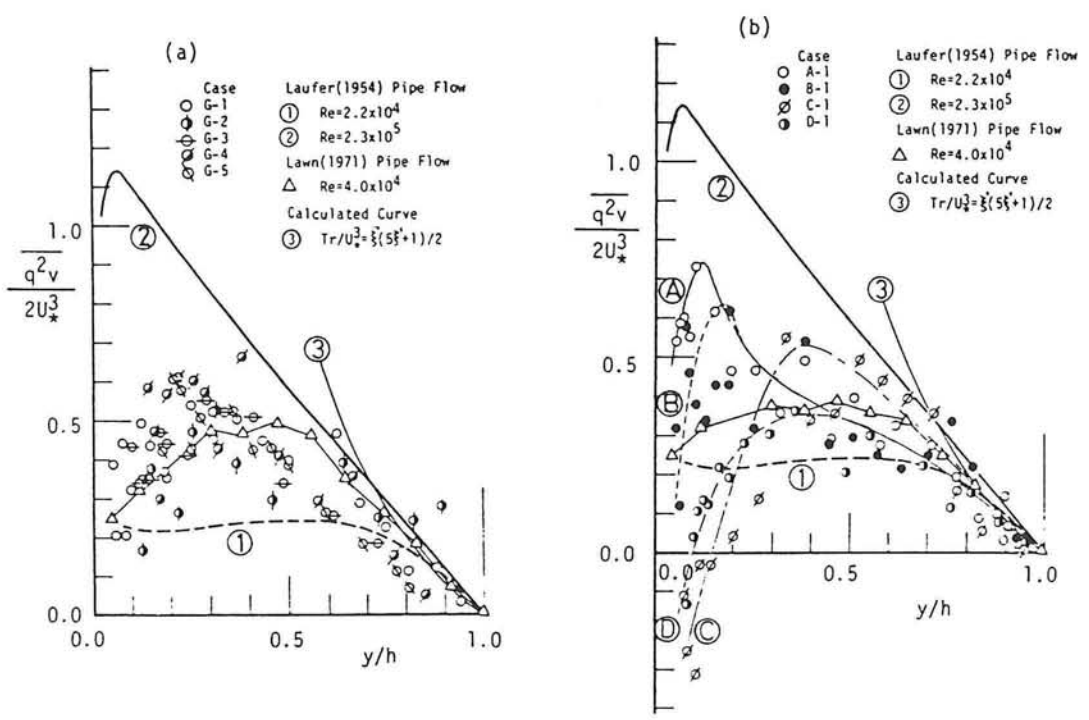


Fig. 4.37 Turbulent energy diffusion $Tr = q^2 v / 2U_*^3$.

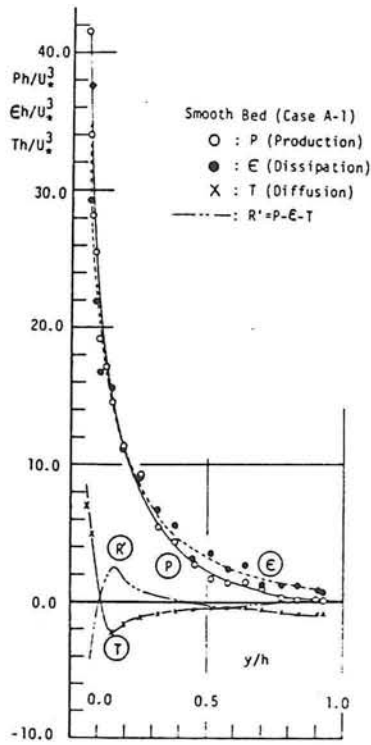


Fig. 4.38 Turbulent energy budget over smooth bed.

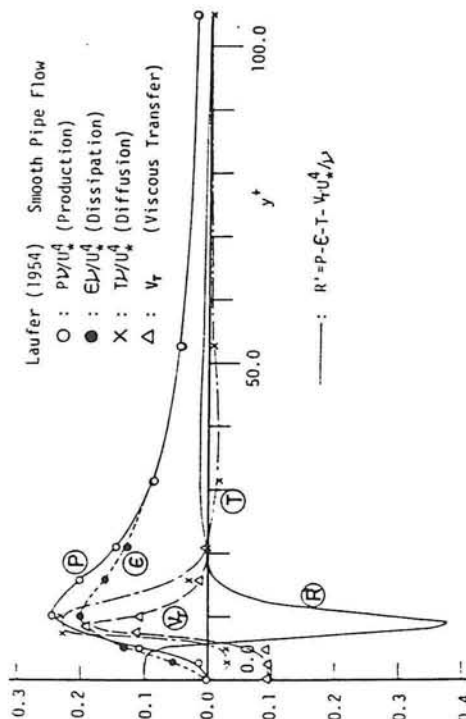


Fig. 4.39 Turbulent energy budget in wall region (after J. Laufer).

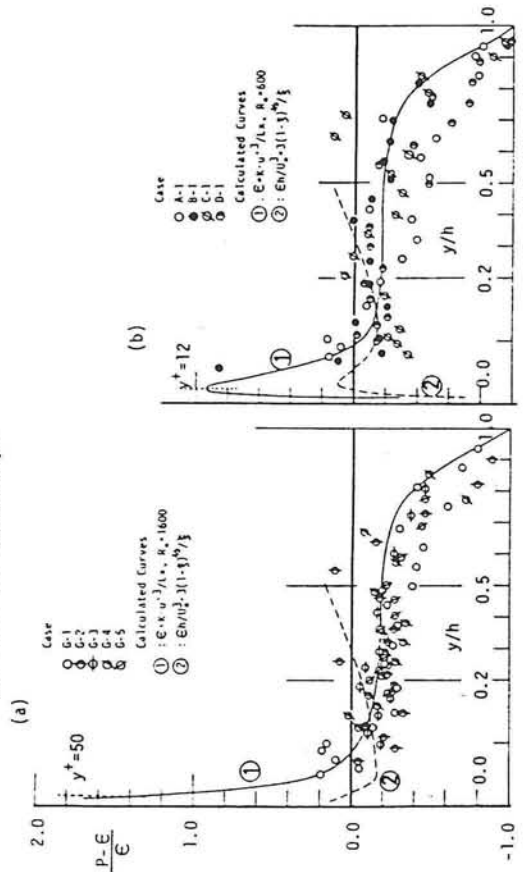


Fig. 4.41 Relationship between production P and dissipation E .

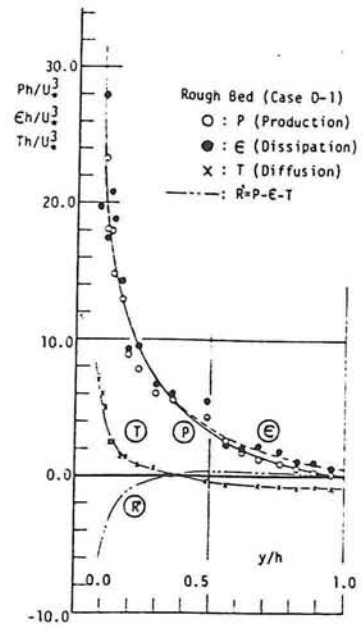


Fig. 4.40 Turbulent energy budget over rough bed.

Chapter 5 Experimental consideration on mechanism of turbulence-production

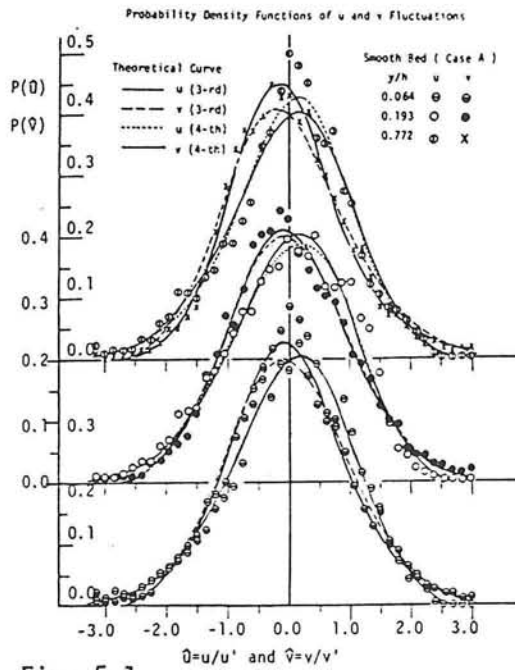


Fig. 5.1 Probability density distributions of u and v (smooth bed).

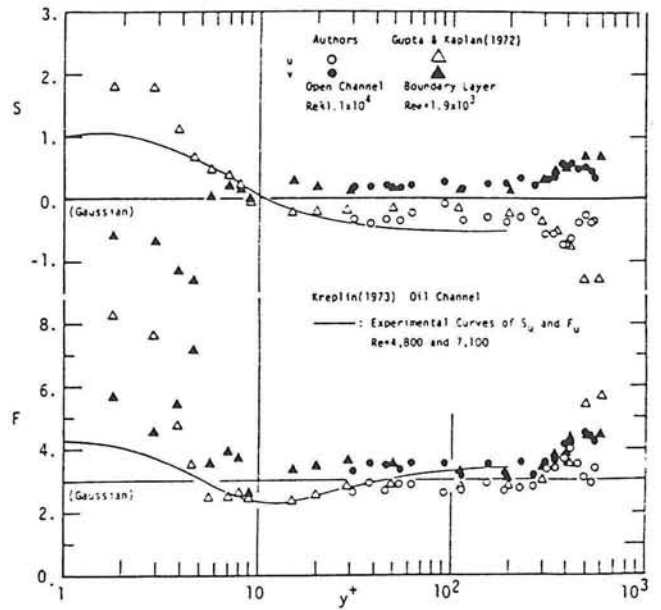


Fig. 5.2 Distributions of skewness and flatness factors of u and v .

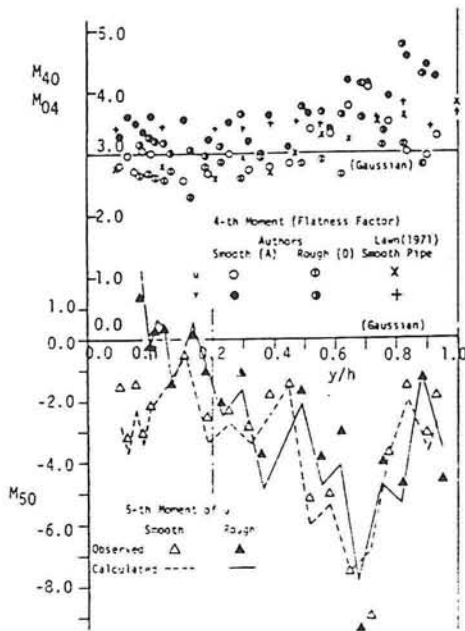


Fig. 5.3 Distributions of the 4-th and 5-th order moments.

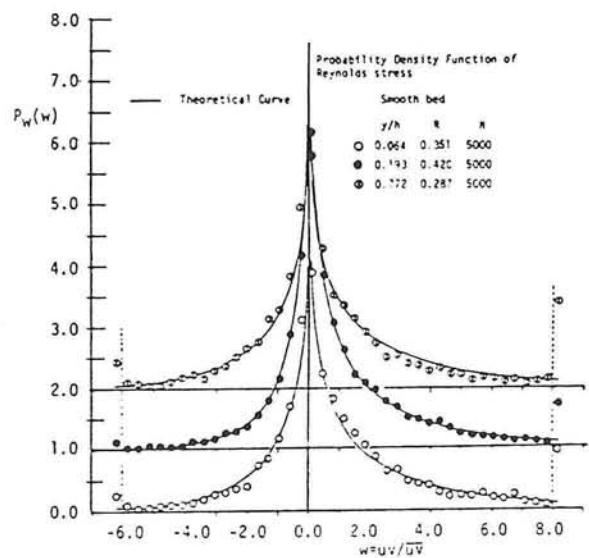


Fig. 5.4 Probability density distributions of Reynolds-stress fluctuations.

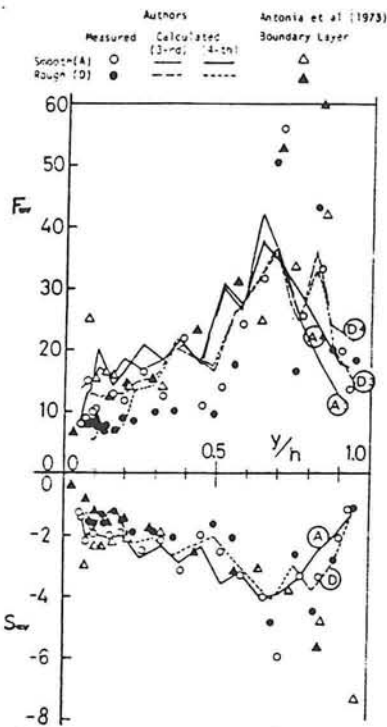


Fig. 5.5 Distributions of skewness and flatness factors of uv .

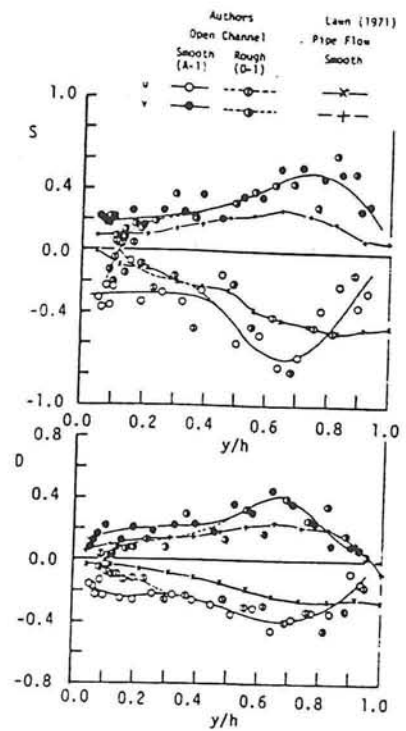


Fig. 5.6 Distributions of s and d .

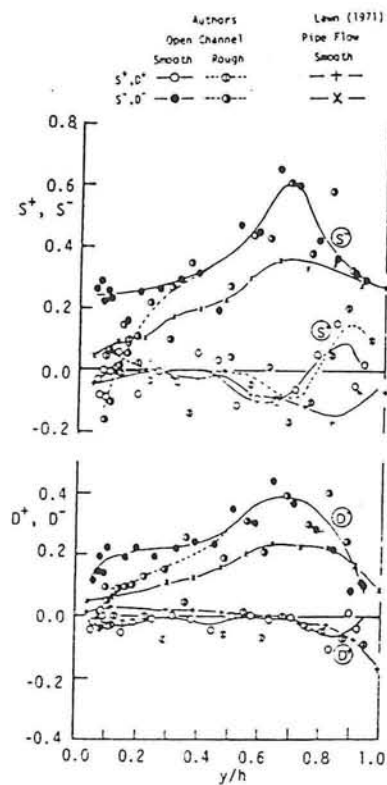


Fig. 5.7 Distributions of s^+ , s^- , d^+ and d^- .

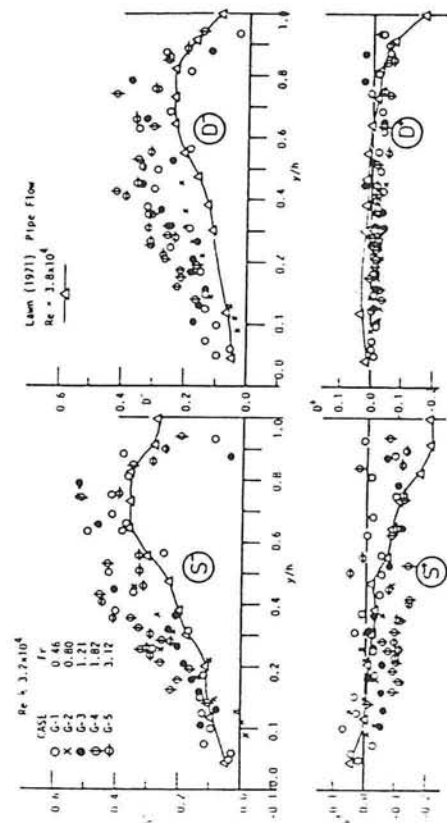


Fig. 5.8 Distributions of s^+ , s^- , d^+ and d^- (higher-velocity group).

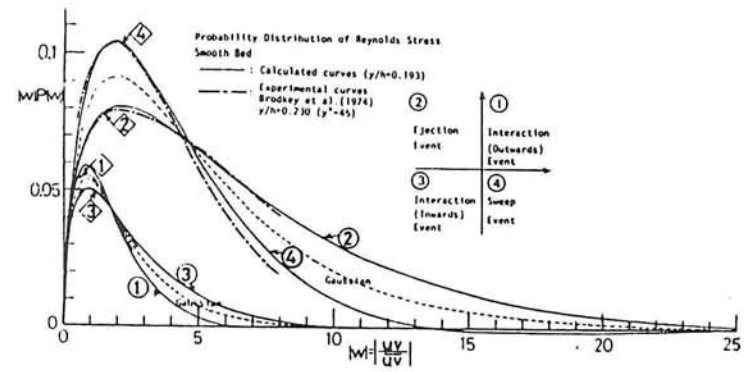
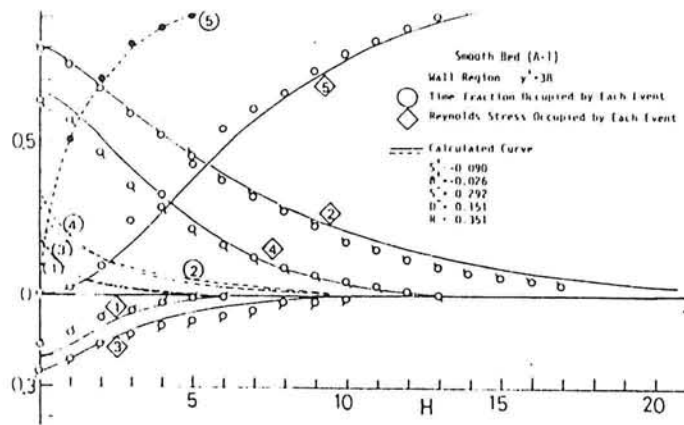


Fig. 5.9 An example of the calculated conditional probability distributions of Reynolds stress.

32

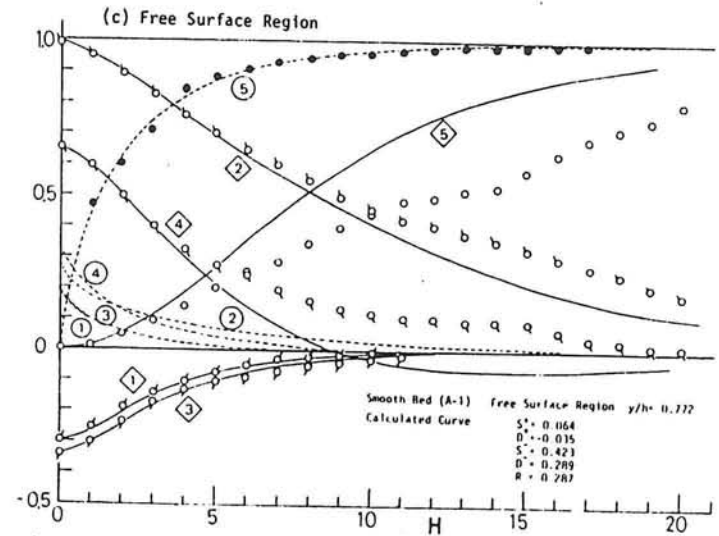
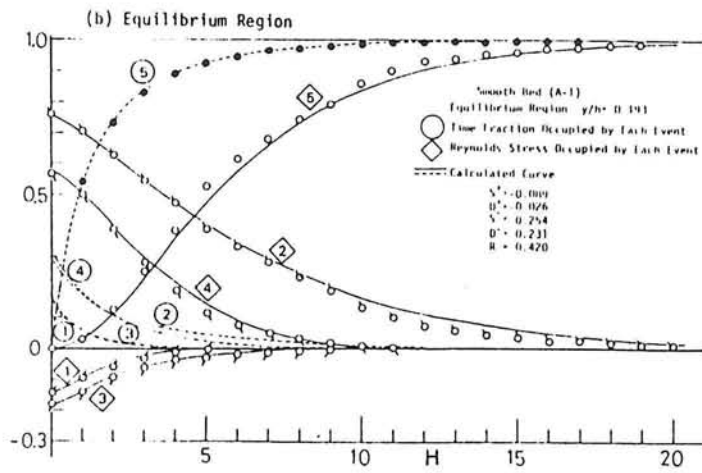


Fig. 5.10 Fractional contributions to Reynolds stress and fraction of time occupied by each event (smooth bed).

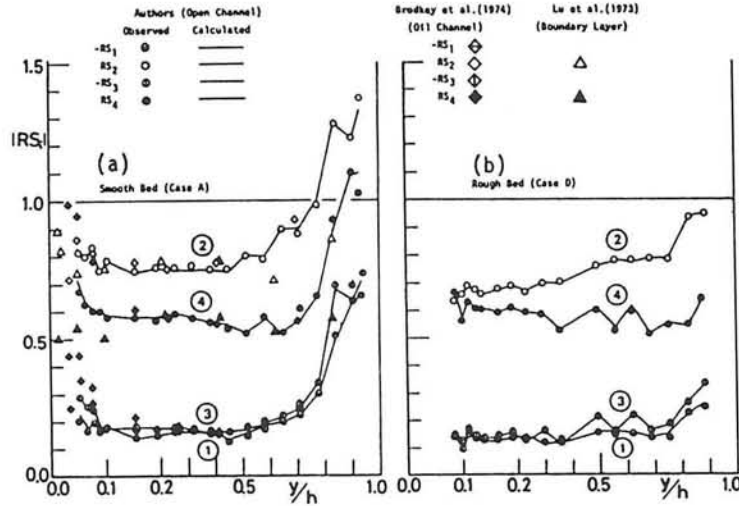


Fig. 5.12 Contributions to Reynolds stress from different events with $H=0$.

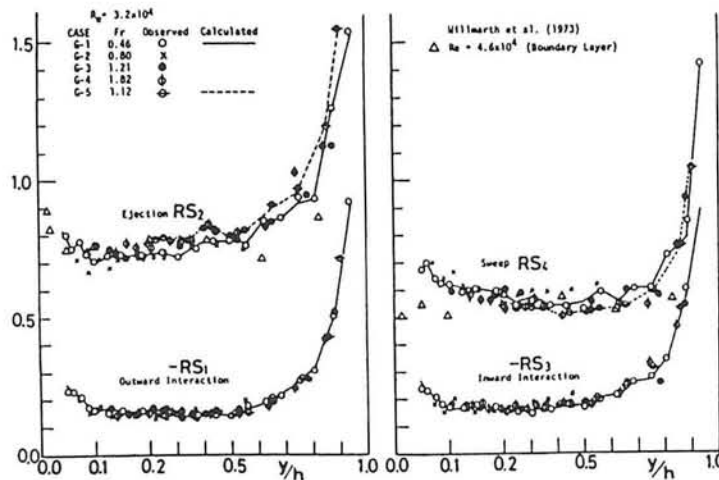


Fig. 5.13 Contributions to Reynolds stress from different events with $H=0$.

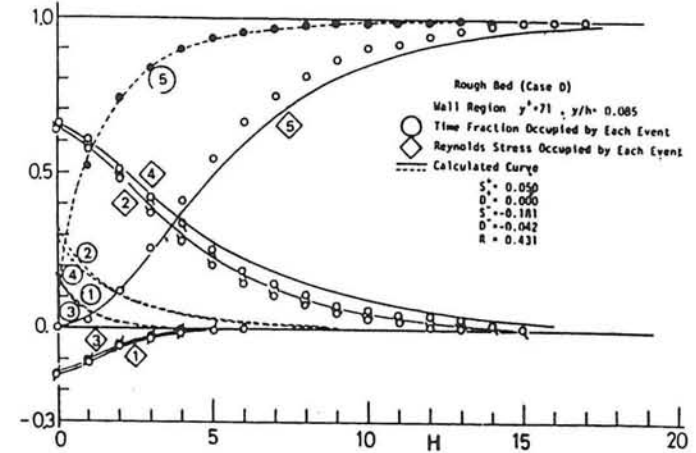


Fig. 5.11 Fractional contributions to Reynolds stress and fraction of time occupied by each event (rough bed).

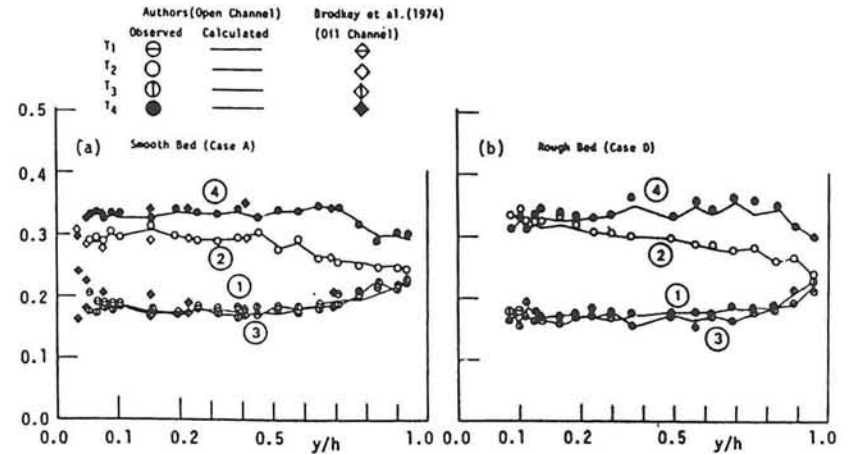


Fig. 5.14 Distributions of fraction of time occupied by each event with $H=0$.

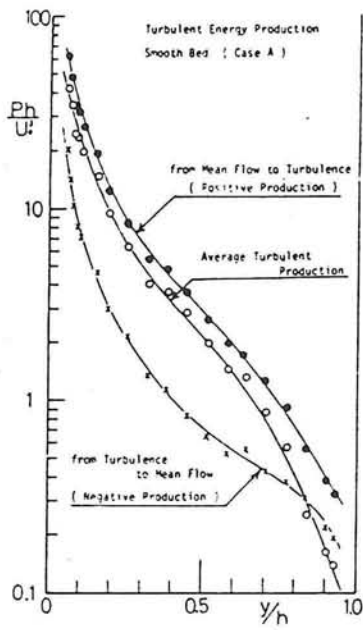


Fig. 5.15
Distributions of turbulent energy production (smooth bed).

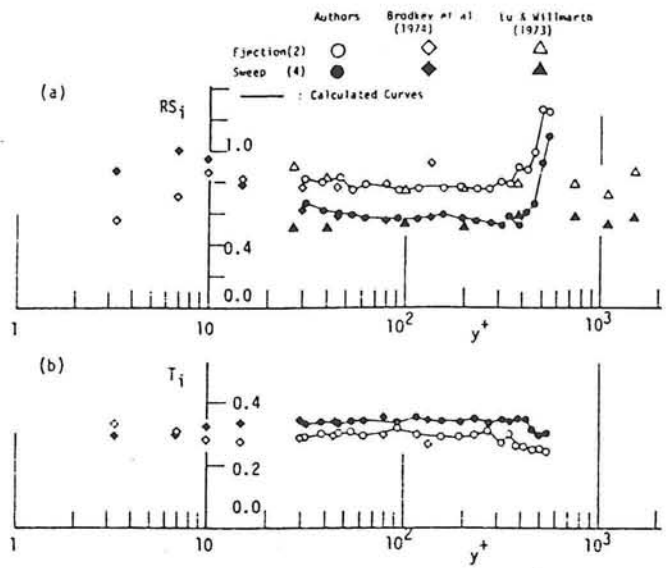


Fig. 5.16
Distributions of RS_i and T_i of ejection and sweep in the wall region ($y^+ < 100$).

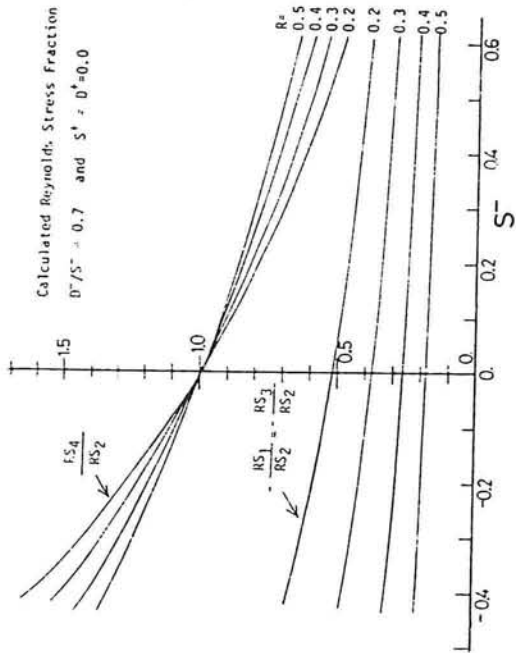


Fig. 5.17 Calculated fractional contributions to Reynolds stress.

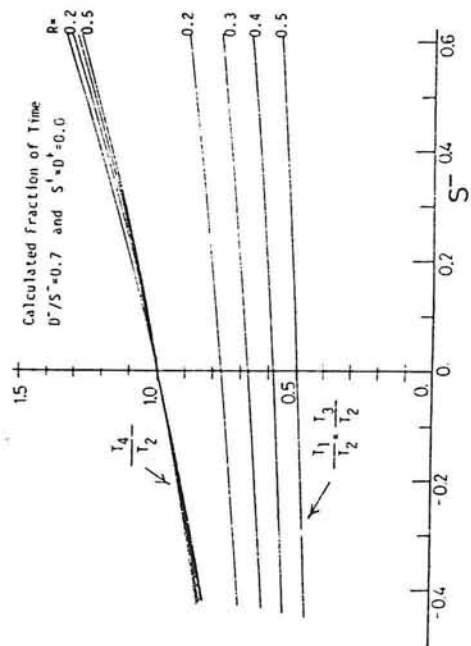


Fig. 5.18 Calculated fraction of time.

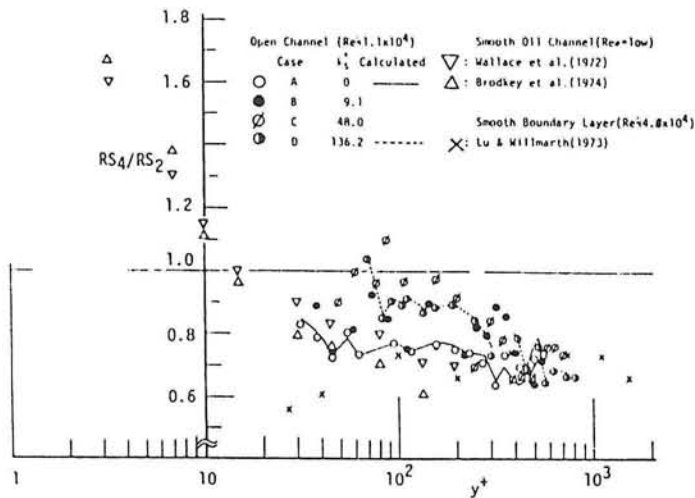


Fig. 5.19 The rate RS_4/RS_2 with $H=0$ as a function of y^+ .

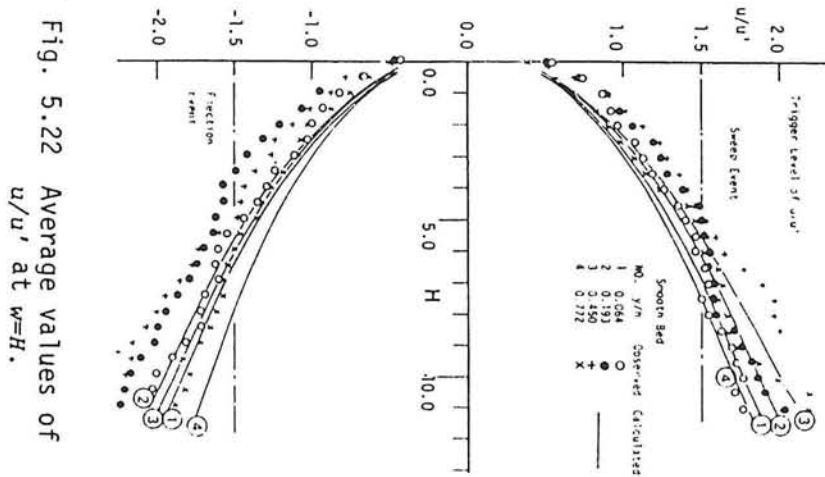


Fig. 5.22 Average values of u/u^+ at $w=H$.

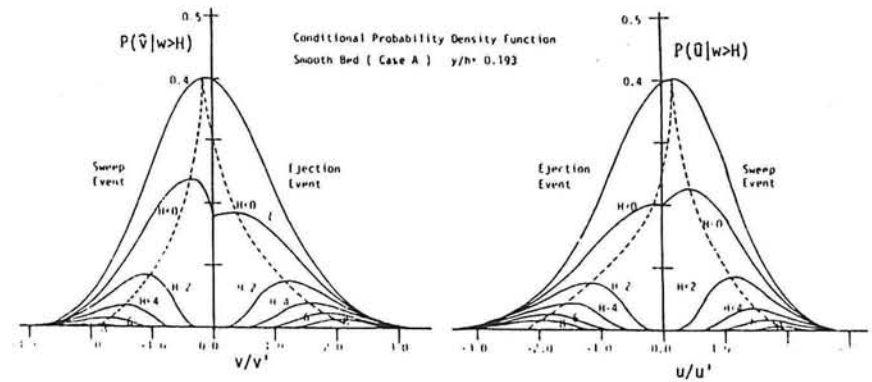


Fig. 5.21 Conditional probability distributions of u and v .

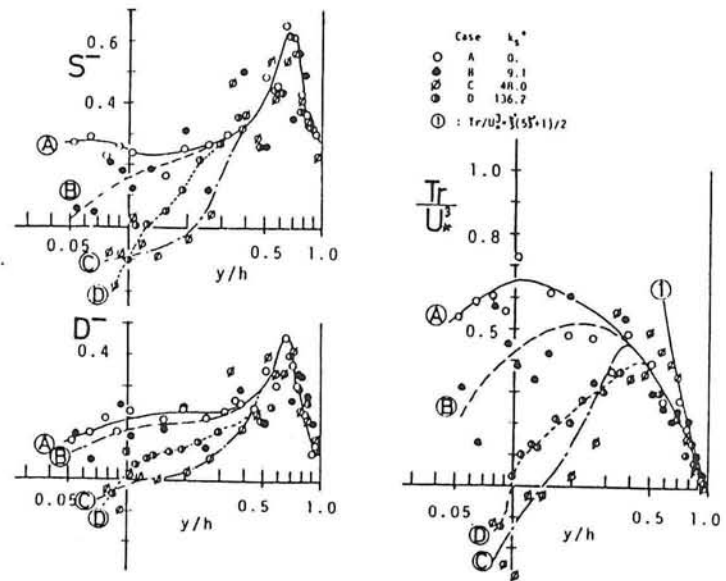
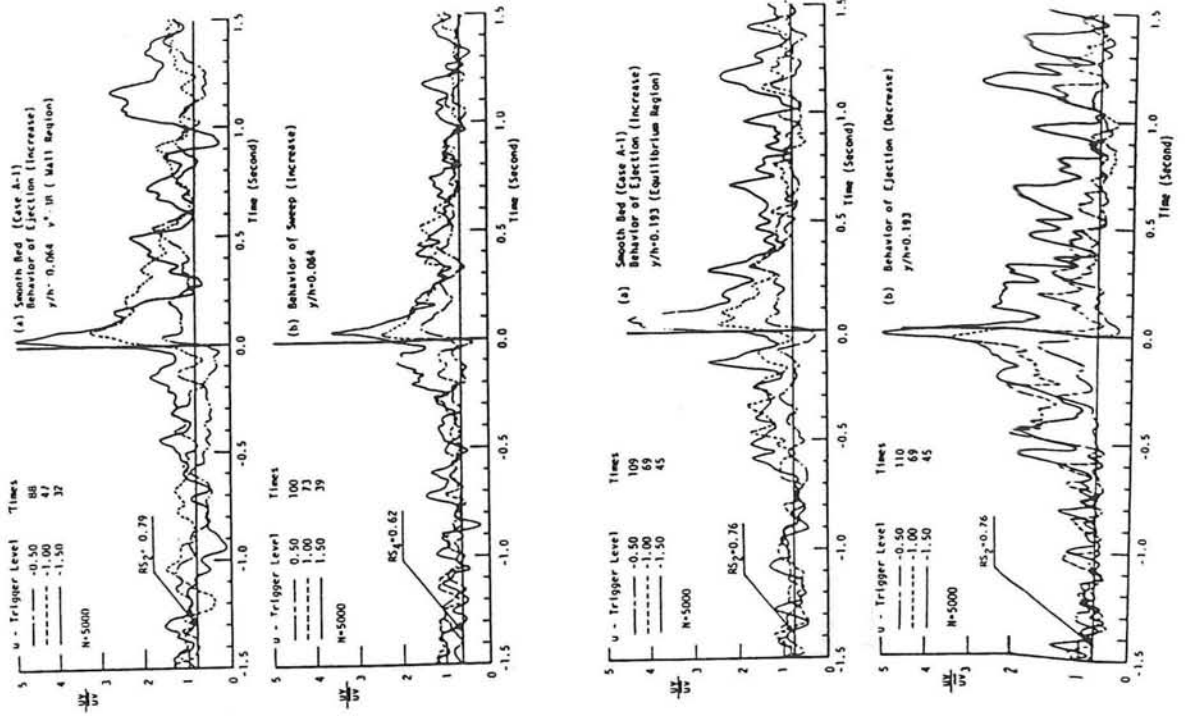


Fig. 5.20 Effects of roughness expressed in terms of S^- , D^- and Tr^+ .



Figs. 5.23 & 5.24 Behavior of ejection or sweep motions at the trigger level u_z in the wall and equilibrium regions.

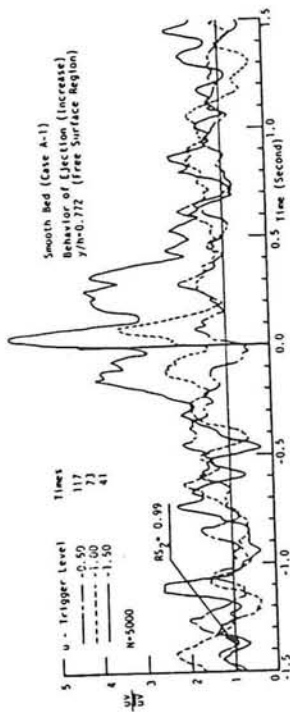


Fig. 5.25 Behavior of ejection motion in the free-surface region.

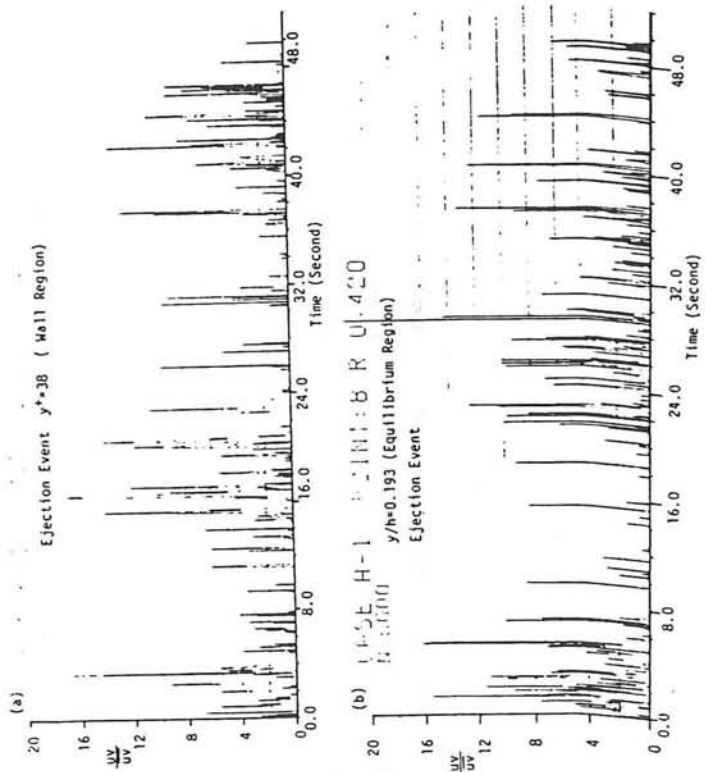


Fig. 5.26 Fluctuations of Reynolds stress at the ejection event.

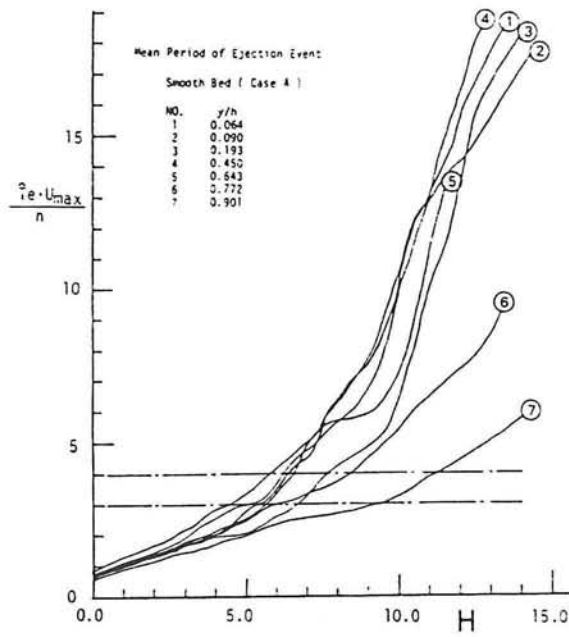


Fig. 5.27 Mean period $\hat{\tau}_e$ of ejection event with H .

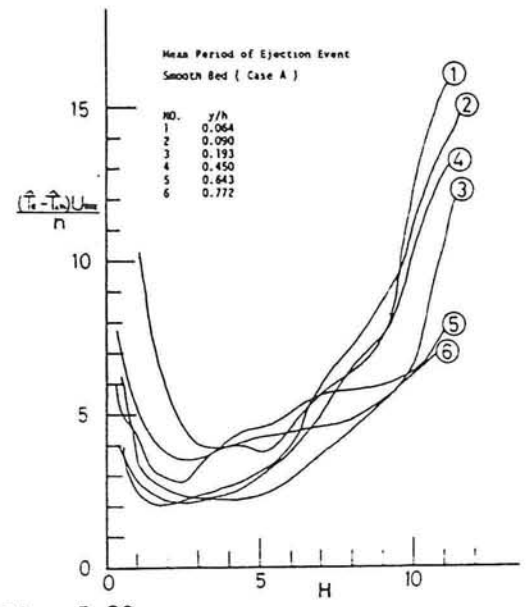


Fig. 5.29 Mean period $(\hat{\tau}_e - \hat{\tau}_{in})$ of ejection event where interaction event is subtracted.

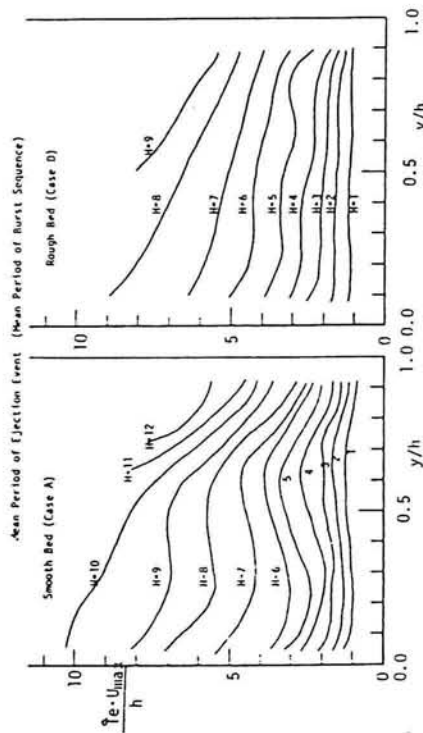


Fig. 5.28 Mean period $\hat{\tau}_e$ of ejection event with y/h .

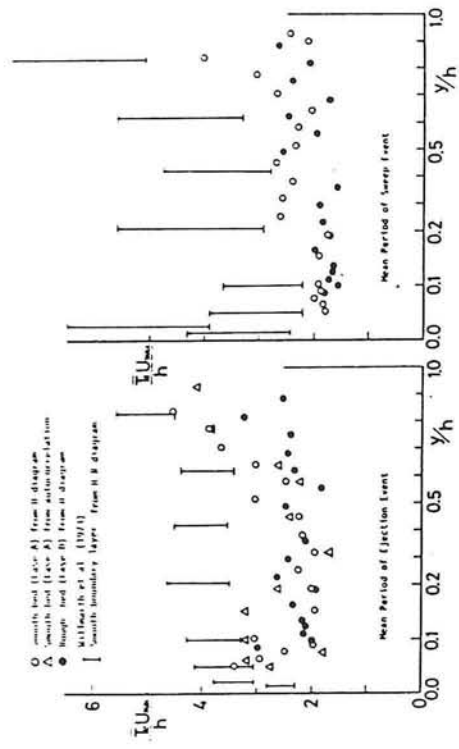


Fig. 5.30 Mean period of bursting phenomenon (lower-velocity group).

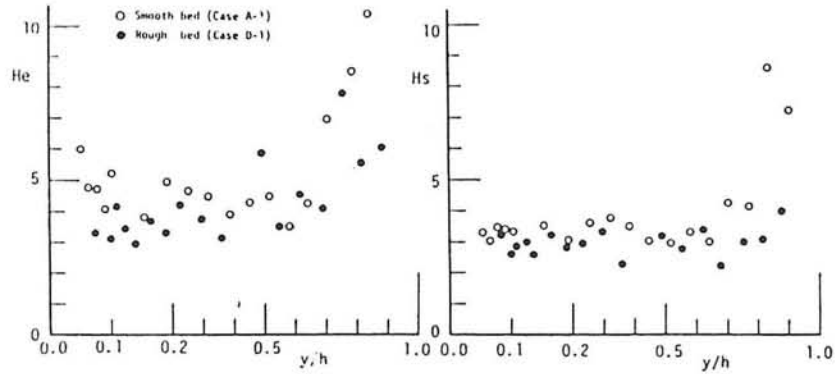


Fig. 5.33 Trigger level H_e (ejection) and H_s (sweep).

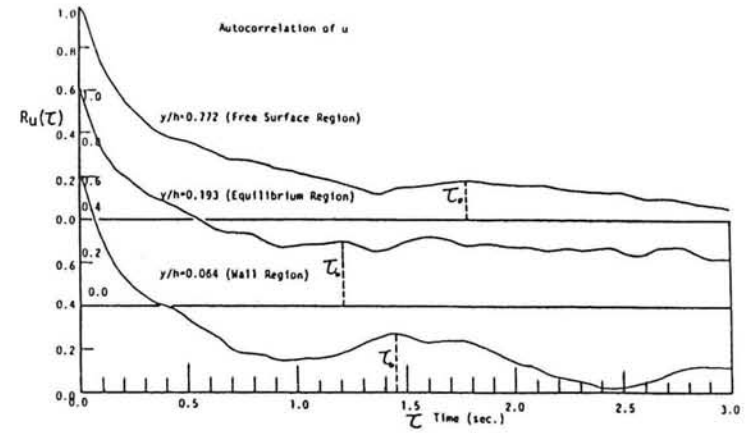


Fig. 5.31 Autocorrelation $R_u(\tau)$ of u .

Fig. 5.34 Trigger level \hat{u}_e (ejection) and \hat{u}_s (sweep).

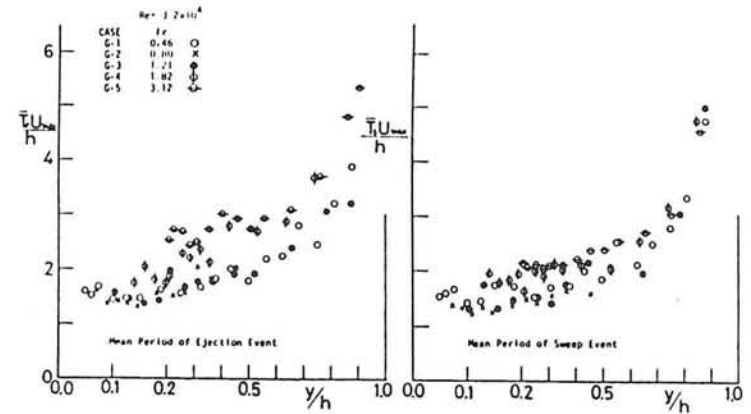
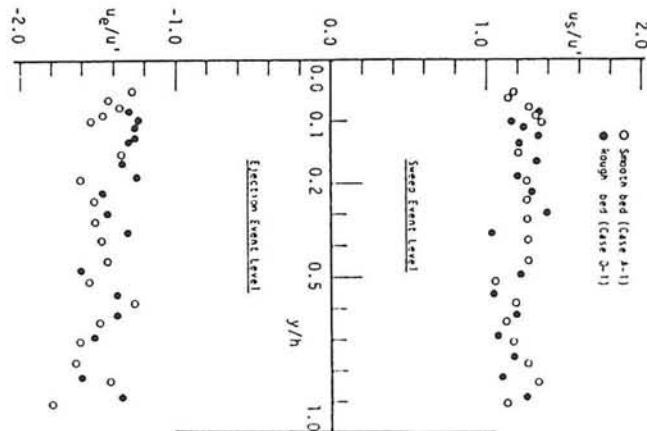


Fig. 5.32 Mean period of bursting phenomenon (higher-velocity group).

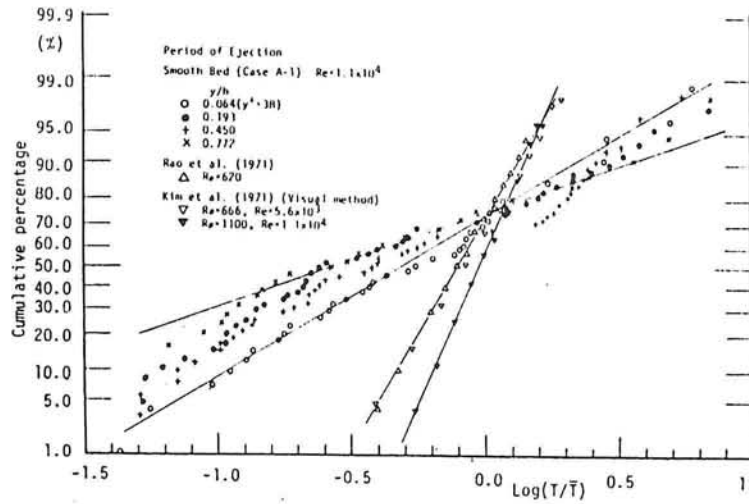


Fig. 5.35 Probability distributions of period of bursting phenomenon.

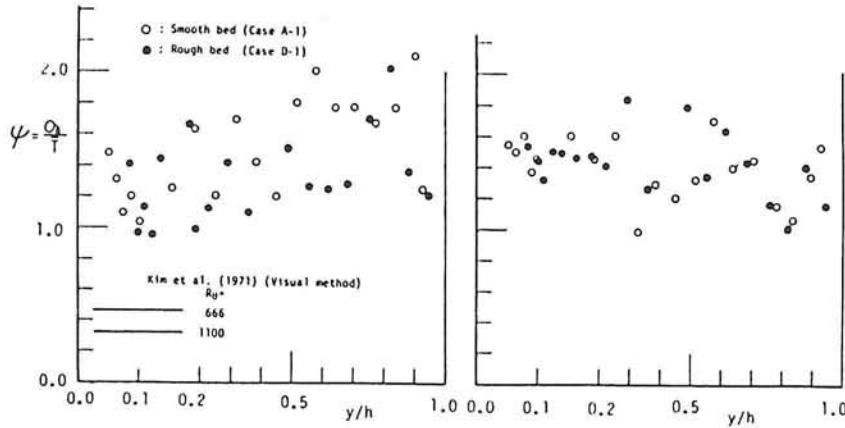


Fig. 5.37 Coefficient of variation $\sigma_T/T̄$ of period of bursting phenomenon.

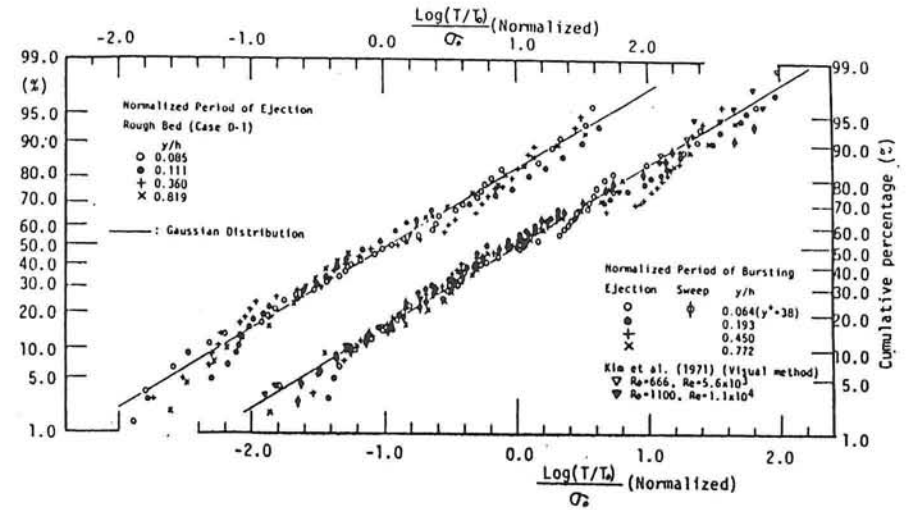


Fig. 5.36 Normalized probability distributions of period τ .

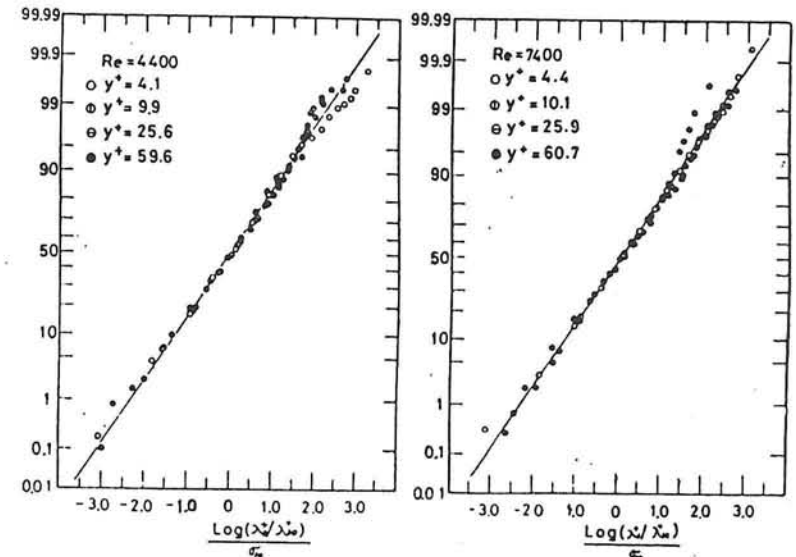
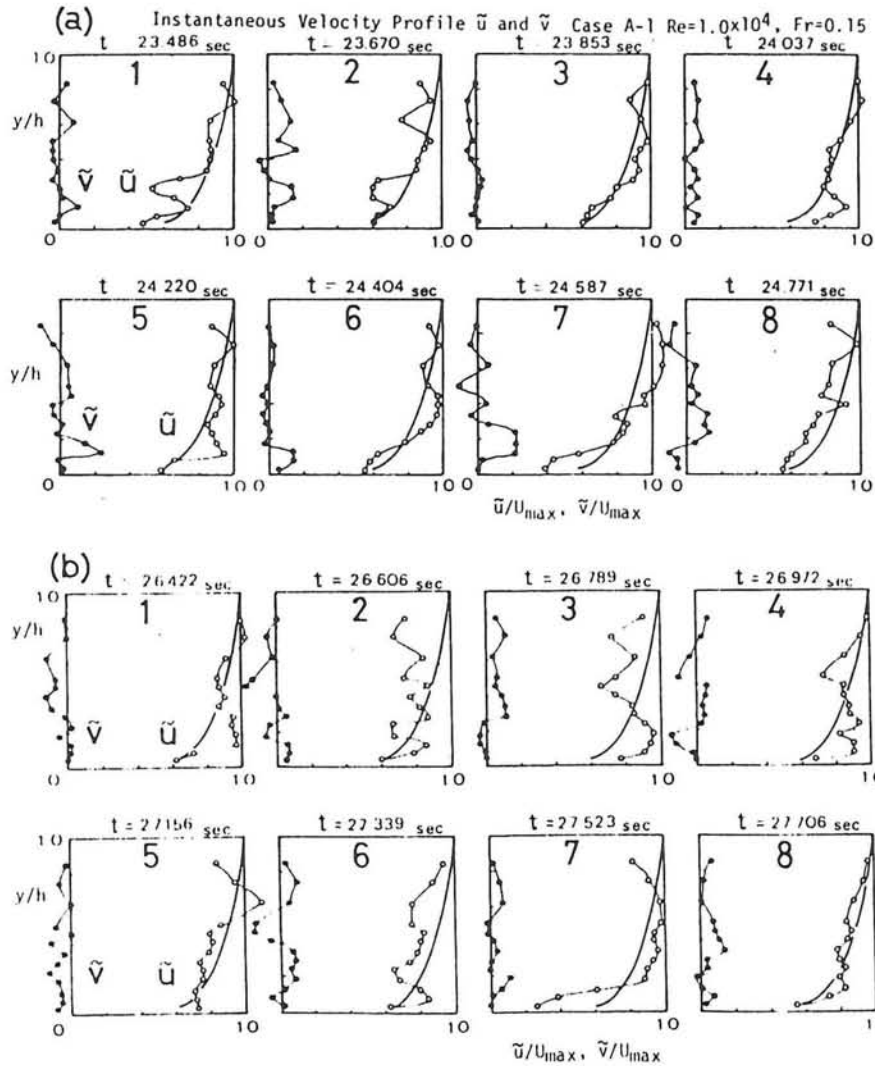


Fig. 5.38 Probability distributions of λ_3^+ of bursting phenomenon.



40

Fig. 5.40 Instantaneous velocity profiles \tilde{u} and \tilde{v} over smooth bed.

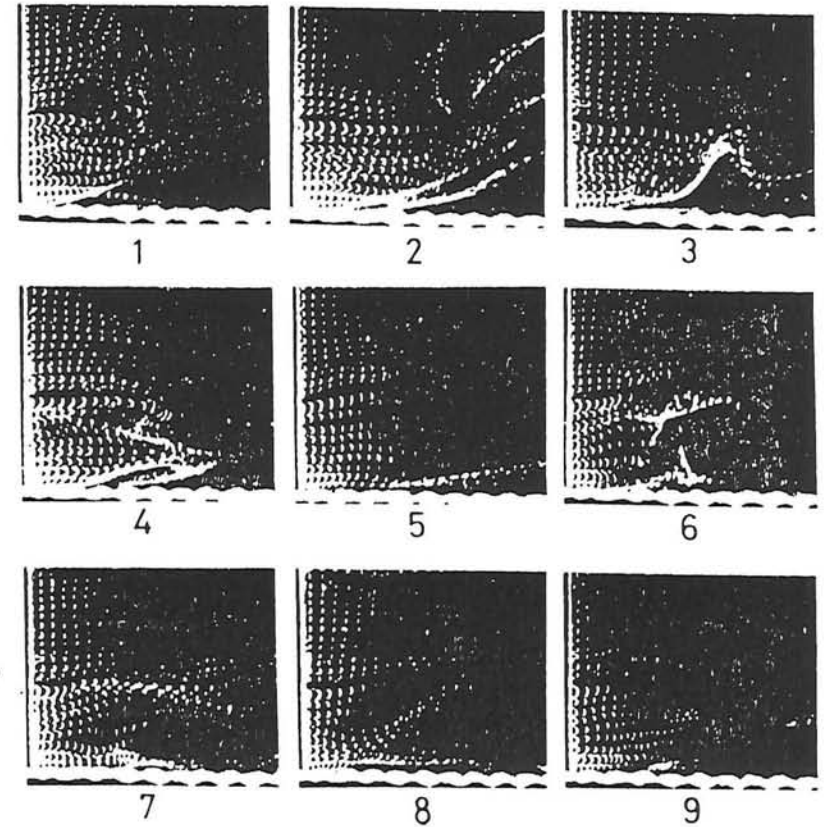


Fig. 5.39 Some typical photographic illustrations of ejection or sweep motion (Case D-1).

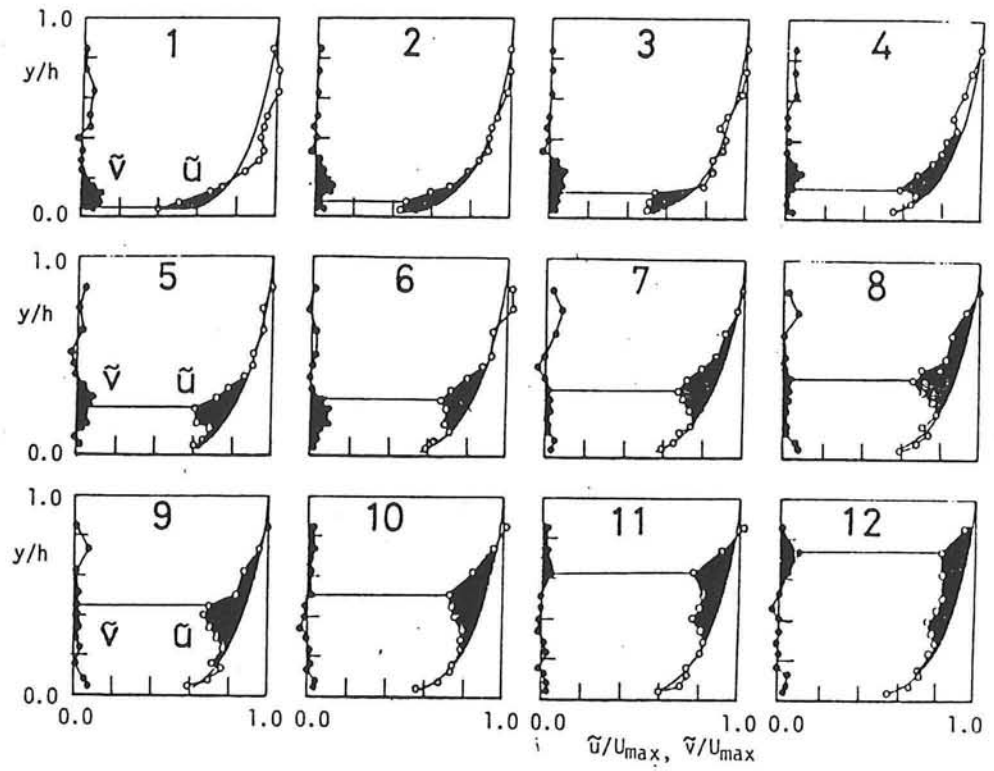


Fig. 5.41 Conditionally averaged instantaneous velocity profiles at instants when \tilde{u} is minimum.

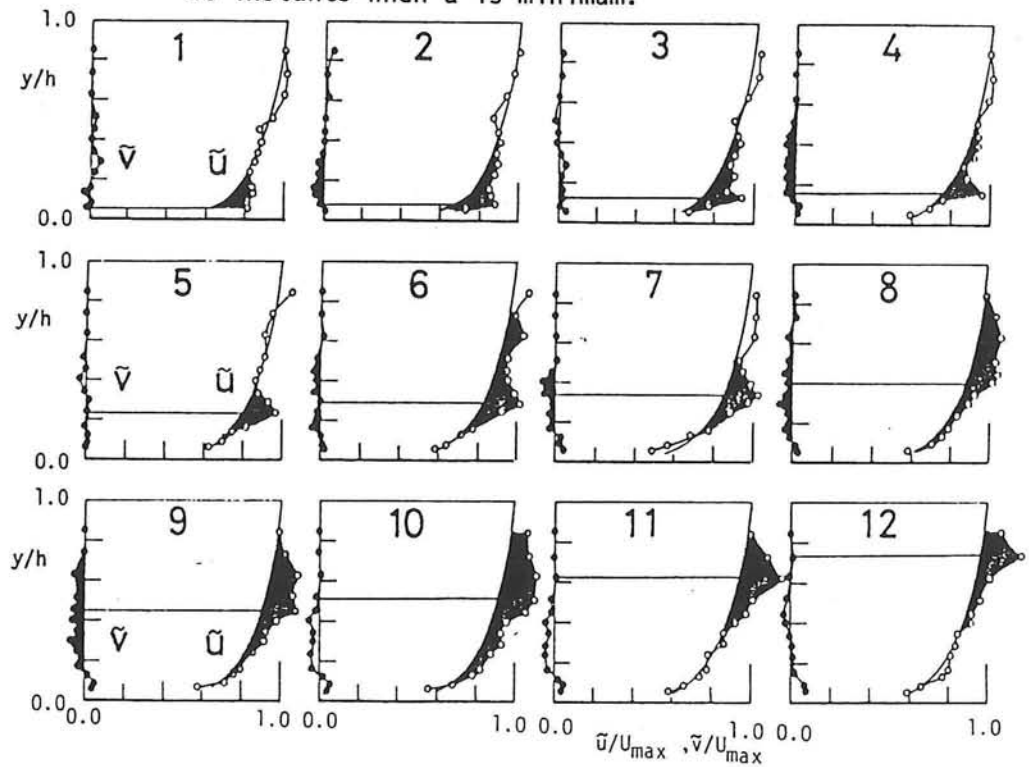
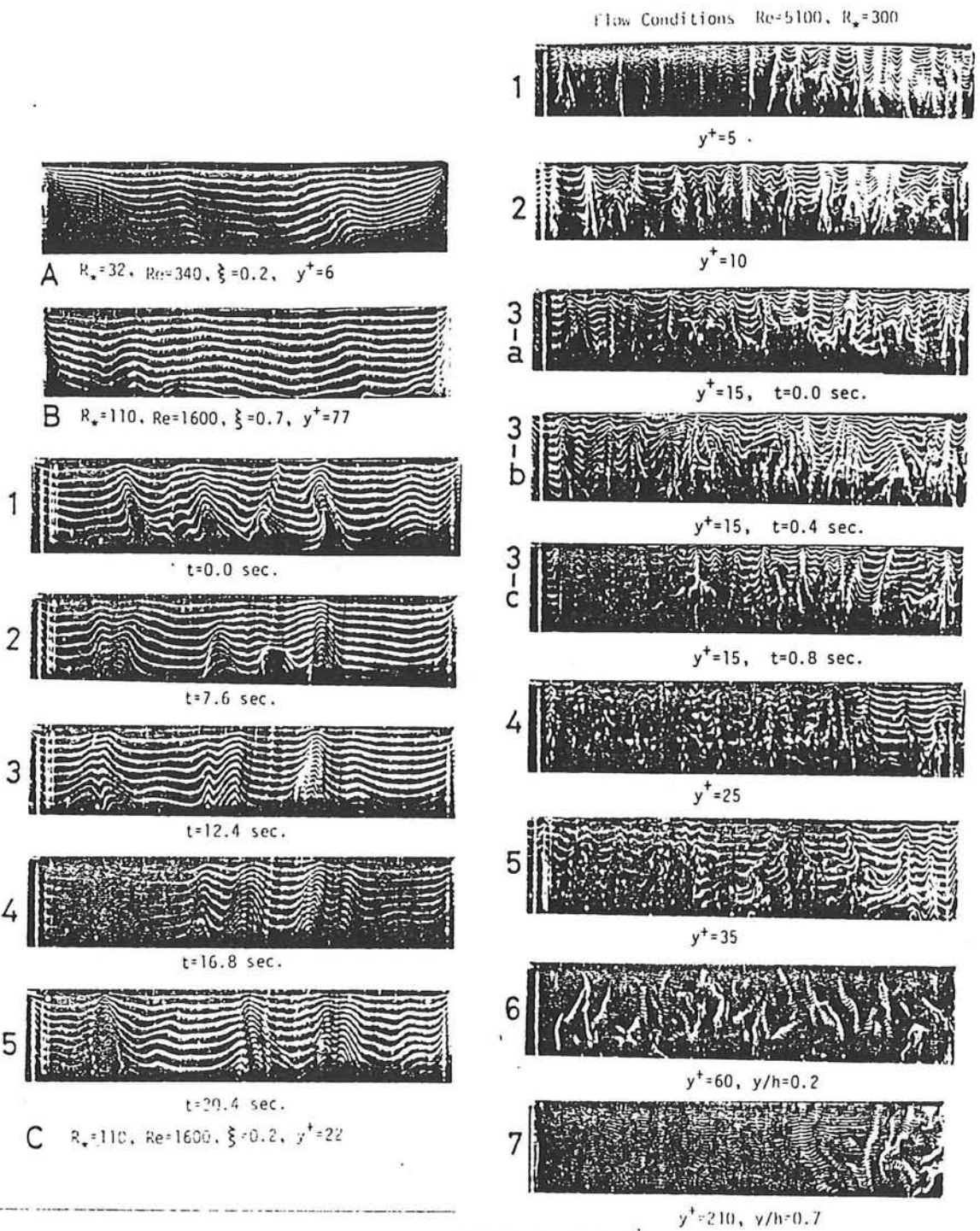


Fig. 5.42 Conditionally averaged instantaneous velocity profiles at instants when \tilde{u} is maximum.



Figs. 5.43 & 5.44 Some typical photos of instantaneous velocity profiles on the horizontal plane ($Re=340, 1600$ and 5100).

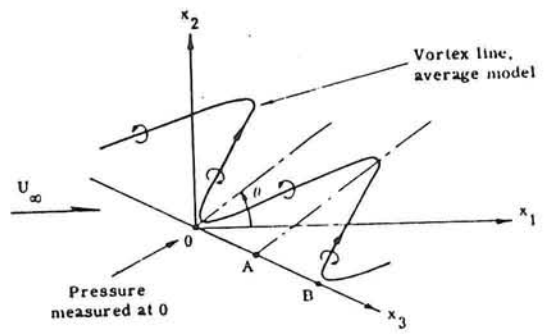


Fig. 6.1 An average model of vortex line near the wall (after Willmarth et al.).

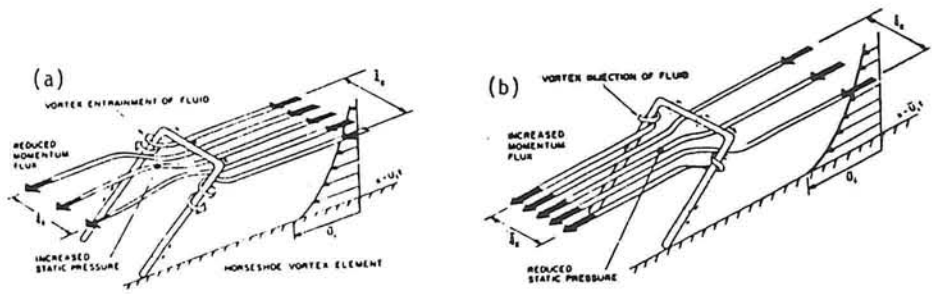


Fig. 6.3 'Turbulent shear stress' mechanism by horseshoe vortex (after T.J.Black).

43

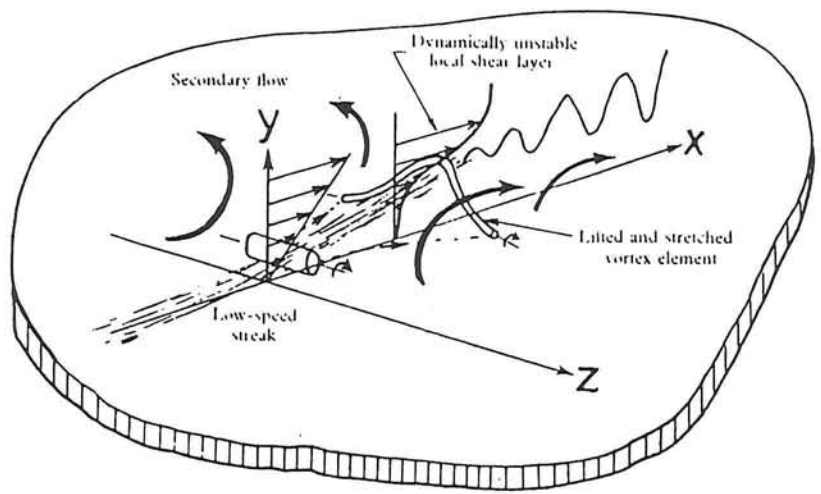


Fig. 6.2 Mechanics of streak breakup (after Kline et al.).

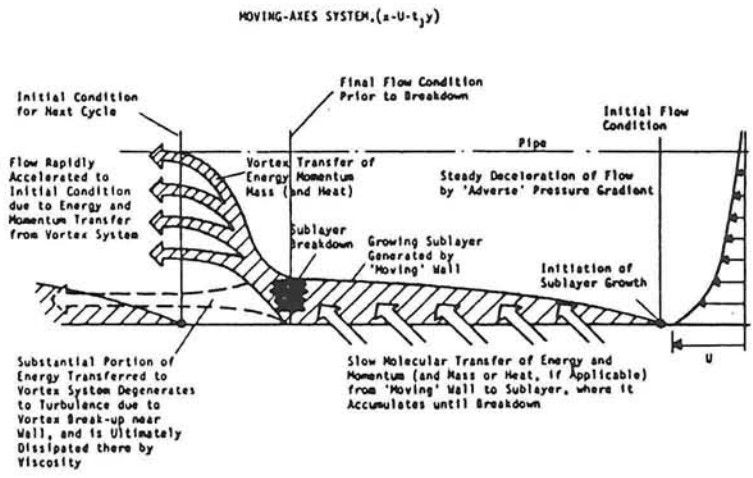


Fig. 6.4 Cyclic development and breakdown of primary motion (after T.J. Black).

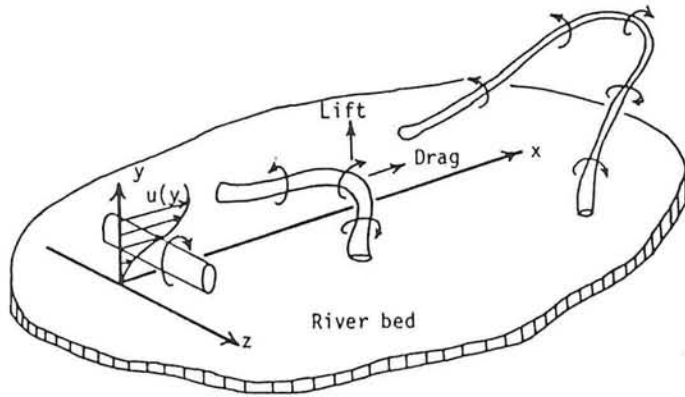


Fig. 6.5 Ω -shaped vortex over river bed
(after S. Yokoshi).

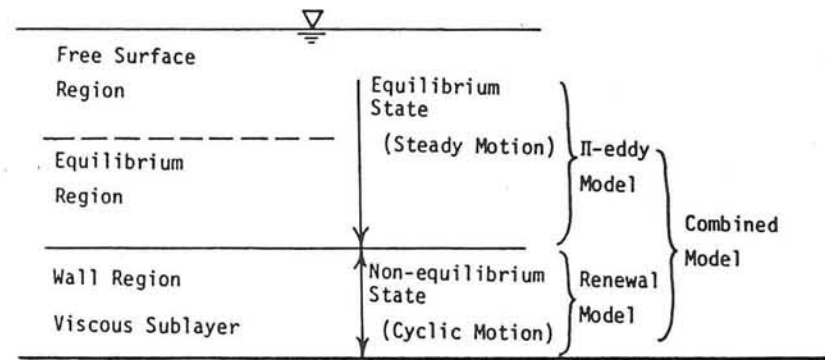


Fig. 6.7 Explanation of eddy model in this chapter.

44

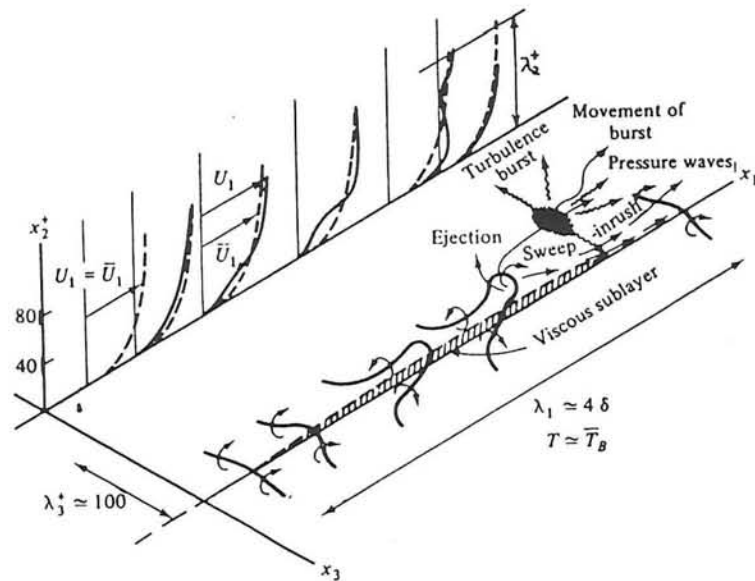


Fig. 6.6 Conceptual model of the turbulence near the wall during a 'cyclic' process (after J.O. Hinze).

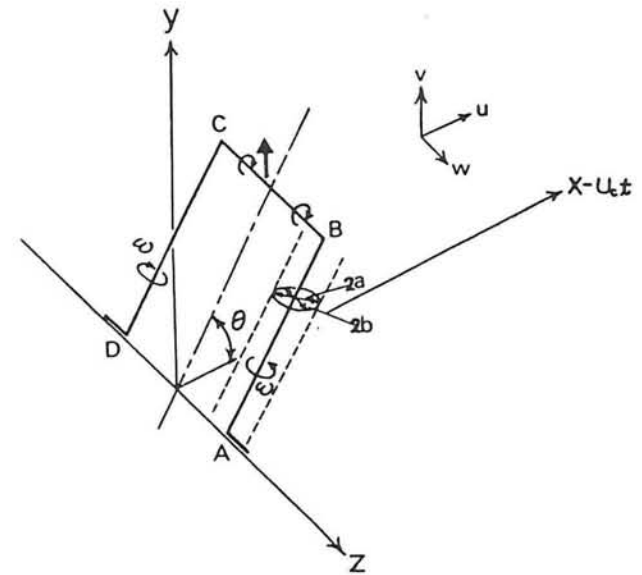


Fig. 6.8 A Π -eddy model in the moving-axes.

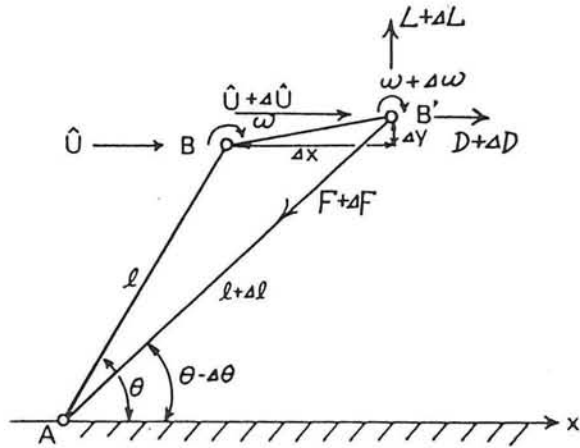


Fig. 6.9 Secondary motion of a Π -eddy (vortex-stretching).

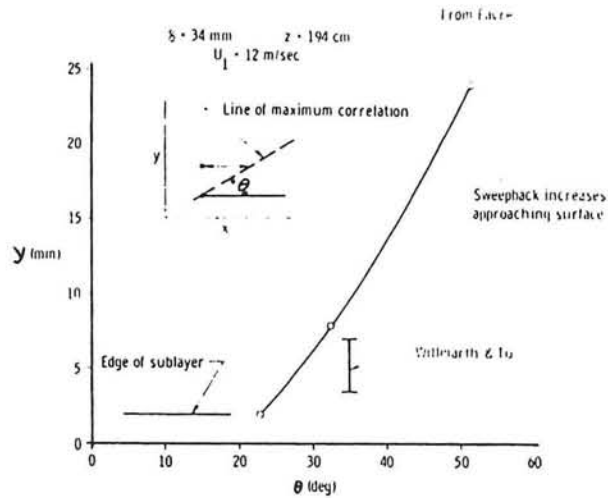


Fig. 6.10 Angle of eddy inclination to the wall (after J. Sternberg).

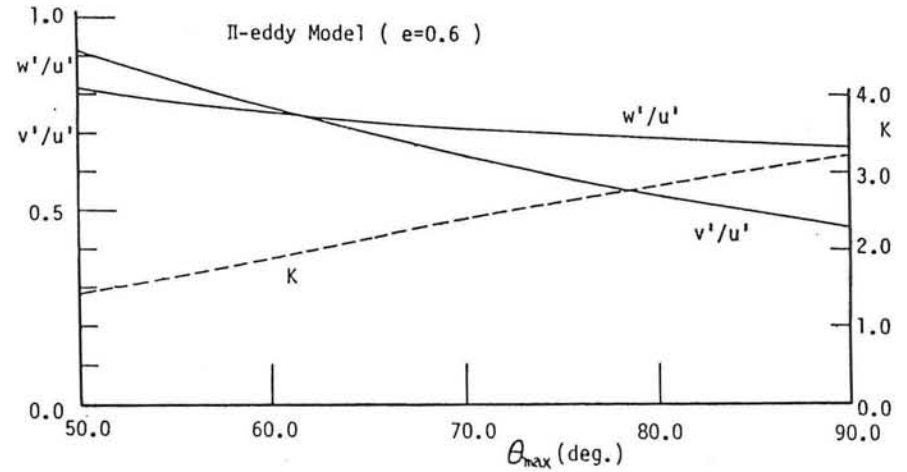


Fig. 6.11 Relative turbulence intensity predicted by Π -eddy model.

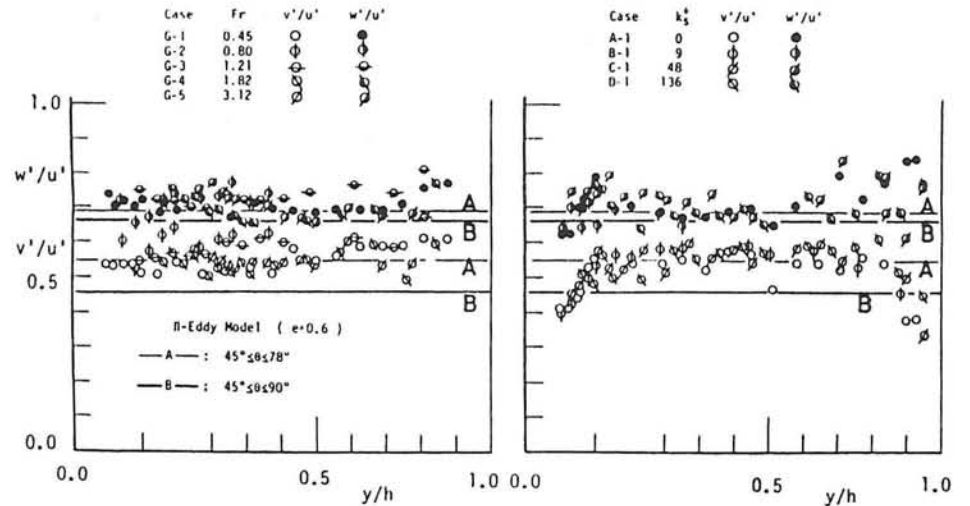


Fig. 6.12 Comparison between Π -eddy model and experimental results.

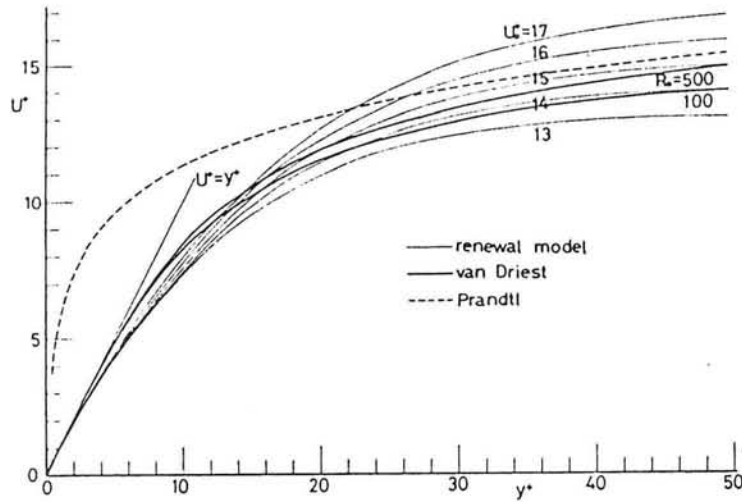


Fig. 6.13 Mean velocity distributions when U_0^+ is varied.

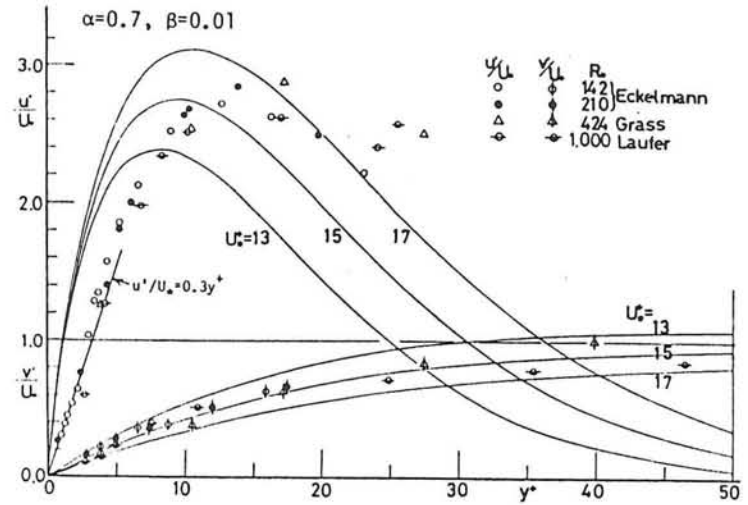


Fig. 6.15 Turbulence intensities when U_0^+ is varied.

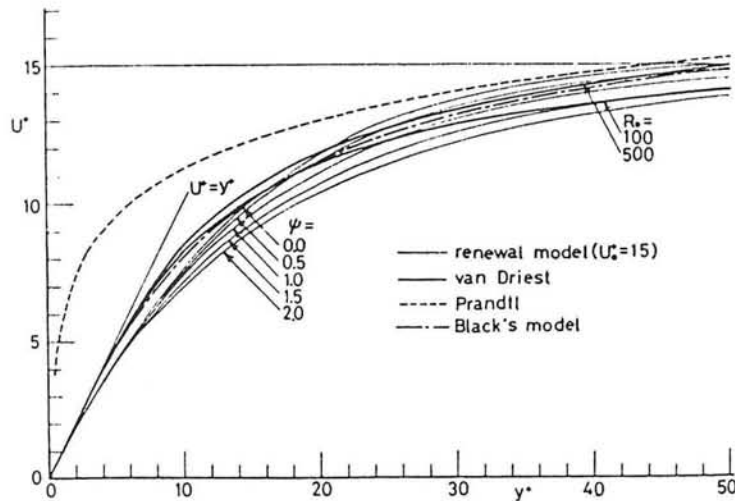


Fig. 6.14 Mean velocity distributions when ψ is varied.

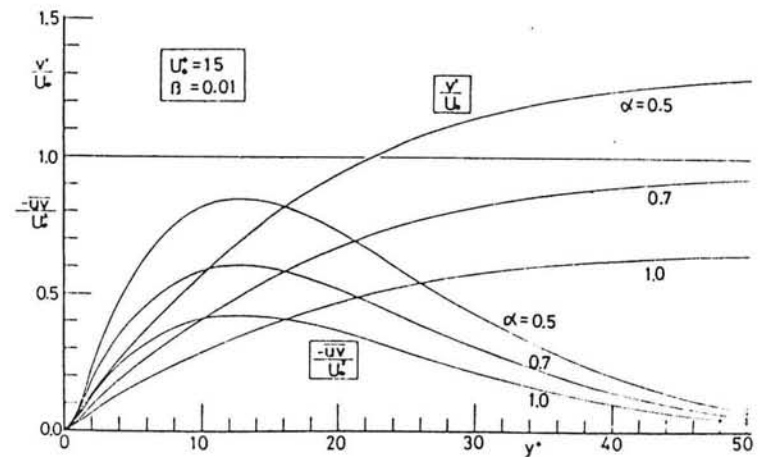


Fig. 6.16 Turbulence intensity and Reynolds stress when α is varied.

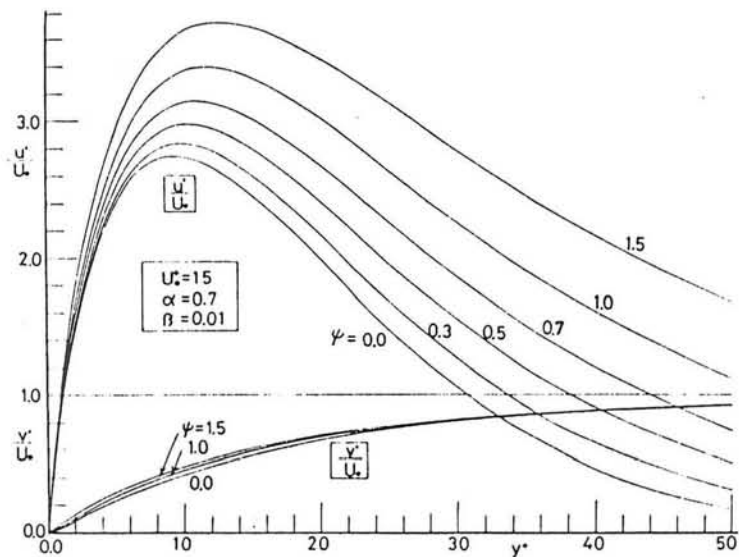


Fig. 6.17 Turbulence intensities when ψ is varied.

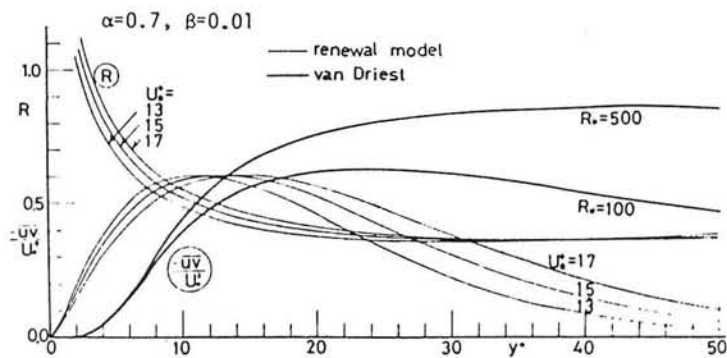


Fig. 6.18 Reynolds stress when U_0^+ is varied.

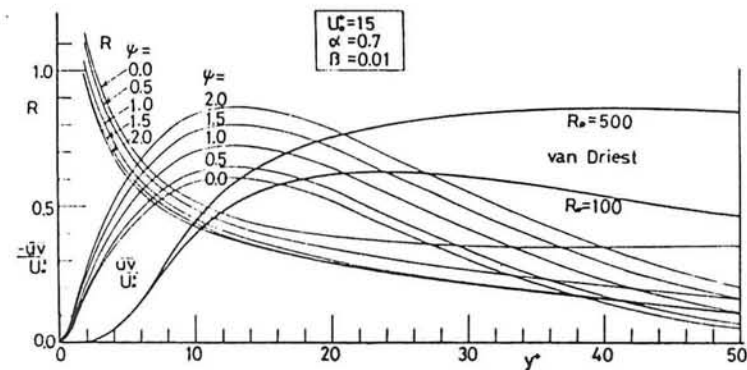


Fig. 6.19 Reynolds stress when ψ is varied.

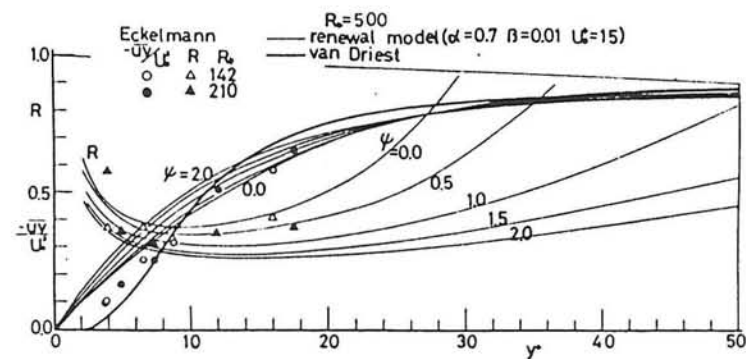


Fig. 6.20 Reynolds stress evaluated from $\partial v_t^+ / \partial y^+$ by renewal model.

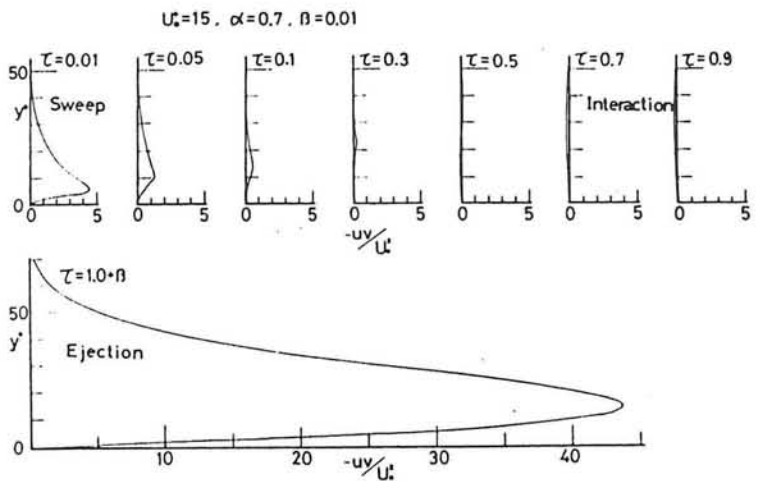


Fig. 6.22 Instantaneous Reynolds stress $-uv$ in a bursting cycle.

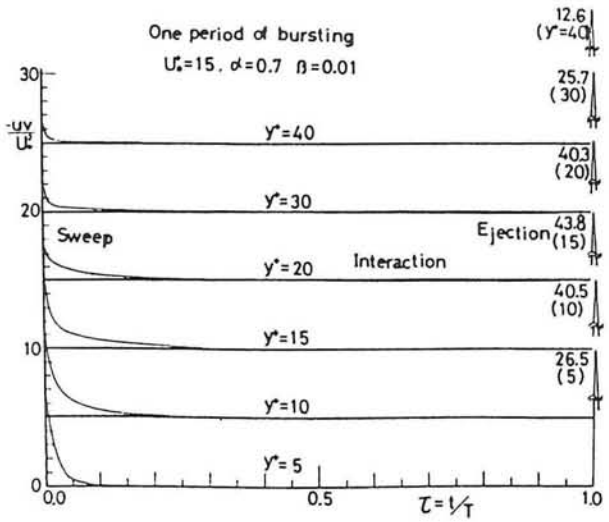


Fig. 6.23 Behaviour of Reynolds stress $-uv$ in a bursting cycle.

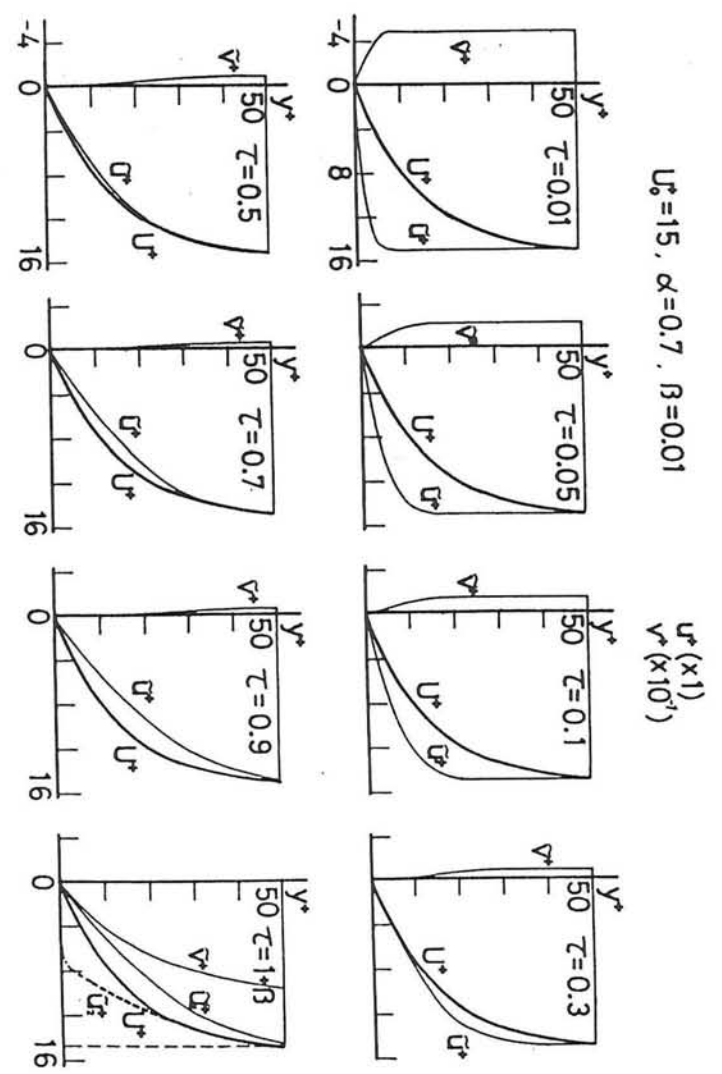


Fig. 6.21 Instantaneous velocity profile U^* and V^* in a bursting cycle.

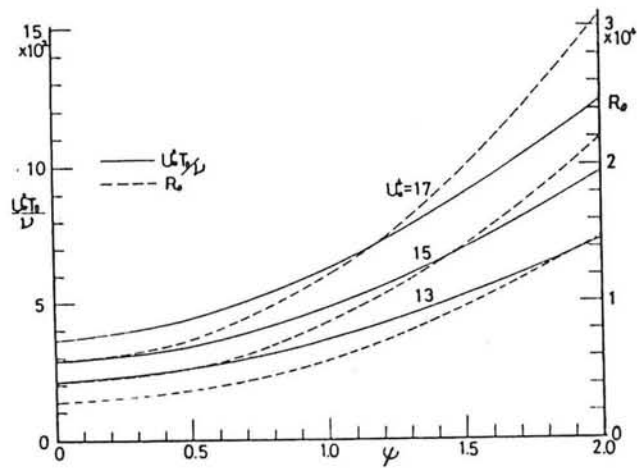


Fig. 6.24 Bursting period estimated by renewal model.

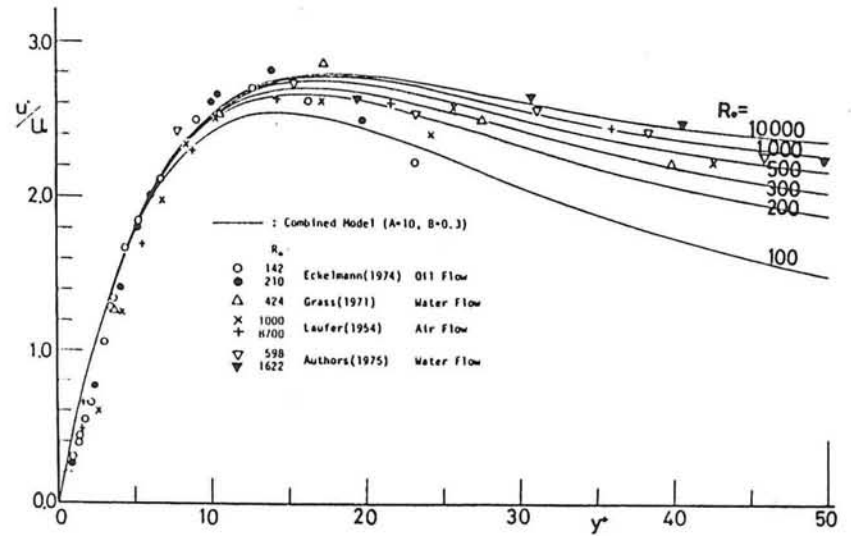


Fig. 6.26 Turbulence intensity estimated by combined model

	Viscous Sublayer	Viscous Superlayer
Height roughly	$y^+ \sim (10 - 15)$	$y^+ \sim \delta$
Interface	Quasi-laminar --- Turbulent	Turbulent --- Nonturbulent
Phenomenon	Bursting	Intermittent
Characteristic Function	Damping Factor Γ	Intermittency Factor γ

Fig. 6.25 Comparison between viscous-sublayer and superlayer.

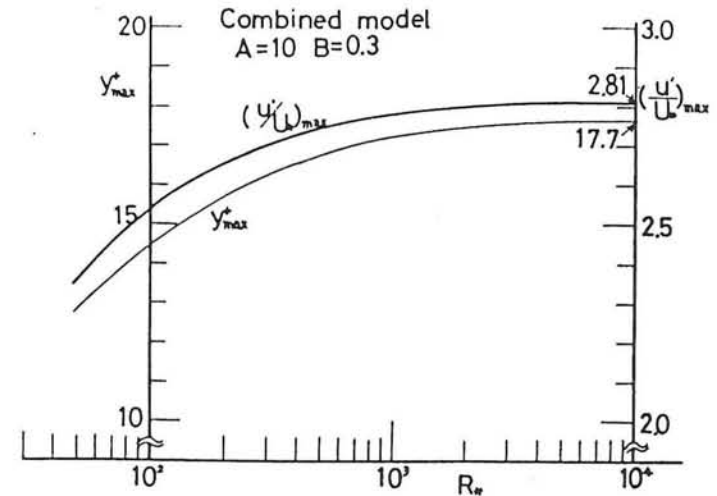


Fig. 6.27 Maximum characteristic of u' / u_* by combined model.

Part 2 Turbulent structure over permeable bed
 Chapter 8 Interaction between main and seepage flows

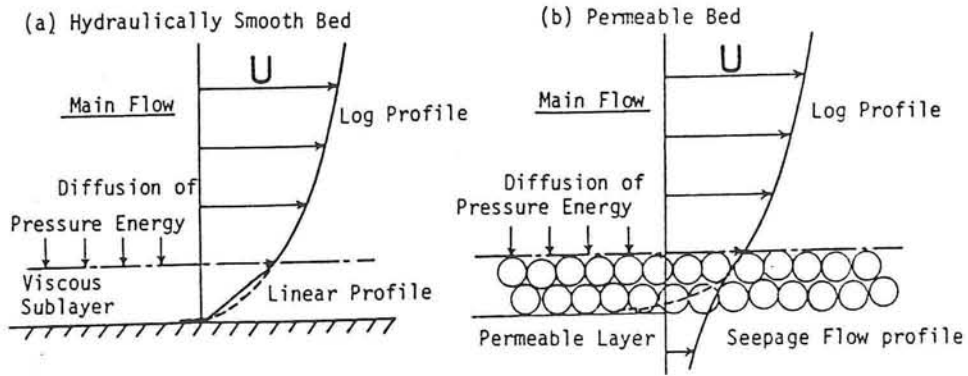


Fig. 8.1 Analogy between smooth and permeable flow fields.

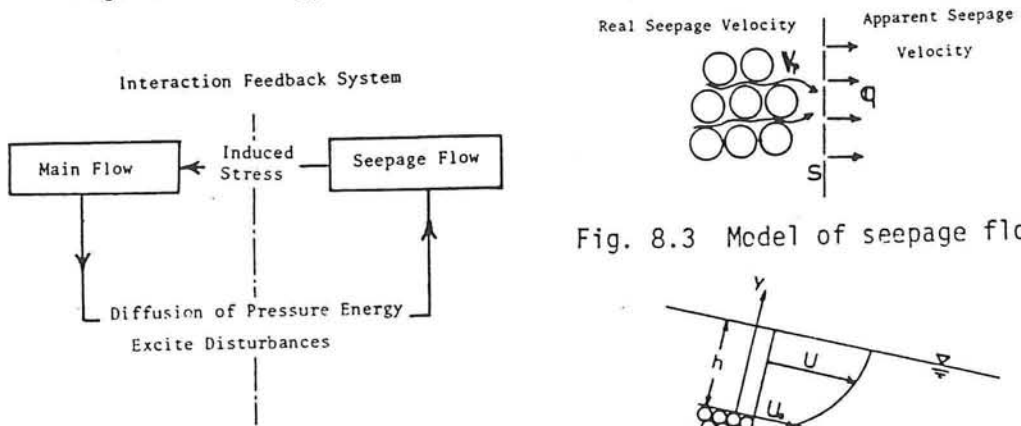


Fig. 8.2 Hydrodynamic interaction mechanism between main and seepage flows.

Fig. 8.3 Model of seepage flow.

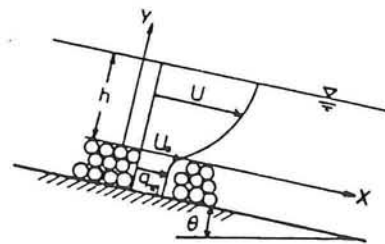


Fig. 8.4 Turbulent permeable open-channel flow field.

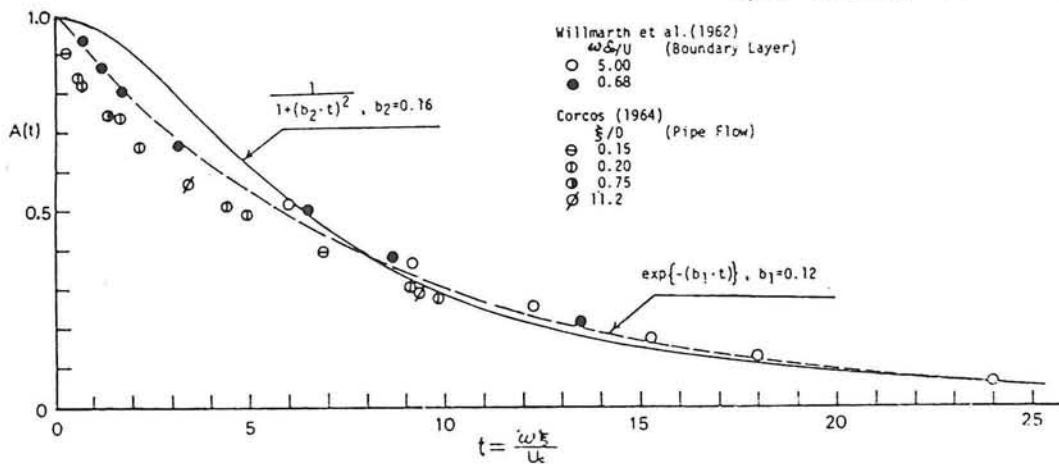


Fig. 8.5 Amplitude of the cross-spectral function.

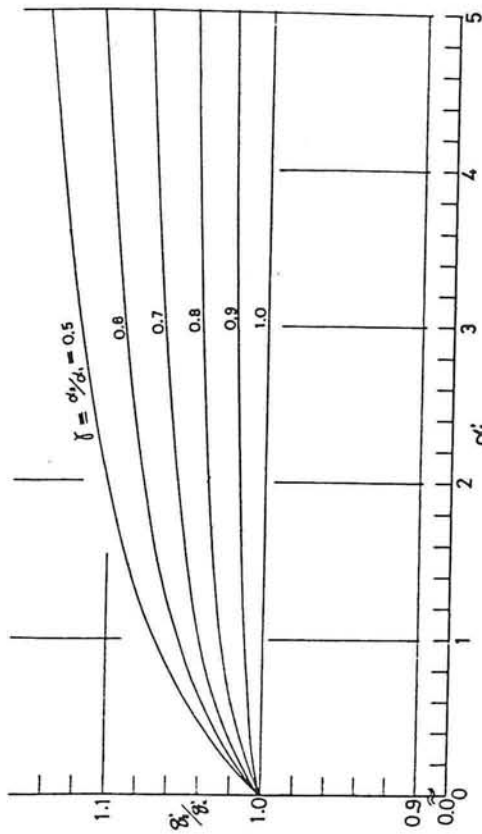


Fig. 8.6 Anisotropy of turbulence intensity in the seepage flow.

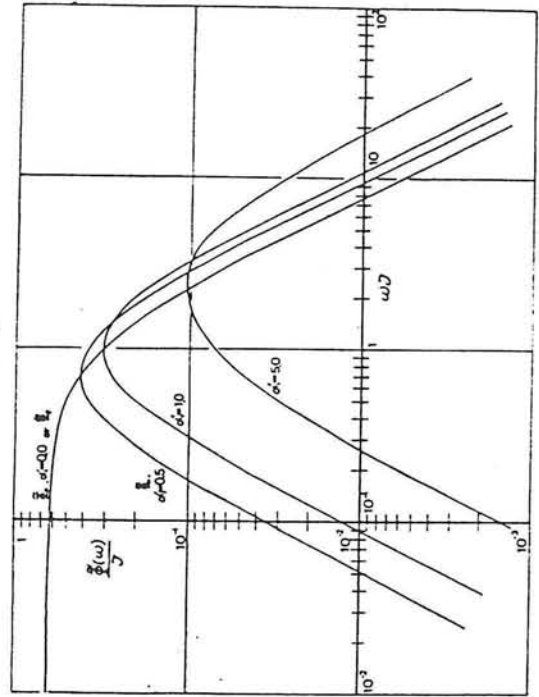


Fig. 8.7 Frequency spectra of turbulence in the seepage flow.

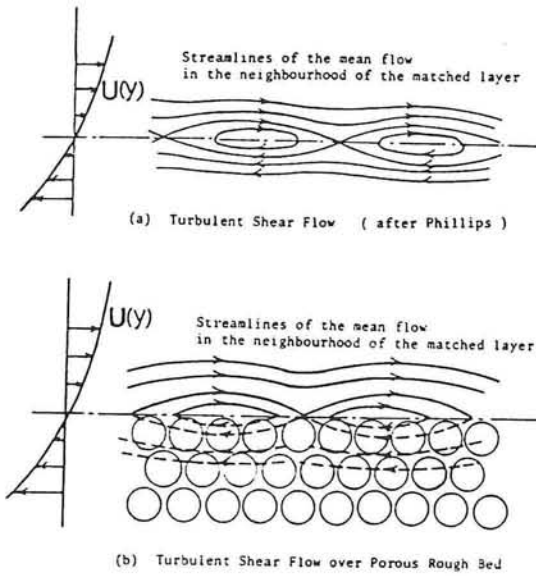


Fig. 8.8 Streamlines of mean flow in the neighbourhood of the matched layer (Cat's eye).

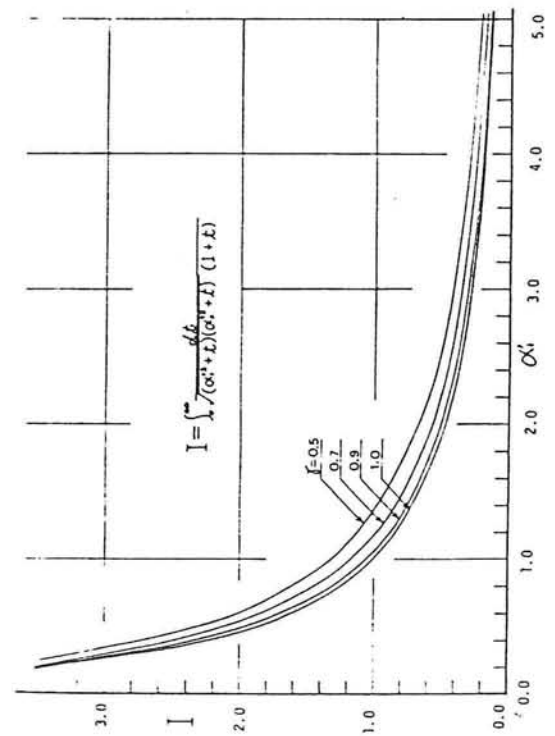


Fig. 8.9 Coefficient I as a function of α_i .

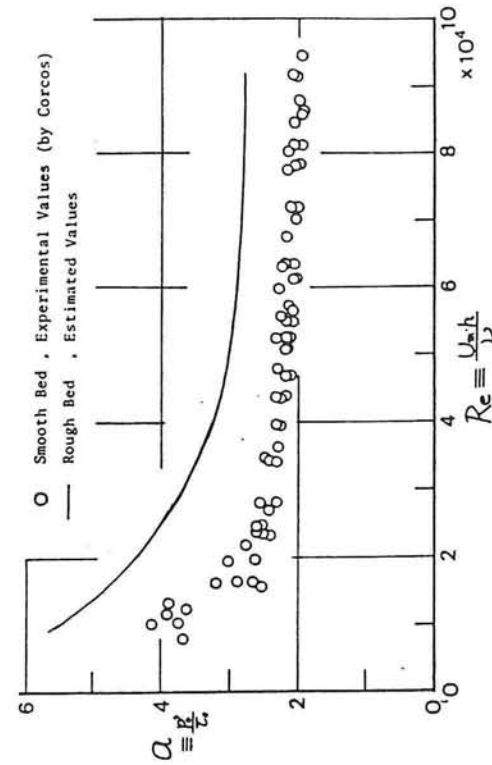


Fig. 8.10 Dimensionless wall-pressure intensity as a function of Re (after G.M. Corcos).

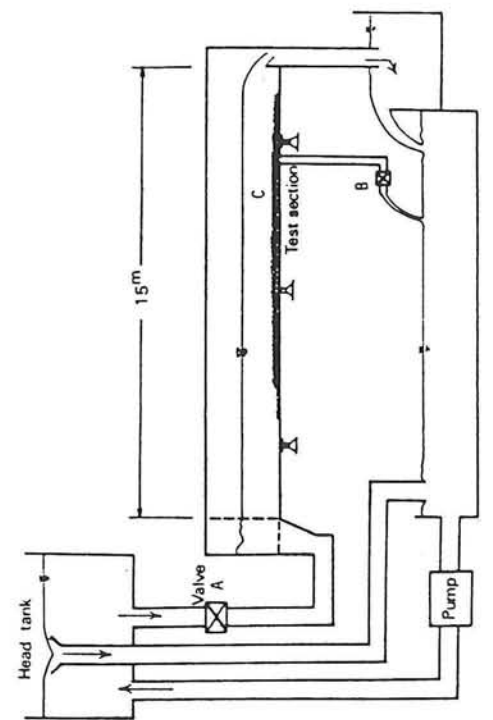


Fig. 8.11 15m recirculating tilting flume.

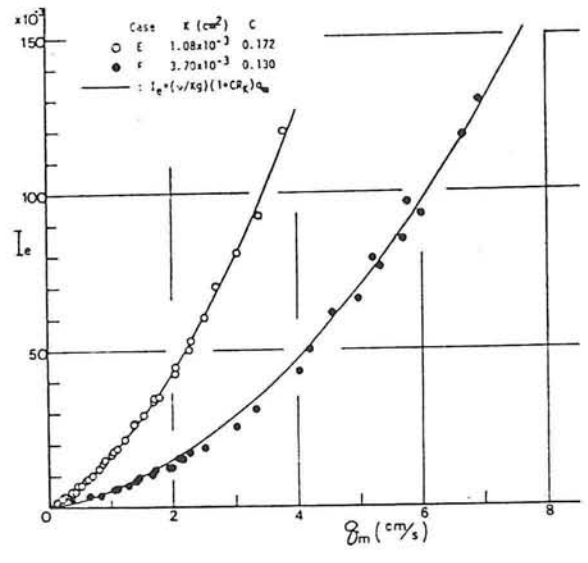


Fig. 8.12 Relationship between seepage velocity q_m and hydraulic gradient I_e .

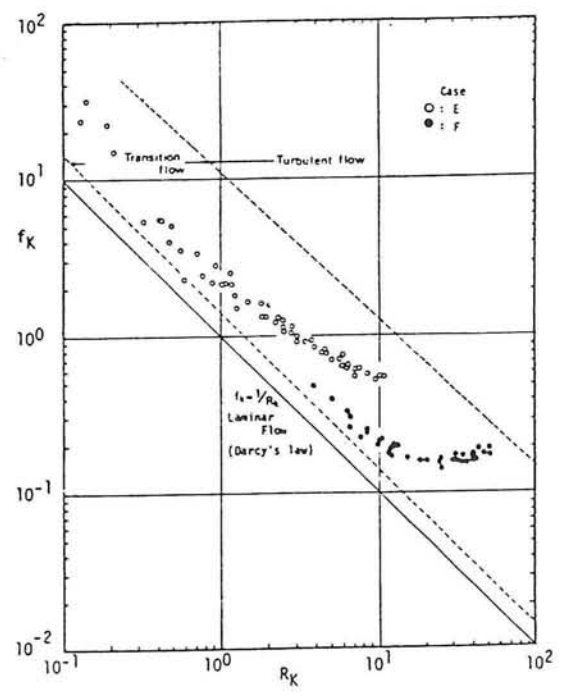


Fig. 8.13 Relationship between R_K and f_K .

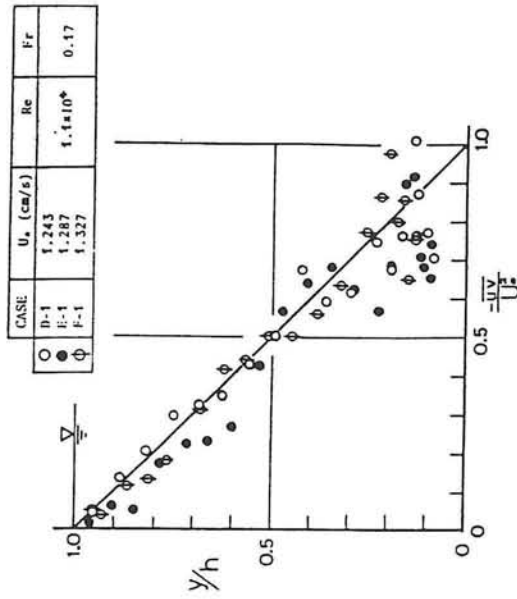


Fig. 8.14 Distributions of Reynolds stress over porous beds.

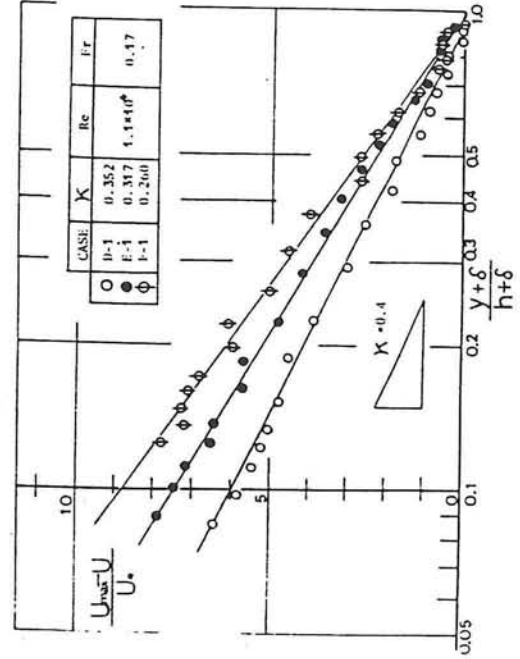


Fig. 8.15 Velocity defect law of the main flow.

CASE	$K(\text{cm}^2)$	C	n	d_m (cm)	porous strata
E	1.08×10^{-1}	0.172	0.39	1.25	3
F	3.70×10^{-1}	0.130	0.54	1.25	5

Table 8.1 Properties of porous media.

CASE RUN	r_i/r_0	α	A_m	
			from b_1	from b_2
E-1	0.0672	5.5	0.184	0.156
F-1	0.1226	5.5	0.096	0.083
E-2	0.0586	3.8	0.149	0.126
F-2	0.1408	3.8	0.190	0.161
E-3	0.0491	3.1	0.140	0.119
F-3	0.1410	3.1	0.138	0.117
Average			0.150	0.127

Table 8.3 Evaluated values of the induced stress.

CASE RUN	h (cm)	h_p/h	$R_e = \frac{U_m h}{\nu}$	$Fr = \frac{U_m}{\sqrt{g h}}$	$\xi_0 = \delta/h$	U^* (cm/sec)	ϵ	$U_j U_*$	R_K	α_1'	α_2'	I
D-1	7.38		0.9×10^4	0.16	3.39×10^{-1}	1.243	0.352					
E-1	7.75	0.44	1.1×10^4	0.17	4.03×10^{-1}	1.287	0.317	5.427	0.057	1.960	1.942	0.476
F-1	7.58	0.45	1.2×10^4	0.18	8.25×10^{-1}	1.327	0.260	5.287	0.409	0.743	0.708	1.355
D-2	7.38		2.6×10^4	0.47	3.39×10^{-1}	3.260	0.358					
E-2	7.59	0.45	3.0×10^4	0.45	4.12×10^{-1}	3.360	0.340	5.632	1.075	0.802	0.694	1.319
F-2	7.45	0.46	3.1×10^4	0.44	8.38×10^{-1}	3.517	0.318	5.709	2.268	0.343	0.280	2.584
D-3	7.42		4.1×10^4	0.68	3.23×10^{-1}	5.024	0.342					
E-3	8.01	0.42	4.4×10^4	0.63	3.90×10^{-1}	5.152	0.334	5.768	0.942	0.567	0.497	1.761
F-3	8.33	0.41	4.4×10^4	0.58	7.50×10^{-1}	5.421	0.270	4.479	4.900	0.541	0.389	1.958

Table 8.2 Hydraulic data for experiments.

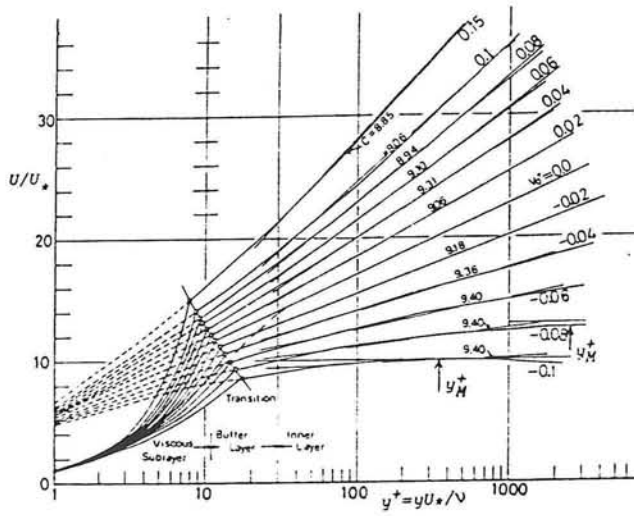


Fig. 9.1 Law of the wall with transpiration.

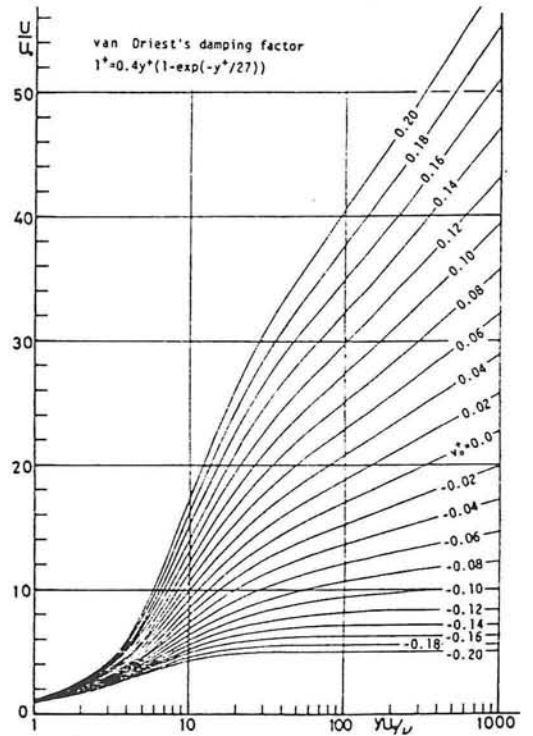


Fig. 9.2 Mean velocity distributions calculated by using *van Driest's* damping factor Γ .

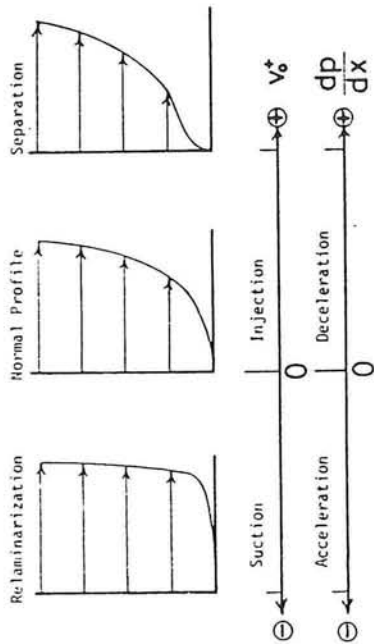


Fig. 9.3 Analogy of effects between transpiration v_w^+ and pressure gradient dp/dx .

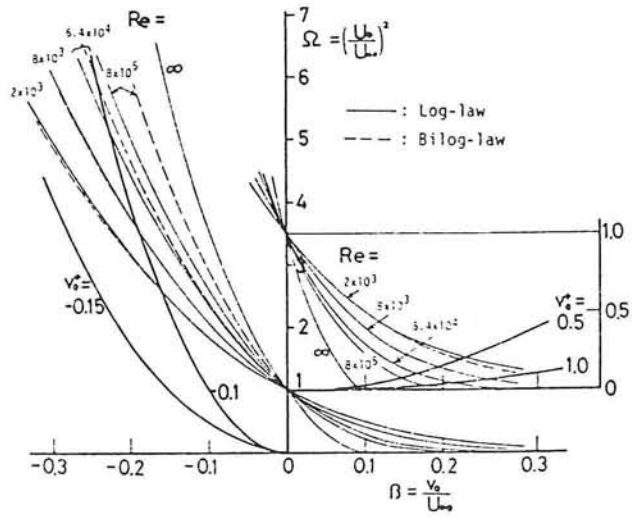


Fig. 9.4 Effects of transpiration on the wall shear stress.

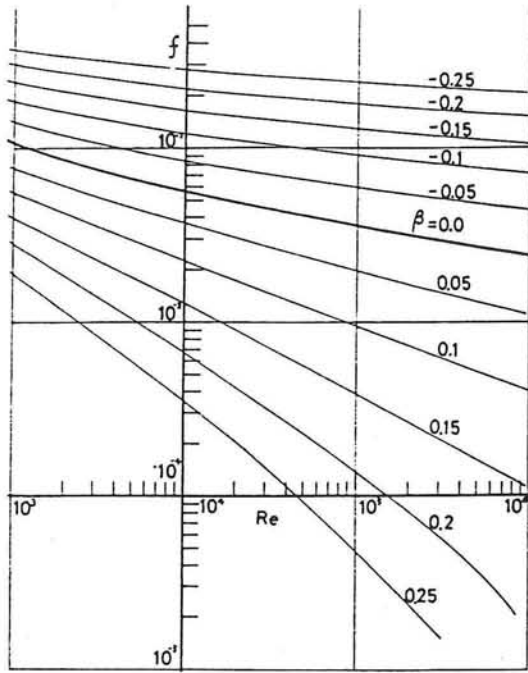


Fig. 9.5 Relationship between f and Re with transpiration.

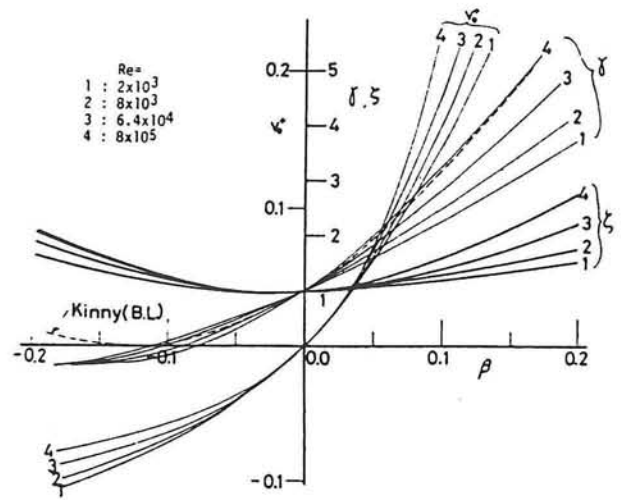


Fig. 9.8 Variation of γ , ζ and v_o^+ against β .

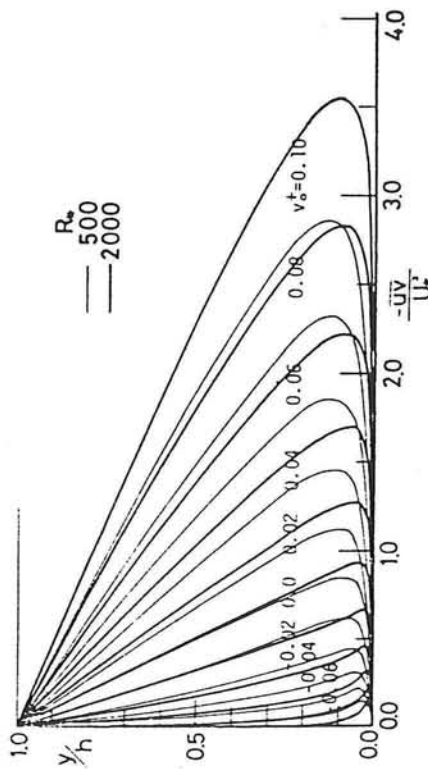


Fig. 9.6 Distributions of Reynolds stress with transpiration ($v_o^+ = v_o/U_*$).

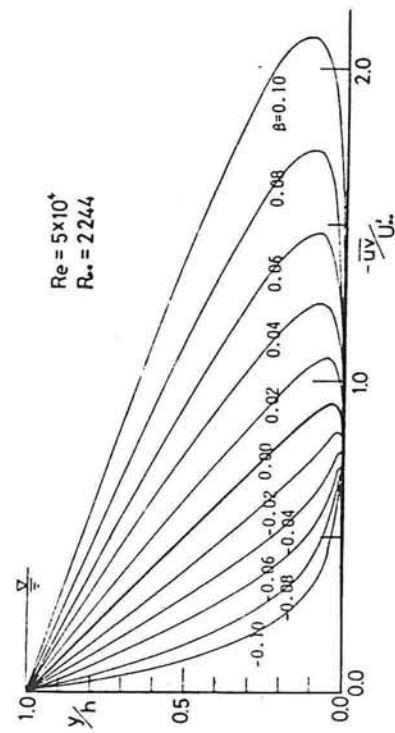


Fig. 9.7 Absolute variation of Reynolds stress by transpiration ($\beta = v_o/U_{*o}$).

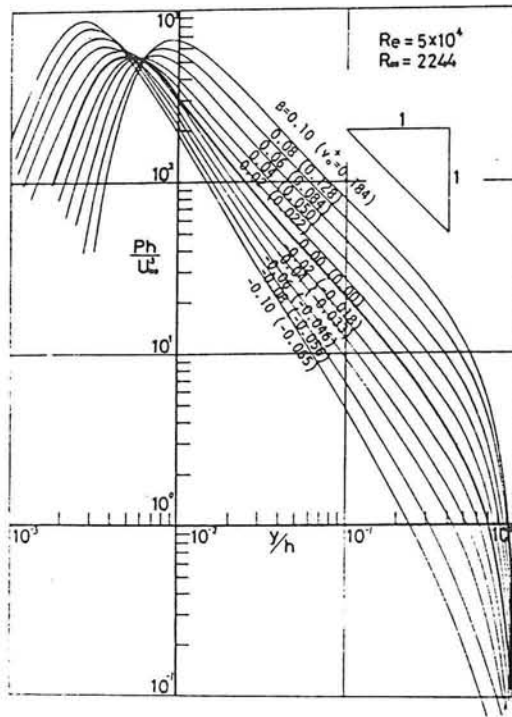


Fig. 9.9 Absolute production of turbulent energy with transpiration.

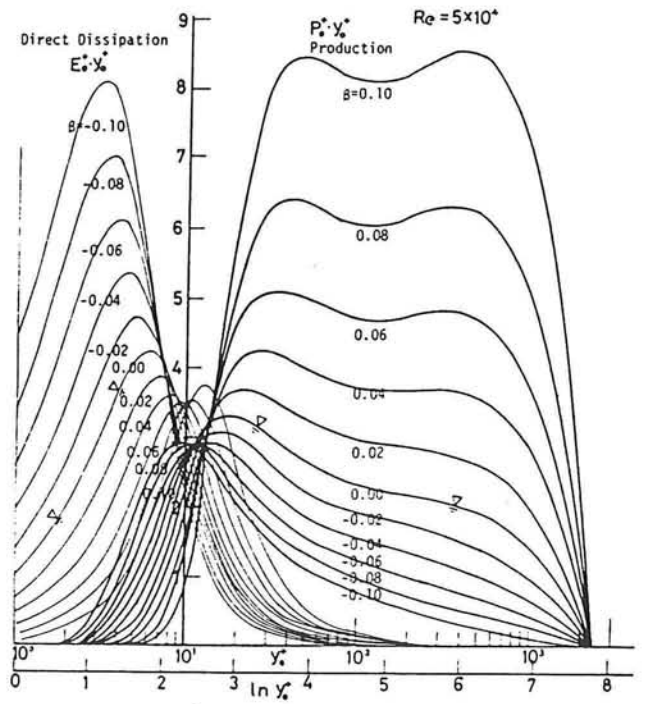


Fig. 9.10 Absolute variations of direct-dissipation and production by transpiration β .

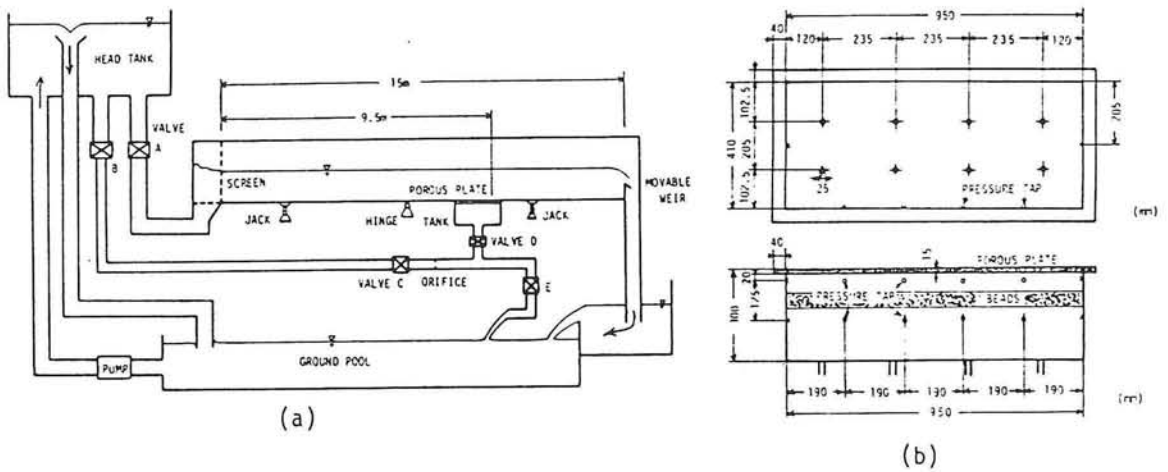


Fig. 9.11 Recirculating tilting flume and apparatus of transpiration flow.

Case	h (cm)	U_{max} (cm/s)	U_m (cm/s)	U_{*e} (cm/s)	R_{*e}	Fr	S $\times 10^{-4}$ (1/s)	Q (l/s)	T_w ($^{\circ}$ C)
H-1	8.07	17.6	14.7	0.804	609	1.11	0.165	0.08	5.92
H-2	4.10	38.8	29.4	1.773	698	1.16	0.463	5.71	6.02
H-3	3.45	44.5	34.8	1.983	669	1.17	0.598	12.8	6.00
H-4	7.94	50.4	40.1	2.150	1654	3.09	0.454	4.58	16.01

Table 9.1 Hydraulic data for experiments with transpiration.

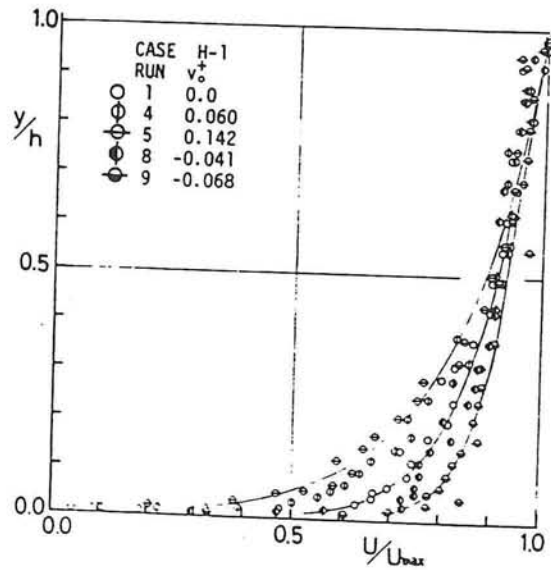


Fig. 9.12 Mean velocity profile with transpiration.

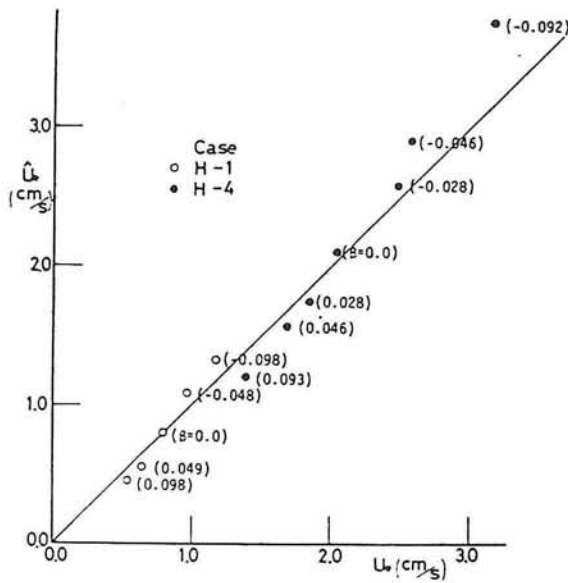


Fig. 9.13 Comparison between u_* and δ_* .

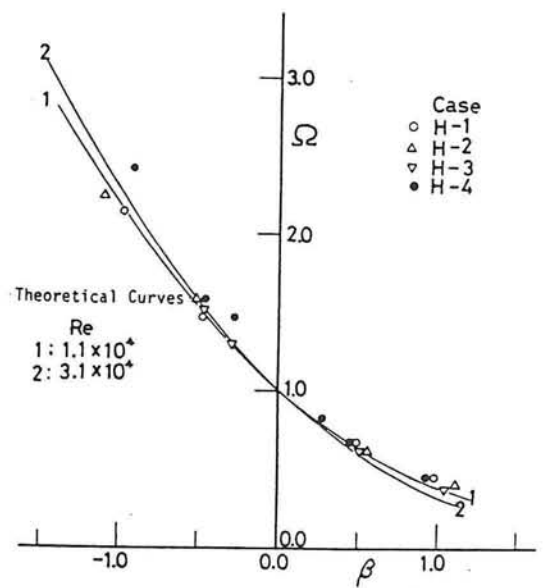


Fig. 9.14 Variation of wall shear stress by transpiration.

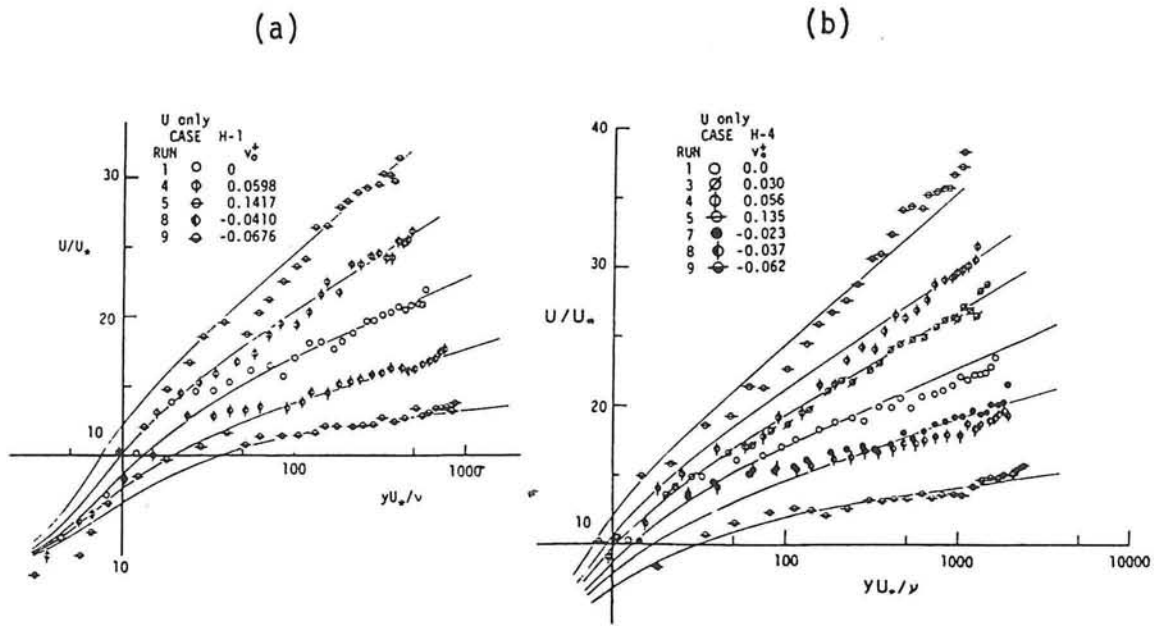


Fig. 9.15 Mean velocity distributions u/u_* (Log-law).

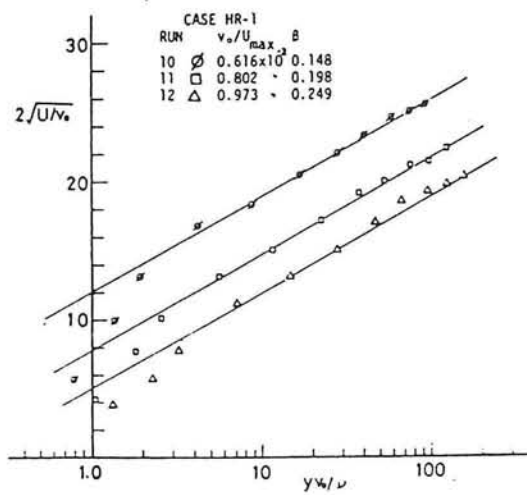


Fig. 9.16 Mean velocity distribution with strong injection.

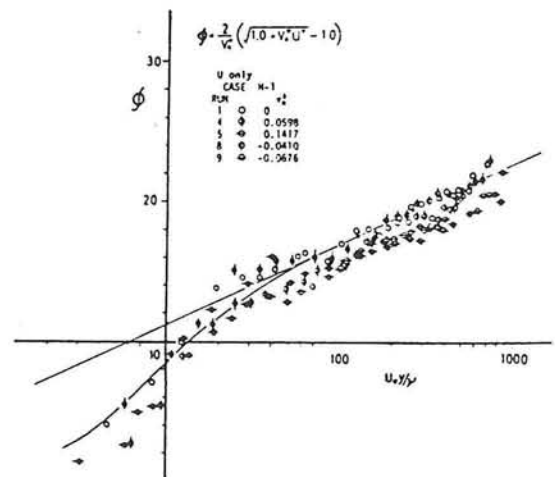


Fig. 9.17 Mean velocity distributions ϕ (Bilog-law).

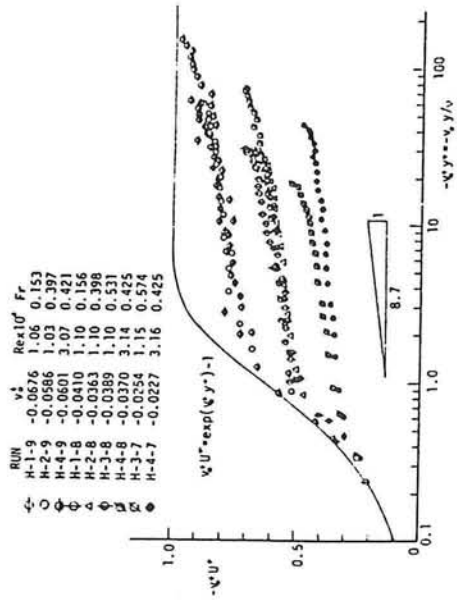


Fig. 9.18 Tennekes' expression with suction.

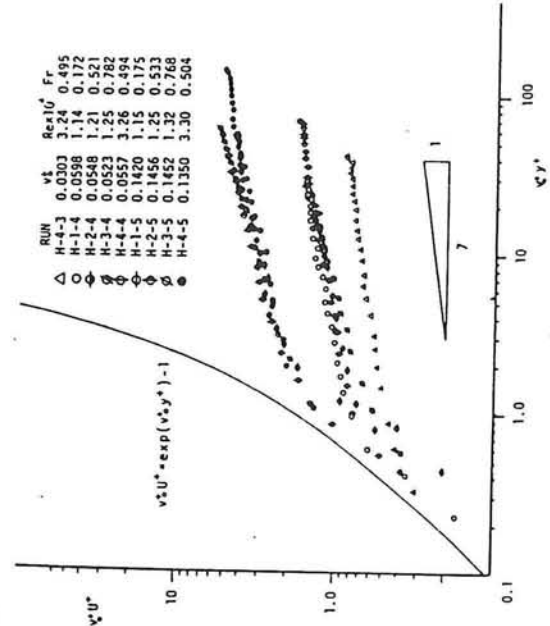


Fig. 9.19 Tennekes' expression with injection.

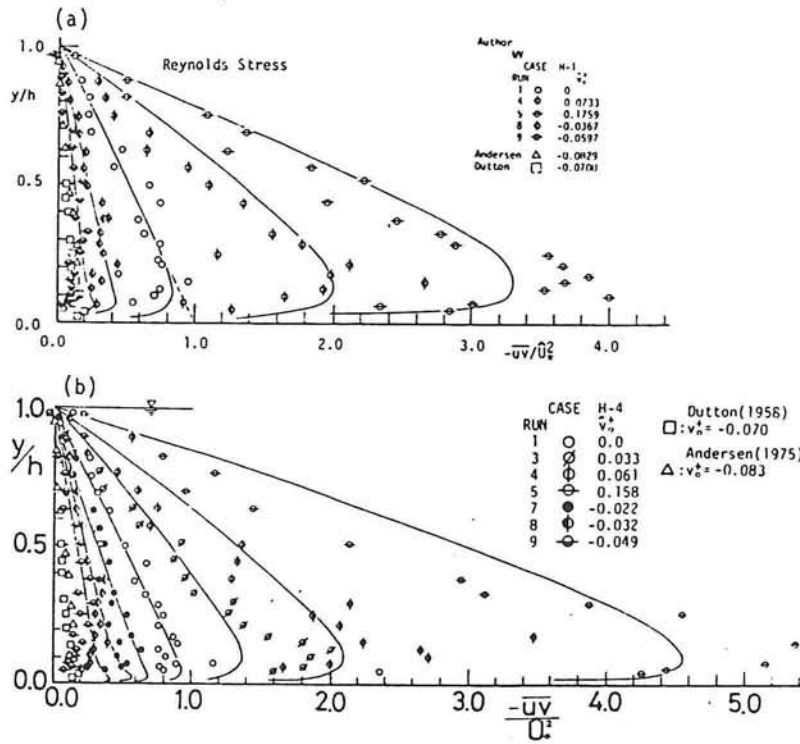


Fig. 9.20 Distributions of Reynolds stress with transpiration.

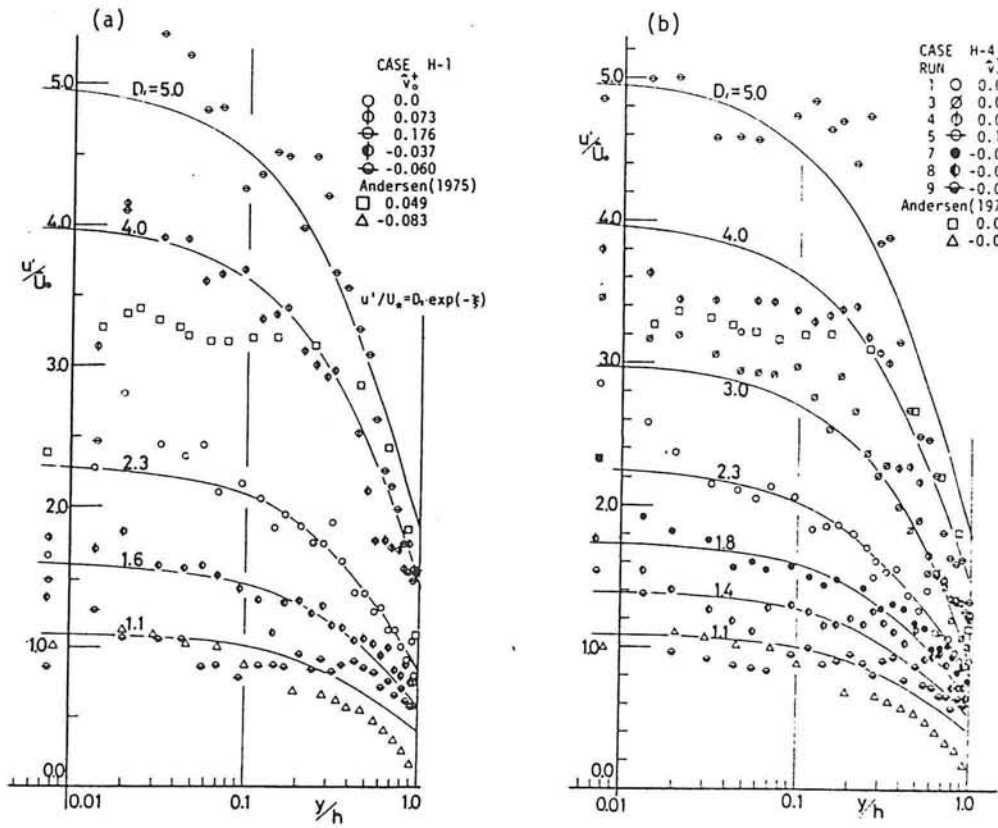


Fig. 9.21 Turbulence intensity u'/\hat{U}_* with transpiration.

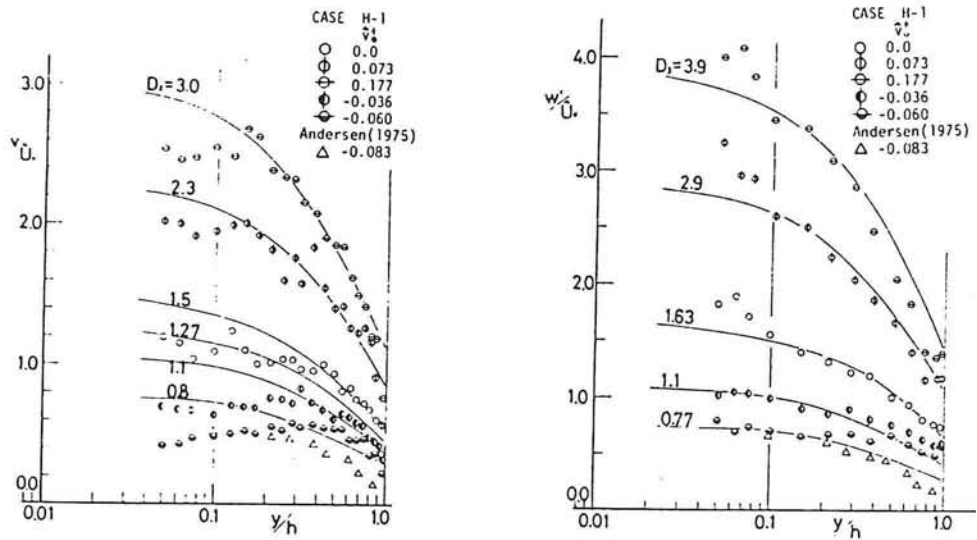


Fig. 9.22 v'/\hat{U}_* with transpiration.

Fig. 9.23 w'/\hat{U}_* with transpiration.

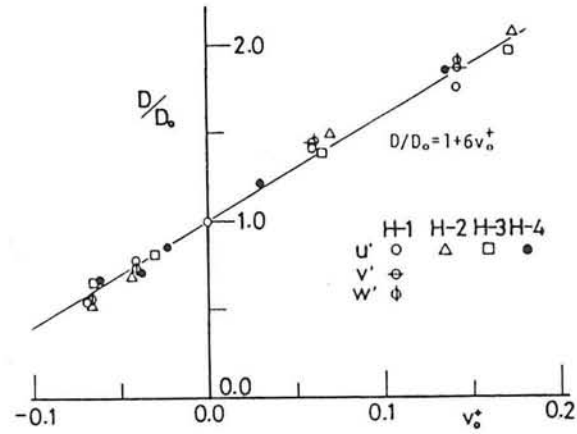


Fig. 9.24 Relationship between D and v_{*o}^+ .

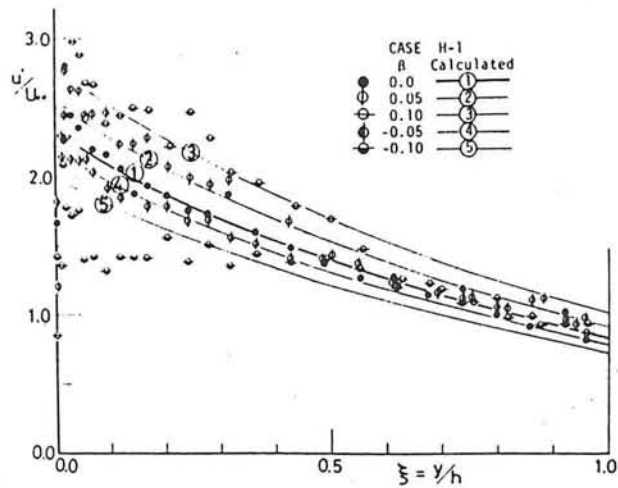


Fig. 9.25 Absolute variation of turbulence intensity u'/U_{*o} .

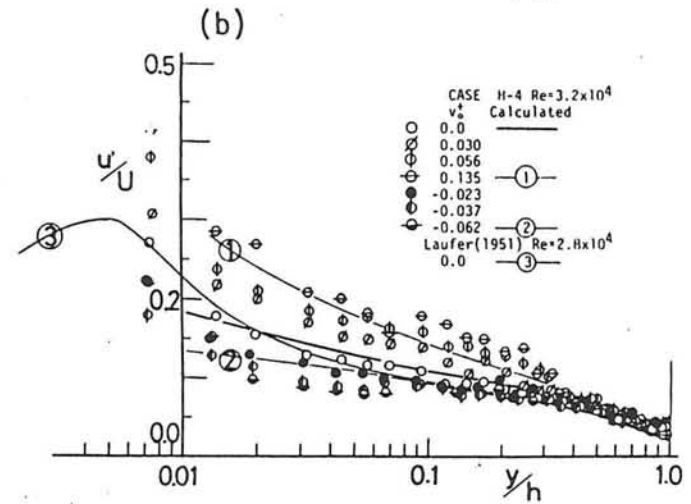
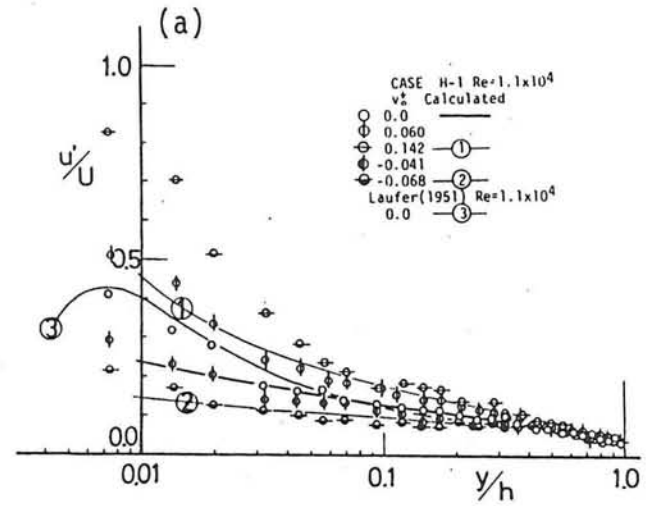


Fig. 9.26 Relative turbulence intensity u'/U with transpiration.

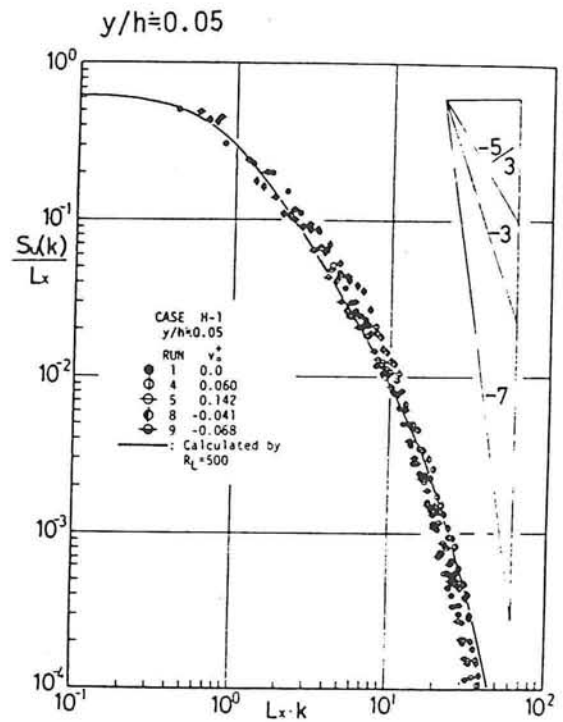
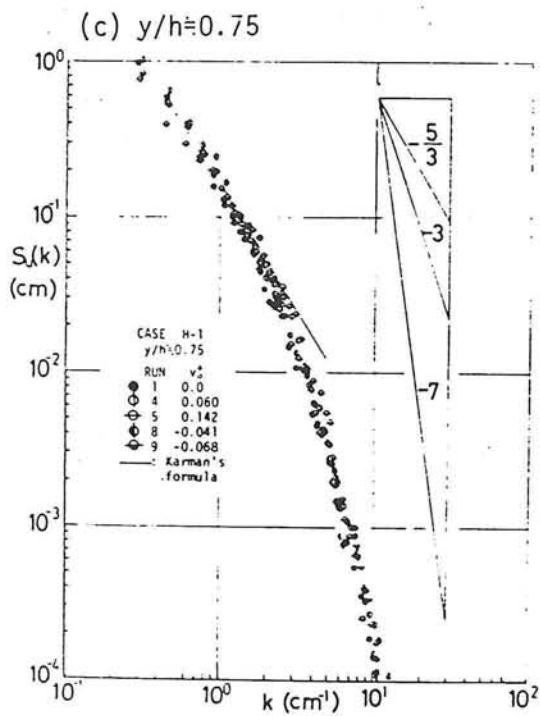
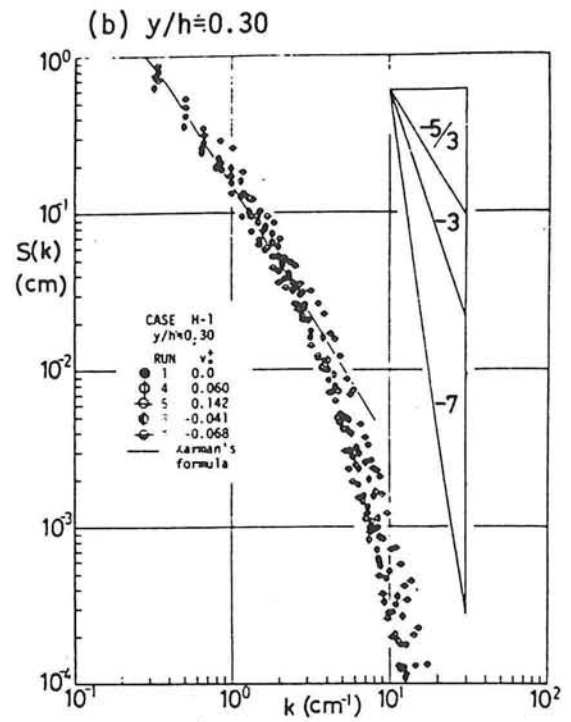
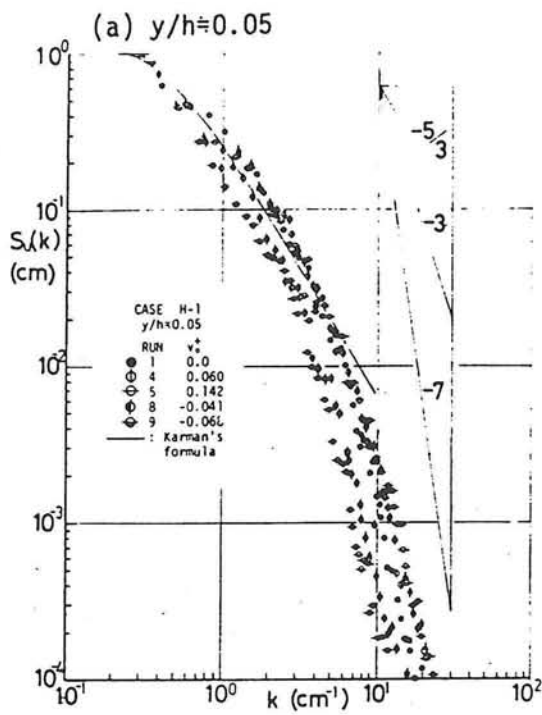


Fig. 9.27
 Spectral distributions $S_u(k)$
 with transpiration.

Fig. 9.28
 An example of spectra $S_u(k)/L_x$
 normalized by L_x .

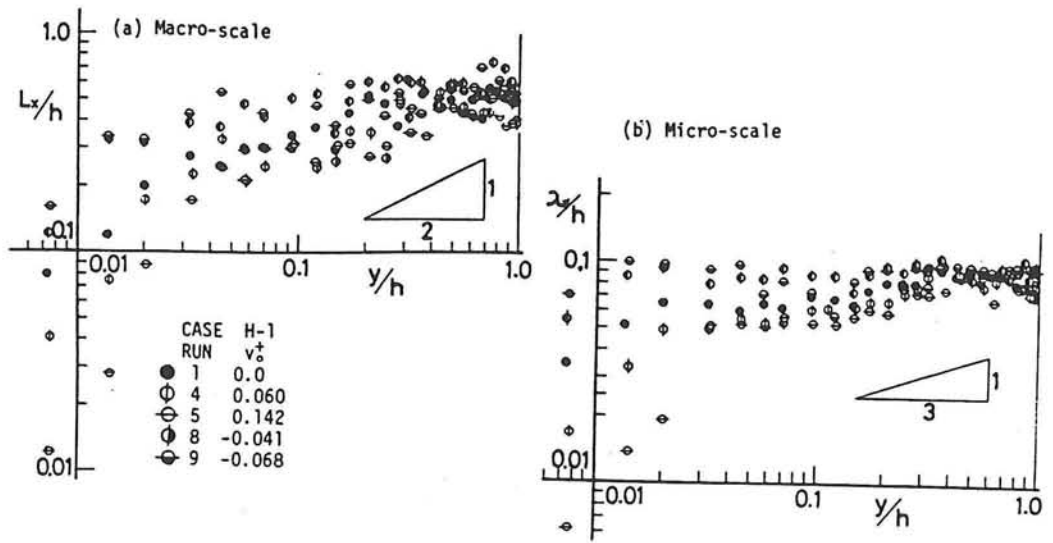


Fig. 9.29 Macro-scale L_x and micro-scale λ_x with transpiration.

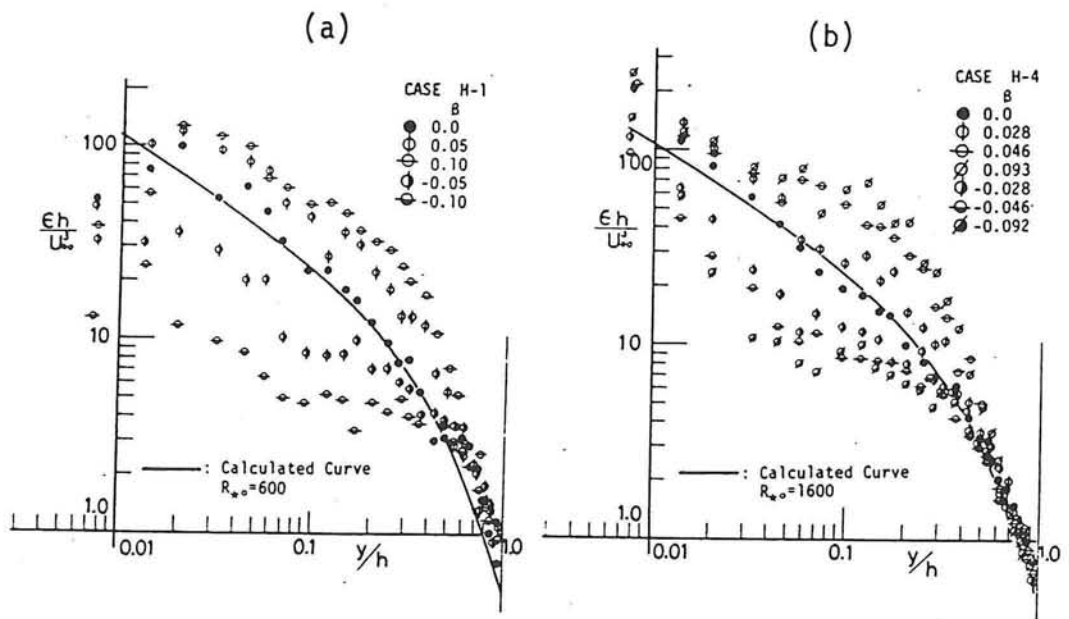


Fig. 9.30 Absolute variations of turbulent dissipation $\epsilon h/U_*^3$.

